Crashworthiness Optimization using difference-based equivalent static Loads

Sizing and Topology Optimization of Structures subjected to Crash
Zur Erlangung des akademischen Grades Doktor-Ingenieur (Dr.-Ing.)
Genehmigte Dissertation von Jens Triller aus Aschaffenburg
Tag der Einreichung: 24.10.2022, Tag der Prüfung: 24.01.2023

1. Gutachten: Prof. Dr. rer. nat. Oliver Weeger
2. Gutachten: Prof. Dr. rer. nat. Lothar Harzheim
Darmstadt, Technische Universität Darmstadt

Mechanical Engineering Department

Fachgebiet Numerische Berechnungsverfahren im Maschinenbau

Crashworthiness Optimization using difference-based equivalent static Loads
Sizing and Topology Optimization of Structures subjected to Crash

Accepted doctoral thesis by Jens Triller

Date of submission: 24.10.2022
Date of thesis defense: 24.01.2023

Darmstadt, Technische Universität Darmstadt

Erklärungen laut Promotionsordnung

§ 8 Abs. 1 lit. c PromO

Ich versichere hiermit, dass die elektronische Version meiner Dissertation mit der schriftlichen Version übereinstimmt.

§ 8 Abs. 1 lit. d PromO

Ich versichere hiermit, dass zu einem vorherigen Zeitpunkt noch keine Promotion versucht wurde. In diesem Fall sind nähere Angaben über Zeitpunkt, Hochschule, Dissertationsthema und Ergebnis dieses Versuchs mitzuteilen.

§ 9 Abs. 1 PromO

Ich versichere hiermit, dass die vorliegende Dissertation selbstständig und nur unter Verwendung der angegebenen Quellen verfasst wurde.

§ 9 Abs. 2 PromO

Die Arbeit hat bisher noch nicht zu Prüfungszwecken gedient.

Darmstadt, 24.10.2022 _____ *J. Triller* _____

Acknowledgment

List of Publications

Papers published in journals or at conferences during the course of the PhD are listed below. This thesis contains some of the illustrations and ideas published therein.

Triller, Jens, Rainer Immel, and Lothar Harzheim (2020). "Nichtlineare dynamische Strukturoptimierung unter Berücksichtigung der Deformationsgeschichte mit differenzenbasierten äquivalenten statischen Lasten". In: *NAFEMS Online-Magazin* 55.3, pp. 74–80. ISSN: 2311-522X.

Triller, Jens, Rainer Immel, and Lothar Harzheim (2022a). "Difference-based Equivalent Static Load Method with adaptive time selection and local stiffness adaption". In: *Structural and Multidisciplinary Optimization* 65 (89). DOI: `10.1007/s00158-021-03160-2`.

Triller, Jens, Rainer Immel, and Lothar Harzheim (2022b). "Topology optimization using difference-based equivalent static loads". In: *Structural and Multidisciplinary Optimization* 65 (226). ISSN: 1615-1488. DOI: `10.1007/s00158-022-03309-7`.

Triller, Jens, Rainer Immel, Alexander Timmer, and Lothar Harzheim (2019). "Difference-based Equivalent Static Load (DiESL) Method , an extension of the ESL method to improve the nonlinear approximation quality". In: *Proceedings of the 13th World Congress of Structural and Multidisciplinary Optimization*. Beijing.

Triller, Jens, Rainer Immel, Alexander Timmer, and Lothar Harzheim (2021). "The difference-based equivalent static load method: an improvement of the ESL method's nonlinear approximation quality". In: *Structural and Multidisciplinary Optimization* 63.6, pp. 2705–2720. ISSN: 16151488. DOI: `10.1007/s00158-020-02830-x`.

Abstract

Structural optimization of crash related problems usually involves nonlinearities in geometry, material, and contact. For such kinds of problems, the sensitivities are either not available or very expensive to compute. Efficient gradient-based optimizers can then not be employed directly. The *Difference-based Equivalent Static Load* (DiESL) method provides a procedure to circumvent the sensitivity calculation of the original nonlinear dynamic problem by creating linear auxiliary load cases enabling gradient-based optimization. Each linear auxiliary load case then represents one specific time step of the original nonlinear dynamic problem.

In this thesis various extensions of the DiESL method are presented and the method is compared to several other relevant approaches in this field. It is demonstrated how an appropriate selection of the time steps in each cycle can improve the DiESL method's approximation quality. For this purpose, the time steps are selected adaptively such that an appropriate curve, indicating the structure's nonlinear behavior, is fitted by the selected time steps. It turns out that this leads to better optimization results and more reliable convergence behavior.

The DiESL method also enables the adaption of path-dependent structural properties of the original nonlinear dynamic problem like material stiffness in each linear auxiliary load case. In this thesis, an adaption of the Young's modulus and Poisson's ratio on element level in the linear auxiliary load cases corresponding to the local plasticization in the nonlinear dynamic problem is tested. Therefore, a bilinear material model is employed in the auxiliary load cases. Here, the test examples indicate that an observable improvement can only be obtained if the material of the nonlinear dynamic problem is also idealized bilinearly and the portion of elements in the elastic and the plastic range is balanced such that the structure's behavior is not dominated by one of both.

Crashworthiness design usually involves two contradictory objectives: the structure's stiffness as well as its energy absorption behavior. To be able to address the latter, an approach for handling crash forces with the DiESL method is developed and tested using sizing optimization examples. The respective results are validated by comparing them to the theoretically known optimum or other state of the art methods.

Moreover, the DiESL method is extended to topology optimization utilizing the *Solid Isotropic Material with Penalization* approach (SIMP). The method is tested using three examples. The first is a rigid pole colliding with a simple beam structure, where the intrusion of the pole is minimized. The initial velocity of the pole is varied in order to examine the influence of inertia effects on the optimized structures. It is shown

that the results differ significantly depending on the chosen initial velocity and, consequently, that they exhibit inertia effects. Moreover, considerable improvement in terms of the resulting objective function's value could be achieved employing the DiESL method when compared with the standard ESL method for high initial velocities. The second example is an extruded rocker colliding with a rigid pole, where also the intrusion of the pole is minimized. The DiESL method yields equally good results as the Graph and Heuristic Topology optimization (GHT) approach does. However, the number of nonlinear analyses necessary to achieve convergence is significantly smaller when using the DiESL method. Finally, a rail reinforced by an additive manufactured rib is optimized. Here, several optimization runs are executed. The reaction force is maximized, while the mass of the rib is constrained to various fractions of the original rib's mass. This formulation aims to find designs where the original rib's mass and thus the related production cycle time is reduced, while its stiffness is almost maintained. In doing so a mass reduction of 30 % could be achieved.

Zusammenfassung

Die Strukturoptimierung von Crash-Problemen beinhaltet in der Regel Nichtlinearitäten in Geometrie, Material und Kontakt. Für diese Art von Problemen sind die Sensitivitäten entweder nicht verfügbar oder sehr teuer zu berechnen. Effiziente gradientenbasierte Optimierer können dann nicht direkt eingesetzt werden. Die DiESL-Methode (Difference-based Equivalent Static Load) bietet ein Prozedere zur Umgehung der Sensitivitätsberechnung des ursprünglichen nichtlinearen dynamischen Problems, indem lineare Hilfslastfälle erstellt werden, die eine gradientenbasierte Optimierung ermöglichen. Jeder lineare Hilfslastfall repräsentiert dann einen spezifischen Zeitschritt des ursprünglichen nichtlinearen dynamischen Problems.

In dieser Arbeit werden verschiedene Erweiterungen der DiESL-Methode vorgestellt und die Methode mit verschiedenen relevanten Ansätzen auf diesem Gebiet verglichen. Es wird gezeigt, wie eine geeignete Wahl der Zeitschritte in jedem Zyklus die Approximationsqualität der DiESL-Methode verbessern kann. Dafür werden die Zeitschritte adaptiv so gewählt, dass der zeitliche Verlauf einer Strukturantwort, die das nichtlineare Verhalten der Struktur anzeigt, durch die gewählten Zeitschritte gefittet wird. Es zeigt sich, dass dies zu besseren Zielfunktionswerten und einem zuverlässigeren Konvergenzverhalten führt.

Die DiESL-Methode ermöglicht auch die Anpassung von Pfad-abhängigen Struktureigenschaften des ursprünglichen nichtlinearen dynamischen Problems wie z.B. der Materialsteifigkeit in jedem linearen Hilfslastfall. In dieser Arbeit wird eine Anpassung des Elastizitätsmoduls auf Elementebene in den linearen Hilfslastfällen entsprechend der lokalen Plastifizierung im nichtlinearen dynamischen Problem getestet. Dazu wird ein bilineares Materialmodell in den Hilfslastfällen verwendet. Dabei zeigen die Versuchsbeispiele, dass eine erkennbare Verbesserung nur dann erreicht werden kann, wenn das Materialmodell des nichtlinearen dynamischen Problems ebenfalls bilinear ist und wenn weder die Elemente im elastischen noch im plastischen Bereich das Verhalten der Struktur dominieren.

Bei der Optimierung von Crashlastfällen werden oft zwei widersprüchliche Ziele verfolgt: die Maximierung der Steifigkeit der Struktur und die Optimierung des Energieabsorptionsverhalten. Um Letzteres adressieren zu können, wird ein Ansatz zur Behandlung von Kontaktkräften mit der DiESL-Methode entwickelt und anhand von verschiedenen Beispielen getestet. Dabei wurden gute Ergebnisse im Vergleich zum theoretisch bekannten Optimum und anderen State-of-the-Art-Methoden erzielt.

Darüber hinaus wird die DiESL-Methode zum Zweck der Topologie-Optimierung unter Verwendung des SIMP-Ansatzes (Solid Isotropic Material with Penalization) erweitert. Die Methode wird anhand von drei Beispielen getestet. Das erste Beispiel ist ein nicht deformierbarer Pfahl, der mit einer einfachen

Balkenstruktur kollidiert, wobei das Eindringen des Pfahls minimiert werden soll. Die Anfangsgeschwindigkeit des Pfahls wird variiert, um den Einfluss von Trägheitseffekten auf die optimierten Strukturen zu untersuchen. Es zeigt sich, dass sich die Ergebnisse je nach gewählter Anfangsgeschwindigkeit deutlich unterscheiden und folglich Trägheitseffekte berücksichtigt werden. Die Ergebnisse der DiESL-Methode zeigen eine erhebliche Verbesserung im Vergleich zur standard ESL-Methode für hohe Geschwindigkeiten. Das zweite Beispiel ist eine gezogene Profilstruktur, die mit einem starren Pfahl kollidiert, wobei auch hier die Intrusion des Pfahls minimiert wird. Die DiESL-Methode liefert ebenso gute Ergebnisse wie der Ansatz der Graph und Heuristik basierten Topologie Optimierung (GHT). Allerdings ist die Anzahl der nichtlinearen Analysen, die notwendig sind, um Konvergenz zu erreichen, bei der DiESL-Methode deutlich geringer. Schließlich wird ein durch eine additiv gefertigte Rippe verstärkter Träger optimiert. Hier werden mehrere Optimierungsläufe durchgeführt. Die Reaktionskraft wird maximiert, während die Masse der Rippe auf verschiedene Bruchteile der Masse der ursprünglichen Rippe beschränkt wird. Diese Formulierung zielt darauf ab, Designs zu finden, bei denen die Masse der ursprünglichen Rippe und dadurch indirekt die Produktionszeit der Rippe reduziert wird, während die Steifigkeit der Rippe nahezu erhalten bleibt. Auf diese Weise konnte eine Massenreduzierung von 30 % erreicht werden.

Contents

List of Acronyms

AT	Adaptive Selection of ESL Times
CA	Cellular Automaton
DiESL	Difference-based Equivalent static Load
DiESLs	Difference-based Equivalent static Loads
DoE	Design of Experiments
EA	Evolutionary Algorithms
ES	Evolutionary Strategy
ESL	Equivalent static Load
ESLs	Equivalent static Loads
ET	Equidistant Distribution of ESL Times
Euro NCAP	European New Car Assesment Programm
EQD	Equidistant spacing of initial ESL times for AT
FEM	Finite Element Method
FEA	Finite Element Analysis
GA	Genetic Algorithms
GHT	Graph and Heuristic Topology Optimization
HCA	Hybrid Cellular Automaton
HPC	High Performance Cluster
LA	Local Adaption of Young's Moduli in LSMs
LSM	Linear Submodel
MMA	Method of Moving Asymptotes
MMO	Multiple Model Optimization
NLA	No local Adaption of Young's Moduli in LSMs
RAMP	Rational Approximation of Material Properties
RSM	Response Surface Model
SBR	Initial ESL times for AT determined by sucessive breakpoint removal
SIMP	Solid Isotropic Material Penelization
SPC	Single Point Constraint
SRSM	Successive Response Surface Method
SSR	Sum of Squared Residuals
STOA	Strength Two Orthogonal Array

List of Symbols

$\mathbf{u}(t)$ Displacements at a specific time t calculated in the analysis domain. Vectors are bold and upright

$\mathbf{u}$ Displacement response of the sub problem solved in the design domain

$\mathbf{u}_j$ Displacement vector of the jth node ($j = 1, ..., n_{\text{N}}$)

$u_{j,l}$ l^{th} component of the displacement of the jth node

$\mathbf{t}$ All ESL times at which the original problem is approximated

t^i The ith ESL time

$_k\square$ The left subscript denotes the cycle

$^m\square$ The left superscript denotes the iteration

$\square^i$ The right superscript denotes the correspondance to the time t^i

LSM^i i^{th} static submodel, which has the same shape as the problem to be approximated at $t \approx t^i$

$\mathbf{u}^i$ Displacement response of the sub problem corresponding to a discret time t^i

$_k\mathbf{u}$ Displacement response of the kth cycle.

$_k^0\mathbf{u}$ Displacement response at the beginning of the static response optimization of cycle k

$_k^m\mathbf{u}$ Displacement response of the mth iteration of the static response optimization of cycle k.

$_k^*\mathbf{u}$ Displacement response resulting of the linear static response optimization of cycle k

$_*\mathbf{u}$ Displacement response in the cycle the DiESL algorithm terminated

$\boldsymbol{\Delta}\mathbf{u}^i$ Incremental displacements reaching from $\mathbf{u}(t^i)$ to $\mathbf{u}(t^{i+1})$

$\mathbf{r}^i$ Contains the coordinates of all nodes of the LSM^i

V Volume

S Surface

$\mathbf{f}$ Force vector

$\mathbf{f}_{\text{int}}$ Internal force vector

$\mathbf{f}_{\text{ext}}$ External force vector

$\mathbf{f}_{\text{ESL}}^i$ Equivalent static load in i^{th} subcase

$\boldsymbol{\Delta}\mathbf{f}_{\text{DiESL}}^i$ Difference-based equivalent static load in LSM^i

$\mathbf{L}$ Operator matrix

$\mathbf{H}$ Shape function's matrix

$\mathbf{B}$ Strain-displacement matrix

$\mathbf{C}$ Material matrix

$\mathbf{M}$	Mass matrix
$\mathbf{D}$	Damping matrix
$\mathbf{K}$	Linear stiffness matrix
$\mathbf{K}^i$	Stiffness matrix of the LSM^i.
$\mathbf{K}^0$	Stiffness matrix of the undeformed model
$\mathbf{K}_{\mathrm{NL}}$	Nonlinear stiffness matrix
σ	Stress
σ_{y}	Yield stress
E	Young's modulus
E_{H}	Hardening modulus
ε	Strain
ε_{e}	Elastic strain
ε_{p}	Plastic strain
ρ	Density
d	Maximum intrusion
n_{D}	Number of design variables
n_{N}	Number of nodes
n_{E}	Number of elements
n_{IC}	Number of inequality constraints
n_{EC}	Number of equality constraints
n_{T}	Number of selected ESL times
$n_{\mathcal{T}}$	Number of possible ESL times or number of available data sets
ϵ_{g}	Maximum tolerated constraint violation for convergence
ϵ_{f}	Maximum tolerated change of the objective function for convergence
ϵ_{D}	Maximum tolerated discreteness change for convergence
δ	Move limit
β	Move limit reduction factor
$\mathbf{x}$	Design variables
$f(\mathbf{x})$	Objective function
$\mathbf{p}$	Search direction
α	Step size
χ_i	Artificial density of i-th element used in the analysis domain
ξ_i	Normalized stiffness of i-th element
D	Discreteness index
ϵ_{vf}	Threshold for the interpretation of density fields resulting of linear static response optimization to derive 0-1 design
ϵ_{v}	Threshold for the interpretation of density fields resulting of linear static response optimization. Elements with densities smaller ϵ_{v} will be deleted (voids)
ϵ_{s}	Threshold for the interpretation of density fields resulting of linear static response optimization. Elements with densities greater ϵ_{s} will be interpreted as solid
Z	Total thickness of solid elements used to model sub-scale shell structure of thickness ζ
ζ	Thickness of sub-sclae shell element modeled by solid elements with bigger thickness Z

List of Figures

1 Introduction

1.1 Motivation

Structural optimization is to be understood as finding a structure's optimal size, shape and/or topology for a set of specified load cases, objective and constraints. The analysis of the structure's behavior in each defined load case is the basis of the optimization. This analysis is usually carried out employing numerical simulations. A prominent approach to do so is the Finite Element Method (FEM). Just as FEM-based simulation is taking an increasingly large role in the development processes in industry, so is structural optimization. Structural optimization is an essential part of the design process in many fields of industry and provides many benefits. Its effective usage can further shorten the development process, save materials, increase the products performance in a desired way and ultimately reduce costs.

This potential is also being leveraged in the automotive industry. One of the most challenging applications is the optimization of crash load cases. During the development of a car, requirements on the car's performance during a crash event need to be fulfilled. These requirements are often related to the occupant's or pedestrian's safety, but can also address potential repair costs and, depending on this, insurance premiums. In this context, both the structure's stiffness as well as its potential to absorb kinetic impact energy are important design criteria. For instance, in order to protect the occupant, parts of the vehicle must be stiff enough to ensure the occupant is not hit by deforming parts in the event of a crash. On the other hand, parts of the car must be able to transform the kinetic impact energy into plastic strain energy and heat. Structural optimization can be a valuable tool to meet those requirements while simultaneously minimizing the car's mass, for example. For this purpose the used optimization algorithm must be able to handle structural responses like displacements quantifying e.g. an impactor's intrusion into the vehicle and accelerations as well as crash forces.

For linear static problems efficient gradient-based optimization methods are at hand and a huge number of design variables can be handled, where the design variables are variable properties of the structure to be optimized. This is not the case when it comes to problems of nonlinear dynamic nature like crash events. Then, a transient problem involving dynamics and nonlinearities in geometry, material and contact needs to be solved. As a result the computational costs for analyzing the structural responses increase massively. In order to keep the computational effort manageable, *explicit time integration* is applied for the analysis. The sensitivities of the structure with regard to a change of the design variables can then

only be determined at considerable computational cost and gradient-based optimization cannot be applied efficiently. Instead, gradient free optimization methods like *evolutionary algorithm* and metamodel-based methods like for example *neural networks* or *kriging* are often used. The drawback of these optimization methods is that the number of design variables is limited to a small number, as the computational effort required increases drastically with the number of design variables. Applications involving a huge number of design variables such as topology optimization are not applicable in this case.

Therefore, current research focuses on alternatives circumventing the calculation of sensitivities of the nonlinear dynamic system and keeping the number of nonlinear dynamic analyzes at a reasonable level. One possibility is to define linear auxiliary load cases enabling linear static response optimization based on nonlinear dynamic analysis. The Equivalent Static Load (ESL) method (Park 2011) provides a procedure to compute such auxiliary load cases. For a selected number of representative time steps, a set of equivalent static loads (ESLs) is computed such that the resulting displacement field in linear statics is identical to the respective field in nonlinear dynamic analysis at the selected times. For each set of ESLs one auxiliary load case is then created by applying the loads to the structure's undeformed initial geometry in linear statics. However, referencing the undeformed geometry in each auxiliary load case leads to some limitations and disadvantages. To overcome these issues the Difference-based Equivalent Static Loads (DiESL) method has been introduced previously for sizing optimization (Triller 2019). Here the structure's displacement path derived in nonlinear dynamic analysis is split into increments each representing one time step or auxiliary load case. Difference-based Equivalent Static Loads (DiESLs) are then calculated to create the incremental displacement field leading from one state to the subsequent deformed state in linear statics. This means the nonlinear deformation path is approximated by a sequence of linear increments. For academic examples, it has been shown that the DiESL method enables a significant increase in approximation quality of the original nonlinear dynamic problem compared to the standard ESL method. It has also been shown that the DiESL method converges to the same optimum as a state of the art metamodel-based approach while requiring significantly less nonlinear analyses. In addition, the number of nonlinear analyses does not directly depend on the number of design variables using the DiESL method. Thus, the method shows high potential for crash applications involving a huge number of design variables like topology optimization. However, problems have also been identified which prevent a robust application of the approach in an industrial context. For instance, the linear static response optimization may terminate with an error before an optimal design could be derived, due to excessively deformed elements and thus poor element quality in intermediate auxiliary load cases. Furthermore, the method has only been tested for stiffness optimization applications yet. The incorporation of other crash relevant structural responses like for example crash forces is not straight forward, since all the applied DiESLs remain constant throughout the linear static response optimization.

1.2 Research Objective

The overall objective of this work can be formulated as follows: The development of an approach for the optimization of structures subjected to crash events involving a huge number of design variables. This includes the capability to perform topology optimization tasks. For this purpose, the previously introduced DiESL method is extended to topology optimization and examined for further potential improvements. In order to enable a robust and efficient application of the methodology in an industrial context several requirements are to be addressed:

Commercial solvers are to be used for analysis and optimization. Not only because they are efficient and are able to handle large models, but also for maintenance reasons. This also guarantees that the methodology can be quickly integrated into the product development process, as simulation models for the corresponding solvers already exist and are used throughout the entire development process.

In practice, the existing models for nonlinear dynamic analysis and linear static response optimization may differ slightly in their geometry, mesh and assembly. Therefore, the methodology must also be able to handle such non-congruent models.

Furthermore, a solution has to be developed to automatically repair the mesh in auxiliary load cases where poor element quality occurs and the optimization process is terminated with an error.

Finally, an approach should be worked out enabling the incorporation of crash forces into the optimization problem using the DiESL method. This is especially important when structural parts are optimized in terms of their energy absorption behavior.

1.3 Structure of Thesis

This thesis is structured in the following way: In chapter 2 the theoretical framework to understand structural optimization for problems of linear static as well as nonlinear dynamic nature is given. Based on this, a literature overview for nonlinear dynamic response optimization is presented and discussed. Furthermore, examples for typical crash load cases as well as the corresponding requirements are given. In chapter 3 the Difference-based Equivalent Static Load method is introduced. In that process, potential improvements are elaborated and discussed. Furthermore, an approach for handling crash forces in DiESL is introduced. Afterwards the implementation of the algorithm is detailed out. Here, the requirements formulated above with regard to a robust and efficient application of the DiESL method are specifically addressed. In chapter 4 the DiESL approach is tested using sizing optimization problems only. First, the approach is compared to the standard ESL method and a metamodel-based approach. Afterwards the elaborated improvements are tested using two different examples. Next, an approach for handling contact forces in DiESL is also tested on the basis of two sizing optimization problems. In chapter 5 the DiESL approach is extended to topology optimization. Thereby all necessary adaptions of the procedure described

in chapter 3 are elaborated. The capability of DiESL for topology optimization tasks is tested afterwards using 3 different numerical examples. Finally, a conclusion and an outlook is worked out in chapter 6.

2 Structural Optimization

2.1 Introduction

2.1.1 General Definition of an Optimization Problem

Frequently, the term optimization is misunderstood to mean "improvement" only. In the mathematical sense, however, it is a much more precise concept: finding the best possible solution of a specified problem often subjected to constraints (Martins and Ning 2021). Formally, an optimization problem can be stated as a minimization problem:

$$\min f(\mathbf{x}); \qquad \mathbf{x} \in \mathbb{R}^{n_{\mathrm{D}}} \qquad (2.1)$$

subject to

$$g_j(\mathbf{x}) \leq 0; \qquad j = 1, ..., n_{\mathrm{IC}} \qquad (2.2)$$

$$h_k(\mathbf{x}) = 0; \qquad k = 1, ..., n_{\mathrm{EC}} \qquad (2.3)$$

$$x_i^{\mathrm{L}} \leq x_i \leq x_i^{\mathrm{U}}; \qquad i = 1, ..., n_{\mathrm{D}}. \qquad (2.4)$$

The objective function $f(\mathbf{x})$ measures the system's performance which is meant to be minimized. The system's responses depend on the design variables $\mathbf{x}$ describing n_{D} variable system properties which can be changed between the explicit bounds x_i^{L} and x_i^{U} in order to minimize $f(\mathbf{x})$. Often the optimization problem is constrained. Therefore, inequality constraints $g(\mathbf{x})$ and equality constraints $h(\mathbf{x})$ may be defined if system responses have to be smaller than or equal to a certain value, respectively. The optimization problems dealt with in this thesis are nonlinear and continuous. This means the objective function and/or constraints are nonlinear functions and the design variables are real numbers and can be varied continuously.

Some optimization problems can be solved analytically. However, in practice the most are to complex to be solved this way. Then, the problem is generally solved using an iterative procedure which is illustrated in Fig. 2.1. Based on an initial design the system is analyzed and the objective function as well as all constraints are evaluated. Afterwards predefined convergence criteria are checked, to determine if it is worthwhile to continue modifying the current design. If not, the procedure terminates. Otherwise, the

design variables are further modified and the procedure is repeated. The effectiveness of this procedure depends on all 3 steps. In most cases, the analysis of the system takes the most time. However, a suitable modification of the design variables is also crucial in order to avoid unnecessary analyses.
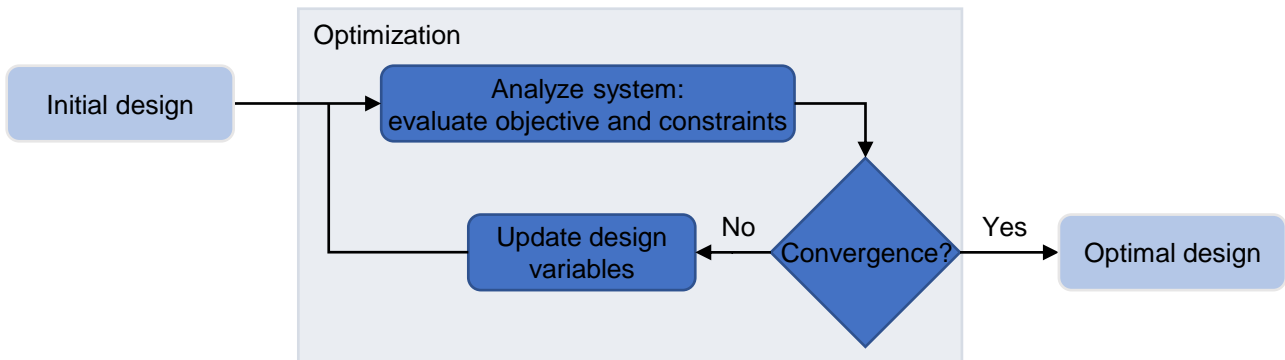
Figure 2.1: Iterative optimization procedure

In the case of structural optimization, a mechanical structure under a distinct load case needs to be analyzed. This analysis is usually performed using numerical methods. We therefore speak of simulation-based optimization. Depending on the load cases and the chosen design variables the complexity of the numerical simulation as well as the optimization can change drastically. It also has a significant impact on the time required to solve the problem under consideration. In this chapter, first different kinds of structural optimization depending on the chosen design variables are presented. Afterwards gradient based procedures to determine a suitable modification of the design variables are introduced. Then, the fundamentals of FEM for the analysis of linear static as well as nonlinear dynamic load cases are derived. Finally, it is worked out how these are embedded in the previously described optimization procedure. In particular, the challenges of nonlinear dynamic problems are discussed and an overview of state of the art optimization approaches to solve such problems is given.

2.1.2 Types of structural Optimization

Depending on the area of application and the design variables selected by the engineer, structural optimization can be divided into 3 types:

Sizing Optimization: thicknesses or cross-sectional areas are varied. The number of design variables usually is comparatively small. Sizing is the most common optimization technique used during the design process in industry. This can be attributed to the fact, that relatively small efforts have to be made for the definition and the post processing including the interpretation of results and only few manufacturing constraints are required for obtaining manufacturable designs (Gerzen et al. 2016).

Shape Optimization: the design variables describe potential shapes of the structure's contour. Determining allowable shape variations can be very time-consuming, which is why shape optimization is one of the more labor-intensive forms of optimization (Harzheim 2014).

Topology Optimization: the design variables describe the distribution of material within a defined design space. It's the most flexible type of structural optimization, since not only variations of the structure's contour are possible, but also holes in the inside can evolve (Harzheim 2014). Due to the high flexibility, topology optimization is especially employed in early stages of the design process for concept finding. The flexibility comes hand in hand with a large number of design variables. The handling of large numbers of design variables becomes challenging especially if problems of nonlinear dynamic nature are to be optimized.

The three types of structural optimization are illustrated in Fig. 2.2.
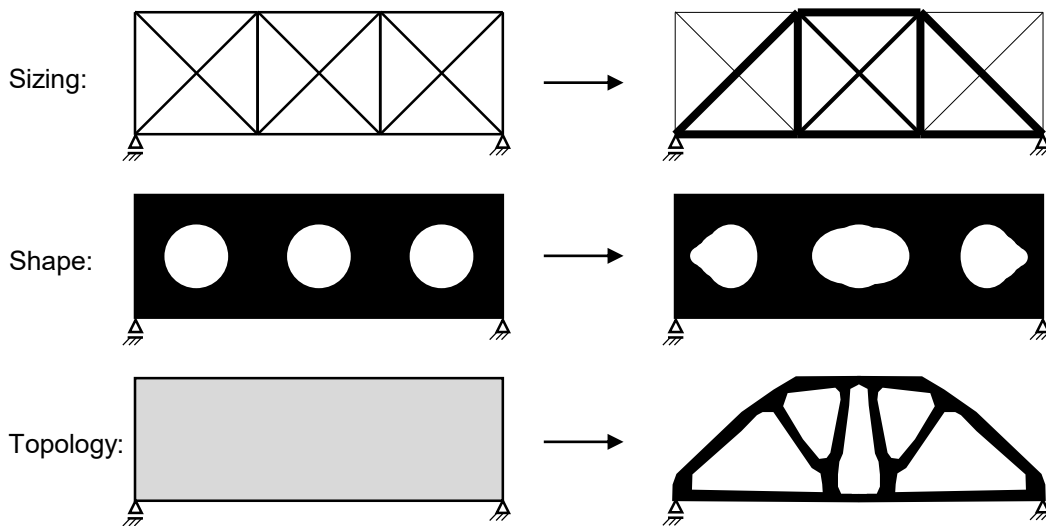
Figure 2.2: Types of structural optimization

2.1.3 Density-based Material Parametrization

In the case of topology optimization the relation between design variables and material distribution is not straight forward, as it is for sizing, where the design variables can directly be linked to sheet thicknesses or cross sectional areas. The voxel or density-based method can be used to establish a spatial relationship between the design variables and the design space (Bendsøe and Kikuchi 1988; Bendsøe and Soares 1993; Bendsøe and Sigmund 2003). Here, the design space is split into many small elements. Each element's normalized density is then related to the corresponding mechanic behavior. Elements with densities close to 0 correspond to void parts of the structure, whereas a normalized density of 1 corresponds to solid parts. This kind of relation is beneficial, since the densities can be varied continuously between the extremes

void and solid and no discrete optimization problem has to be solved. The most prominent density-based material parameterization approaches are explained in the following.

The homogenization method was used in the initial work of topology optimization of continuum structures (Bendsøe and Kikuchi 1988), where the design space is filled with a porous material. This is modeled utilizing a periodic microstructure consisting of small square or cube micro cells with rectangular holes. For the two-dimensional case the orientation of each hole can be changed by the angle Θ and the size of the hole by varying a or b respectively (Fig. 2.3). Thus, each micro cell – its density and mechanical behavior – is defined by three design variables. The normalized density of each element depends only on a and b: $\rho = 1 - ab$. The macroscopic material properties depends on all 3 design variables and can be obtained using numerical homogenization. The design variables are then optimized to maximize the performance of the structure. One of the benefits of this approach is that intermediate densities have an actual physical meaning. Unfortunately the resulting orthotropic and multi-scale structures (Wu et al. 2021) are often hard to interpret in reality due to manufacturability problems, although advances in additive manufacturing technologies are pushing the boundaries nowadays. In the past, this often led to the approach that only the material representation or densities and not the orthotropic material properties have been evaluated for the practical realization (Harzheim 2014). If the resulting design consists only of densities of $\rho = 0$ and $\rho = 1$, the orthothropic material behavior changes to isotropic material behavior in the homogenization approach. In this case, it is valid to use only the densities for the interpretation of the optimization result. Unfortunately, the homogenization approach has no inherent mechanism to enforce such designs.
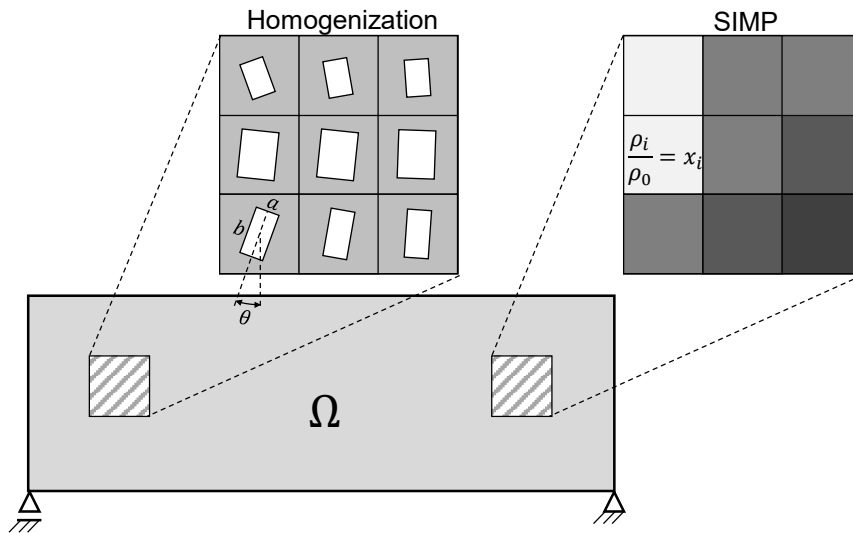
Figure 2.3: 2D example of material parametrization schemes: the homogenization approach (left) and Solid Isotropic Material Penalization (right)

The Solid Isotropic Material Penalization (SIMP) tries to overcome this issue (Bendsøe 1989; Zhou and Rozvany 1991; Bendsøe and Sigmund 1999). Here the distribution of a homogeneous isotropic material is

optimized and only one design variable x_i per element – the normalized density – is used, instead of three design variables:

$$x_i = \frac{\rho_i}{\rho_{i,1}}; \qquad i = 1, ..., n_{\mathrm{E}}, \tag{2.5}$$

where n_{E} is the number of elements and $\rho_{i,1}$ and is the density of a solid element. The normalized density is related to the element's stiffness. In order to enforce a design consisting only of solid and void elements intermediate densities are penalized using the following relation:

$$E_i = E_{i,1} x_i^p; \qquad p > 1; \qquad i = 1, ..., n_{\mathrm{E}}, \tag{2.6}$$

where E_i is the adapted Young's modulus and $E_{i,1}$ is the Young's modulus corresponding to solid elements. The relation of the normalized density and Young's modulus is illustrated in Fig. 2.4 for different exponents p. The structure's mass scales linearly with the density, but for exponents $p > 1$ the structure's stiffness scales nonlinearly. For normalized densities close to 1 an increase in density yields a high stiffness increase. Whereas, for normalized densities close to 0 the change in stiffness depending on the density is relatively small. This combination thus favors the evolution of a design consisting only of void and solid elements. In the following we will refer to such designs as 0-1 designs. For three-dimensional structures, a penalty exponent of $p = 3$ is usually chosen. The choice of higher p-values increases the risk of getting stuck in local optima (Schumacher 2020).
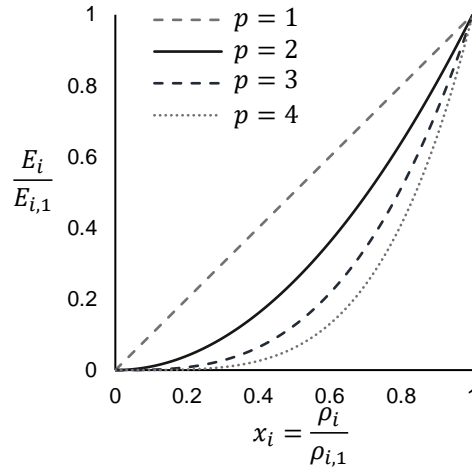
Figure 2.4: Relation between normalized density and Young's modulus using the SIMP approach with different penalty exponents

The SIMP method is the most prominent approach for topology optimization and is implemented in many commercial tools such as MSC NASTRAN, Altair OptiStruct, or VRAND GENESIS. Beside of the homogenization and the SIMP approach, there are several other methods which are worth mentioning,

but are not further elaborated here: The Soft Kill Option (SKO) (Baumgartner et al. 1992), Evolutionary Structural Optimization (ESO) (Xie and Steven 1993; Huang et al. 2010), the Phase Field method (Bourdin and Chambolle 2003), and the Level Set method (Wang et al. 2003; Allaire et al. 2004). For a comparative overview refer for example to Sigmund and Maute 2013.

2.2 Structural Analysis based on Finite Element Method

As already described, the analysis of the system to be optimized is a fundamental part of the optimization process. The Finite Element Method (FEM) is the most prominent method for structural analysis or more generally for solving partial differential equations (e.g. structural mechanics, heat transfer). The method is not only used for solving linear static, but also for nonlinear dynamic problems like crash applications. In the following the derivation and concept of linear and nonlinear FEM is explained, in order to lay a foundation for understanding the DiESL method and potential improvements and to clarify the differences and commonalities of FEM for linear static and nonlinear dynamic problems. For a more detailed explanation please refer to Bathe 1996; Wriggers 1998.

2.2.1 The weak Form

As starting point of the Finite Element approximation, the weak form of the equation of motion is used. This can be derived from the balance of momentum of a volume V with boundary S in current configuration:

$$\underbrace{\int_V \rho \ddot{\mathbf{a}} dV}_{\text{change of momentum}} = \underbrace{\int_S \boldsymbol{\Gamma} dS}_{\text{surface forces}} + \underbrace{\int_V \rho \mathbf{g} dV}_{\text{volume forces}} \qquad (2.7)$$

Where $\mathbf{a}$ denotes the displacement of an arbitrary point of the structure[1] and $\boldsymbol{\Gamma}$ the stress vector applied to the boundary S. All relevant measures and notations as well as the differences between the initial and current configuration are illustrated in Fig. 2.5.
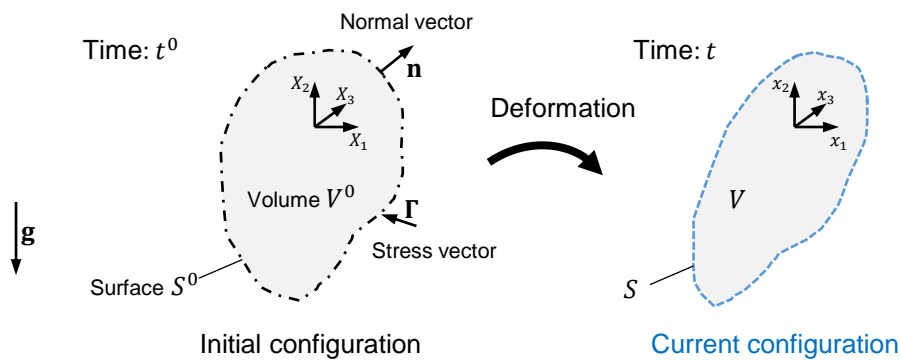
Figure 2.5: Initial and current configuration of continuum structure

Substituting $\boldsymbol{\Gamma} = \mathbf{n} \cdot \boldsymbol{\sigma}$ into equation 2.7, where $\boldsymbol{\sigma}$ is the symmetric stress tensor, and applying the divergence

---

[1]This may be unusual, but since the later introduced nodal displacements $\mathbf{u}$ of the spatially discretized equation of motion are used much more often in this thesis, the more common variable $\mathbf{u}$ is saved.

theorem yields

$$\int_V \nabla \cdot \boldsymbol{\sigma} + \rho \mathbf{g} - \rho \ddot{\mathbf{a}} \, dV = 0. \tag{2.8}$$

This must hold for each subpart of V and hence

$$\nabla \cdot \boldsymbol{\sigma} + \rho \mathbf{g} = \rho \ddot{\mathbf{a}}. \tag{2.9}$$

Employing *voigt*-notation

$$\boldsymbol{\sigma}^{\mathrm{T}} = (\sigma_{\mathrm{xx}}, \sigma_{\mathrm{yy}}, \sigma_{\mathrm{zz}}, \sigma_{\mathrm{yz}}, \sigma_{\mathrm{xz}}, \sigma_{\mathrm{xy}}), \tag{2.10}$$

the operator ∇ can be represented by the operator matrix $\mathbf{L}$

$$\mathbf{L}^{\mathrm{T}} = \begin{bmatrix} \frac{\partial}{\partial x} & 0 & 0 & 0 & \frac{\partial}{\partial z} & \frac{\partial}{\partial y} \\ 0 & \frac{\partial}{\partial y} & 0 & \frac{\partial}{\partial z} & 0 & \frac{\partial}{\partial x} \\ 0 & 0 & \frac{\partial}{\partial z} & \frac{\partial}{\partial y} & \frac{\partial}{\partial x} & 0 \end{bmatrix} \tag{2.11}$$

$$\mathbf{L}^{\mathrm{T}} \boldsymbol{\sigma} + \rho \mathbf{g} = \rho \ddot{\mathbf{a}}. \tag{2.12}$$

The weak form is now obtained by integrating over the domain V and multiplying by a virtual displacement $\delta \mathbf{a}$

$$\int_V \delta \mathbf{a}^{\mathrm{T}} \left(\mathbf{L}^{\mathrm{T}} \boldsymbol{\sigma} + \rho \mathbf{g} - \rho \ddot{\mathbf{a}} \right) dV = 0 \quad \forall \quad \delta \mathbf{a} \tag{2.13}$$

and employing the divergence theorem again

$$\int_V \left(\rho \delta \mathbf{a}^{\mathrm{T}} \ddot{\mathbf{a}} + (\mathbf{L} \delta \mathbf{a})^{\mathrm{T}} \boldsymbol{\sigma} \right) dV = \int_V \rho \delta \mathbf{a}^{\mathrm{T}} \mathbf{g} \, dV + \int_S \delta \mathbf{a}^{\mathrm{T}} \boldsymbol{\Gamma} \, dS \quad \forall \quad \delta \mathbf{a}. \tag{2.14}$$

with given boundary tractions $\boldsymbol{\Gamma} = \bar{\boldsymbol{\Gamma}}$ or alternatively boundary displacements $\mathbf{a} = \bar{\mathbf{a}}$ prescribed on the structures surface and the initial conditions $\mathbf{a}(t^0) = \mathbf{a_0}, \dot{\mathbf{a}}(t^0) = \dot{\mathbf{a}_0}$. It should be noted that for the derivation of the weak form of the equation of motion no assumptions regarding material behavior nor the magnitude of strains or displacements have been made. Consequently, equation 2.14 is valid for linear statics ($\ddot{\mathbf{a}} = 0$) as well as nonlinear dynamic problems.

2.2.2 Spatial Discretization
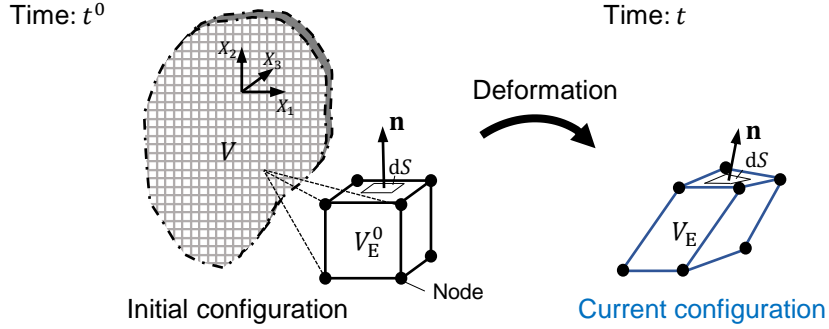
Figure 2.6: Spatial discretization using Finite Elements

Like illustrated in Fig. 2.6 the basic idea of FEM is to reduce the degree of freedom of the fundamental continuum equations to a finite number, by dividing the domain of interest into several subdomains. Therefore, the structure is discretized using finite elements connecting structural nodes. The nodal displacements then represent a finite number of unknowns. The continuous displacement field $\mathbf{a}$ can then be approximated elementwise using so-called shape functions $h_k(\mathbf{X})$ depending on the global coordinates $\mathbf{X}$: [2]

$$\mathbf{a}(\mathbf{X}) = \sum_{k=1}^{n} h_k(\mathbf{X})\mathbf{u}_k. \tag{2.15}$$

Each element is supported by n nodes and $\mathbf{u}_k$ is the displacement vector of a node containing the components $(u_\mathrm{x}, u_\mathrm{y}, u_\mathrm{z})$. The displacements of all nodes n of an element are collected in the vector

$$\mathbf{u}_\mathrm{E} = \left(\mathbf{u}_{\mathrm{E},1}^\mathrm{T}, \mathbf{u}_{\mathrm{E},2}^\mathrm{T}, ..., \mathbf{u}_{\mathrm{E},n}^\mathrm{T}\right)^\mathrm{T} \tag{2.16}$$

in matrix-vector notation the approximation of the continuous displacements within an element can be written more compact

$$\mathbf{a}(\mathbf{X}) = \mathbf{H}(\mathbf{X})\mathbf{u}_\mathrm{E} \tag{2.17}$$

where $\mathbf{H}$ is a $3 \times 3n$ matrix containing the shape functions h_k of all nodes of the used element type in an appropriate order. The global displacement vector $\mathbf{u}$ containing the displacements of all n_N nodes can be related to the e-th element's displacements $\mathbf{u}_{\mathrm{E},e}$ employing an incidence-matrix $\mathbf{Z}_{\mathrm{E},e}$, which defines the finite elements' topology:

$$\mathbf{u}_{\mathrm{E},e} = \mathbf{Z}_{\mathrm{E},e}\mathbf{u}. \tag{2.18}$$

---

[2]For generality and implementation purposes, natural coordinates are usually employed here instead of the global coordinates $\mathbf{X}$. The global coordinates are used here only for the sake of illustrating the shape function's spatial dependencies and are not further detailed.

With equations 2.17 and 2.18 the spatial discretization can be implemented in the weak form of the equation of motion 2.14 considering all n_E elements

$$
\sum_{e=1}^{n_\text{E}} \int_{V_{\text{E},e}} \rho \left(\mathbf{H} \mathbf{Z}_{\text{E},e} \delta \mathbf{u} \right)^\text{T} \mathbf{H} \mathbf{Z}_{\text{E},e} \ddot{\mathbf{u}} dV + \sum_{e=1}^{n_\text{E}} \int_{V_{\text{E},e}} \left(\mathbf{H} \mathbf{Z}_{\text{E},e} \mathbf{L} \delta \mathbf{u} \right)^\text{T} \boldsymbol{\sigma} dV
$$
$$
= \sum_{e=1}^{n_\text{E}} \int_{V_{\text{E},e}} \rho \left(\mathbf{H} \mathbf{Z}_{\text{E},e} \delta \mathbf{u} \right)^\text{T} \mathbf{g} dV + \sum_{e=1}^{n_\text{E}} \int_{S_{\text{E},e}} \left(\mathbf{H} \mathbf{Z}_{\text{E},e} \delta \mathbf{u} \right)^\text{T} \boldsymbol{\Gamma} dS. \tag{2.19}
$$

Since the incidence-matrices and the virtual displacements do not depend on the spatial coordinates they can be brought outside the integral. The virtual displacements can be brought outside the summation sign as well. Since this must hold for any virtual displacement, the semi-discrete balance of momentum follows:

$$
\mathbf{M} \ddot{\mathbf{u}} + \mathbf{f}_\text{int} = \mathbf{f}_\text{ext} \tag{2.20}
$$

with the mass matrix,

$$
\mathbf{M} = \sum_{e=1}^{n_\text{E}} \mathbf{Z}_{\text{E},e}{}^\text{T} \int_{V_{\text{E},e}} \rho \mathbf{H}^\text{T} \mathbf{H} dV \mathbf{Z}_{\text{E},e} \tag{2.21}
$$

the external force vector,

$$
\mathbf{f}_\text{ext} = \sum_{e=1}^{n_\text{E}} \mathbf{Z}_{\text{E},e}{}^\text{T} \int_{V_{\text{E},e}} \rho \mathbf{H}^\text{T} \mathbf{g} dV + \sum_{e=1}^{n_\text{E}} \mathbf{Z}_{\text{E},e}{}^\text{T} \int_{S_{\text{E},e}} \mathbf{H}^\text{T} \boldsymbol{\Gamma} dS \tag{2.22}
$$

and the internal force vector:

$$
\mathbf{f}_\text{int} = \sum_{e=1}^{n_\text{E}} \mathbf{Z}_{\text{E},e}{}^\text{T} \int_{V_{\text{E},e}} \left(\mathbf{B} \right)^\text{T} \boldsymbol{\sigma} dV \tag{2.23}
$$

where

$$
\mathbf{B} = \mathbf{L} \mathbf{H} \tag{2.24}
$$

where $\mathbf{B}$ is the strain-displacement matrix. The term $\mathbf{M} \ddot{\mathbf{u}}$ is known as inertia term, which has to be in balance with the external $\mathbf{f}_\text{ext}$ and internal forces $\mathbf{f}_\text{int}$. By introducing the kinematic (*strain-displacement*) and constitutive (*stress-strain*) relations the tangent stiffness $\mathbf{K}_\text{t}$ can be derived as $\frac{d\mathbf{f}_\text{int}}{d\mathbf{u}}$. The differences that arise depending on the chosen relations for linear statics and nonlinear dynamic problems are elaborated in the following. Note that for the modeling of nonlinear dynamic problems a damping term $\mathbf{D} \dot{\mathbf{u}}$ may also be included to the semi-discrete balance of momentum. The damping matrix $\mathbf{D}$ is often calculated as a linear combination of mass and stiffness matrices. For notational simplicity this term is excluded here.

2.2.3 Linear Statics

For many applications in structural optimization, assumptions can be made, which allow to considerably reduce the computational effort for solving the problem at hand. The linear FE-equations can be derived if

the following assumptions apply:

Kinematic relations: small displacement justify the application of a linear strain-displacement relation

$$\varepsilon_{ij} = \frac{1}{2}\left(\frac{\partial a_i}{\partial x_j} + \frac{\partial a_j}{\partial x_i}\right). \tag{2.25}$$

or in matrix-vector notation

$$\boldsymbol{\varepsilon} = \mathbf{L}_{\mathrm{L}}\mathbf{a}. \tag{2.26}$$

The subscript L is used in the following to denote the linear dependency.

Constitutive relations: small strains justify the usage of the linear elastic material law

$$\boldsymbol{\sigma} = \mathbf{C}_{\mathrm{L}}\boldsymbol{\varepsilon} \tag{2.27}$$

where $\mathbf{C}_{\mathrm{L}}$ is the material matrix containing the instantaneous stiffness moduli – Young's modulus E and Poisson's ratio ν in the case of isotropic material behavior.

Boundary conditions: due to small displacements it can be assumed that all applied boundary conditions do not change with progressing deformation. All conditions apply to the undeformed structure.

Reference configuration: small displacements and no path-dependent changes of constitutive relations and boundary conditions enable the evaluation of all measures with reference to the undeformed initial configuration V^0 and S^0. It is assumed that the error resulting of this is sufficiently small since current and initial configuration are similar in this case.

Inertia effects: static behavior implicates that time plays no role and inertia effects do not need to be considered anymore. The inertia term $\mathbf{M\ddot{u}}$ in the equation of motion vanishes and reduces to

$$\mathbf{f}_{\mathrm{ext}} - \mathbf{f}_{\mathrm{int}} = \mathbf{0}. \tag{2.28}$$

On basis of the above assumptions the stress-displacement relation follows as

$$\boldsymbol{\sigma} = \mathbf{C}_{\mathrm{L}}\mathbf{L}_{\mathrm{L}}\mathbf{H}\mathbf{Z}_{\mathrm{E}}\mathbf{u} = \mathbf{C}_{\mathrm{L}}\mathbf{B}_{\mathrm{L}}\mathbf{Z}_{\mathrm{E}}\mathbf{u} \tag{2.29}$$

and thus the internal force vector as

$$\mathbf{f}_{\mathrm{int}} = \sum_{e=1}^{n_{\mathrm{E}}} \mathbf{Z}_{\mathrm{E},e}{}^{\mathrm{T}} \int_{V_{\mathrm{E},e}^0} \mathbf{B}_{\mathrm{L}}{}^{\mathrm{T}}\mathbf{C}_{\mathrm{L}}\mathbf{B}_{\mathrm{L}}\mathbf{Z}_{\mathrm{E},e}\mathbf{u}dV. \tag{2.30}$$

As the nodal displacements $\mathbf{u}$ are independent of the spatial coordinates, they can be brought outside the integral. Then the equation of linear FEM is derived:

$$\mathbf{Ku} = \mathbf{f}. \tag{2.31}$$

With the linear stiffness matrix:

$$\mathbf{K} = \mathbf{K}^0 = \sum_{i=1}^{n_{\mathrm{E}}} \mathbf{Z}_{\mathrm{E},e}{}^{\mathrm{T}} \int_{V_{\mathrm{E},e}^0} \mathbf{B_L}^{\mathrm{T}} \mathbf{C_L} \mathbf{B_L} \mathbf{Z}_{\mathrm{E},e} dV \tag{2.32}$$

and the force vector:

$$\mathbf{f} = \mathbf{f}_{\mathrm{ext}} = \sum_{e=1}^{n_{\mathrm{E}}} \mathbf{Z}_{\mathrm{E},e}{}^{\mathrm{T}} \int_{V_{\mathrm{E},e}^0} \rho \mathbf{H}^{\mathrm{T}} \mathbf{g} dV + \sum_{e=1}^{n_{\mathrm{E}}} \mathbf{Z}_{\mathrm{E},e}{}^{\mathrm{T}} \int_{S_{\mathrm{E},e}^0} \mathbf{H}^{\mathrm{T}} \boldsymbol{\Gamma} dS. \tag{2.33}$$

This system of n_{N} linear equations can be solved using direct methods like Cholesky method or iterative methods like conjugated gradient methods, which are implemented in many commercial FEM solvers.

2.2.4 Nonlinear Dynamics

If a crash related problem is considered there are several nonlinearities which must be taken into account. These can be of geometrical and/or physical nature. The latter include nonlinearitites in material and contact. In the case of crash problems, both usually occur. In the following, the cause of the nonlinearities is briefly addressed, but the handling is not detailed. For more details, refer to Wriggers 1998. Instead, attention is drawn to the differences to linear statics, which are ultimately noticeable in the resulting tangent stiffness matrix or internal forces and inertia effects.

Kinematic relations: if large deformations and rotations occur, then geometrical nonlinearities arise and the strain-displacement relation cannot be assumed to be linear. Nonlinear strain measures have to be used:

$$\mathrm{E}_{ij} = \frac{1}{2} \left(\frac{\partial a_i}{\partial x_j} + \frac{\partial a_j}{\partial x_i} + \frac{\partial a_k}{\partial x_i} \frac{\partial a_k}{\partial x_j} \right) \tag{2.34}$$

or in matrix-vector notation

$$\mathbf{E} = \mathbf{L}_{\mathrm{NL}} \mathbf{a} \tag{2.35}$$

where the subscript NL denotes the nonlinear dependency. As a result the nonlinear tangent stiffness matrix $\mathbf{K}_{\mathrm{NL}}$ depends on the displacements $\mathbf{u}$.

Constitutive relations: during a crash typically non-reversible deformations occur. Then, the material behavior can no longer be assumed to be elastic only and inelastic path-dependent material-laws have to be employed. The behavior of metals used in automotive engineering can often be described sufficiently precise by an isotropic elasto-plastic material model. In the case of high strain rates the dependence of the material behavior on time must also be considered. Then visco-plastic material models should be employed. In the following the fundamental components of the numerical implementation of such material models are explained on the basis of a one dimensional tensile test, for more details please refer to Simo and Hughes 2006.
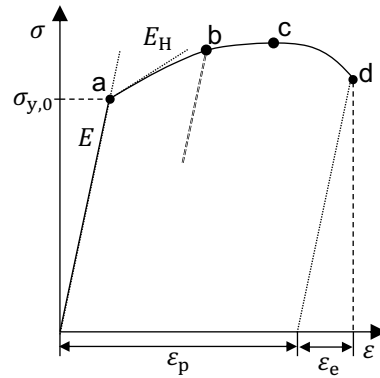
Figure 2.7: Elasto-plastic material behavior for the 1D case

In Fig. 2.7 the stress-strain relation of such a tensile test is shown. Here the total strain is additively split into two components, each related to the corresponding effects on the structure:

$$\varepsilon = \varepsilon_e + \varepsilon_p, \tag{2.36}$$

where ε_e and ε_p are the elastic and plastic strains, respectively. This additive split is valid for small strains only.[3]

Before the yield stress $\sigma_{y,0}$ is reached in *point a*, the material behavior is purely elastic and the stresses σ scale linearly with the strains ε. Afterwards, the material begins to deform plastically, this means the material undergoes a non-reversible change of shape. The *yield condition* indicates the initiation of this phase:

$$f(\sigma) = |\sigma| - \sigma_y(\varepsilon_p) \leq 0, \tag{2.37}$$

If the *yield function* $f(\sigma) = 0$ and the structure is further loaded hardening initiates. Then the plastic strains increase according to the *flow rule*, which gives an evolutionary equation for the plastic strains (Simo and Hughes 2006). As the plastic strains increase, the yield stress $\sigma_y(\varepsilon_p)$ does according to the defined hardening law[4]. In this phase the stresses can be approximated using the elasto-plastic tangent modulus E_H (bilinear material), or more accurately using many elastoplastic tangent moduli $E_{H,i}$, each representing a different slope (piecewise linear material). In *point b* the structure undergoes *elastic relaxation* or *unloading*. This is illustrated just to exemplify the possibility of unloading after initially reaching the yield stress, but is not mandatory. In this case the elastic contribution to the strains are reduced but the plastic remains. In *point c* the ultimate stress is reached and *Necking* starts. After this point, increasing strains come with a reduction of stresses until *point d* is reached and fracture or damage occurs.

---

[3]For large strains a multiplicative decomposition of the deformation gradient into elastic and plastic parts has to be employed.
[4]For isotropic hardening $\sigma_y(\varepsilon_p) = \sigma_{y,0} + H|\varepsilon_p|$, where H is the hardening modulus and $E_H = \frac{EH}{E+H}$.

Please note that in the three dimensional case a scalar stress measure is used in the yield function as well. Often the *Von Mises* stress is employed, which depends on the deviatoric stresses only and therefore attributes the volumetric constancy of ductile materials such as metals during hardening.

As we see, in contrast to linear statics the material behavior is strongly dependent on the deformation history of the structure now, therefore we speak of path-dependent material behavior. As mentioned previously, the constitutive relations can also depend on the strain rate, i.e. how fast the strains are changing. Consequently, for visco-plasticity the material matrix

$$\mathbf{C}_{\text{NL}} = \mathbf{C}(\mathbf{a}, \dot{\mathbf{a}}) \tag{2.38}$$

depends on the displacements $\mathbf{a}$ as well as on the velocities $\dot{\mathbf{a}}$. Then, e.g. the strain-curve shifts towards higher stress with increasing strain rates. For the sake of simpilicity, in this thesis mainly elasto-plastic material behavior is assumed. However, the last examined example is extended to visco-plasticity to exemplify the practical use-case for automotive crash problems. Furthermore, the material is idealized in the regard that fracture and necking is omitted.

Boundary conditions: during a crash event, the major part of external forces act on the structure through contacting with impacting structures and as a consequence of heavy deformations through self contact with the structure's own members. The magnitude but especially the location of contact can change fast within milliseconds. Hence, the boundary conditions change with progressing deformation. To model such contacting the *Lagrange*-multiplier method and the *Penalty*-method are to be named. For crash-applications usually the later one is used. In contrast to the Lagrange-method, the structure of the stiffness matrix does not change using the Penalty-method. After contacting partners have been determined, so-called penalty forces are calculated which counteract the penetration of the contact partners. This penalty force e.g. increases proportionally to the penetration, so that one can easily imagine it as a result of spring elements between the contact partners. In reality, however, no spring elements are inserted, but only the respective forces are added as a penalty term to the nodes in the contact zone. For more details please refer to Wriggers 2006 or e.g. Belytschko et al. 2014.

Reference configuration: the presence of path dependent-changes of the constitutive relations (e.g. plasticity) also implies the usage of an updated Lagrange formulation of the balance of momentum, which means the equation is evaluated with reference to the current configuration (De Borst et al. 2012). Then all integral measures are not evaluated with respect to the undeformed but the current deformed geometry V (Fig. 2.5).

Inertia effects: If a dynamic problem is to be solved, time is not only a parameter to order the sequence of events. The inertia term in equation 2.20 needs to be taken into account and the semi-discrete balance of momentum remains an ordinary differential equation with a derivative with respect to time on the left side.

$$\mathbf{M}\ddot{\mathbf{u}}(t) = \mathbf{f}_{\text{ext}}(t) - \mathbf{f}_{\text{int}}(t, \dot{\mathbf{u}}, \mathbf{u}) \tag{2.39}$$

The semi-discrete balance of momentum is called semi-discrete, because it is only discretized in the spatial domain but not in the time domain. In order to indicate the time dependency as well as the nonlinear dynamic background we use (t) in the following. For example $\mathbf{u}(t)$ is the displacement vector at time t resulting of the nonlinear dynamic analysis. The discretization in time can be accomplished by applying a time integration scheme.

Based on the above described considerations, the internal force vector is calculated as follows:

$$\mathbf{f}_{\text{int}}(t, \dot{\mathbf{u}}, \mathbf{u}) = \sum_{e=1}^{n_{\text{E}}} \mathbf{Z}_{\text{E},e}{}^{\text{T}} \int_{V_{\text{E},e}} \mathbf{B}_{\text{NL}}{}^{\text{T}} \mathbf{C}_{\text{NL}} \mathbf{B}_{\text{NL}} \mathbf{Z}_{\text{E},e} \mathbf{u}(t) dV. \tag{2.40}$$

The internal force vector therefore summarizes all nonlinear kinematic and constitutive relations. Furthermore, the integral is evaluated in the current domain now. The same applies for the external force vector $\mathbf{f}_{\text{ext}}$.

There are several different time integration schemes at hand to solve the semi-discrete balance of momentum. These schemes can be subdivided into two different classes – implicit and explicit methods. In the following the basic concepts of both classes are elaborated.

Implicit time integration

Implicit time integration schemes satisfy the balance at time $t + \Delta t$. As a starting point the semi-discrete balance of momentum is reformulated into an incremental equation (Bathe 1996)

$$\mathbf{M}\ddot{\mathbf{u}}(t + \Delta t) + \mathbf{K}_{\text{NL},0}^{t} \Delta \mathbf{u}(t) = \mathbf{f}_{\text{ext}}(t + \Delta t) - \mathbf{f}_{\text{int}}(t). \tag{2.41}$$

The right side of the equation then describes an out of balance force vector, which enforces the incremental displacements

$$\Delta \mathbf{u}(t) = \mathbf{u}(t + \Delta t) - \mathbf{u}(t). \tag{2.42}$$

The matrix $\mathbf{K}_{\text{NL},0}^{t}$ denotes the tangential stiffness matrix at the beginning of a time step, which can be derived by linearization of the internal force vector $\mathbf{f}_{\text{int}}(t)$ (Simo and Hughes 2006). This tangential stiffness matrix is eventually updated during time integration.

One of the most well known implicit integration schemes is the second-order Newmark Method (Newmark 1959):

$$\dot{\mathbf{u}}(t + \Delta t) = \dot{\mathbf{u}}(t) + \left[(1 - \delta) \ddot{\mathbf{u}}(t) + \delta \ddot{\mathbf{u}}(t + \Delta t) \right] \Delta t \tag{2.43}$$

$$\Delta \mathbf{u}(t) = \dot{\mathbf{u}}(t) \Delta t + \left[\left(\frac{1}{2} - \alpha \right) \ddot{\mathbf{u}}(t) + \alpha \ddot{\mathbf{u}}(t + \Delta t) \right] \Delta t^2 \tag{2.44}$$

where depending on the parameters α and δ different schemes can be obtained. The parameters can be set to influence stability and accuracy of the integration. For the parameters $\alpha = \frac{1}{4}$ and $\delta = \frac{1}{2}$ the

trapezoidal rule is realized. Substituting equation 2.43 and 2.44 into the incremental semi-discrete balance of momentum 2.41 at time step $t + \Delta t$ yields a system of nonlinear equations:

$$\left(\frac{4}{\Delta t^2} \mathbf{M} + \mathbf{K}_{\mathrm{NL},0}^t \right) \Delta \mathbf{u}(t) = \mathbf{f}_{\mathrm{ext}}(t + \Delta t) - \mathbf{f}_{\mathrm{int}}(t) + \mathbf{M} \left(\ddot{\mathbf{u}}(t) + \frac{4}{\Delta t} \dot{\mathbf{u}}(t) \right). \tag{2.45}$$

The equations are nonlinear, since $\mathbf{K}_{\mathrm{NL},0}$ depends on the displacements $\mathbf{u}$ in a nonlinear fashion. The term $\frac{4}{\Delta t^2} \mathbf{M} + \mathbf{K}_{\mathrm{NL},0}^t$ is called effective stiffness. To obtain the displacements $\mathbf{u}(t + \Delta t)$, an iterative procedure like the Newton-Raphson method has to be employed. Therefore, the effective stiffness matrix needs to be factorized at least once each time step. The computational effort per time step is thus comparatively high. For linear analyses this fact can be compensated, since the method is unconditionally stable for some parameter configurations (e.g. trapezoidal approach), which means there is no restriction on the time step size. However, the size of the time step Δt must be justified physically. If nonlinearities in contact or material occur and high frequencies are dominating the problem, the time step size must be chosen adequately small, which especially applies for crash related problems. Otherwise the iterative solver may fail to converge.

Explicit time integration

Explicit time integration schemes directly use equation 2.39, and values at times $t + \Delta t$ are evaluated using a finite difference scheme. Then, the solution for a time $t + \Delta t$ is based on the equilibrium at time t. In the following the explicit approach is illustrated using the second-order central differences scheme as an example. These differences can be written as:

$$\dot{\mathbf{u}}(t) = \frac{\mathbf{u}(t + \Delta t) - \mathbf{u}(t - \Delta t)}{2\Delta t} \tag{2.46}$$

$$\ddot{\mathbf{u}}(t) = \frac{\mathbf{u}(t + \Delta t) - 2\mathbf{u}(t) + \mathbf{u}(t - \Delta t)}{\Delta t^2} \tag{2.47}$$

Substituting equation 2.47 into the semi-discrete balance of momentum at time t and rearranging yields:

$$\mathbf{u}(t + \Delta t) = \Delta t^2 \mathbf{M}^{-1} \left(\mathbf{f}_{\mathrm{ext}}(t) - \mathbf{f}_{\mathrm{int}}(t) \right) + 2\mathbf{u}(t) - \mathbf{u}(t - \Delta t) \tag{2.48}$$

which can be solved directly. Therefore the mass-matrix $\mathbf{M}$ must be brought to the right side. Usually a costly inversion can be avoided by diagonalizing the mass matrix using a lumping scheme. This is especially important, since the time step Δt is restricted to a very small size in order to maintain the algorithm stable. An inversion in each time step would thus be very costly. After the displacements $\mathbf{u}(t + \Delta t)$ have been calculated, the strains, stresses, internal forces, velocities and accelerations at time $t + \Delta t$ can be calculated for each integration point. Afterwards all necessary measures for calculating the displacements $\mathbf{u}(t + 2\Delta t)$ are available and the process can be repeated. This step-by-step solution does not require a factorization of an effective stiffness matrix and can thus be performed fast.

When it comes to the simulation of crash problems, small time steps must be chosen when using either an explicit or an implicit solver. Since the computational effort per time step is significantly higher with implicit time integration, explicit solvers are usually used for crash simulations. Nevertheless there are examples for the use of implicit solvers in crash applications, especially for low-speed dynamic or quasi-static problems. Kazanci and Bathe, for example, examined the axial crushing behavior of a crash box using the Bathe implicit time integration method (Kazanc and Bathe 2012). Overall, they found good agreement with experimental results. However, the nonlinear dynamic analysis of the crash box model with 10332 shell elements took about 2.5 h to run, using 450 implicit time steps on a desktop computer equipped with an Intel i7 X990 CPU 3.47 GHz. Jonsson et al. 2019 analyzed a roof crush of a Volvo XC40 using the implicit solver of the commercial solver LS-DYNA and compared the results to those of an explicit solver. Both results are similar, but the computational costs differ considerably. The implicit solver took 73.9 h on a High Performance Cluster (HPC) with 448 cores, whereas the explicit solver only took 2.05 h. These examples show that, in principle, it is possible to achieve convergence with implicit time integration methods for crash problems. Still, the computational costs are significantly higher compared to explicit schemes.

2.3 Gradient based Optimization

After the theoretical framework for the analysis of structures subjected to linear static as well as nonlinear dynamic load cases has been elaborated, the concept of gradient-based optimization is presented in the following. As explained at the beginning, a suitable modification of the design variables is of decisive importance for the efficiency of the optimization algorithm. The modification of the design variables can be expressed mathematically:

$$^{k+1}\mathbf{x} = {}^{k}\mathbf{x} + {}^{k}\Delta\mathbf{x}, \tag{2.49}$$

where $^{k}\Delta\mathbf{x}$ is the change of the design variables $^{k}\mathbf{x}$ in iteration k. In gradient-based optimization, the modification of the design variables can be split into two major steps: Identifying a suitable search direction $\mathbf{p}$ in which the design variables are varied and performing a *line search* afterwards to determine how far to step in that direction. This way an n_{D}-dimensional optimization problem can be solved by solving a series of one-dimensional optimization problems (e.g. Fletcher and Reeves 1964). The name gradient-based relates to the fact that the search direction is determined based on the value of the sensitivities of the objective function and constraints with respect to the design variables. The sensitivities give a measure of the extent to which the constraints and the objective function change depending on the design variables. This is summarized by the gradient containing the partial derivatives with respect to each design variable x_i, exemplary for the objective function:

$$\boldsymbol{\nabla}^{\mathrm{T}} f(\mathbf{x}) = \left(\frac{\partial f(\mathbf{x})}{\partial x_1}, \frac{\partial f(\mathbf{x})}{\partial x_2}, ..., \frac{\partial f(\mathbf{x})}{\partial x_i} \right); \quad i = 1, ..., n_{\mathrm{D}}. \tag{2.50}$$

2.3.1 Line Search

After a search direction $\mathbf{p}$ has been set and in the absence of constraints, the increment $^{k}\Delta\mathbf{x}$ can be determined by solving the following one-dimensional optimization problem:

$$\min_{\alpha} f({}^{k}\mathbf{x} + \alpha \cdot {}^{k+1}\mathbf{p}), \tag{2.51}$$

which can be solved easily using *the method of golden ratio* or *polynomial interpolation* for example. Then $^{k}\Delta\mathbf{x}$ follows as:

$$^{k}\Delta\mathbf{x} = {}^{*}\alpha \cdot {}^{k+1}\mathbf{p}, \tag{2.52}$$

where $^{*}\alpha$ is the solution of equation 2.51. The new design thus follows as:

$$^{k+1}\mathbf{x} = {}^{k}\mathbf{x} + {}^{*}\alpha \cdot {}^{k+1}\mathbf{p}. \tag{2.53}$$

In Fig. 2.8 two subsequent iterations or line searches are illustrated.
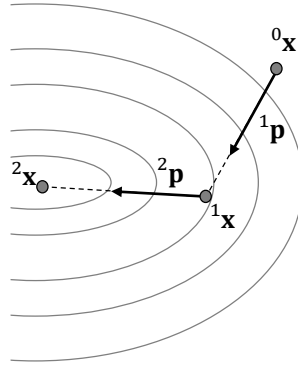
Figure 2.8: Two subsequent gradient-based line search iterations (modified from Harzheim 2014)

This is especially efficient, if a *local approximation* is used for all function analyses necessary during the line search. A local approximation provides good approximation in the immediate vicinity of the starting point $^k\mathbf{x}$. A *Taylor Series Expansion* can provide such approximation. The easiest way is to use a linear approximation $\tilde{f}_{\mathrm{L}}(\mathbf{x})$ only (Harzheim 2014):

$$\tilde{f}_{\mathrm{L}}(\mathbf{x}) = f(^k\mathbf{x}) + \sum_{i=1}^{n_{\mathrm{D}}} \frac{\partial f(^k\mathbf{x})}{\partial x_i}(x_i - {}^k x_i). \tag{2.54}$$

Since the gradients need to be calculated to determine the search direction $\mathbf{p}$ anyway, the computation of a linear approximation does not cause additional computational effort. In order not to exceed the local approximation's validity, the change of the design variables $^k\Delta\mathbf{x}$ must be limited. Therefore, so called *move limits* are introduced, defining a lower and an upper bound $\bar{\mathbf{x}}^{\mathrm{L}}$ and $\bar{\mathbf{x}}^{\mathrm{U}}$, respectively. Each design variable may vary only within this bounds during each iteration (Harzheim 2014):

$$
\begin{aligned}
\bar{x}_i^{\mathrm{L}} &= \max\left(x_i^{\mathrm{L}}, x_i^{(k-1)} - \delta|x_i^{k-1}|\right) \\
\bar{x}_i^{\mathrm{U}} &= \min\left(x_i^{\mathrm{U}}, x_i^{(k-1)} + \delta|x_i^{k-1}|\right); \qquad \delta \in [0, 1].
\end{aligned}
\tag{2.55}
$$

The usage of the min and max functions ensure that the explicit constraints are not exceeded. The parameter δ controls the size of the move limits. Often the value $\delta = 0.5$ is used. However, this value may be reduced with progressing iterations (Harzheim 2014). The validity and quality of the local approximation can be significantly improved if the knowledge about the approximated function or structural response is considered. While responses such as mass or volume often relate linearly to the design variables, this may not be the case for displacements or stresses.[5] Then, it is beneficial to use a reciprocal dependency. In this

---

[5]For the deflection u of a cantilever with height h loaded at one end and fixed at the other end $u \sim 1/h^3$ applies.

case, the Taylor series expansion in equation 2.54 changes to

$$\tilde{f}_{\mathrm{R}}(\mathbf{x})(\mathbf{x}) = f(^k\mathbf{x}) + \sum_{i=1}^{n_{\mathrm{D}}} \frac{\partial f(^k\mathbf{x})}{\partial x_i} \frac{^k x_i}{x_i}(x_i - {}^k x_i). \tag{2.56}$$

The Method of Moving Asymptotes (MMA) allows to flexibly switch between linear $\tilde{f}_{\mathrm{L}}(\mathbf{x})$ and reciprocal approximation $\tilde{f}_{\mathrm{R}}(\mathbf{x})$ and all intermediate stages (Svanberg 1987).

2.3.2 Determining the Search Direction

There are several options to define the search direction $\mathbf{p}$. The easiest way is to use the direction of *steepest descent* of the objective function. This direction is defined by the inverse gradient:

$$\mathbf{p} = -\boldsymbol{\nabla} f(\mathbf{x}). \tag{2.57}$$

Like illustrated in Fig. 2.9 (left) this simple approach often leads to unnecessary iterations, since subsequent search directions must be perpendicular to each other. An alternative approach, where oscillations are damped, is the *conjugate gradient method* (Fig. 2.9 , right). For further details, refer to (Harzheim 2014; Martins and Ning 2021).
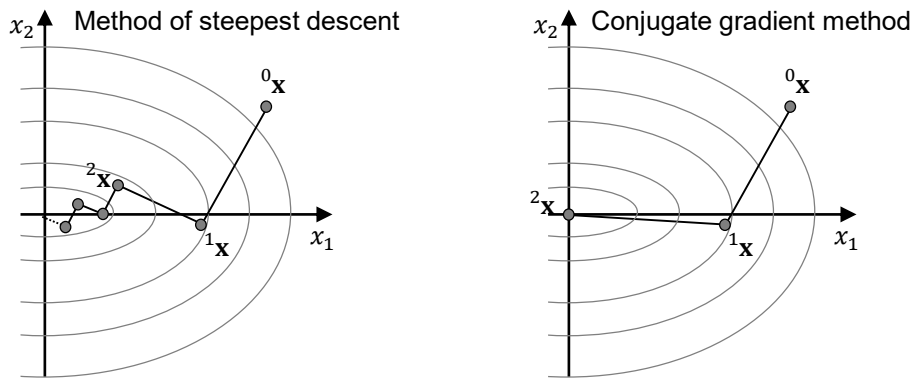
Figure 2.9: Comparison of method of steepest descent and conjugate gradient method (modified from Harzheim 2014)

The above methods take into account the objective function $f(\mathbf{x})$ only. Since most optimization problems also involve constraints, the strategy for choosing the search direction must be adopted if constraints are violated or active. In the first case, a strategy must be applied to find a feasible design with priority. In the second case the design lies at the border of the feasible region. The new search direction then should be feasible and descend. This means, $\mathbf{p}$ points into regions which are feasible and where the objective's value reduces. The *Method of feasible Directions* satisfies both conditions and is illustrated in Fig. 2.10. If the search direction is selected in this way, the optimizer usually moves along the borders of the feasible region

until optimality is found. The *Karush-Kuhn-Tucker* (KKT) conditions provide a criterion to asses the current design's optimality. For each regular point $\mathbf{x}$ [6], and if only inequality conditions are involved, they can be summarized as:

$$\boldsymbol{\nabla} f(^*\mathbf{x}) + \sum_{J \in I_c} \lambda_j \boldsymbol{\nabla} g(^*\mathbf{x}) = \mathbf{0}; \qquad \lambda_j \geq 0; \qquad j \in I_c, \tag{2.58}$$

where I_c is a set containing all active inequality constraints and λ_j is the *Lagrange* multiplier corresponding to constraint g_j. If any $\lambda_j \geq 0$ exist, for which equation 2.58 is satisfied, then no feasible and descent region exists like illustrated in Fig. 2.11. However, it is unclear if this point is a local or a global optimum. As depicted in Fig. 2.12, the *global optimum* is defined by the objective's best possible value in the entire feasible region, whereas a *local optimum* is the best possible value within a small neighborhood only. Therefore, the found optimum can only be ensured to be a global optimum if the optimization problem is *convex*. Unfortunately, for the most practical applications one cannot tell if the function is convex, without analyzing the function over the entire design space, which is prohibitive because of the required computational effort. Thus, it remains unclear if the found optimum is a local or a global optimum. It can be expected that most crash problems are highly *multimodal*, which means many different optima exist. Gradient-based optimizer explore the design space from a selected initial design point and thus only small parts of the entire design space are usually examined. Due to this fact, gradient-based optimizer are very efficient especially for higher dimensional problems. The downside is that the probability of ending up in a local optimum is relatively high. To address this issue most of the examples in this thesis are examined based on several initial designs uniformly distributed all over the design space.

So far, it has not been elaborated how the gradients are calculated. The possibility and effort for this depends strongly on the type of optimization problem considered. In the following, the possibilities for linear static and nonlinear dynamic problems are explained and alternatives to gradient-based optimization are shown.

---

[6]$\mathbf{x}$ is regular if $\mathbf{x}$ is feasible and the gradients of all active constraints are linearly independent.
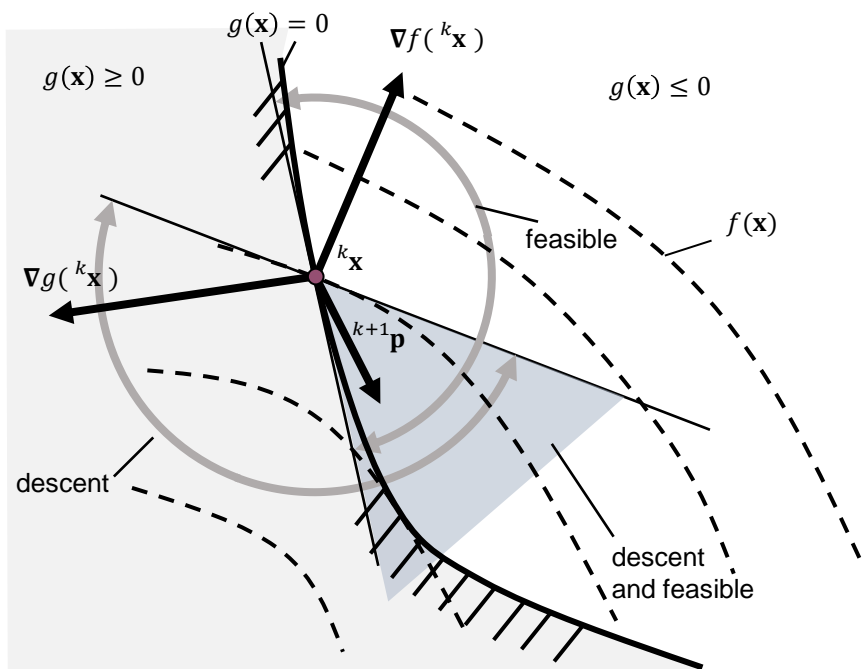
Figure 2.10: Descent and feasible regions for design $^k\mathbf{x}$ at the border of the feasible region (modified from Harzheim 2014)
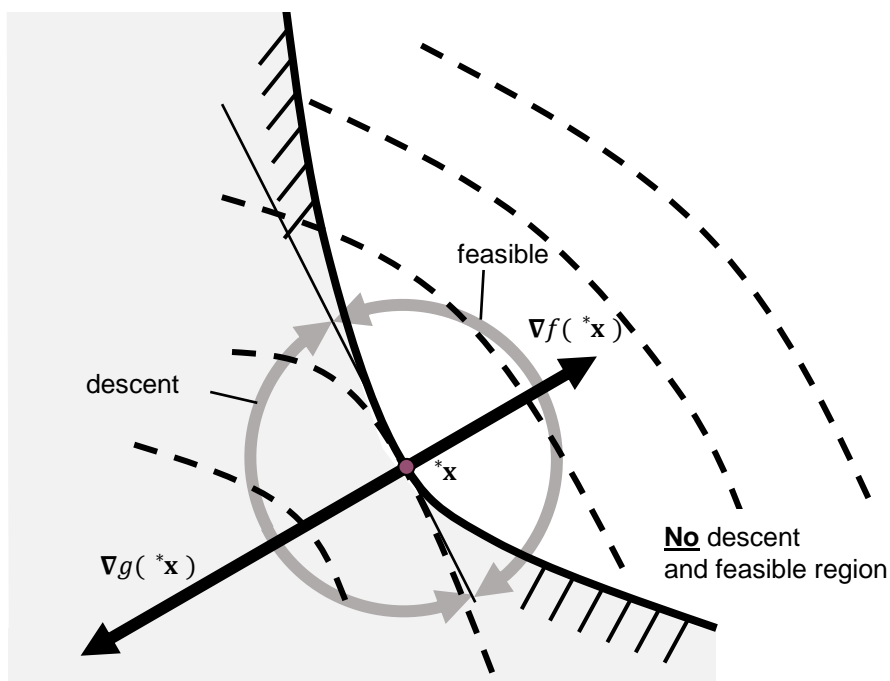
Figure 2.11: Descent and feasible regions for optimum $^*\mathbf{x}$ (modified from Harzheim 2014)
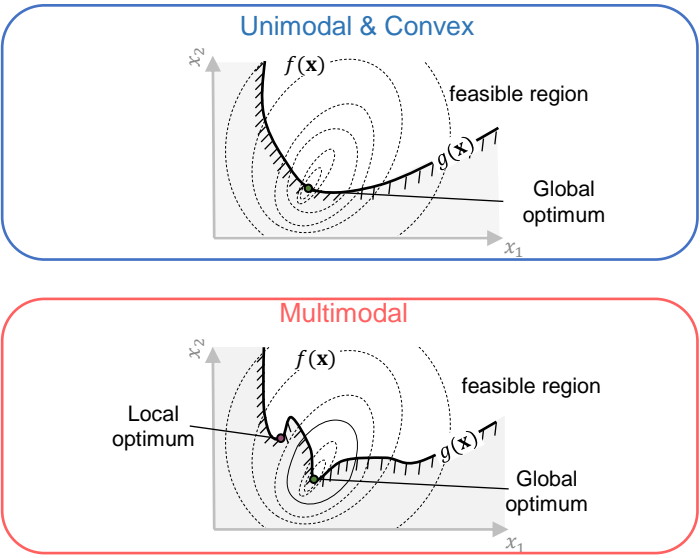
Figure 2.12: Global and local optima and convex optimization problem

2.4 Linear static Response Optimization

The term linear static response optimization describes the optimization of a problem where the analysis is performed based on the linear statics FE-equation. Mathematically this problem reads as follows [7]:

$$\min f(\mathbf{x}, \mathbf{u}); \qquad\qquad \mathbf{x} \in \mathbb{R}^{n_\mathrm{D}} \qquad (2.59)$$

subject to

$$g_j(\mathbf{x}, \mathbf{u}) \leq 0; \qquad\qquad j = 1, ..., n_\mathrm{UC} \qquad (2.60)$$

$$x_i^\mathrm{L} \leq x_i \leq x_i^\mathrm{U}; \qquad\qquad i = 1, ..., n_\mathrm{D}, \qquad (2.61)$$

where the displacement vector $\mathbf{u}$ is the solution of the linear FE-equation:

$$\mathbf{K}(\mathbf{x})\mathbf{u} = \mathbf{f}. \qquad (2.62)$$

For this kind of problems often the mass is minimized, while the structure's stiffness is constrained or vice versa. The structural responses reflecting the structure's stiffness are for example either the intrusions of the node subjected to an external force, or the compliance. The compliance is mostly used in case of topology optimization and is defined as:

$$Compl = \sum_i \mathbf{f}_i \mathbf{u}_i; \qquad\qquad i = 1, ..., n_\mathrm{N} \qquad (2.63)$$

The sensitivities can be calculated efficiently for linear statics problems. In the following, different possibilities for deriving the sensitivities are elaborated following the assumptions of linear statics.

2.4.1 Sensitivity Analysis

The concept of gradient-based optimization requires the sensitivities of objective and constraints for defining the search direction $\mathbf{p}$ in each iteration. The sensitivity analysis can require a considerable part of the total time for optimization. Furthermore, the convergence behavior of the optimization depends strongly on the chosen search directions and therefore on the accuracy of the sensitivities. Efficient and accurate sensitivity computations are thus essential for gradient-based optimization schemes. One way to quantify changes of the objective or constraints with respect to design changes is using finite differences. If forward differences are used each sensitivity analysis requires $n_\mathrm{D} + 1$ analyses, which is extremely expensive. Furthermore, finite differences schemes tend to be inaccurate. Thus, numerical procedures like finite difference schemes should only be used for sensitivity analysis if no other method can be applied (Harzheim 2014). There are two efficient (semi-) analytical alternatives available for linear static response optimization: the *direct*

---

[7]Equality constraints are omitted here, as they are usually not used in practice.

and the *adjoint* method (Arora and Haug 1979; Haftka and Adelman 1989; Haftka et al. 2012; Schwarz 2001; Tortorelli and Michaleris 1994; Van Keulen et al. 2005; Kleiber et al. 1997; Komkov et al. 1986; Hsieh and Arora 1984). In the following, both approaches are illustrated using the example of linear static response optimization. The total derivative with respect to the design variables $\mathbf{x}$ of a structural response as for example the objective function f, involved in the optimization problem, can be obtained using the chain rule:

$$\frac{\mathrm{d}f(\mathbf{x},\mathbf{u})}{\mathrm{d}x_i} = \frac{\partial f(\mathbf{x},\mathbf{u})}{\partial x_i} + \left(\frac{\partial f(\mathbf{x},\mathbf{u})}{\partial \mathbf{u}}\right)^T \frac{\partial \mathbf{u}}{\partial x_i} \tag{2.64}$$

The derivatives $\frac{\partial f}{\partial \mathbf{u}}$ and $\frac{\partial f}{\partial x_i}$ are explicit quantities and their calculation is straight forward. In contrast the derivative $\frac{\partial u_j}{\partial x_i}$ is an implicit quantity because the system response $\mathbf{u}$ is implicitly defined through the equation of linear statics. Therefore, the implicit term needs special treatment. It can either be calculated using the direct method or be eliminated in 2.64 using the adjoint method.

The Direct Method

Employing the direct method, the partial derivatives $\frac{\partial u_j}{\partial x_i}$ are calculated, by solving n_D pseudo load cases. These pseudo load cases can be derived by differentiating the linear statics FE-equation (equation 2.31) with respect to $\mathbf{x}$

$$\frac{\partial \mathbf{K}}{\partial x_i}\mathbf{u} + \mathbf{K}\frac{\partial \mathbf{u}}{\partial x_i} = \frac{\partial \mathbf{f}}{\partial x_i} \tag{2.65}$$

and rearranging

$$\mathbf{K}\frac{\partial \mathbf{u}}{\partial x_i} = \phi, \tag{2.66}$$

where ϕ is called the pseudo load vector

$$\phi = \frac{\partial \mathbf{f}}{\partial x_i} - \frac{\partial \mathbf{K}}{\partial x_i}\mathbf{u}. \tag{2.67}$$

The factorization of $\mathbf{K}$ has already been done for analysis, but the partial derivatives $\frac{\partial \mathbf{f}}{\partial x_i}$ and $\frac{\partial \mathbf{K}}{\partial x_i}$ have to be calculated in order to solve 2.66. Often the force vector $\mathbf{f}$ is independent of the design variables in linear statics and thus $\frac{\partial \mathbf{f}}{\partial x_i}$ is zero. If this is not the case, the dependence of $\mathbf{f}$ with respect to x_i is usually known explicitly and $\frac{\partial \mathbf{f}}{\partial x_i}$ can be determined analytically (e.g. body loads). The remaining term $\frac{\partial \mathbf{K}}{\partial x_i}$ can either be calculated analytically or by using finite differences. If finite differences are employed, one speaks of semi-analytical sensitivity analysis and otherwise of analytical sensitivity analysis. Since the term $\frac{\partial u_j}{\partial x_i}$ has to be calculated only once for each structural response f, the direct method is insensitive to the number of constraints n_C imposed to the problem. However, the drawback is obviously, that one pseudo load case must be solved for each design variable and the method is therefore not suitable for topology optimization.

The adjoint Method

Instead of calculating the partial derivatives $\frac{\partial \mathbf{u}}{\partial x_i}$, one can also eliminate them from equation 2.64 using the adjoint method. Therefore, equation 2.66 must be rearranged

$$\frac{\partial \mathbf{u}}{\partial x_i} = \mathbf{K}^{-1} \boldsymbol{\phi} \tag{2.68}$$

and inserted into equation 2.64

$$\frac{\mathrm{d} f(\mathbf{x}, \mathbf{u})}{\mathrm{d} x_i} = \frac{\partial f(\mathbf{x}, \mathbf{u})}{\partial x_i} + \left(\frac{\partial f(\mathbf{x}, \mathbf{u})}{\partial \mathbf{u}} \right)^T \mathbf{K}^{-1} \boldsymbol{\phi}. \tag{2.69}$$

Instead of solving the pseudo loadcase 2.68 as a first step like in the direct method, now the adjoint variable $\boldsymbol{\lambda}$ is calculated

$$\boldsymbol{\lambda}^T = \left(\frac{\partial f(\mathbf{x}, \mathbf{u})}{\partial \mathbf{u}} \right)^T \mathbf{K}^{-1}. \tag{2.70}$$

Using the symmetry of the stiffness matrix $\mathbf{K}$ the adjoint variable $\boldsymbol{\lambda}$ can be calculated by solving the following system of equations

$$\mathbf{K}\boldsymbol{\lambda} = \frac{\partial f(\mathbf{x}, \mathbf{u})}{\partial \mathbf{u}}, \tag{2.71}$$

which is in fact another pseudo load case. This time the pseudo load vector is given by the partials $\frac{\partial f(\mathbf{x}, \mathbf{u})}{\partial \mathbf{u}}$. Their calculation is straight forward and can be done analytically. In order to finally derive the sensitivities the remaining partials in equation 2.69 can either be calculated analytically or semi-analytically, like already described before. The main difference between the direct and the adjoint method thus is the sequence of matrix operations and therefore the resulting number of overall operations (Firl and Bletzinger 2010; Schwarz 2001; Harzheim 2014). If the direct method is used n_D pseudo loadcases must be solved, whereas for the adjoint method $n_C + 1$ pseudo load cases must be solved. This means for problems with a high number of design variables n_D and a small number of constraints n_C the adjoint method is much more efficient, which is why it is typically used for topology optimization problems.

2.5 Nonlinear dynamic Response Optimization

The optimization of structures subjected to a crash event can be classified in the category of nonlinear dynamic response optimization. Here, the optimized systems are of nonlinear dynamic nature and the optimization problem can be formulated as follows:

$$\min f(\mathbf{x}, \mathbf{u}(t)); \qquad \qquad \mathbf{x} \in \mathbb{R}^{n_\mathrm{D}} \qquad \qquad (2.72)$$

subject to

$$g_j(\mathbf{x}, \mathbf{u}(t)) \leq 0; \qquad \qquad j = 1, ..., n_\mathrm{UC} \qquad \qquad (2.73)$$

$$x_l^\mathrm{L} \leq x_l \leq x_l^\mathrm{U}; \qquad \qquad l = 1, ..., n_\mathrm{D} \qquad \qquad (2.74)$$

where the displacement vector $\mathbf{u}(t)$ is the solution of the nonlinear dynamic FE-equation:

$$\mathbf{M}(\mathbf{x})\ddot{\mathbf{u}}(t) + \mathbf{D}_\mathrm{NL}(\mathbf{x}, \mathbf{u})\dot{\mathbf{u}}(t) + \mathbf{K}_\mathrm{NL}(\mathbf{x}, \mathbf{u})\mathbf{u}(t) = \mathbf{f}_\mathrm{ext}(t). \qquad \qquad (2.75)$$

Inertia effects as well as nonlinearities in geometry, material and contact need to be considered. The sensitivities cannot be derived as efficiently as in the case of linear static response optimization (Michaleris et al. 1994; Kleiber et al. 1997). Furthermore, the structural responses involved in optimization problems usually differ from those used in linear static response optimization. The dependency of e.g. the objective function on time varies depending on the selected load case. One could for example be interested of the maximum or final value of $f(x, \mathbf{u}(t))$ over time or an integral quantity. In the following, it is first elaborated which structural responses are most relevant for a structure's crashworthiness and an overview of typical crash load cases is given. Afterwards, approaches based on sensitivities of the nonlinear dynamic system as well as approaches circumventing the sensitivity analysis are presented.

2.5.1 Crashworthiness Design

Crashworthiness design aims to increase the passive safety of vehicles while simultaneously reducing material and manufacturing costs. Passive safety refers to safety measures that reduce the consequences of an accident for vehicle occupants and pedestrians after an accident has become unavoidable. A number of load cases are used by automotive manufacturers to design crash structures according to these aspects. These load cases follow, on the one hand, the regulations established by the legislator that must be met within the homologation of a vehicle on the relevant market. On the other hand, voluntary vehicle safety rating systems, like e.g. the *European New Car Assessment Program* (Euro NCAP), provide independet information for consumers based on other crash load cases. The performance of the vehicles in these load cases thus becomes a relevant bench-marking criterion for customers and automotive companies. In the following some of the load cases are described schematically:

Side Impact: Like illustrated in Fig. 2.13 a car with an initial velocity of 32 km/h is colliding sideways with a rigid pole. This simulates the collision with roadside objects such as trees, after the driver lost control over the vehicle. The ability of the car to protect the driver's head and body is tested here. Therefore, the pole impacts at the position of the driver's head. The intrusion of the pole is limited. Otherwise, the pole would hit the driver's head and cause severe injuries. Please note that before 2015 EURO NCAP placed the car perpendicular to the direction of motion.

Front Impact: The vehicle drives at a speed of 50 km/h against a rigid barrier that covers the full width of the vehicle (Fig. 2.14). The test is designed to simulate what happens when the front of a vehicle collides with another vehicle or an roadside object. After collision the car decelerates rapidly and the whole kinetic energy of the car must be absorbed by the car's body. The deceleration can cause severe injuries to the occupants and must therefore be limited. Also, structural parts striking against the occupants can cause injuries. In order to prevent parts buckling towards the occupant, most vehicles have stiff safety cages encapsulating the occupant compartment. However, these stiff structural members are not able to absorb the kinetic crash energy and do not keep the acceleration at a moderate level. For that purpose, so called crush zones are designed to crush and absorb the crash energy and reduce forces on the safety cage. Besides the shown frontal crash there are many other configurations. Mostly the velocity of the car and the overlap width and stiffness of the barrier differ, such that for example only the driver's side of the car hits a deformable barrier.

Roof Crush: The purpose of this load case is to reduce deaths and injuries due to the crushing of the roof into the passenger compartment during an rollover accident. Therefore, the resistance of the vehicle's roof is measured while a rigid rectangular block moves downwards at a defined angle (Fig. 2.15). The rigid block moves with constant velocity until 127 mm intrusion is reached. If the measured force exceeds a defined threshold during the deformation process, the roof's resistance is considered sufficient. Since the crushing of the roof during a rollover also depends on the vehicle's mass, the resistance is calculated as a quotient of reaction force and the vehicle's weight.
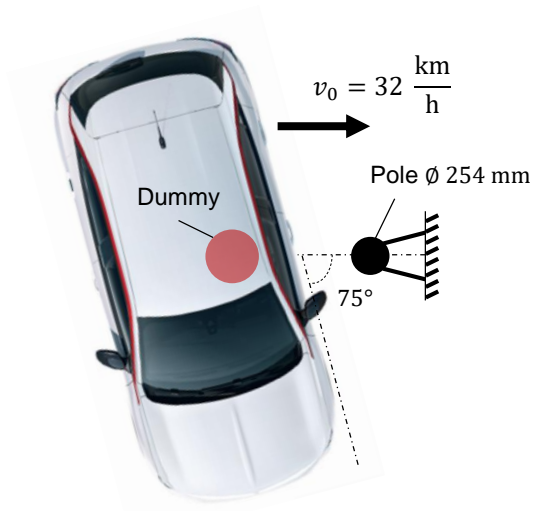
Figure 2.13: Side impact crash load case: Vehicle colliding sideways with rigid pole
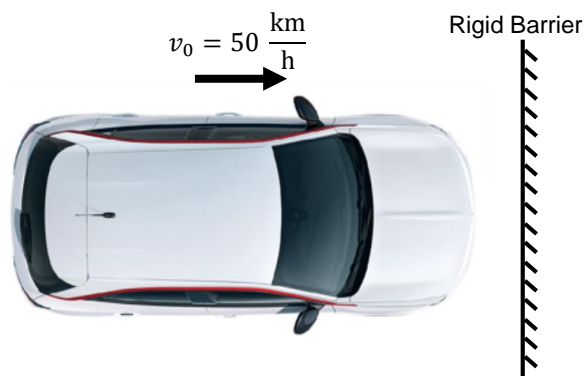
Figure 2.14: Front impact crash load case with full width barrier according to Euro NCAP 2022: Vehicle colliding with rigid barrier
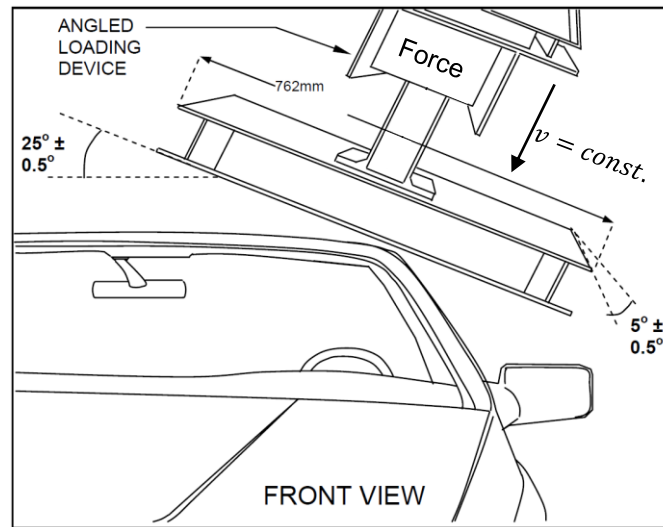
Figure 2.15: Roof crush load case (modified from National Highway Traffic Safety Administration 2009): Application to measure a vehicle's roof crush resistance

The above exemplary load cases illustrate that often several criteria must be considered when optimizing crash load cases. The criteria are partly contradictory. Stiff structures must be realized for the design of the occupants compartment, which can be targeted by optimizing intrusions (e.g. side impact) or reaction forces (e.g. roof crush). The crush zone, on the other hand, is purposely designed to convert the kinetic crash energy into plastic deformation and heat. This can for example be accomplished by maximizing the plastic work or plastic strain energy, which is given as the area below the *stress-plastic strain* curve (cf. figure 2.7). In order to avoid damaging spot welds or structural parts of the occupant compartment, the maximum reaction force of the crush zone must also be limited.

Instead of the plastic work, an approach based on the force-displacement curve of a structural member of the crush zone can also be used for optimization. Such a force-displacement curve is illustrated in Fig. 2.16. Here, the reaction or crash force of a structural part subjected to a crash is plotted over the impactor's displacement in force direction. The integral of the force-displacement curve is the internal energy. Point d marks the maximum intrusion. At this point the kinetic crash energy has been transferred to internal energy completely. The structure rebounds afterwards and the elastic part of the internal energy is transformed to kinetic energy again. With consideration of the constraint of the maximum force F_U and a maximum feasible displacement d_U, a rectangular force-displacement curve results as the theoretical optimum of the force-displacement curve. Thereby, the deformation is limited by the available deformation space and the maximum force to prevent the parts in the occupant compartment or spot welds from damage. Such a force-displacement curve can therefore be targeted, for example, by minimizing the maximum force and constraining the maximum displacement.
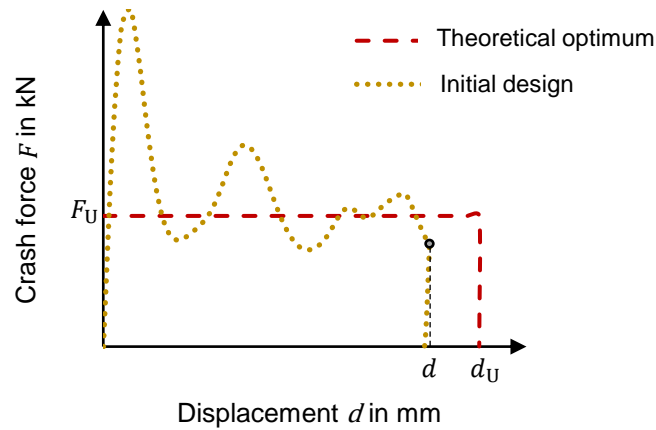
Figure 2.16: Crash force vs. displacement for a structure subjected to a crash event

In addition to the crash forces and intrusions, the accelerations imposed on the occupants also play an important role during the crash event. These should in principle be as low as possible. Accelerations are directly related to the crash forces occurring. In this work, therefore, we focus on the incorporation of crash forces and intrusions in the optimization problems solved.

2.5.2 Approaches based on Sensitivities of the nonlinear dynamic System

For nonlinear dynamic problems, sensitivities can only be derived under special circumstances and with high computational effort. As elaborated before for linear statics, also for nonlinear dynamics either the direct or the adjoint method can be used. However, the methods are much more complicated in this case. In the following, a short explanation of sensitivity analysis for nonlinear dynamics is given to elaborate its limitations and drawbacks. In doing so, the explanation is limited to the adjoint method, because just as for linear statics, the computational effort of the direct method increases with the number of design variables n_D. Therefore, the direct method is not suitable for topology optimization. For more detailed information please refer for example to Michaleris et al. 1994 or Kleiber et al. 1997, who give more detailed explanations of both direct and adjoint methods for nonlinear dynamics.

The basic idea of the adjoint method for nonlinear dynamics is similar to the procedure explained before. First the sensitivity of the structural response of interest is split into explicit and implicit quantities. Afterwards the implicit quantities are annihilated by introducing the adjoint variables. In contrast to linear static response optimization, the adjoint variables can only be derived by solving a terminal value problem, which must be solved backwards in time. The computational effort of this calculation is similarly high as of the forward time integration used for the nonlinear dynamic analysis. However, there are some synergies that can potentially be employed: The factorized tangent stiffness matrix is required in each time step of the backward integration. To derive the tangent stiffness matrices there are two options: If an implicit

time integration scheme is used for the primal nonlinear dynamic analysis, the factorized tangent stiffness can be stored for each time step and reused for solving the adjoint problem. If an explicit time integration scheme is employed the tangent stiffness matrices have to be set up and factorized after the primal analysis. While the first option is more demanding in terms of storage usage, the computational effort of the second option is higher. This might be the reason, why current research on adjoint sensitivity analysis of crash related problems is focused on using implicit solvers (Ivarsson et al. 2018; Weider and Schumacher 2018; Weider and Schumacher 2019). At this point I want to remind the readers of the comparison of the elapsed times for explicit and implicit time integration schemes in chapter 2.2.4. Although, it may be beneficial to employ implicit time integration schemes here, it still is very time consuming. Therefore, nonlinear dynamic response optimization employing the adjoint method cannot be considered an option for large scale industrial application yet.

Nevertheless, efforts are made towards crashworthiness topology optimization using adjoint sensitivity analysis for highly nonlinear problems. Weider for example calculates the so-called topological derivative, which is the sensitivity of a functional for introducing an infinitesimal hole into the structure. These sensitivities can be used afterwards for level set optimization. In Weider and Schumacher 2019 the sensitivities for the functionals: internal energy and displacement have been introduced. However, some boundary integrals occur in the explicit terms which cannot be calculated directly. A metamodel-based approximation as described in Weider and Schumacher 2018 for the internal energy functional, can be used to approximate the missing explicit terms. Ivarsson et al. 2018 also used the adjoint sensitivity analysis for topology optimization of visco-plastic structures under transient loads. They used the RAMP material interpolation scheme[8] and optimized the normalized densities using MMA. The approach was tested employing several numerical examples. These are 2D beam structures that are clamped at both ends and deformed in the middle by a transient load. They differ in the measurements of the beam and the exact implementation of the clamping. For each example the loading rate is varied between very fast and slow (quasi-static), while the maximum deformation of the structure in the loading area remains the same. The objective is to maximize the absorbed visco-plastic energy. The results of all examples have in common that at high load rates the mass accumulates in the middle of the structure, i.e. close to the loading area. This reflects the increasing influence of inertia effects with higher loading rates. The results demonstrate the functionality of the methodology, taking into account dynamic/inertia effects and material nonlinearities. However, contact remains unconsidered, which is an elementary component of most crash problems.

2.5.3 Approaches without Sensitivity Calculation of the nonlinear dynamic System

Due to the circumstances described above, efforts are made to avoid the calculation of sensitivities of the nonlinear dynamic system. In the following relevant approaches for both sizing and topology optimization are presented.

---

[8]*Rational approximation of material properties* (RAMP) is a material interpolation scheme developed by Stolpe and Svanberg 2001. It has some similarities with the SIMP approach. For a comparative review refer to Sigmund and Maute 2013.

Metamodel based Approaches

A *metamodel,* or also known as *surrogate model,* or *response surface model* (RSM), approximates responses over the design space based on underlying data points. The overall goal of a metamodel is to enable much faster analysis than the original nonlinear dynamic system. However, in order to create a sufficiently accurate metamodel, the analysis of several points in the data space is necessary. The procedure of selecting these design points is called *Sampling*. This should be accomplished such that the entire design space is covered sufficiently while their number remains at a moderate level. Such points can be generated for example by using *Latin Hypercube* sampling or *Strenght-Two Orthogonal Arrays* (STOA). The latter is said to have a very even distribution of points over the design space (space filling design) (Harzheim 2014).

It can generally be distinguished between global and local metamodels. For the first, a global approximation of the entire design space is made, while for the second only local approximations of predefined sub-spaces are created. An example for the latter is the *Successive Response Surface Method* (SRSM) (Stander 2001; Stander and Craig 2002), which is implemented in the commercial tool LS-Opt (LSTC 2015). Here, starting from an initial design ^{0}x, the optimum of a local approximation of the sub-space spanned around the starting point is determined. A new approximation is then created in a new sub-space around the newly found optimum, based on which again the optimum is determined. This process is repeated until certain convergence criteria are met. Building accurate local approximation usually involves less computational effort than building a sufficiently accurate global approximation. In contrast to global approximations no computational efforts are made to approximate obviously sub-optimal regions. However, since only parts of the design space are explored using SRSMs the chance of getting stuck in a local optimum is higher than when using global approximations. If global approximations are used for optimization purposes, the metamodel usually is not highly accurate at the beginning but is improved by adding new design points during the optimization until convergence is reached.

There are basically two different ways to fit the metamodels: *Regression* and *Interpolation*. Regression, does not necessarily match the underlying data points exactly, instead they give a smooth trend of the data points. This is especially advantageous if the available data is noisy. Examples for regressions are *Neural Networks* (Hornik et al. 1990; Hornik et al. 1992; Waszczyszyn 1999) and *Polynomials* (Lancaster and Salkauskas 1981). In contrast, interpolations like *Radial Basis Functions* (Powell 1992) and *Kriging* (Krige 1951; Matheron 1963; Cressie 1988; Cressie 1990) build functions that exactly fit the data points. If the optimization problem to be solved is highly multimodal, the usage of an interpolating metamodel ensures that the underlying physical effects reflected in the responses are not smoothed away. One limitation of metamodels is the poor scalability with regard to the number of design variables: the computational effort for constructing a sufficiently accurate metamodel increases significantly with the number of design variables. Hence, it can be used for sizing and shape optimization but not for topology optimization.

Hybrid Cellular Automaton

An alternative heuristic approach for topology optimization of nonlinear dynamic systems is the *Hybrid Cellular Automaton* (HCA) (Patel 2007; Patel et al. 2009), which is an extension of the previously introduced methodology by Tovar et al. 2006 for linear static response optimization. Similar to the SKO (Baumgartner et al. 1992), Tovar aims to simulate the process of structural adaption in bones and homogenizes the strain energy density for this purpose. Therefore, the *Cellular Automaton* (CA) paradigm (Von Neumann 1951) is combined with FEM. In a CA, the structure is subdivided into several cells by a homogeneous grid. The state of a cell is then varied depending on its own state and those of the neighboring cells. In the simplest case, each cell corresponds to an element in the FE-discretization, and the states are used as optimization design variables. The mechanical properties and structural responses of each cell can then directly be used to modify the design variables according to the cellular paradigm. This results in an iterative sequence of *Finite Element Analysis* (FEA) and modification of the design variables as described in Fig. 2.1. The name *Hybrid* Cellular Automaton reflects the coupling of the FEM with the concept of CA.[9]

Patel directly transfers Tovar's idea to crashworthiness optimization and homogenizes the strain energy density of elasto-plastic crash structures subjected to a mass constraint. For this purpose, the normalized density of the cells is varied until – if possible – a state of homogeneous strain energy is reached. The normalized densities are related to the structure's mechanical properties using the SIMP approach. This requires the SIMP approach to be extended to elasto-plastic material behavior. In addition to the Young's modulus E, the yield stress σ_y and the hardening modulus E_H are scaled analogously here. For the numerical examples the penalty exponent $p = 1$ is used. In order to fulfill the mass constraint, a target value for the strain energy density is defined in each iteration using a heuristic rule. For this purpose it is assumed that the strain energy density increases with decreasing mass.

Since the heuristic described above does not take into account structural responses besides the strain energy density and mass, Patel presents an approach to incorporate constraints referencing other relevant responses. By adjusting the mass constraint during the optimization procedure, the stiffness of the resulting structure is varied until these constraints are met. To exemplify this, we imagine a deformed structure. If its deflection exceeds the feasible range, then the mass constraint and thus – as assumed – the stiffness is increased, in order to reduce the deflection. Patel demonstrates the functionality of this approach using a maximum displacement constraint as well as a maximum force constraint.

The HCA is available as the commercial tool LS-TASC (Roux 2016; Gandikota et al. 2019). Weider et al. 2017 published a systematic study testing LS-TASC for crashworthiness applications. They found that the tool yields reliable results for stiffness applications. However, they also state that for objectives considering responses such as crash forces and accelerations the results highly depend on the load case. It is questionable, if an homogenized energy density leads to optimal structures, when considering a metal crash boxes for example. These are an essential part of the crush zone in many cars. The desired energy absorption behavior

---

[9]While in a CA the state of a cell does only depend on its one and those of the neighboring cells, the combination with FEM makes it a "Hybrid" Cellular Automaton, since the FEA's result depends on the states of all cells.

is reached by an progressive folding of the box through plastic hinges and subsequent self-contacting. In this case the absorbed energy concentrates at the plastic hinges and is rather not homogeneously distributed. This example may illustrate the major drawback of the HCA. Nevertheless, the approach is advantageous for stiffness optimization especially because of its comparably small computational effort.

Evolutionary Algorithm

Another possibility of gradient free optimization, is the use of *Evolutionary Algorithms* (EA). The methodology is based on the basic principles of *Darwin's Theory of Evolution* (Darwin 1859), in which the individuals of a population who possess traits that enable them to adapt to their surrounding environment best, reproduce most frequently (survival of the fittest). The offspring of these individuals will inherit those superior traits and over time those traits will become more frequent within the entire population. In addition to the simple passing on of traits, reproduction also involves recombination with other individuals and the random mutation of traits. As a result, a natural variety within the population remains and the population adapts better and better to its environment over time.
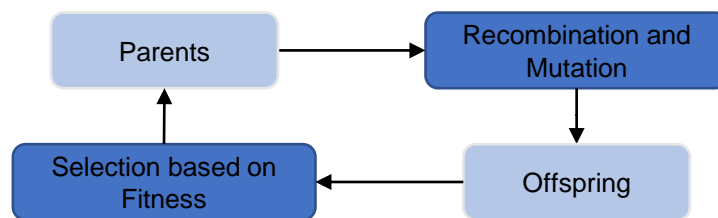
Figure 2.17: Procedure of an evolutionary algorithm (Harzheim 2014)

This process is simulated by the EA and is illustrated in Fig. 2.17. Parents produce offspring by recombination and mutation. The fitness of these offspring is then assessed based on predefined criteria to select the best-fitting among them, which will then become the parents of the next generation. This process is repeated until defined convergence criteria are met.

The idea of transferring this methodology to optimization purposes has been pursued since the 1970s (Rechenberg 1970; Höfler et al. 1973). Accordingly, there is a large number of different implementations and application examples for sizing, shape and topology optimization. The explanation of all publications would go beyond the scope of this work. For an overview please refer to, e.g., Kicinger et al. 2005 or Aulig and Olhofer 2016. However, the most prominent subcategories of evolutionary algorithms should be mentioned at this point: the *Evolution Strategy* (ES) (Rechenberg 1970; Rechenberg 1994) and the *Genetic Algorithms* (GA) (Holland 1992).

The advantage of the procedure described above is certainly that the fitness of the offspring can be represented by any calculable measure. This means that any structural responses calculated in the analysis

can be used for the selection and thus be optimized. Furthermore, the likelihood of ending up in a local optimum is smaller, than when using gradient-based approaches. However, these advantages come at the cost of a considerable disadvantage: the number of analyses necessary to evaluate the offspring is relatively high and increases significantly with the number of design variables.

To get an idea of the involved computational effort, Bujny 2020 should be mentioned, for example, who uses a combination of the level set method and evolutionary algorithms (EA-LSM) for the topology optimization of crash structures. Bujny uses level set functions, in particular moving morphable components, to describe the geometry only. This way the number of design variables can be reduced compared to the previously described density-based approaches, where each voxel or element corresponds to at least one design variable. The design variables specifying the level set functions are then varied and optimized using the evolutionary algorithm. The method's functionality is illustrated by various linear static as well as nonlinear dynamic examples. The latter includes a three-dimensional beam clamped on both sides, which is deformed by the impact of a rigid pole[10]. The beam's topology is described employing 144 design variables and the intrusion of the impactor into the beam is minimized while the beam's mass is constrained. The plausibility of the results is shown by a comparison with those of the HCA method. However, the number of analyses required exceeds that of the HCA method considerably and is given as approximately 6000 (Bujny 2020). This is extremely expensive, and the optimization of full vehicle models is completely unrealistic under these circumstances. Such methods should therefore only be employed if no other method is applicable.

Graph and heuristic based Topology Optimization

Ortmann et. al. developed an alternative approach: The *Graph and heuristic based Topology Optimization* (GHT) combined with sizing and shape optimization (Ortmann and Schumacher 2013; Ortmann 2015). In contrast to the density-based approaches explained before, mathematical graphs are used to describe the topology of constant cross sections of profile structures. Thus, only planar graphs are necessary to describe the cross-sections, although the simulated structures are three dimensional. The optimization is organized in two nested loops: The topology modification is performed based on heuristic rules in the outer loop. These heuristics have been derived from expert knowledge. The heuristics applied in each loop are selected by prioritizing and ranking all heuristics based on the current structural behavior. An example is the heuristic "Delete unnecessary Walls". In order to simplify the structure, unnecessary connections are deleted. They are identified by comparing the maximum internal strain energy density of each connection. Those with comparably small values may be removed without significant influence on the performance of the structure. The sizing and shape optimization is performed in the inner loop using GA or sequential optimization procedures with domain reduction (Ortmann and Schumacher 2013). Both are gradient-free algorithms and typically require a large number of analyses. The approach has been tested using numerical examples, where both stiffness and energy absorption were optimized. Good results

---

[10]In terms of complexity and formulation of the optimization problem, the example is comparable to that examined in chapter 5.2.1. However, a direct comparison of the results is not valid due to differences in material and geometry.

have been achieved for both objectives. The method has recently been extended, such that the results of different heuristics are pursued through the following optimization as competing designs (Ortmann et al. 2021). The goal is to reduce the chance of getting stuck in a local minimum. For testing this extension the inner loop optimization is only performed once at the end in order to save computational effort. According to Ortmann et al. 2021 the number of nonlinear analyses required for convergence can then been reduced from approximately 3500 to 500 using the extension. Although, this is a significant improvement, 500 analyses is still very expensive, especially if large automotive structures are optimized. No qualitative results of the extension compared to the previous implementation has been published. Hence, we cannot tell which approach yields the better results in terms of the structure's performance.

The biggest advantage of the GHT may be the usability of arbitrary structural responses for the definition of objective and constraints. For the particular optimization of profile structures with constant cross-sections it is also advantageous that no interpretation of the resulting structures is necessary as in the case of the density-based approach. The latter may require to transfer the resulting voxel structures to shell structures. This transfer in general opens various possibilities and therefore involves uncertainties. On the other hand, the density-based approach is applicable to a much broader field of problems and is not limited to the optimization of constant cross-sections only. To overcome this issue, efforts are made to extend the GHT to use graphs describing three dimensional structures (Beyer et al. 2020). However, it is questionable if the available heuristics can be directly transferred to three dimensional structures and other problems. Another disadvantage is the high computational cost, which can be attributed in particular to the large number of analyses and the usage of the inner loop optimization algorithms.

The Equivalent Static Load Method

The basic idea of the ESL method is to create linear auxiliary load cases for a nonlinear and/or dynamic problem, enabling gradient-based linear static response optimization. Therefore, the optimization problem is split into an analysis and a design domain. In the analysis domain the original problem is analyzed. Based on these results the linear auxiliary load cases are created in the design domain. These auxiliary load cases are used afterwards to optimize the structure employing efficient gradient-based optimization. The method has initially been introduced by W. S. Choi and Park 2002 for linear dynamic response sizing and shape optimization. Thereafter is has gradually been extended to other types of problems and optimizations, like nonlinear static response optimization (Shin et al. 2007) and nonlinear dynamic response optimization (Kim and Park 2010). It has successfully been applied for sizing, shape and topology optimization (H. A. Lee et al. 2007; Jeong et al. 2008; Hong et al. 2010; Park 2011; Jang et al. 2012; J. J. Lee et al. 2013; H. A. Lee and Park 2015; W. H. Choi et al. 2018; Karev et al. 2018; Karev et al. 2019). The general procedure of the ESL method for all applications remains the same. The main difference is the governing equation to be solved in the analysis domain. Fig. 2.18 illustrates the procedure for nonlinear dynamic response optimization.
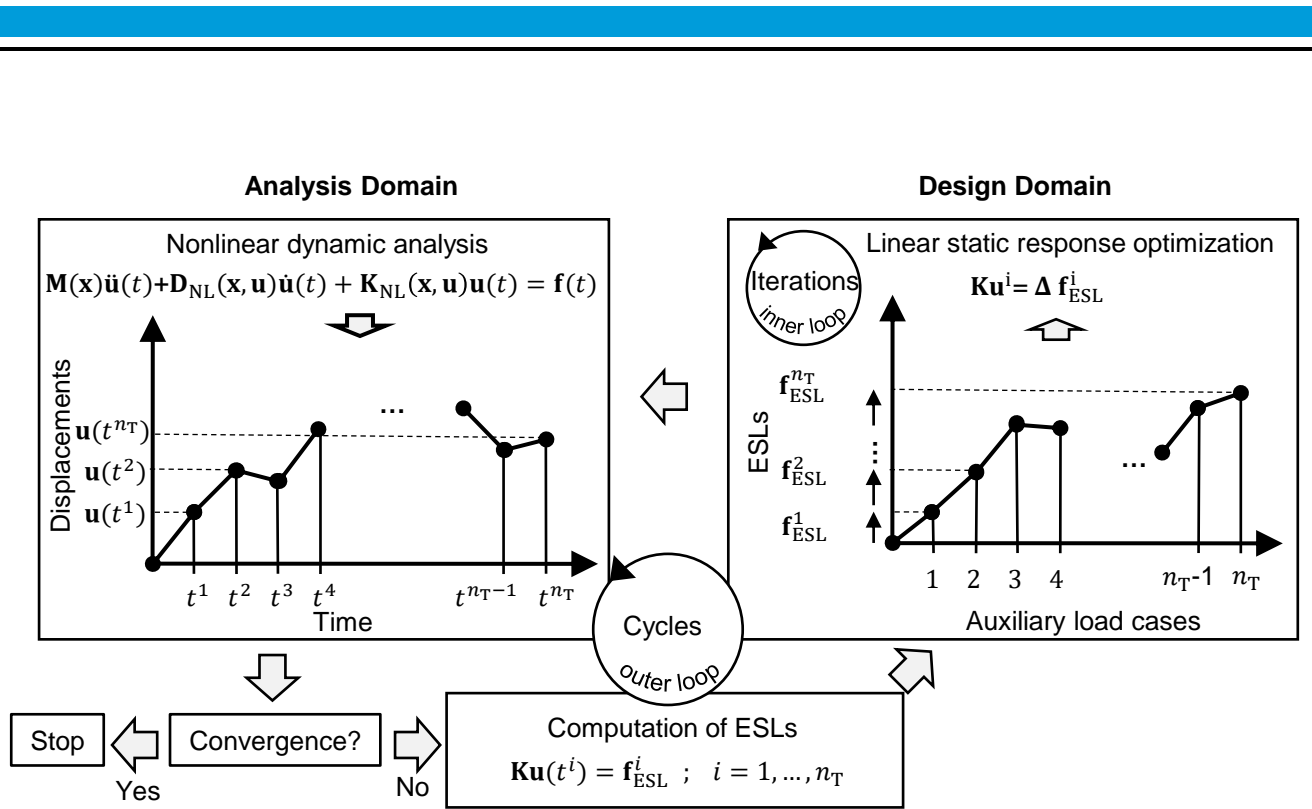
Figure 2.18: Procedure of the ESL method for nonlinear dynamic response optimization

It starts with a nonlinear dynamic analysis. Based on the resulting displacement fields $\mathbf{u}(t^i)$ in the analysis domain for n_T selected times t^i, the ESLs $\mathbf{f}_\mathrm{ESL}$ are calculated in the design domain. This is achieved by multiplying the linear stiffness matrix $\mathbf{K}(\mathbf{x})$ with the given displacement fields for each ESL time:

$$\mathbf{K}(\mathbf{x})\mathbf{u}(t^i) = \mathbf{f}_\mathrm{ESL}^i; \qquad\qquad i = 1, ..., n_\mathrm{T}. \qquad (2.76)$$

The resulting ESLs $\mathbf{f}_\mathrm{ESL}$ are thus equivalent in the sense that they lead to the same displacement fields in linear statics. Each ESL $\mathbf{f}_\mathrm{ESL}^i$ is used to create one auxiliary load case representing the corresponding time t^i. Based on these n_T load cases, linear static response optimization is performed in the design domain afterwards, where the following linear static sub-problem is solved:

$$\min f(\mathbf{x}, \mathbf{u}^i); \qquad\qquad \mathbf{x} \in \mathbb{R}^{n_\mathrm{D}} \qquad (2.77)$$

subject to

$$g_j(\mathbf{x}, \mathbf{u}^i) \leq 0; \qquad\qquad j = 1, ..., n_\mathrm{UC} \qquad (2.78)$$

$$x_l^\mathrm{L} \leq x_l \leq x_l^\mathrm{U}; \qquad\qquad l = 1, ..., n_\mathrm{D} \qquad (2.79)$$

where $\mathbf{u}^i$ is the solution of the auxiliary load case:

$$\mathbf{K}(\mathbf{x})\mathbf{u}^i = \mathbf{f}_{\mathrm{ESL}}^i; \qquad\qquad i = 1, ..., n_{\mathrm{T}}, \qquad (2.80)$$

and the ESLs $\mathbf{f}_{\mathrm{ESL}}$ are the solution of equation 2.76 using the displacement fields $\mathbf{u}(t^i)$ resulting of the nonlinear dynamic FE-equation 2.75. Since for the calculation of the ESLs the stiffness matrix $\mathbf{K}(\mathbf{x})$ describing the undeformed initial geometry is used for all load cases, only one FE-model is required for linear static response optimization.

At the beginning of the linear static response optimization, the displacement fields are identical to those derived from the nonlinear dynamic analysis by definition. As soon as, the design variables $\mathbf{x}$ are changed, this is no longer the case. The responses of the linear auxiliary load cases are only an approximation of those of the nonlinear dynamic system. In order to maintain the approximation's validity, the inner loop should not change the design too much. This can be achieved by executing the inner loop only for a few iterations without achieving convergence. Then the nonlinear dynamic model is updated and evaluated. The responses obtained can be compared to those of the design domain. If their difference is too high the process is iterated in an outer loop until the difference is small enough and additional termination criteria are fulfilled (Park 2011; H. A. Lee and Park 2015). In the following the outer loop iterations are called cycles to distinguish them from the iterations of the inner loop in the design domain.

Since this method requires only one analysis of the nonlinear dynamic system per cycle, the overall number of analyses is usually limited to a low two-digit number. The comparably small computational effort is one of the advantages of the ESL approach. Futhermore, the number of nonlinear dynamic analyses required for convergence does not scale with the number of design variables n_{D}. The method's applicability to sizing, shape, and topology optimization can therefore be stated as another advantage. Moreover, well developed commercial software can be used for nonlinear dynamic analysis and linear static response optimization. This is especially advantageous when employed in an industrial context.

Besides these advantages, there are also some obstacles and disadvantages. Dynamic responses such as velocities, and accelerations are not directly available in the linear static response optimization. Their consideration requires the definition of proper approximations in the design domain. For velocity and acceleration simple finite forward (Jeong et al. 2010) or central (Karev et al. 2019) differences between adjacent auxiliary load cases can be used. The consideration of crash forces is also not straight forward, because the ESL methodology dictates that the ESLs remain constant in each inner loop. In Faß 2017 an approach is introduced and validated, where the reaction force in a roof crush test is approximated using a reciprocal dependency between the displacements in force direction and the reaction force. Due to the impactor's constant velocity the roof crush test is seen as a crash load case with moderate complexity. It therefore needs to be checked whether the approach is applicable for highly nonlinear examples with more complexity.

The *Equivalent Static Displacement* (ESD) method has been presented by Ma et al. 2020 as an alternative approach. The procedure is similar to the ESL method, but instead of the displacements, nodal forces in

the crash zone are extracted from the nonlinear dynamic analysis. They are used to calculate equivalent static displacements which in turn define the load cases for linear static response optimization. In this case the applied nodal forces correspond exactly to those from the nonlinear dynamic analysis, but the resulting displacement fields do not match. However, the displacements remain constant during optimization and forces can thus be considered directly in the formulation of the linear static sub problem. The functionality of the approach has been illustrated using a side impact and a quasi-static crash box example. The examples are used later in the thesis and compared with the results of the DiESL methodology.

The ESL and ESD method have one decisive disadvantage in common, which is the fact that each linear auxiliary load case is based on the *undeformed* initial structure and thus the same stiffness matrix $\mathbf{K}(\mathbf{x})$. As shown in chapter 2.2 the stiffness matrices $\mathbf{K}$ and $\mathbf{K}_{\mathrm{NL}}$ differ considerably, if geometric and material nonlinearities occur as in the case of crash problems. Thus, it can be expected that the sensitivities in the linear auxiliary load cases differ significantly from those of the actual nonlinear dynamic problem and may not even match in sign.

Furthermore, the ESLs used in the linear auxiliary load cases are completely different from the nodal forces in the original nonlinear dynamic problem (c.f. equation 2.30 and 2.33). Also, since the validity of linear statics are exceeded by far, the linear strain and stress measures lead to completely different results in comparison to the appropriate measures in nonlinear dynamics. Constraints on damage and fracture are often based on these responses and are therefore not applicable.

It should also be noted that there is an ongoing debate regarding the transferability of the optimality of the auxiliary sub-problem's solution to the original optimization problem. It was stated for linear dynamic response optimization by Park and Kang 2003 that the KKT-conditions of the linear static auxiliary load cases and the original dynamic problem are identical if certain termination criteria are satisfied. Stolpe 2014 showed that the proof is incomplete and incorrect. He, furthermore, showed that the sensitivities in the auxiliary load cases are not necessarily the same as in the original dynamic problem. In Stolpe et al. 2018 this is supported by a simple counterexample, where the ESL method fails to find the optimum of a linear dynamic response optimization problem. In the example shown, the compliance of a harmonically actuated truss consisting of two members has been optimized. The optimal design has been obtained for structures with eigenfrequencies far away from the driven frequency. However, when using the ESL method, resonance effects are not considered, and the method does not converge towards the actual optimum. This clearly shows a weak point of the ESL method. However, it is questionable whether this issue applies to crash load cases, since resonance effects play a subordinate role here. As a response to Stolpe, Park and Y. Lee 2019 added additional termination criteria and claimed that the solution of the ESL method is a KKT point of the original problem under these conditions. However, this topic is still under discussion. This history perfectly demonstrates the difficulties that may arise when proving convergence and optimality criteria of engineering approaches such as the ESL method.

3 The difference-based equivalent static Load Method

The DiESL method attempts to eliminate the previously described weaknesses of the ESL method by splitting the deformation path into linear increments. The method has initially been presented in Triller 2019. For sizing optimization, it has been shown that the DiESL method enables a significant improvement in approximating the nonlinear dynamic problem using linear auxiliary load cases. The DiESL method found a true optimum of the nonlinear dynamic problem where the ESL method converged to a design point that is not an optimum at all. However, also some obstacles have been observed preventing a robust application of the approach in an industrial context. Furthermore, the method has only been tested for stiffness optimization yet and thus only displacement responses have been considered during optimization. In this chapter, the basic procedure of the DIESL method is explained first. Then, the computation of other crash relevant responses like crash forces is worked out. Afterwards, further potential improvements of the methodology are elaborated and discussed. Finally, the implementation of the methodology is detailed out, addressing the previously observed problems regarding the robust applicability of the method in an industrial context. For the latter the use of commercial solvers is advantageous, but also leads to some limitations which are discussed.

3.1 General Procedure

The general procedure of the DiESL method is similar to the ESL method. As a starting point the basic differences may be illustrated best graphically, like depicted in Fig. 3.1.
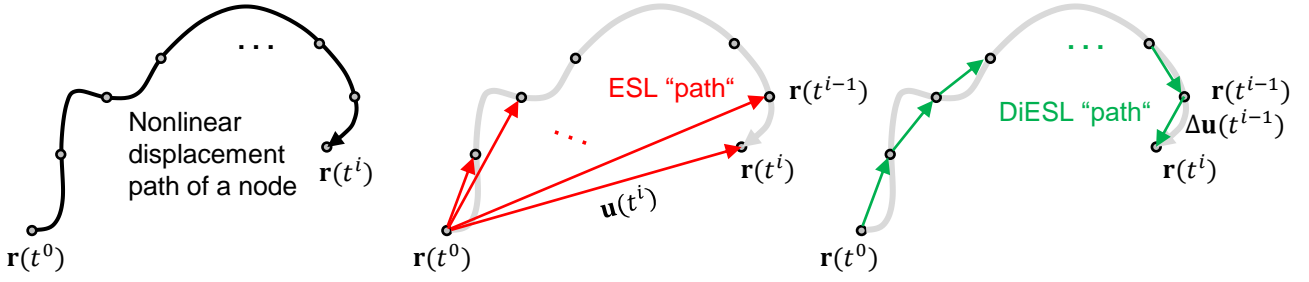
Figure 3.1: Displacement path of an arbitrary node during the deformation of a structure (left) and the corresponding displacement $\mathbf{u}(t^i)$ (middle) and $\Delta\mathbf{u}(t^i)$ (right) used for the computation of the ESLs and DiESLs at time steps t^i, respectively

Here, the displacement path of an arbitrary node, i.e. its coordinates $\mathbf{r}(t)$ as obtained by a nonlinear dynamic analysis is illustrated (Fig. 3.1, left). Results are given at selected discrete times $t^0, ..., t^i$. The ESL method uses the undeformed geometry at time t^0 to assemble the stiffness matrix $\mathbf{K}$. The loads $\mathbf{f}^i_{\mathrm{ESL}}$ to derive the nodal displacements $\mathbf{u}(t^i)$ are calculated for each given time t^i (Fig. 3.1, middle). Consequently, it falls short of following the given nonlinear displacement path (Fig. 3.1, left) but rather jumps from the starting point to each point on the path. In contrast, the DiESL method follows the nonlinear displacement path by splitting it into linear increments (Fig. 3.1, right). This can be accomplished by using an individual linear sub model with the corresponding deformed geometry at each time t^i. Consequently, the DiESL approach requires n_{T} linear sub models, one for each time step $t^i; i = 0, ..., n_{\mathrm{T}} - 1$. We call such a *Linear Sub Model* at time t^i LSM^i in the following. The handling of all LSMs in one optimization run can be realized employing *Multiple Model Optimization* (MMO)[1]. The LSM^i is defined by the coordinates of all nodes at time step t^i which can be combined in the vector

$$\mathbf{r}^T(t^i) = \left(\mathbf{r}_1^T(t^i), \mathbf{r}_2^T(t^i), ..., \mathbf{r}_{n_{\mathrm{N}}}^T(t^i)\right) \tag{3.1}$$

containing the coordinates $\mathbf{r}_j(t^i)$ of all nodes of the FE-model. Since all LSMs share the same mesh topology and only differ in the coordinates $\mathbf{r}(t^i)$, the coordinates of LSM^i can be calculated by

$$\mathbf{r}(t^i) = \mathbf{r}(t^0) + \mathbf{u}(t^i), \tag{3.2}$$

where $\mathbf{r}(t^0)$ are the coordinates of the undeformed structure and $\mathbf{u}(t^i)$ are the displacement fields derived from nonlinear dynamic analysis. And the incremental displacement fields $\Delta\mathbf{u}(t^i)$ leading from $\mathbf{r}(t^i)$ to $\mathbf{r}(t^{i+1})$ are calculated as

$$\Delta\mathbf{u}(t^i) = \mathbf{u}(t^{i+1}) - \mathbf{u}(t^i) = \mathbf{r}(t^{i+1}) - \mathbf{r}(t^i). \tag{3.3}$$

---

[1]In MMO multiple FE-models are taken into account simultaneously in one linear static response optimization run

The corresponding incremental equivalent static loads $\Delta \mathbf{f}_{\text{DiESL}}^i$ can be calculated for each LSM^i using

$$\mathbf{K^i} \Delta \mathbf{u}(t^i) = \Delta \mathbf{f}_{\text{DiESL}}^i; \qquad\qquad i = 0, ..., n_\text{T} - 1, \qquad (3.4)$$

where the tangent stiffness matrix $\mathbf{K}^i = \mathbf{K}(\mathbf{x}, \mathbf{r}(t^i))$ is defined by the design variables $\mathbf{x}$ and the nodal coordinates $\mathbf{r}(t^i)$ of LSM^i and therefore incorporates the arising geometric nonlinearities, but non due to path-dependent material. [2] Like in the ESL method, the incremental equivalent static loads $\Delta \mathbf{f}_{\text{DiESL}}^i$ are used in the design domain for solving the following optimization problem:

$$\min f\left(\mathbf{x}, \Delta \mathbf{u}^0(\mathbf{x}), ..., \Delta \mathbf{u}^{n_\text{T}-1}(\mathbf{x})\right); \qquad\qquad \mathbf{x} \in \mathbb{R}^{n_\text{D}} \qquad (3.5)$$

subject to

$$g_j\left(\mathbf{x}, \Delta \mathbf{u}^0(\mathbf{x}), ..., \Delta \mathbf{u}^{n_\text{T}-1}(\mathbf{x}))\right) \leq 0; \qquad\qquad j = 1, ..., n_\text{IC} \qquad (3.6)$$

$$x_l^\text{L} \leq x_l \leq x_l^\text{U}; \qquad\qquad l = 1, ..., n_\text{D} \qquad (3.7)$$

where $\Delta \mathbf{u}^i$ is the solution of the auxiliary load case:

$$\mathbf{K}^i \Delta \mathbf{u}^i = \Delta \mathbf{f}_{\text{DiESL}}^i; \qquad\qquad i = 0, ..., n_\text{T} - 1, \qquad (3.8)$$

and the DiESLs $\Delta \mathbf{f}_{\text{DiESL}}$ are the solution of equation 3.4 with the displacements $\Delta \mathbf{u}(t^i) = \mathbf{u}(t^{i+1}) - \mathbf{u}(t^i)$ derived from nonlinear dynamic analysis 2.75.

To exemplify the resulting benefits from employing the deformed geometries $\mathbf{r}(t^i)$ for assembling the stiffness matrices $\mathbf{K}^i$, we consider a three-point bending example with a beam of height h as illustrated in Fig. 3.2.

Figure 3.2: Different states of deformation in three-point bending illustrating the benefits of the DiESL approach (modified from Triller et al. 2021)

At time $t^0 = 0$ the structure is subjected to bending only, but due to the deformation at later times t^i there are also tensile contributions. Assuming that the beam is optimized, only the bending contributions are considered by the ESL method, since the ESL method employs the undeformed structure in each auxiliary

---

[2]This is driven by the requirement of using commercial software for analysis and optimization. The grid coordinates and design variables are standard input parameters for commercial FE software for linear static problems and can therefore be easily adjusted. Adjustment of material properties at the element level is not as straightforward and is addressed in Chapter 3.2.2.

load case. In contrast, with the DiESL method the tensile contributions are considered as well, because the deformed structures as illustrated in Fig. 3.2 by the dotted lines are employed as LSMs. Thus, the DiESL method provides a better approximation when optimizing the height h of the beam. In Triller 2019 this advantage has been confirmed, minimizing the mass of a similar three point bending example, while the deflection of the beam was constrained. It has been shown, that the DiESL method converges significantly faster to the known optimum than the ESL method.

The overall program flow of the DiESL method is similar as for the ESL method explained before. This is illustrated in Fig. 3.3. Exactly as described for the ESL method, there is an outer optimization loop involving analysis and design domain until certain convergence criteria are satisfied. Keeping this iterative scheme enables the usage of commercial solvers for the DiESL method as it is the case for the ESL method.
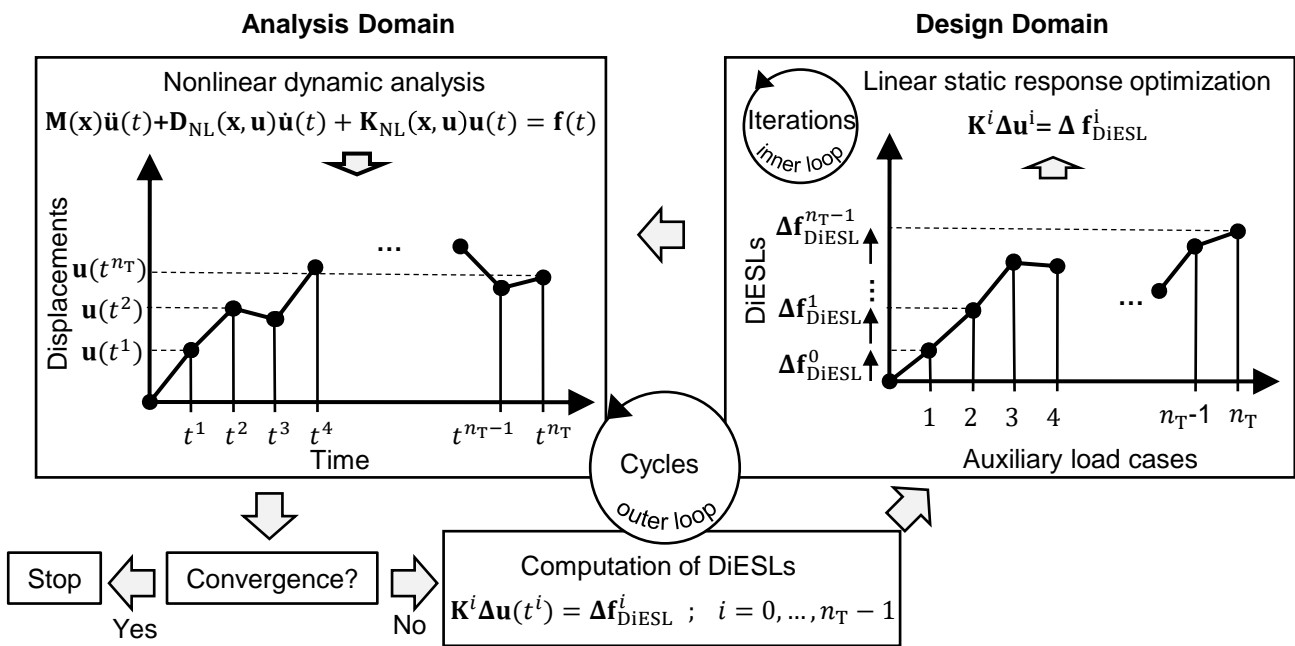
Figure 3.3: General optimization process of the DiESL method for nonlinear dynamic response optimization (Triller et al. 2022b)

Splitting the deformation path into increments and optimizing each LSM using MMO, however, requires some efforts for the reconstruction of the total response values during the inner loop optimization. Furthermore, some structural responses such as velocities, accelerations, and crash forces are not available in linear statics or remain constant during the linear static response optimization due to the ESL methodology. In the following it is worked out how these responses can be computed using the DiESL method and MMO.

3.1.1 Computation of Displacements

Each LSM yields the incremental displacement $\mathbf{\Delta u}^i$. The total displacement $\mathbf{u}^i$ can then be computed recursively as

$$\mathbf{u}^i = \mathbf{u}^{i-1} + \mathbf{\Delta u}^{i-1} \tag{3.9}$$

or as an accumulated sum

$$\mathbf{u}^i = \sum_{j=0}^{i-1} \mathbf{\Delta u}^j \tag{3.10}$$

where $\mathbf{\Delta u}^{i-1}$ are the nodal displacement results of LSM^{i-1} during optimization. This accumulation is performed by the MMO process, which manages all LSMs.

3.1.2 Computation of Strains and Stresses

Just like displacements, the strains and stresses need to be accumulated as well. The procedure is exemplified for strains in the following. The strain component ε^i in LSM^i can be calculated recursively as

$$\varepsilon^i = \varepsilon^{i-1} + \alpha^{i-1}\Delta\varepsilon^{i-1}, \tag{3.11}$$

or as an accumulated sum

$$\varepsilon^i = \sum_{j=0}^{i-1} \alpha^j \Delta\varepsilon^j \tag{3.12}$$

where α is a scaling factor. It is introduced to attribute for nonlinearities arising in the kinematic and constitutive relations. The scaling factor is defined as

$$\alpha^i = \frac{\varepsilon(t^i) - \varepsilon(t^{i-1})}{^0\Delta\varepsilon^{i-1}} \tag{3.13}$$

where $^0\Delta\varepsilon^{i-1}$ is the incremental strain in LSM^{i-1} at the beginning of the linear static response optimization (i.e. iteration 0) in each cycle and $\varepsilon(t^i)$ is the strain at corresponding time t^i obtained from nonlinear dynamic analysis. For strains the scaling factor $\alpha = 1$ can usually be used, since the kinematic relations can be assumed to be linear at least if the ESL time increments are selected sufficiently small (Triller et al. 2021). This is not the case for the constitutive relations and hence the computation of stresses, e.g. the hardening modulus E_{H} in the plastic area considerably differs from the Young's modulus E.

3.1.3 Computation of Velocities and Accelerations

Like mentioned before for the ESL method, velocities and accelerations can be approximated using finite differences between adjacent time steps if the time steps are sufficiently small. In DiESL the incremental

solution $\mathbf{\Delta u}^i$ can be directly used, as it already is a difference. The velocities at time t^i follows as a forward difference:

$$\dot{\mathbf{u}}^i = \frac{\mathbf{\Delta u}^i}{\Delta t^i}, \tag{3.14}$$

where $\Delta t^i = t^{i+1} - t^i$. The accelerations follow as

$$\ddot{\mathbf{u}}^i = \frac{2(\dot{\mathbf{u}}^i - \dot{\mathbf{u}}^{i-1})}{\Delta t^i + \Delta t^{i-1}}, \tag{3.15}$$

3.1.4 Computation of Forces

As elaborated before, the consideration of forces is an elementary part of crashworthiness optimization. Since the DiESLs $\mathbf{\Delta f}_{\text{DiESL}}$ remain constant during the linear static response optimization per definition, an alternative approach to approximate the changes of forces during the linear static response optimization must be found. For the ESL method, Faß 2017 used a reciprocal dependency between the contact force F and a node's displacement u in the contact zone in the direction of the force [3]. This dependency in the linear static system can be derived from the following considerations: at the beginning of each linear static response optimization the ESLs yield the displacement $^0u^i = u(t^i)$ derived from nonlinear dynamic analysis. This displacement can be related to the contact force $^0F^i = F(t^i)$ (Point A in Fig. 3.4), by introducing a global stiffness $k(\mathbf{x})$:

$$\frac{^0F^i}{^0u^i} = {}^0k, \tag{3.16}$$

where $^0k = k(^0\mathbf{x})$ is the global stiffness at the beginning of the optimization. The force F^i to be approximated can also be related to $^0u^i$ and a corresponding stiffness $k(\mathbf{x})$ as (Point B in Fig. 3.4):

$$\frac{F^i(\mathbf{x})}{^0u^i} = k(\mathbf{x}). \tag{3.17}$$

Since the ESLs remain constant during linear static response optimization, we try to find the displacements u^i corresponding to the global stiffness $k(\mathbf{x})$ at a constant force level $^0F^i$ (Point C in Fig. 3.4):

$$\frac{^0F^i}{u^i(\mathbf{x})} = k(\mathbf{x}). \tag{3.18}$$

Using 3.17 = 3.18 yields the reciprocal dependency between F^i and u^i:

$$F^i(\mathbf{x}) = \frac{^0F^i}{u^i(\mathbf{x})} {}^0u^i. \tag{3.19}$$

This means the force F^i can be reduced by increasing the displacement u^i and vice versa. Assuming a reduction of the displacement is equivalent with increasing the stiffness, it follows that the increase of the

---

[3]For the sake of simplicity the vector notation is omitted in the following, since the discussed contact force F and the node's displacement u are collinear

stiffness leads to an increase of the contact force.
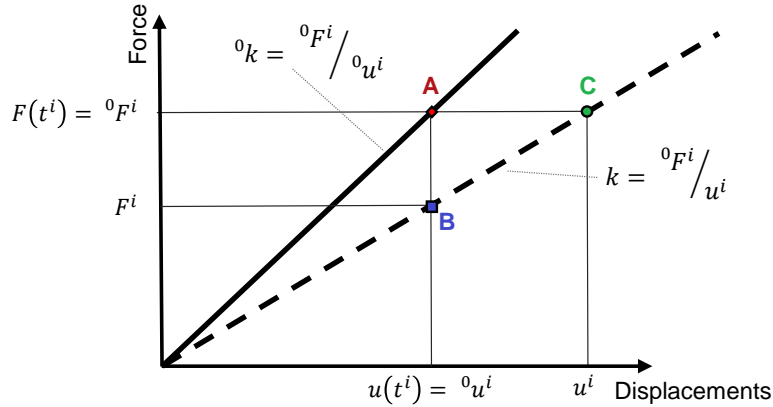
Figure 3.4: Relation between contact force F^i and displacements u^i in ESL

The presented approach will now be transferred to the incremental DiESL methodology. The most obvious solution is to transfer the approach directly to an increment or LSM. This will be called *Inc* approach in the following. The force increment in an LSM is defined as:

$$\Delta F^i(\mathbf{x}) = \frac{{}^0\Delta F^i}{\Delta u^i(\mathbf{x})}\,{}^0\Delta u^i. \tag{3.20}$$

The total force then follows as the sum of all increments

$$F^i = \sum_{j=0}^{i-1} \Delta F^j. \tag{3.21}$$
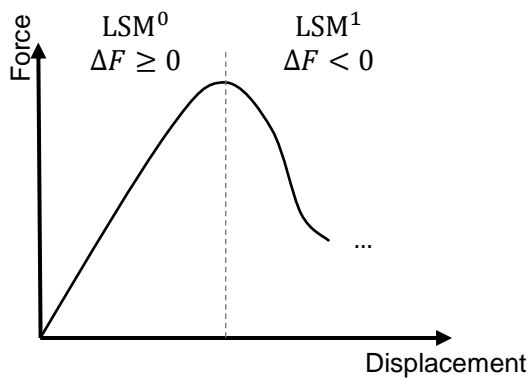
Figure 3.5: Contact force curve describing elastic compression ($\Delta F > 0$) followed by plastic crushing ($\Delta F < 0$)

When geometric nonlinearities are involved there is another phenomenon that needs to be considered. It is

observed in both displacement-driven (e.g. roof crush) and initial velocity-driven (e.g. front crash) crash events. It is illustrated by the following simplified example. The force curve shown in Fig. 3.5 describes the deformation of a crash structure in 2 steps: initially, there is only elastic compression of the structure, and the force increases linearly. Subsequently, the force drops with increasing displacement. This behavior can be explained with the formation of a plastic hinge as a result of the geometric changes, e.g. buckling. Each of the two steps is covered in the following by one respective LSM. As illustrated in Fig. 3.5, the incremental forces $^0\Delta F^0 > 0$ and $^0\Delta F^1 < 0$ differ in their sign sign while the incremental displacements are both positive. As a result, the sensitivities $\frac{\partial \Delta F^0}{\partial \Delta u^0}$ and $\frac{\partial \Delta F^1}{\partial \Delta u^1}$ have opposite signs as well. This means for increasing the total force $F^1 = \Delta F^0 + \Delta F^1$, the displacement Δu^0 has to be reduced, whereas Δu^1 has to be increased. The latter is in contradiction to the original assumption – total force F increases with an increase in the stiffness or a reduction of displacement, respectively – reflected by equation 3.19.

In Fig. 3.6 the dependencies between force and displacement are illustrated by the black line for the *Inc* approach. On the left side the reciprocal dependency between ΔF and Δu for $\Delta F \geq 0$ is given according to equation 3.19. On the right side the curve is plotted for $\Delta F < 0$. Obviously the approximated force ΔF increases (i.e., moves towards positive infinity) as the displacement increases for the *Inc* approach. This behavior contradicts the assumption – total force F increases with an increase in the stiffness or a reduction of displacement. To remedy this inversed behavior we introduce an alternative approximation for LSMs where $\Delta F^i < 0$:

$$\Delta F^i(\mathbf{x}) = \frac{^0\Delta F^i}{2\,^0\Delta u^i - \Delta u^i(\mathbf{x})}\,^0\Delta u^i. \tag{3.22}$$

Geometrically, this is a reflection of the *Inc* curve about the line $\Delta u = {}^0\Delta u$. We will use the abbreviation *IncS* in the following to reference this approach. As illustrated in Fig. 3.6 by the red dashed line, the general assumption holds for this approach. Summarizing this approximation in one equation within the optimization for both cases, we introduce the transformation variable θ:

$$\theta^i = \begin{cases} 1 & if & \Delta F^i \geq 0 \\ -1 & if & \Delta F^i < 0, \end{cases} \tag{3.23}$$

and $\Delta F^i(\mathbf{x})$ follows as

$$\Delta F^i(\mathbf{x}) = \frac{2\,^0\Delta F^i}{(1+\theta^i)\Delta u^i + (1-\theta^i)\left(2\,^0\Delta u^i - \Delta u^i(\mathbf{x})\right)}\,^0\Delta u^i. \tag{3.24}$$

In chapter 4.3 both the *Inc* and *IncS* approach are tested using sizing optimization examples.

$$\Delta F \geq 0 \qquad\qquad \Delta F < 0$$
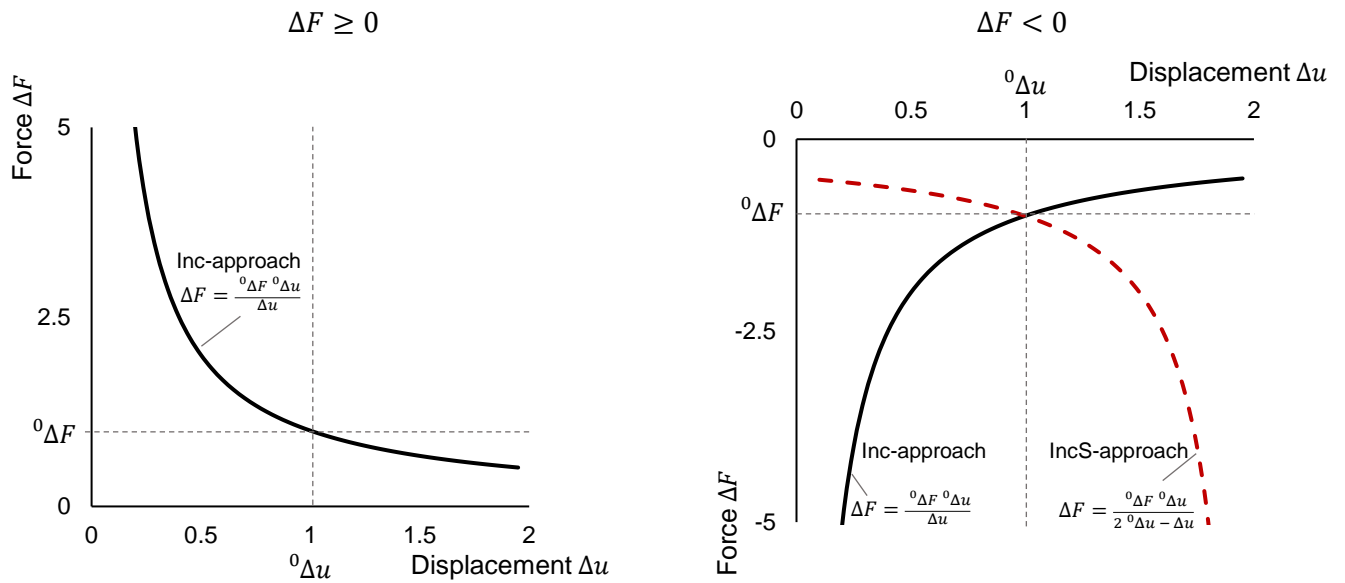
Figure 3.6: Relationship between incremental displacement Δu and incremental force ΔF when using the *Inc* and *IncS* approach for approximation

3.2 Potential Improvements

In the following further potential improvements of the previously presented DiESL method are elaborated and discussed. These improvements should enhance the approximation quality of linear auxiliar load cases when compared to the nonlinear dynamic system.

3.2.1 Discretization in Time

The DiESL method incorporates geometric nonlinearities into the auxiliary load cases by employing multiple LSMs with one subcase each instead of using one model with multiple subcases. Compared to the ESL method, this advantage comes with additional efforts, since not only one FE-model is employed in linear static response optimization, but n_T different FE-models simultaneously. To keep the computational costs low, the number of ESL times n_T should therefore be limited[4]. So far equidistant ESL times $\mathbf{t}$ have been used (Triller 2019). However, in most crash problems the nonlinearities and hence the changes of the stiffness matrix do not occur at regular time intervals. As an example, the contact force curve and three different states of deformation for a crash box colliding with a rigid impactor are illustrated in Fig. 3.7. The oscillating course of the contact force reflects the creation of plastic hinges and subsequent contacting and therefore the occurrence of nonlinearities. It can be assumed that the stiffness matrix changes only

---

[4]To get an impression of the computational efforts involved depending on n_T please refer to appendix 7.3.

moderately while the contact force is linearly increasing. In contrast, at the curve's extrema strong changes are to be expected. Hence, the ESL times should be placed at these extrema where nonlinearities dominate, in order to capture the changes of the stiffness matrix.
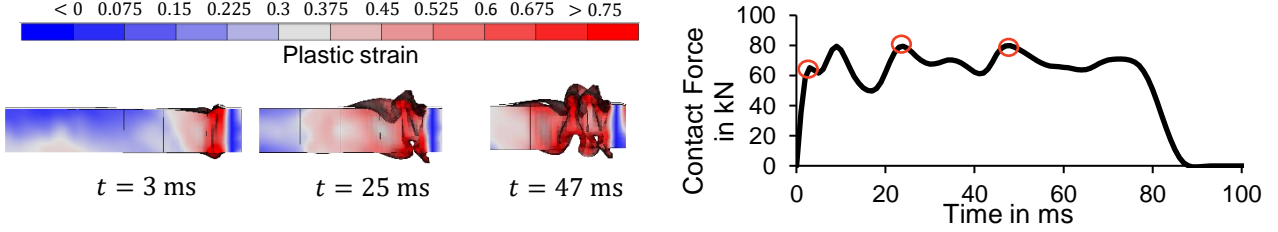
Figure 3.7: Deformation of a crash box model at three different times and corresponding contact force curve between impactor and crash box (times of deformations indicated with red circles) (Triller et al. 2022a)

This can be accomplished by an adaptive selection of ESL times in each cycle directly after the nonlinear dynamic analysis (Triller et al. 2022a). The idea is to fit a representative curve $f(t)$ by a piecewise linear line $l(t)$ with the ESL times $\mathbf{t} = \{t_0, t_1, t_2, ..., t_{n_{\mathrm{T}}}\}$ as breakpoints. Since in most crash-problems, a rigid impactor collides with a structure, the contact force curve between both can be used as an indicator of the nonlinearities and therefore be considered as representative.

Before the nonlinear dynamic analysis is executed, the ESL times are not yet defined. A set of possible ESL times $\boldsymbol{\tau}$ needs to be defined for which the displacement results are output from the nonlinear solver. This means, the results of the nonlinear dynamic analysis (i.e. contact force and displacement field) must be stored for all $n_\tau + 1$ possible ESL times $\boldsymbol{\tau} = \{\tau_0, \tau_0 + \Delta\tau, \tau_0 + 2\Delta\tau, ..., \tau_{n_\tau} - \Delta\tau, \tau_{n_\tau}\}$. Due to storage requirements n_τ should also be limited. Consequently, no continuous description of the function $f(t)$ to be fitted is available. To avoid the usage of a discrete optimizer in the following, the function $f(t)$ is approximated as a piecewise linear function, based on the stored data f_i:

$$f(t) = f_{i-1} + \frac{f_i - f_{i-1}}{\tau_i - \tau_{i-1}}(t - \tau_{i-1}); \qquad \tau_{i-1} \leq t < \tau_i; \qquad i = 1, ..., n_\tau. \qquad (3.25)$$

To determine the optimal selection of $\mathbf{t}$ from the set $\boldsymbol{\tau}$, the piecewise linear function $l(t)$, defined by the ESL-times $\mathbf{t}$ as breakpoints

$$l(t) = f(t_{j-1}) + \frac{f(t_j) - f(t_{j-1})}{t_j - t_{j-1}}(t - t_{j-1}); \qquad t_{j-1} < t \leq t_j; \qquad j = 1, ..., n_{\mathrm{T}} \qquad (3.26)$$

is defined. It is fitted to represent the piecewise linear function $f(t)$ in an optimal way as illustrated in Fig. 3.8. For this purpose, the *Sum of Squared Residuals* (SSR) between $l(t)$ and $f(t)$ is defined:

$$SSR(\mathbf{x}) = \frac{1}{n_\tau} \sum_{i=0}^{n_\tau} (f(\tau_i) - l(\tau_i))^2; \qquad \mathbf{x} \in \mathbb{R}^{n_{\mathrm{D}}}. \qquad (3.27)$$

The vector of ESL times $\mathbf{t}$ is then obtained as solution of the following optimization problem:

$$\min SSR(\mathbf{x}); \tag{3.28}$$

subject to

$$|x_j - x_i| \geq \Delta\tau; \qquad i \neq j; \qquad j = 1, ..., n_{\mathrm{D}}; \qquad i = 1, ..., n_{\mathrm{D}} \tag{3.29}$$

$$x_{fix(i)} = t_{i,\mathrm{fix}}; \qquad\qquad\qquad i = 1, ..., n_{\mathrm{fix}} \tag{3.30}$$

where $\mathbf{x} = \mathbf{t}$ is the vector of ESL-times. The inequality constraints 3.29 are used to define a minimum spacing of ESL times that is no smaller than the spacing $\Delta\tau$ of the stored data f_i. The equality constraints 3.30 enforce a set of n_{fix} predefined ESL times $t_{i,\mathrm{fix}}$ that must be contained in the solution and are mapped via the function $fix(i)$ to the corresponding ESL times. Examples for such predefined ESL times are:

- The initial time $t_0 = 0$ must always be prescribed.

- The last ESL time must always be prescribed. The simulation end time may be used here. Alternatively, a characteristic event may be used to define this time. For example, this may be the time of maximum intrusion t_d where any response value after this time is ignored during the linear static response optimization. This has the advantage that the ESL times are distributed more densely in the range of interest.

- An intermediate ESL time may be prescribed to match a characteristic event. An example here would be to enforce an ESL time to match the time of maximum contact force $t_{F_{\mathrm{max}}}$.

The optimization problem is solved using continuous ESL times $\mathbf{x}$ and a sequential least square programming optimization algorithm. The results are rounded afterwards, according to the spacing $\Delta\tau$ of the stored data points τ:

$$^*x_{i,\mathrm{r}} = \lfloor \frac{^*x_i}{\Delta\tau} + 0.5 \rfloor \Delta\tau; \qquad\qquad i = 0, ..., n_{\mathrm{D}}. \tag{3.31}$$

As a result, the fitted ESL times $^*\mathbf{t}$ follow from the rounded results $^*x_{i,\mathrm{r}}$.
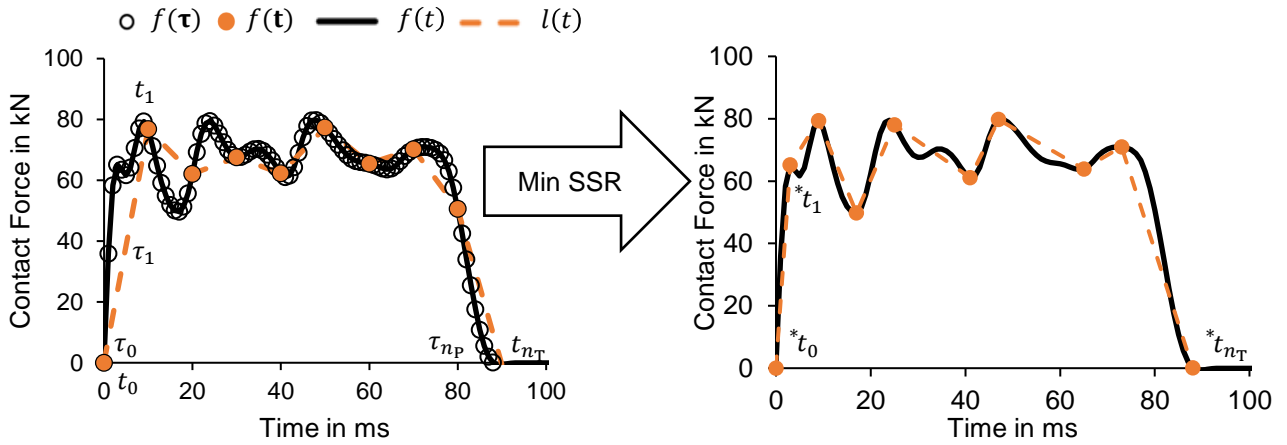
Figure 3.8: Piecewise linear fit of contact force curve $f(t)$ by polygonal line $l(t)$ with ESL-times $\mathbf{t}$ as breakpoints before (left) and after (right) optimization (Triller et al. 2022a));
Note: in the right diagram the stored data points $f(\tau)$ are omitted for clarity

When solving the optimization problem 3.28 using sequential least square programming the starting values $^0\mathbf{x}$ can have decisive influence on the results. Therefore, two different strategies for selecting $^0\mathbf{x}$ are compared in the following. The first strategy is simple and uses *equidistant spacing* (EQD). In the second strategy the initial values are determined by *successive breakpoint removal* (SBR) of breakpoints with small impact on the SSR: the number of design variables n_D is initially set to the largest value possible n_τ, such that each of the breakpoints t_j of $l(t)$ is located on a time τ_i. In that case, $SSR(\mathbf{x}) = 0$ because the piecewise linear function $l(t)$ is identical to $f(t)$. Then one breakpoint is removed, namely the breakpoint, for which the SSR increases the least. It is prohibited to remove a prescribed breakpoint. If the last ESL time does not match the simulation end time, then only the relevant times τ_j are taken into consideration. This process of removing one breakpoint is repeated successively until the desired number of design variables n_D or ESL times is obtained.

Fig. 3.9 compares both strategies using the curve $f(t)$ illustrated on the right side. Like suggested before, the time of maximum contact force $t_{F_\mathrm{max}} = 35$ ms is prescribed as well as time $\tau_0 = 0$ ms and the simulation end time $\tau_{80} = 80$ ms. The curve is fitted for $n_\mathrm{T} = 10, 11, ..., 39, 40$ ESL times. On the left side of Fig. 3.9 the resulting SSR is plotted for both strategies over n_T. On the right side of Fig. 3.9 the fit for both strategies is plotted for $n_\mathrm{T} = 12$. It can be seen clearly that SBR leads to significantly better results. The curve $f(t)$ is characterized by an uneven distribution of extremes. Here, SBR draws its benefits from the ability to unevenly distribute the initial values $^0\mathbf{x}$ before and after the intermediate prescribed ESL time t_{F_max}: for $n_\mathrm{T} = 12$ the distribution is 9:3 (left:right) by SBR and 6:6 by EQD. Note that one weakness of the optimization problem stated in equation 3.28 is the fact that a breakpoint cannot pass any prescribed time due to the inequality constraints 3.29. This is detrimental if the occurrence of local extrema is not balanced before and after a prescribed breakpoint as is the case in Fig. 3.9. Furthermore, the optimization

problem suffers from a multitude of local minima. It is a strength of the SBR method to provide an excellent initial value with a low SSR value and therefore it is used in the following. The additional computational effort compared to EQD is limited, since the number of possible ESL-times n_τ should also be limited due to storage requirements. The adaptive selection of ESL times is tested in chapter 4.2 for sizing optimization.
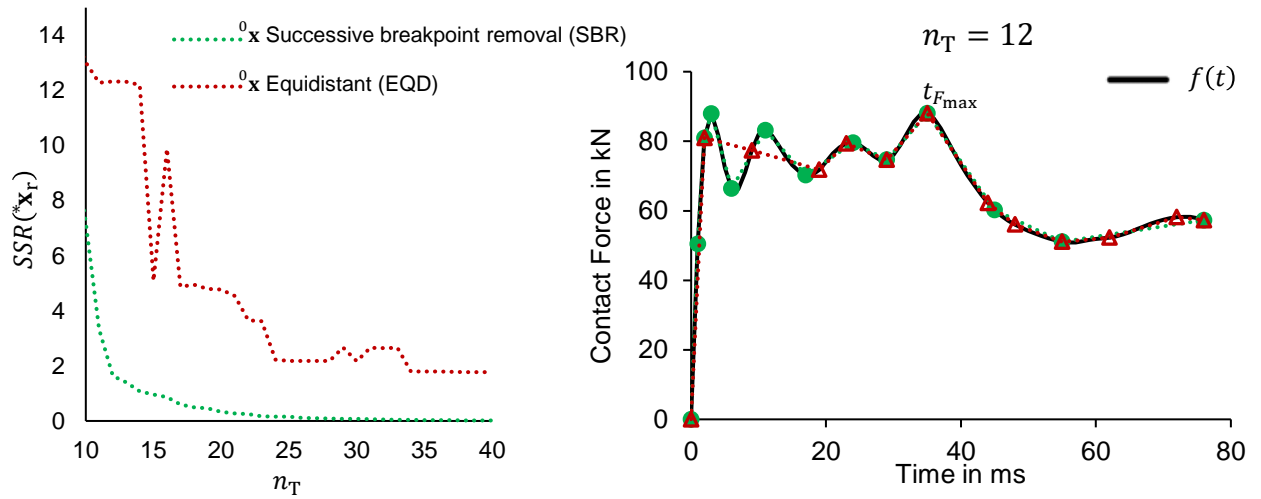
Figure 3.9: $SSR\left({}^{*}\mathbf{x}_{\mathrm{r}}\right)$ for different choices of starting values ${}^{0}\mathbf{x}$: equidistant (EQD) versus successive breakpoint removal (SBR) (left) and corresonding curve $f(t)$ as well as fits for $n_{\mathrm{T}} = 12$ (right) (Triller et al. 2022a)

3.2.2 Adaption of path depended properties

Splitting the deformation path into increments with DiESL, also enables the adaption of path depended structural properties in the LSMs such as the material stiffness. As explained in chapter 2.2.4 the constitutive relations become nonlinear in the case of crash problems. For example, plasticization occurs during deformation, and the stiffness of the plasticized regions is drastically reduced. The significantly lower material stiffness of elements exceeding yield stress can be adopted in the corresponding LSMs by adapting the Young's modulus on element level. For this purpose, we employ a bilinear material model in the design domain, which is defined by two material containers representing the Young's modulus E and the hardening modulus E_H (Fig. 3.10).
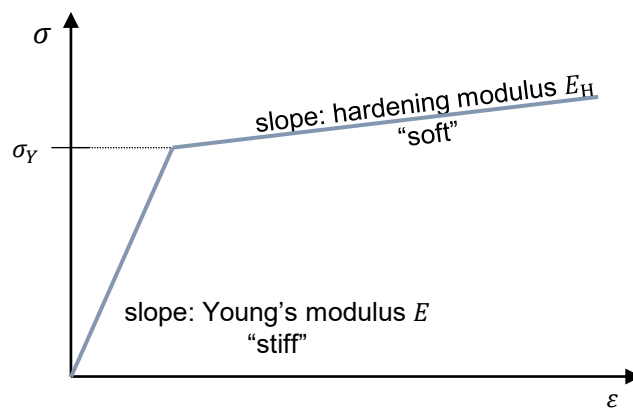
Figure 3.10: Effective strain vs. stress for a bilinear material model

As elaborated previously, during the nonlinear dynamic analysis the yield function is evaluated to determine if the structure deforms either elastically or plastically. However, since the time increment represented by one LSM is significantly larger than those used within the explicit time integration, this logic may not be suited here. The time difference is such big that we cannot exclude the possibility that elements are in several different states during the time step represented by an LSM. In this case, both E and E_H would not correctly represent the material behavior in the design domain. In order to find an easy criterion to decide which material stiffness is assigned to an element in the design domain, the following considerations are made. During an automotive crash, the force is typically transferred from the contact zone with the colliding structure via specific load paths into the vehicle structure. Those load paths have major influence on the structural behavior and are hence of special interest when it comes to crashworthiness design. During the crash, parts of the structure deform plastically along the load path and plastic joints are formed. Due to the low stiffness of these plastic joints, it is likely that they will continue to deform plastically until the load path changes. This may happen as a result of the folding process and subsequent contacting as exemplified in Fig. 3.7, where already plastified structural parts leave the load path in the consequence of

such event. Furthermore, we assume that plasticized elements outside the load path have little influence on the structural behavior. If these elements relax elastically, this consequently also has little influence on the structural behavior. Following the above considerations, it is essential that already plastified elements are assigned to the smaller stiffness E_{H}. Therefore, the element's plastic strain $\varepsilon_{\mathrm{p}}(t^i)$ calculated during nonlinear dynamic analysis is used as criterion to decide if either the Young's modulus or the hardening modulus is used for the respective element in the corresponding LSM^i. If $\varepsilon_{\mathrm{p}}(t^i) > 0$ the hardening modulus is used, otherwise the Young's modulus. Furthermore, the Poisson's ratio is set to 0.49 to account for the incompressibility of the plastic deformation. The adapted stiffness matrix $\hat{\mathbf{K}}^i$ assembled in LSM^i then also depends on the plastic strain vector

$$\varepsilon_{\mathrm{p}}^T(t^i) = \left(\varepsilon_{\mathrm{p},1}^T(t^i), \varepsilon_{\mathrm{p},2}^T(t^i), ..., \varepsilon_{\mathrm{p},n_{\mathrm{E}}}^T(t^i) \right), \tag{3.32}$$

and thus

$$\hat{\mathbf{K}}^i = \mathbf{K}\left(\mathbf{x}, \mathbf{r}(t^i), \varepsilon_{\mathrm{p}}(t^i) \right). \tag{3.33}$$

In Fig. 3.11 the procedure of adapting the material stiffness in the linear auxiliary load cases is exemplified using a deformed steel frame structure with bilinear material behavior ($E = 210$ GPa, $E_{\mathrm{H}} = 0.6$ GPa) subjected to a pole impact. On the left side the present plastic strains at time $t = 82$ ms and on the right side the used materials in the corresponding LSM are illustrated. The non-plasticized purple elements are assigned to a material with $E = 210$ GPa in the LSM. The remaining elements are assigned to a material representing the hardening modulus with $E = 0.6$ GPa.

In chapter 4.2 it is tested if the approximation capability of the DiESL method can be improved by adapting the material properties of the LSMs using the bilinear material model in the design domain. For this purpose nonlinear dynamic sizing optimization problems involving a bilinear as well as a piecewise linear material model are employed. For the latter, the hardening modulus does not remain constant after yielding. However, the changes of the hardening modulus are small in relation to the Young's modulus. Thus, it is assumed that the hardening modulus can be properly approximated using a bilinear material model in the design domain. Note that in general it is conceivable to define additional intermediate material containers in the LSMs to account for the changes of the hardening modulus when piecewise linear material behavior is employed in the analysis domain. However, the effort for this is relatively high, since the way of assembling an LSM's stiffness matrix cannot be directly prescribed when employing a commercial solver for linear static response optimization. Instead, a part must be created for each material container. An element is then not directly assigned to a material but to the associated part. The complexity increases, as the design variables for sizing are related to the respective mechanical properties by referencing the corresponding part. To keep it simple, we limit ourselves here to the use of a bilinear material model in the design domain.

Nonlinear dynamic analysis at time t^i

elements without plastic strain: $\varepsilon_p = 0$

elements with plastic strain: $\varepsilon_p > 0$

Corresponding LSM^i

use Young's modulus: E = 210.0 GPa

use hardening modulus: E = 0.6 GPa

Plastic strain, Max of Inn, Out and Mid

>0.008
0.007
0.006
0.005
0.004
0.003
0.002
0.001
<0
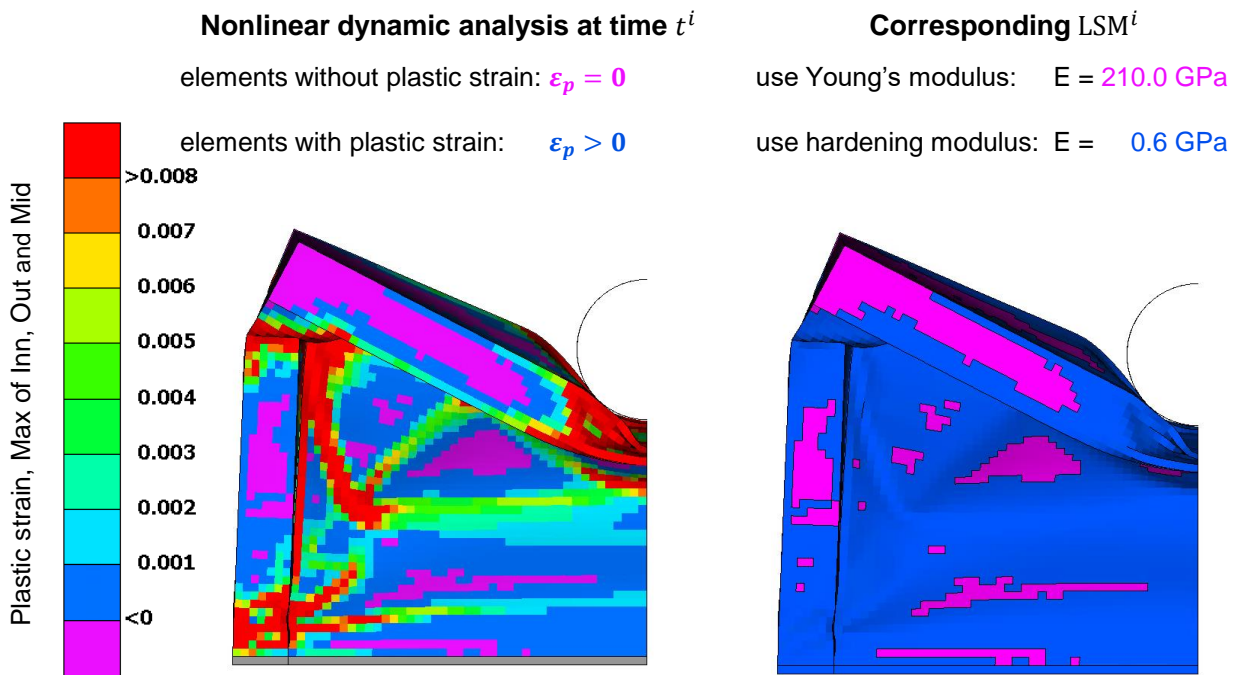
Figure 3.11: Plastic strain of nonlinear dynamic analysis of a frame structure subjected to a pole impact (chapter. 4 $x_i = 0.8$ mm) at time $t = 82$ ms and corresponding LSM (Triller et al. 2022a)

3.3 Implementation

In the following the implementation of the DiESL method is detailed out. For this purpose first the employed commercial software is presented. Afterwards, the used convergence criteria and techniques for limiting the length of the optimization path in the design domain are described. Furthermore, obstacles preventing the application of the DiESL method in an industrial context are addressed. This includes the introduction of a mechanism for automatically repairing the meshes of LSMs with distorted elements, failing the element quality check, as well as the handling of non-congruent FE-models in analysis and design domain. Finally, the overall program flow is summarized.

3.3.1 Used Software

As previously worked out, the DiESL method enables the application of commercial solvers for both nonlinear dynamic analysis as well as linear static response optimization. This is advantageous for several reasons: no additional effort is required for the development of own solvers, maintenance work is carried out by the software supplier, the software is efficient and tested and the same software used during the product development process can be used for optimization. Hence, a time-consuming conversion of the FE-models is not required. For the latter reason the software to be employed is selected according to the standards of

the *Opel Automobile GmbH*. This means, *LS-DYNA* (LSTC 2015) is employed for nonlinear dynamic analysis using explicit time integration and *OptiStruct* (HyperWorks 2021) is used for the computation of the ESLs and for the linear static response optimization. It is worth mentioning, that the employed software can easily be substituted by any other software as only the interfaces for reading the output files and writing the input decks need to be adapted while the basic program flow does not change.

3.3.2 Termination Criteria

Three termination criteria are used in this thesis for sizing optimization. The first criterion checks if the current design is feasible. Since the linear static auxiliary load cases only provide estimations for the actual problem, the optimized responses of the linear static analysis often differ from those of the subsequent nonlinear dynamic analysis. Therefore, the convergence check is performed after the nonlinear dynamic analysis has been run. A small constraint violation is tolerated. Summarizing, the implemented first convergence criterion is that the maximum normalized constraint violation $g_{\max}$ must be smaller than a specified limit $\epsilon_g > 0$:

$$g_{\max} \leq \epsilon_g \tag{3.34}$$

The second criterion checks the relative change of the objective function between subsequent cycles $k - 1$ and k

$$_k\Delta\bar{f} = \frac{|f(_k\mathbf{x}) - f(_{k-1}\mathbf{x})|}{|f(_k\mathbf{x})|}. \tag{3.35}$$

The left subscript is used for the specification of the cycle(outer loop) to distinguish it from the iteration(inner loop) counter denoted as left superscript. The second criterion is satisfied if the relative change of objective is smaller than $\epsilon_f > 0$ in two subsequent cycles

$$_k\Delta\bar{f} \leq \epsilon_f \wedge {}_{k-1}\Delta\bar{f} \leq \epsilon_f. \tag{3.36}$$

If this criterion is satisfied, the objective hardly changes and continuing the optimization is not worthwhile in most cases. We check $_k\Delta\bar{f}$ of two subsequent cycles to reduce the likelihood that the criterion is satisfied by coincidence. The reason is that the objective function can potentially remain almost constant between two cycles although the design variables are changing strongly. The optimization terminates if both equations 3.34 and 3.36 are satisfied in the same cycle. In the entire thesis $\epsilon_g = \epsilon_f = 0.01$ is used.

The third individual criterion is based on the number of performed cycles. After 40 cycles the optimization is terminated if no convergence has been achieved before.

$$k \geq 40 \tag{3.37}$$

This is because the design variables do hardly change afterwards, in particular, because of the actions to limit the length of the optimization path presented in the following (section 3.3.3).

3.3.3 Limitation of Optimization Path

As the linear auxiliary load cases are only an approximation of the actual nonlinear dynamic problem, the length of each inner loop optimization path is limited by two combined measures. First, we employ move limits like introduced in equation 2.55:

$$
\begin{aligned}
{}_k\bar{x}_i^{\mathrm{L}} &= \max\left(x_i^{\mathrm{L}},\, {}_{k-1}x_i - {}_k\delta|{}_{k-1}x_i|\right) \\
{}_k\bar{x}_i^{\mathrm{U}} &= \min\left(x_i^{\mathrm{U}},\, {}_{k-1}x_i + {}_k\delta|{}_{k-1}x_i|\right); \qquad {}_k\delta \in [0,1].
\end{aligned}
\tag{3.38}
$$

These are used to constrain the change of each design variable per iteration. The Parameter ${}_k\delta$ controls the size of the move limit in cycle k. Based on an intial value δ_{ini}, ${}_k\delta$ is reduced in each cycle using the reduction factor β:

$$
{}_0\delta = \delta_{\mathrm{ini}}; \qquad\qquad\qquad\qquad if \qquad k = 0 \tag{3.39}
$$

$$
{}_k\delta = \delta_{\mathrm{ini}}\,\beta^k; \qquad\qquad\qquad if \qquad k > 0 \tag{3.40}
$$

In this thesis the parameter set $\delta_{ini} = 0.2$ and $\beta = 0.9$ are used in all sizing examples. The second measure is limiting the number of iterations per cycle. Therefore, the parameter max_{iter} is introduced, defining the maximum number of iterations per cycle. For all sizing examples $max_{\mathrm{iter}} = 2$ is used. This means each cycle contains 2 iterations.

3.3.4 Handling of failed Elements

In Triller 2019, issues were observed, due to excessively distorted elements in LSMs at later ESL times. These elements failed the element quality check in OptiStruct. This is a severe issue since it causes the entire optimization to terminate with an error before an optimal design can be derived. To realize a robust application of DiESL, an automated repair mechanism for the mesh must be realized. In Fig. 3.12 such distorted elements are illustrated. Here, a crash box is crushed by a rigid impactor (green) with initial speed v_0. The element highlighted by the red outline failed the element quality check. The nonlinear dynamic solver handles such distorted elements, by deleting them after the distortion becomes critical. It is therefore obvious to automatically delete the elements also in the LSMs if their element quality check fails. This element deletion is not permanent but is applied to the affected LSMs in the current cycle only. After the linear static response optimization is finished all elements will be restored in the subsequent cycle. This repair mechanism is applied in all following examples.
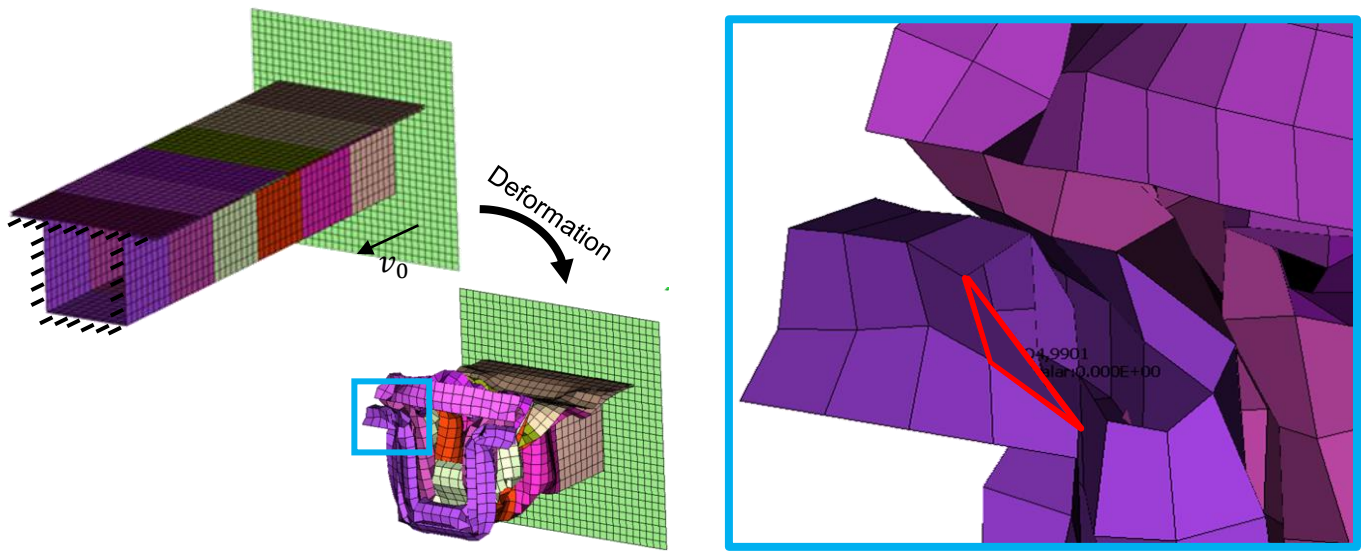
Figure 3.12: Initial and deformed crash box subjected to an impact exemplifying strongly distorted elements

3.3.5 Handling of non-congruent Models

As the product's design changes during the development process, the nonlinear (analysis domain) and linear (design domain) models available for optimization may differ slightly in geometry. This may happen if the model version does not match or if they are not synchronized. In Fig. 3.13 this is exemplified. Parts may have different geometric topology in the linear and nonlinear models (A, left). Another example is that the linear model may contain irrelevant extra parts compared to the nonlinear model (B, right). If only the meshes of the models differ, there is no problem, because the structural responses derived from nonlinear dynamic analysis can be mapped to the mesh of the linear model. Dealing with non-congruent models is a different issue, since for the geometry only defined in the linear model no information can be derived from nonlinear dynamic analysis. The nodal coordinates $\mathbf{r}(t^i)$ are then not available to build the LSMs. In order to avoid a time-consuming pre-processing for adjusting the models, another solution has been developed. [5]

---

[5]This procedure is also employed later in this thesis in the context of topology optimization.

A.

linear model
nonlinear model

B.

parts only
in linear model
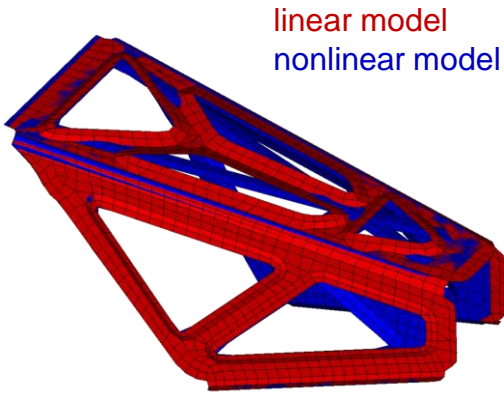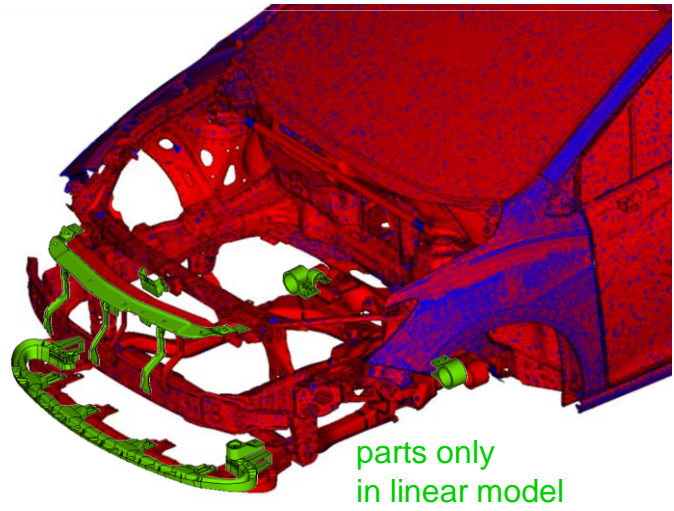
Figure 3.13: Examples for non-congruent models

The approach presented here prescribes the known displacements $\mathbf{u}(t^i)$ from the nonlinear dynamic solution as Single Point Constraints (SPCs) to the undeformed structure, in order to derive the deformations of the nodes missing in the analysis domain. For this purpose, a dedicated reconstruction FEA is executed. For each ESL time t^i a subcase is created to solve the following problem:

$$\mathbf{K}(\mathbf{x})\tilde{\mathbf{u}}(t^i) = \mathbf{f}; \qquad\qquad i = 1, ..., n_{\mathrm{T}}. \qquad\qquad (3.41)$$

Here, the vector $\tilde{\mathbf{u}}(t^i)$ contains both the known displacements $\mathbf{u}(t^i)$ from the analysis domain as well as the unknown displacements of the nodes exclusively defined in the design domain. The goal of this reconstruction FEA is to have the nodes with missing displacements follow the nodes with given displacement. This idea is illustrated in Fig. 3.14. As a result, the nodes with missing displacements are dragged along and follow the prescribed deformation of the surrounding mesh (Fig. 3.14, bottom right) and are solution of 3.41. All missing displacements can be computed in a single linear static analysis using the undeformed mesh and representing the deformation of each ESL time t^i by a subcase. This approach is tested in the latter parts of this thesis in the context of topology optimization in chapter 5.
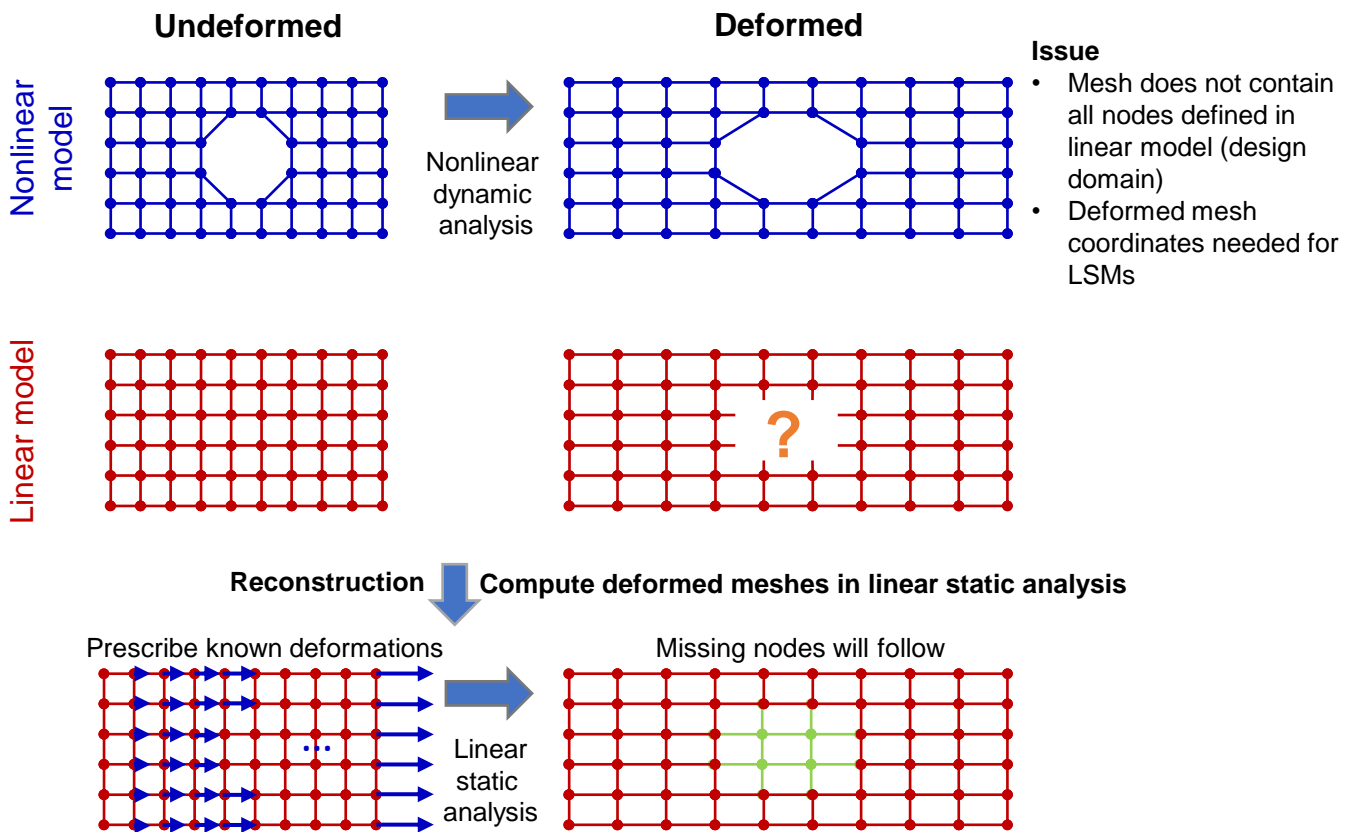
Figure 3.14: Computation of deformations of nodes missing in analysis domain using a linear static reconstruction analysis

3.3.6 Detailed Program Flow

The overall program flow explained before is implemented in *Python* following the steps below:

1: Set the initial design variables and parameters ($k = 0$, ${}_0\mathbf{x}$, ϵ_f, ϵ_g, β, max_iter, n_T, δ_ini).

2: perform nonlinear dynamic analysis with ${}_k\mathbf{x}$.

3: If the ESL times are determined adaptively, determine ${}^*\mathbf{t}$ by fitting appropriate curve, e.g. contact force according to chapter 3.2.1.

4: If $k > 1$, check convergence criteria: If equations 3.34 and 3.36 or 3.37 are satisfied then terminate the process.

5: If non-congruent models are employed in analysis and design domain, calculate displacement of all nodes in LSMs using equation 3.41 and set $\mathbf{u}(t^i) = \tilde{\mathbf{u}}(t^i)$ afterwards.

6: Calculate the incremental displacements $\mathbf{\Delta u}(t^i)$ and the nodal coordinates $\mathbf{r}(t^i)$ of all LSMs for all selected time steps t^i.

7: Check the element-quality of each LSM's FE-mesh. If check was not successful, delete failed elements in respective LSM and repeat Step 6 for the remaining mesh.

8: If material is adapted in the LSMs, check maximum plastic strain of each element: If $\varepsilon_{\mathrm{p},j}(t^i) > 0$ then adapt Young's modulus and Poisson's ratio of element j in LSM^i to E_{H} and $\nu_{\mathrm{H}} = 0.49$.

9: Calculate the incremental equivalent static loads $\mathbf{\Delta f}^i_{\mathrm{DiESL}}$.

10: Update the move limit $_k\delta$ according to equation 3.39.

11: Solve the linear static response optimization problem using the difference-based equivalent static loads $\mathbf{\Delta f}^i_{\mathrm{DiESL}}$. This includes the computation of sensitivities as well as subsequent line searches for the defined number of iterations max_{iter} .

12: Update the design variables in the nonlinear dynamic model, set $k = k + 1$ and go to step 2.

4 Sizing Optimization

In the following, the DiESL method and the previously presented extensions are tested using sizing optimization examples. For this purpose, the solutions of the ESL method, DiESL method and a metamodel-based approach are first compared with each other using a side impact example. A similar comparison has already been started in Triller 2019. At that time, the study could not be finished because in some runs failed elements led to an abrupt termination of the optimization and the automated repair mechanism had not been implemented yet. The same side impact example as well as a crash box example are used to evaluate the adaptive selection of ESL times as well as the local adaption of the Young's modulus on element level with regard to the DiESL method's approximation capabilities. Finally, the proposed approaches for approximating crash forces in the design domain are tested, using the previously mentioned crash box model and a side impact example including a B-Pillar. The following evaluation criteria are employed:

1. The number of cycles or nonlinear dynamic analyses required to complete the optimization process. Since the nonlinear dynamic analysis is the most time intense process in nonlinear dynamic response optimization this criterion is therefore considered to reflect the methods efficiency.

2. The optimized design's objective value. This is used to assess the quality of the optimization result.

Both criteria are related to the approximation quality provided by the respective method. For gradient-based optimization the chosen search direction depends on the quality of the approximated problem. Bad approximations result in wrong search directions and hence an increased number of analyses. Moreover, good results in terms of the objective function are more likely achieved if the original problem is sufficiently accurate approximated. In the following, these criteria are partially complemented by individual criteria related to the investigated problem. This will only be done in exceptional cases and with detailed justification. Furthermore, to achieve statistical independence from the initial design, the comparisons are widely based on several starting points uniformly distributed in the design space. These initial designs are created as a STOA.

4.1 Comparison of the ESL Method, DiESL Method and RSM

For the first comparison, a frame structure subjected to an impact is optimized, it is illustrated in Fig. 4.1. A rigid pole ($mass = 44.67$ kg) with initial speed $v_\mathrm{y} = -8\,\mathrm{m/s}$ collides with the frame structure

specified by seven design variables. To decrease computational effort and increase numerical stability, symmetry conditions are applied and only half the structure is computed. Furthermore, the structure is clamped along the distant edge with regard to the pole in all six degrees of freedom using SPCs. The pole's degrees of freedom are all locked except for the y-direction. The frame structure is made of steel (Young's modulus: $E = 210$ GPa, density: $\rho = 7850\,\mathrm{kg/m^3}$, Poison's ratio: $\nu = 0.3$) and bilinear material behavior is applied (hardening modulus: $E_\mathrm{H} = 0.6$ GPa, yield stress: 0.25 GPa). For the modeling of the frame structure fully integrated shell elements are employed (LSTC 2006). The total number of nodes is 6412. To get an impression of how the frame structure deforms for the design $x_i = 0.8$ mm; $i = 1, ..., 7$ please see Fig. 3.11.
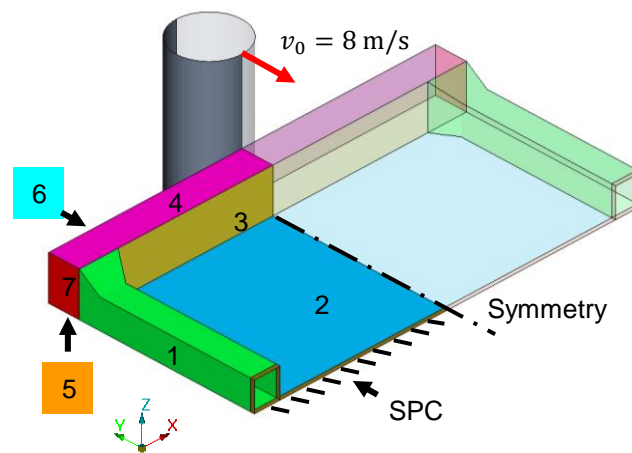
Figure 4.1: Side impact – FE-model and labeling of design variables (Triller et al. 2022a)

There is a contact defined between pole and frame structure in both models, i.e. analysis and design domain. However, the contact in linear static response optimization is not a contact in the correct sense of the concept. During crash, the contact points usually change very quickly. The nonlinear dynamic analysis is performed employing explicit time integration and is thus capable of resolving the quick opening and closing of contacts with time. Here the contact is modeled using the Penalty approach (LSTC 2006). The time increment represented by an LSM is much larger than in explicit time integration. According to the assumptions of linear statics, a contact defined in an LSM remains either closed or open during the respective time increment. Modeling contact by inserting invariant contact elements between the contact partners in the LSMs is therefore expected to be inaccurate. In order to measure the intrusion of the impactor, however, the pole in the linear static model must be connected to the frame structure. For this purpose, very soft contact elements between pole and frame are defined. The contact elements are sufficiently soft, compared to the remaining elements, such that their influence on the frame structure is negligible, but the impactor is pulled along with the structure. The impactor is used as a mere measuring device but does not affect the structure's deformation. This is necessary, because no representative node in the structure's impact zone could be found to reliably reflect the pole's intrusion. This circumstance

is caused by parts of the structure buckling away from the pole, as it can be seen in Fig. 3.11. The optimization's objective is to minimize the mass of the frame structure, while the maximum intrusion $d(\mathbf{x})$ of the pole is constrained and the design variables must remain in the corridor between 0.5 and 3 mm:

$$\min mass\,(\mathbf{x})\,; \qquad\qquad \mathbf{x} \in \mathbb{R}^7 \qquad\qquad (4.1)$$

subject to

$$d\,(\mathbf{x}) \leq 200\text{mm}; \qquad\qquad\qquad (4.2)$$

$$0.5 \leq x_j \leq 3.0; \qquad\qquad j = 1, ..., 7 \qquad (4.3)$$

To begin with, ESL and DiESL are compared exemplary on the basis of a run with the initial values $_0x_i = 0.8$ mm; $i = 1, ..., 7$. Then, the results are compared with those of a metamodel-based approach, in particular a SRSM employing multi-quadratic radial basis functions. The optimization is executed using the commercial software *LS-Opt*. To confirm the validity of the ESL and DiESL results, a multistart study is performed for the gradient-based methods, in which the start values are varied as described before. Please note that at this point neither the Young's moduli in the LSMs are adopted nor are the ESL times are selected adaptively. This study uses $n_\text{T} = 20$ equidistantly distributed ESL times $\mathbf{t} = 5, 10, ..., 95, 100$ ms. This captures the maximum intrusion of the pole for the initial design, where the constraint is severely violated. The optimizer is expected to generate stiffer designs, hence the time of maximum intrusion will shift to earlier times and will thus be captured with the selected ESL times.
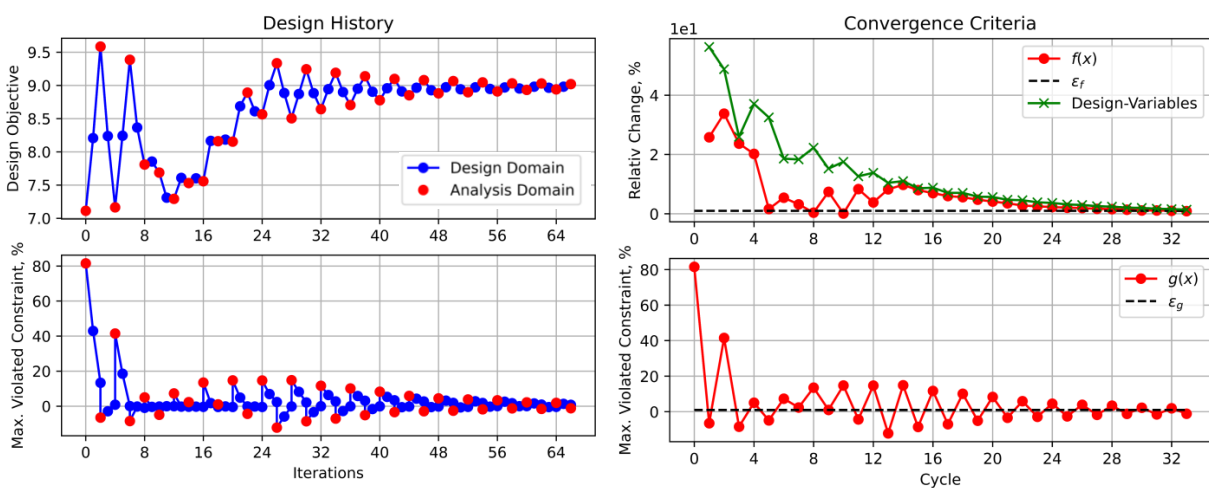
Figure 4.2: Side impact – objective function and max. relative constraint violation over iterations (left) and (max.) relative change of objective and design variables over cycles (right) using ESL
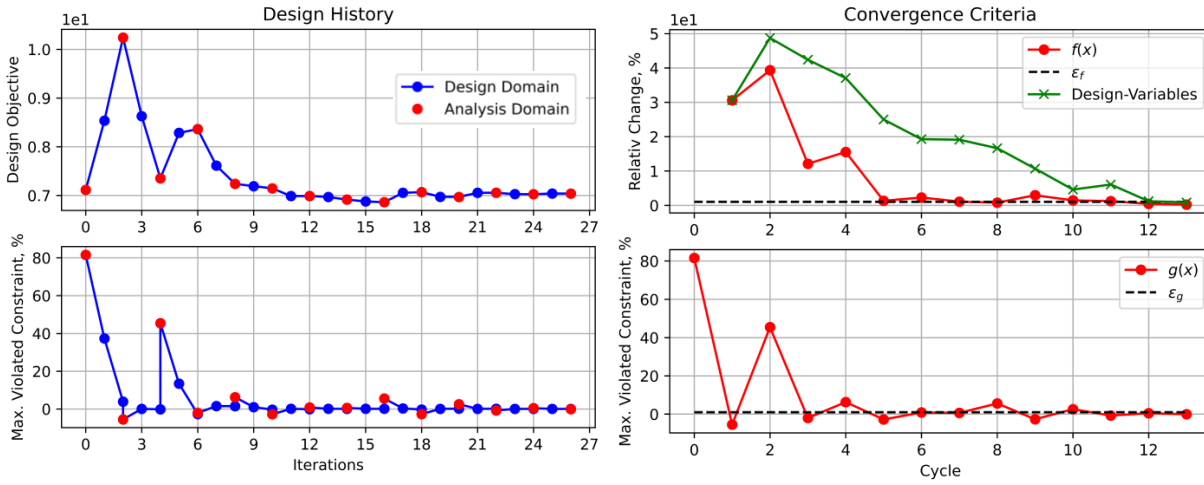
Figure 4.3: Side impact − objective function and max. relative constraint violation over iterations (left) and (max.) relative change of objective and design variables over cycles (right) using DiESL

The optimization history of the ESL and DiESL method are plotted in Fig. 4.2 and Fig. 4.3, respectively. The objective function and the normalized maximum constraint violation are plotted in the left diagrams. Blue circles denote the values resulting in the design domain and red circles mark those from the analysis domain. Each inner loop executes two iterations, hence in every second iteration there are two dots: one is the solution of the linear static response optimization in the design domain, the other is the result of the nonlinear dynamic analysis in the analysis domain evaluating the optimized design. The difference between the two can therefore be interpreted as the approximation error in the design domain. In this example, there is obviously no approximation error in the objective function since the mass is used. However, there is an approximation error visible in the maximum violated constraints representing the maximum intrusion of the pole. The relative change of both, the objective function and the design variables can be seen in the upper right diagrams of Fig. 4.2 and Fig. 4.3. The lower right shows the maximum constraint violation versus cycles. The values are the same as in the lower left diagram except it does not show the values of the inner loop iterations.

As can be seen in Fig. 4.2, the ESL method converges after 33 cycles, which required 34 nonlinear dynamic analyses. The final objective function value is 9.02 kg. Initially the optimizer strives towards a relatively good design (iteration 8-16). Thereafter, strong oscillations occur. These oscillations are damped by the decreasing move limits until the method converges. The DiESL method shows a very different convergence behavior (Fig. 4.3). It converges smoothly after 13 cycles already and yields an objective value of 7.03 kg.

Besides the above described findings, the final designs $_*\mathbf{x}$ are given in table 4.1 and are compared to the metamodel-based results. Comparing LS-Opt and DiESL, LS-Opt yields a slightly better design than DiESL does. However, the number of nonlinear analyses to achieve this is almost 10 times as high as for DiESL. The resulting designs differ slightly in the design variables x_3, x_4, x_5 and x_7. This similarity confirms that the optimum found by the DiESL method is an actual optimum of the nonlinear dynamic problem. This is

not the case for the ESL method. Here, major differences to LS-Opt and DiESL can be found in x_4 and x_6. For x_6, ESL converges to the opposite bound than both other methods. This design variable represents the thickness of the vertical panel in contact with the impactor. According to linear static theory, the bending stiffness of this panel grows with the third power of its thickness. Obviously, the ESL method aims at a more bending resistant design, whereas the two other methods increase the tensile stiffness by increasing x_4. This reconfirms the conclusions drawn from the three-point bending example illustrated in Fig. 3.2 and exemplifies the benefits of using the deformed geometries in the LSMs and thus incorporating geometrical nonlinearities.

Table 4.1: Side impact – optimization results for $^0x_i = 0.8$ mm using ESL, the DiESL and LS-Opt

Method	# nonlinear analyses	$_*mass$	$_*x_1$	$_*x_2$	$_*x_3$	$_*x_4$	$_*x_5$	$_*x_6$	$_*x_7$
		kg	mm	mm	mm	mm	mm	mm	mm
ESL	34	9.02	0.53	0.73	0.5	0.79	2.41	3.0	0.5
DiESL	14	7.03	0.5	0.5	0.5	1.79	2.87	0.5	0.5
LS-Opt	131	6.85	0.5	0.5	0.59	1.31	2.94	0.5	0.62

To ensure the statistical independence of both ESL and DiESL results of the initial design, a multistart study with 20 different uniformly distributed initial designs (Appendix 7.1) was performed as described previously. Fig. 4.4 shows the resulting $_*mass$ against the cycles necessary for convergence for each initial design for both ESL and DiESL methods. Table 4.2 reports the measures $\overline{_*cycle}$ and $\overline{_*mass}$ as average over all 20 multistart results. The results consistently confirm the previous findings obtained with the initial design $_0x_i = 0.8$ mm; $i = 1, ..., 7$.
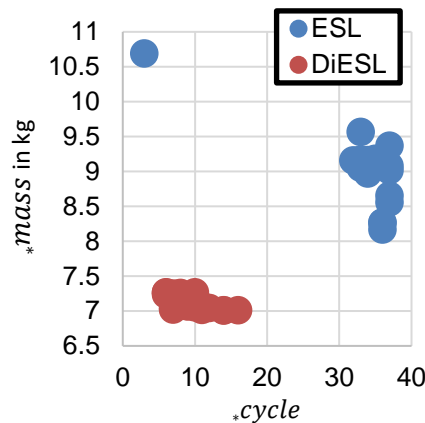
Figure 4.4: Side impact – resulting masses and corresponding cycles of all multistart optimization runs for the ESL and DiESL method

Summarizing, the DiESL method significantly outperforms the ESL method. It converges to a better

optimum while requiring considerably less cycles. Furthermore, the optimal design found by ESL has been examined by using it as starting design in LS-Opt using a narrow local initial sub-space. It turned out that LS-Opt converged to the same optimum as for the initial design $_0x_i = 0.8$ mm $i = 1, ..., 7$. This gives rise to the conclusion that the solution found by ESL is not even a local optimum of the nonlinear problem – it is not an optimum at all.

In contrast to the study in Triller 2019 no failed elements occurred here. This may be attributed to two changes in the simulation models: First, symmetry conditions were applied, and secondly, the element formulation in the analysis domain was changed from reduced to fully integration. The deletion of failed elements is tested using the crash box example.

Table 4.2: Side impact – optimization results using ESL and DiESL methods

Method	$_*cycle$	$_*\overline{mass}$
		kg
ESL	33.30	9.03
DiESL	9.55	7.11

4.2 Adaptive Selection of ESL Times and Local Adaption of Young's Modulus

After having shown the advantages of the DiESL method over both ESL method and SRSM, it is now tested whether the approximation quality of the DiESL method can be improved by adaptively selecting the ESL times and adjusting the material stiffness locally in the LSMs. The influence of each extension is tested both separately as well as in combination using two examples: the previously introduced side impact and a crash box example.

4.2.1 Side Impact

First, the adaptive selection of ESL times (AT) is compared to equidistantly distributed ESL times (ET) solving the side impact optimization problem introduced before (Chapter 4.1). The number of ESL times n_T is varied between 5, 10, and 20. The ET are set such that the last ESL time remains $t_{n_T} = 100$ ms, regardless of n_T. Fig. 4.5 illustrates the distribution of ESL times for both methods. It plots the contact force curve $f(t)$ for the design $x_i = 0.8$ mm; $i = 1, ..., 7$ and the respective fit $l(t)$ using $n_T = 20$. For AT, the time of maximal contact is prescribed. Also, the time of maximum intrusion t_d is set as last ESL time rather than the fixed value 100 ms.
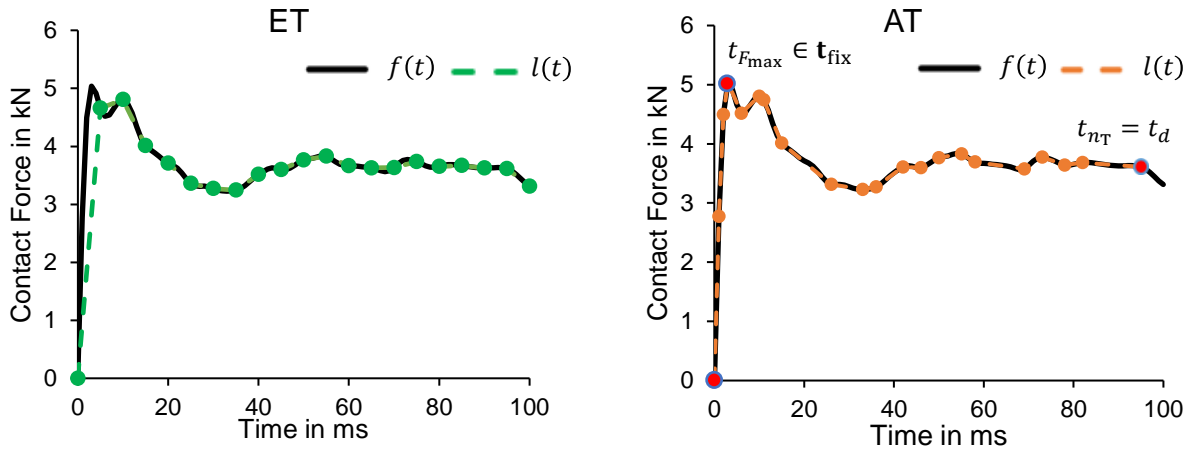
Figure 4.5: Side impact − contact force curve $f(t)$ and corresponding optimized fit $l(t)$ using ET (left) and AT (right) for $n_T = 20$ and design $x_i = 0.8$ mm; $i = 1, ..., 7$ (Triller et al. 2022a)

Fig. 4.6 shows 3 diagrams, one for each of the selected numbers of ESL times n_T. In each diagram the resulting $_*mass$ is plotted against the cycles necessary for convergence for each initial multistart design for both configurations ET and AT. All results can be grouped into two clusters distinguished by their $_*mass$. These clusters represent two different local optima. Table 4.3 shows the average results of all configurations. The averaged results for the two clusters are also shown. The average $_*mass$ is similar for ET and AT, regardless of the observed scenario (all runs or individual clusters). However, the averaged number of cycles until convergence is slightly better if AT is employed, this can clearly be observed in Fig. 4.6. This faster convergence of AT becomes more pronounced for smaller numbers of ESL times n_T, it may be attributed to the better utilization of available resources in each cycle: By setting the last ESL time as the time of maximum intrusion of the impactor, the ESL times are concentrated on the relevant deformation process.

Table 4.3: Side impact − averaged multistart results for equidistant distribution of ESL times (ET) and adaptive time selection (AT) (Triller et al. 2022a)

n_T	ESL times		All runs			Runs $_*mass \leq 7.1$ kg			Runs $_*mass > 7.1$ kg	
		#	$\overline{_*cycle}$	$\overline{_*mass}$ kg	#	$\overline{_*cycle}$	$\overline{_*mass}$ kg	#	$\overline{_*cycle}$	$\overline{_*mass}$ kg
20	ET	20	9.6	7.11	13	10.8	7.04	7	7.29	7.25
	AT	20	9.5	7.15	9	9.2	7.02	11	9.64	7.26
10	ET	20	13.7	7.12	8	12.3	7.02	12	15.88	7.27
	AT	20	10.1	7.17	8	10.1	7.03	12	10.08	7.27
5	ET	20	15.2	7.20	5	19.4	7.03	15	13.80	7.26
	AT	20	11.3	7.21	4	11.0	7.03	16	11.31	7.25
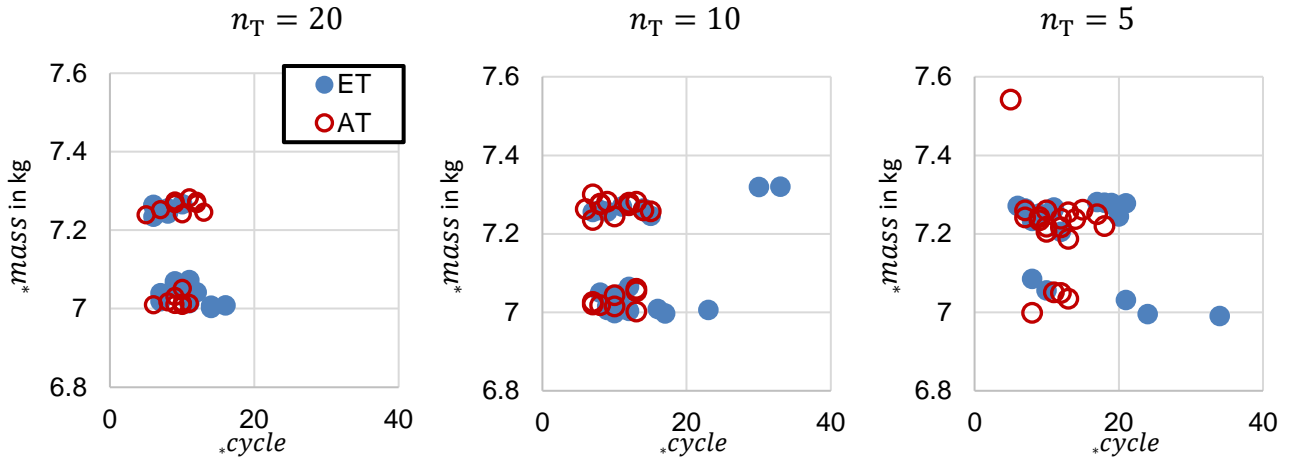
Figure 4.6: Side impact – resulting $_*mass$ and corresponding $_*cycle$ of all multistart optimization runs, varying n_T and the selection of ESL times (Triller et al. 2022a)

As a second step, the local adaption of Young's moduli (LA) in the LSMs is tested in combination with ET and AT employing $n_T = 20$ ESL times. The averaged results are given in table 4.4, and the individual results are plotted in Fig. 4.7. Using LA a considerable number of runs converged to a new and better optimum than before with $_*mass \leq 7.0$ kg. It can also be seen that the runs converging to this optimum need more cycles than the remaining runs. For the remaining runs $_*mass > 7.0$ kg, the average number of cycles to converge is smaller when LA is applied. The convergence issues to the new optimum can be attributed to oscillations of some design variables near the optimum. This is illustrated in Fig. 4.8, where the optimization history of one of these runs is given as an example. The diagram showing the design variable history reveals that the design changes significantly within the first 7 cycles. Thereafter, the oscillation of the design variables x_1 and x_4 prevent the algorithm from converging. The large number of cycles required for convergence is therefore not associated with poor approximation quality, but with the choice of termination criteria and the nature of the new optimum.

Table 4.4: Side impact – multi-start results for equidistant distribution of ESL times (ET) and adaptive time selection (AT) with (LA) and without (NLA) local adaption of Young's moduli (Triller et al. 2022a)

n_T	Method	ESL times		All runs			Runs $_*mass \leq 7.0$ kg			Runs $_*mass > 7.0$ kg	
			#	$\overline{_*cycle}$	$\overline{_*mass}$ kg	#	$\overline{_*cycle}$	$\overline{_*mass}$ kg	#	$\overline{_*cycle}$	$\overline{_*mass}$ kg
20	NLA	ET	20	9.5	7.11	0	-	-	20	9.6	7.11
	LA	ET	20	11.2	7.15	9	16.0	6.96	13	8.6	7.18
20	NLA	AT	20	9.5	7.11	0	-	-	20	9.5	7.15
	LA	AT	20	14.8	7.11	8	23.9	6.94	12	8.7	7.22
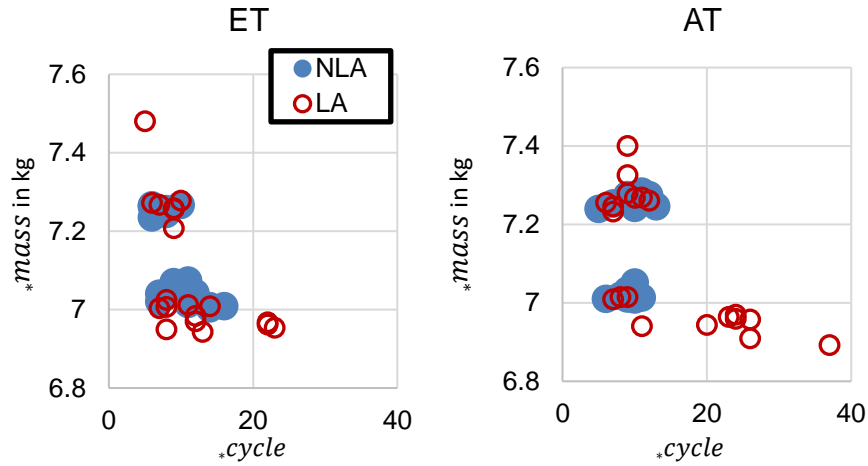
Figure 4.7: Side impact – resulting masses and corresponding cycles of all multistart results using $n_{\mathrm{T}} = 20$ for equidistant ESL times (left) and with adaptive ESL times selection (right) (Triller et al. 2022a)
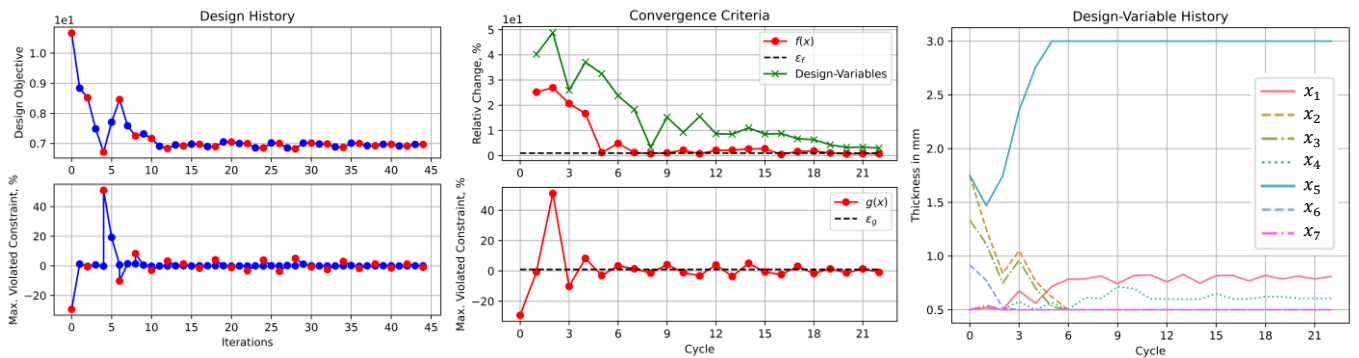
Figure 4.8: Side impact – optimization history of one multistart run involving oscillations in the design variables. Objective function and maximum relative constraint violation over iterations (left), convergence criteria and maximum relative change of design variables over cycles (middle), and design variables over cycles (left)

The following investigation aims at a better understanding of why LA converges to a better optimum. The intrusion constraint's contour line for the original nonlinear dynamic problem and for the corresponding DiESL approximation are compared for selected design points. To visualize the contour lines, suitable regions must be identified, in which only 2 design variables are relevant. For that purpose, the optima resulting of all multistart optimization runs summarized in table 4.4 are compared. The results $_*mass$ and $_*\mathbf{x}$ are used to cluster the optima as follows: in Fig. 4.9 (left) the averaged values of the design variables and the corresponding standard deviation of four different optima (a-d) are illustrated as parallel coordinates. All design variables except for $_*x_1$, $_*x_4$, and $_*x_5$ are at their lower bound. Each cluster can

be uniquely identified by the value $_*x_4$, this is highlighted with the rectangular box. In Fig. 4.9 (right) $_*x_1$ and $_*x_5$ are plotted against $_*x_4$. For $_*x_4 \leq 1.1\,\mathrm{mm}$ all values $_*x_5$ are at their upper bound. It is thus concluded that x_5 is irrelevant in this range. For $_*x_4 > 1.1\,\mathrm{mm}$ $_*x_1$ remains at the lower bound, while $_*x_5$ changes with $_*x_4$. Hence, we can identify two regions, each spanned by only two relevant design variables (Triller et al. 2022a).
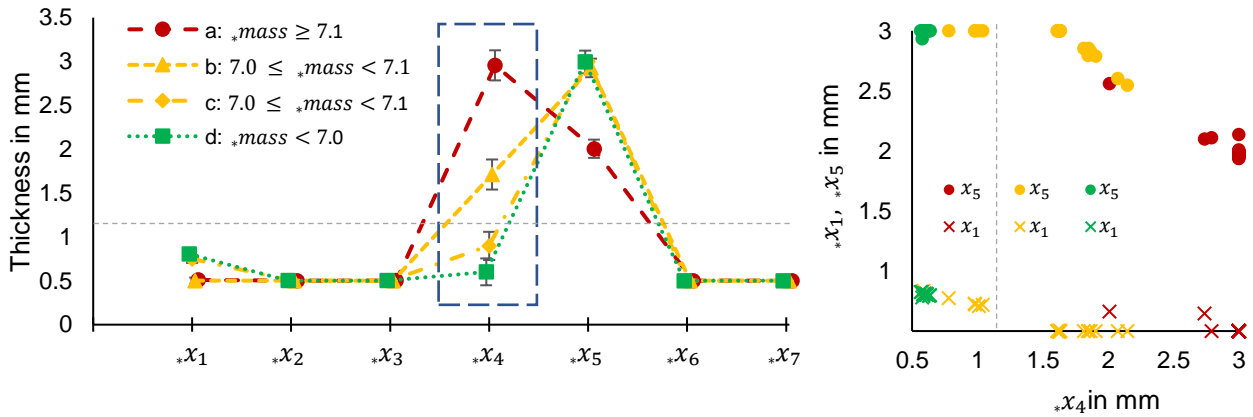
Figure 4.9: Side impact − averaged $_*\mathbf{x}$ with corresponding standard deviation (left) and thicknesses $_*x_1$ (cross), $_*x_5$ (circle) over $_*x_4$ (right) for runs with $n_\mathrm{T} = 20$ clustered according:
a) $_*mass \geq 7.1\,\mathrm{kg}$,
b) $7.0\,\mathrm{kg} \leq _*mass < 7.1\,\mathrm{kg}$ and $x_4 > 1.1\,\mathrm{mm}$ runs,
c) $7.0\,\mathrm{kg} \leq _*mass < 7.1\,\mathrm{kg}$ and $x_4 \leq 1.1\,\mathrm{mm}$,
d) $_*mass < 7.0\,\mathrm{kg}$
(Triller et al. 2022a)

In each of those ranges one focal design point near a local optimum is selected for which a DiESL approximation is created. The approximation as well as the nonlinear dynamic system are then evaluated on a grid of closely spaced design points spanning the whole region. The resulting intrusions for each grid point are then used to compute a contour (iso-)line of the maximum intrusion $d(\mathbf{x})$. Fig. 4.10 shows the focal design points and the resulting contour lines for both regions. The contour lines for the mass objective are added such that the local minima can be seen visually. It is striking in both regions that the contour lines of mass objective and intrusion constraint are almost parallel. This makes it extremely hard to identify a local optimum, especially with the jagged shape of the nonlinear intrusion contour line. The DiESL contour lines are computed for all four combinations of ET/AT and LA/NLA. They are now compared to those of the actual nonlinear dynamic problem to asses their approximation quality.[1] The DiESL method fits the global trend of the nonlinear dynamic problem well in both design regions. The noisy contour line of the nonlinear dynamic problem is smoothed by DiESL which is beneficial when gradient-based optimization is applied. LA improves the approximation quality of the DiESL method in both design regions while ET has

---

[1] In the appendix in Fig. 7.1 the ESL approximation of the two design points is given as well. Please note that the above assumptions for identifying the two ranges based on the DiESL DoE results do not apply for the ESL method.

a minor influence. In range 2 the improvement by LA is more pronounced, this is where the new optimum $_*mass \leq 7.0$ kg was found by using LA. It is obvious why this optimum is only found using LA: The angle between the objective's and the constraint's contour line switches sign when LA is used. Specifically, the NLA DiESL approximations indicate that an increase in x_4 leads to a smaller mass at constant intrusion, whereas both LA approximations suggest the opposite. Moreover, for LA, both mass and intrusion contour lines are almost parallel near $x_4 = 0.6$ mm, which could explain the observed oscillations of design variables x_1 and x_4 in the region of the new optimum: Two design points close to each other may result in angles between mass and intrusion contour lines with opposite sign, causing the optimizer to invert its search direction over and over again. The delayed convergence for the LA runs to the new optimum can therefore indeed be attributed to the nature of the optimum and is not an inherent weakness of LA. On the contrary, the fact that the new optimum is reached only with LA shows the improved approximation quality achieved by the extension.
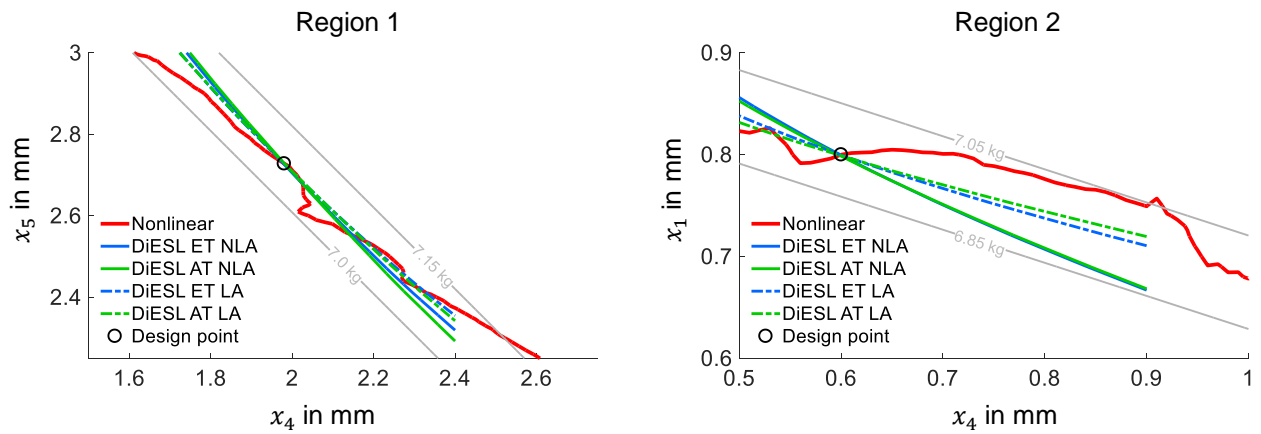
Figure 4.10: Side impact – contour lines of objective mass (grey) and maximum intrusion d for the nonlinear dynamic problem and the DiESL approximation for
region 1: design point $x_1 = 0.5$ mm; $x_4 = 1.98$ mm; $x_5 = 2.73$ mm; $d(\mathbf{x}) = 199.1$ mm (left) and
region 2: design point $x_1 = 0.8$ mm; $x_4 = 0.6$ mm; $x_5 = 3$ mm; $d(\mathbf{x}) = 200.6$ mm (right).
Note: all design variables x_2, x_3, x_6, x_7 are set to the lower bound (0.5 mm)

Fig. 4.11 and Fig. 4.12 show the contour lines in range 2 for each ESL time for ET and AT, respectively. The legends are omitted for sake of clarity, they are identical to Fig. 4.10.

Fig. 4.11 and Fig. 4.12 perfectly illustrate why DiESL approximates the global trend of the original nonlinear dynamic problem. As elaborated in chapter 3.1.1, the displacements $\mathbf{u}^i$ in DiESL are the accumulated sums of the incremental displacements $\mathbf{\Delta u}^i$ resulting from each LSM. Consequently, the sensitivities or the orientation of the contour lines are also sums of all previous LSMs. The orientation of the contour lines or direction of sensitivities can therefore also be understood as the weighted average of the LSMs sensitivities, where the weight factors are the sensitivity magnitudes (Triller et al. 2022a).

From examining Fig. 4.11 and Fig. 4.12 the previous findings can also be reconfirmed. Both extensions AT

as well as LA improve the DiESL method's approximation quality. ET seems to introduce an angle offset between the nonlinear and its DiESL approximation contour lines in the first ESL time $t_1 = 5$ ms. This offset propagates through all subsequent ESL times and has a negative impact on the overall approximation. This poor approximations in early time steps may be attributed to the rough discretization with ET. In case of AT the approximation is much more accurate for the early times.
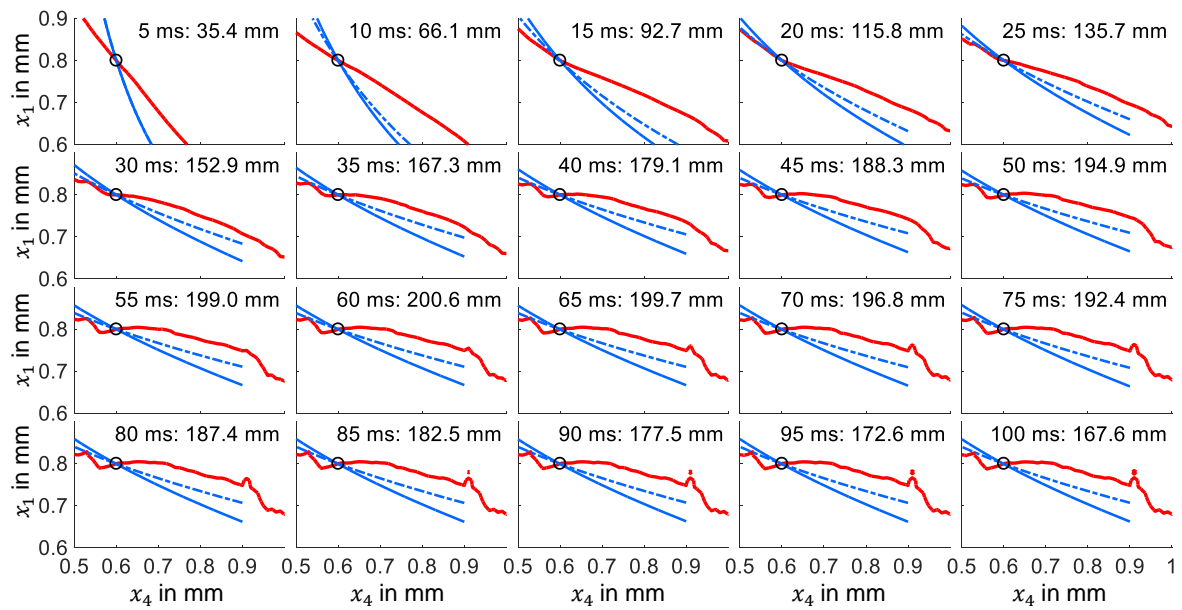
Figure 4.11: Side impact – contour lines of maximum intrusion for the nonlinear dynamic problem and the ET DiESL approximation for range 2: design point $x_1 = 0.8\,\mathrm{mm}$; $x_4 = 0.6\,\mathrm{mm}$; $x_5 = 3\,\mathrm{mm}$ for all equidistant ESL times and respective intrusions. Note: the legend is given in Fig. 4.10 (Triller et al. 2022a)
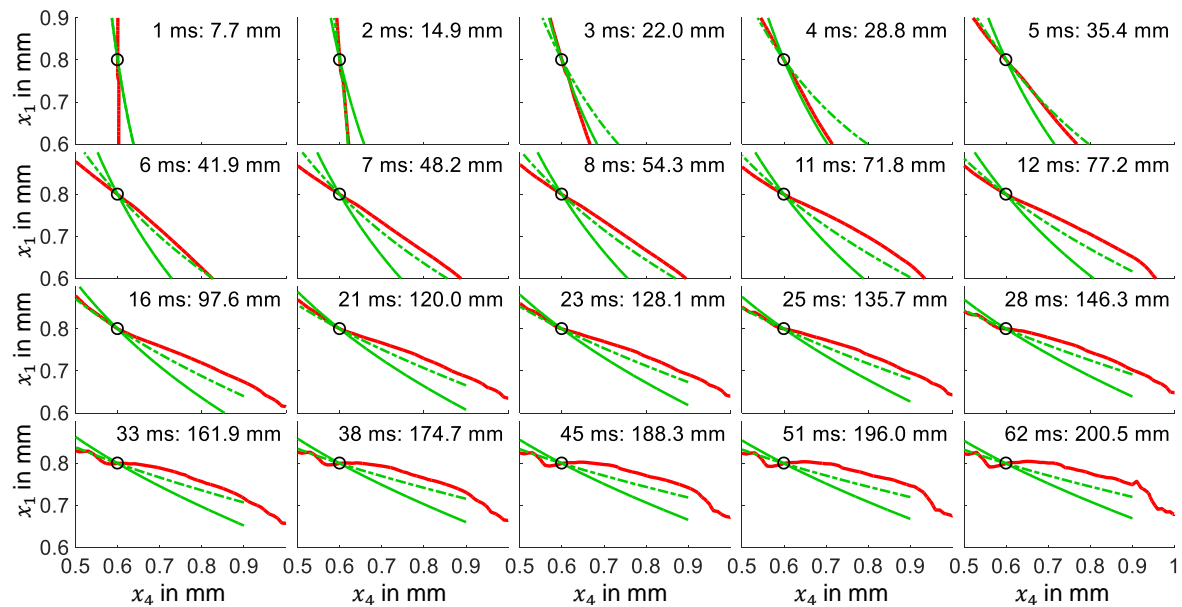
Figure 4.12: Side impact – contour lines of maximum intrusion for the nonlinear dynamic problem and the AT DiESL approximation for range 2: design point $x_1 = 0.8\,\mathrm{mm}$; $x_4 = 0.6\,\mathrm{mm}$; $x_5 = 3\,\mathrm{mm}$ for all adaptively selected ESL times and respective intrusions. Note: the legend is given in Fig. 4.10 (Triller et al. 2022a)

4.2.2 Crash Box

After showing the functionality and benefits of adaptive selection of ESL times and local adaption of Young's moduli using the side impact example, in the following a more complex crash box example is optimized. In Fig. 4.13 the load case is shown: a crash box being crushed by a rigid impactor ($mass = 622$kg) with initial speed $v_{\mathrm{y}} = 4.167$ m/s. This model has been published by Ma et al. 2020. However, in comparison to Ma several changes have been made. The biggest difference refers to the impactor's velocity. Instead of constant velocity only the initial velocity is prescribed. This is to incorporate dynamic effects and to simulate the realistic practical use case of crash boxes in the automotive crush zone. For the sake of numerical stability and computational effort, symmetry conditions with respect to the yz-plane are employed. The crash box is clamped at the distant edge using SPCs locking all 6 degrees of freedom. Furthermore, the impactor's degrees of freedom except of the one in y-direction are locked. The crash box is discretized using fully integrated elements connecting 5842 nodes. The crash box is made of steel (Young's modulus: $E = 210$ GPa, density: $\rho = 7850\,\mathrm{kg/m^3}$, Poison's ratio: $\nu = 0.3$) and in contrast to the side impact example piecewise linear material behavior is applied (Fig. 4.13 right). Thus, the material behavior cannot be adapted correctly using a bilinear material model in the design domain. Based on the assumption given in chapter 3.2.2, the stiffness of the plastified elements in the design domain is globally approximated using $E_{\mathrm{H}} = 0.4$ GPa as illustrated in Fig. 4.13 by the dashed line. As shown in Fig. 4.14 many elements are in the plastic range (blue) even at the very beginning of the deformation process at time $t^i = 8ms$. For each of these elements the smaller hardening modulus $E_{\mathrm{H}} = 0.4$ GPa is then applied in the corresponding LSMs. This approximation is considered valid, since a significant number of elements have plastic strains $\varepsilon_{\mathrm{p}} \geq 0.3$ already in early LSMs. The models used in the design and analysis domain employ the same mesh to avoid results mapping. A contact between the impactor and the crash box is defined in the nonlinear dynamic model only. Furthermore, the crash box is stiffened in the area of the impact zone employing RBE2 elements in order to improve the force transmission between impactor and crash box. In the design domain neither a contact nor an impactor is modeled. The impactor's intrusion in the LSMs is approximated from a structural node (red dot in Fig. 4.13 left) in the impact zone.
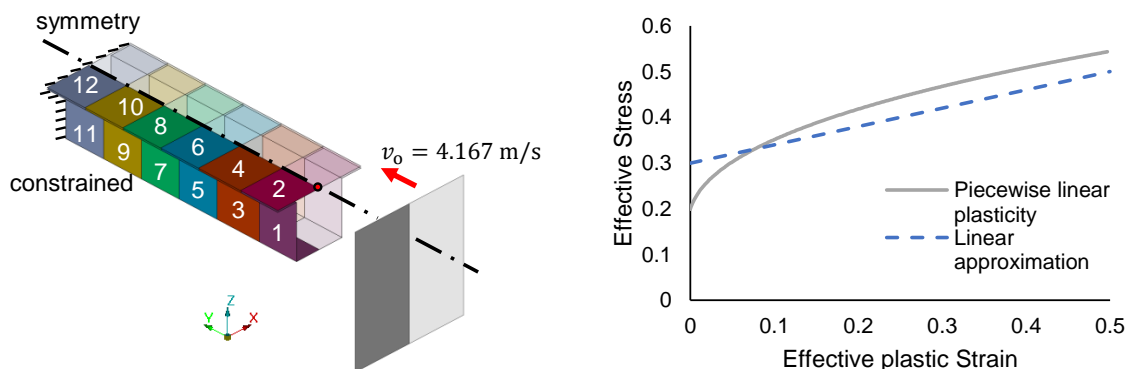
Figure 4.13: Crash box − FE-model and labeling of design variables (left); applied material model and corresponding approximation for local adaption of Young's moduli (right) (Triller et al. 2022a)

Nonlinear dynamic analysis at time t^i

elements without plastic strain: $\boldsymbol{\varepsilon_p = 0}$

elements with plastic strain: $\boldsymbol{\varepsilon_p > 0}$

Corresponding LSM^i

use Young's modulus: E = 210.0 GPa

use hardening modulus: E = 0.4 GPa

Plastic strain, Max of Inn, Out and Mid

>0.008	
0.007	
0.006	
0.005	
0.004	
0.003	
0.002	
0.001	
<0	
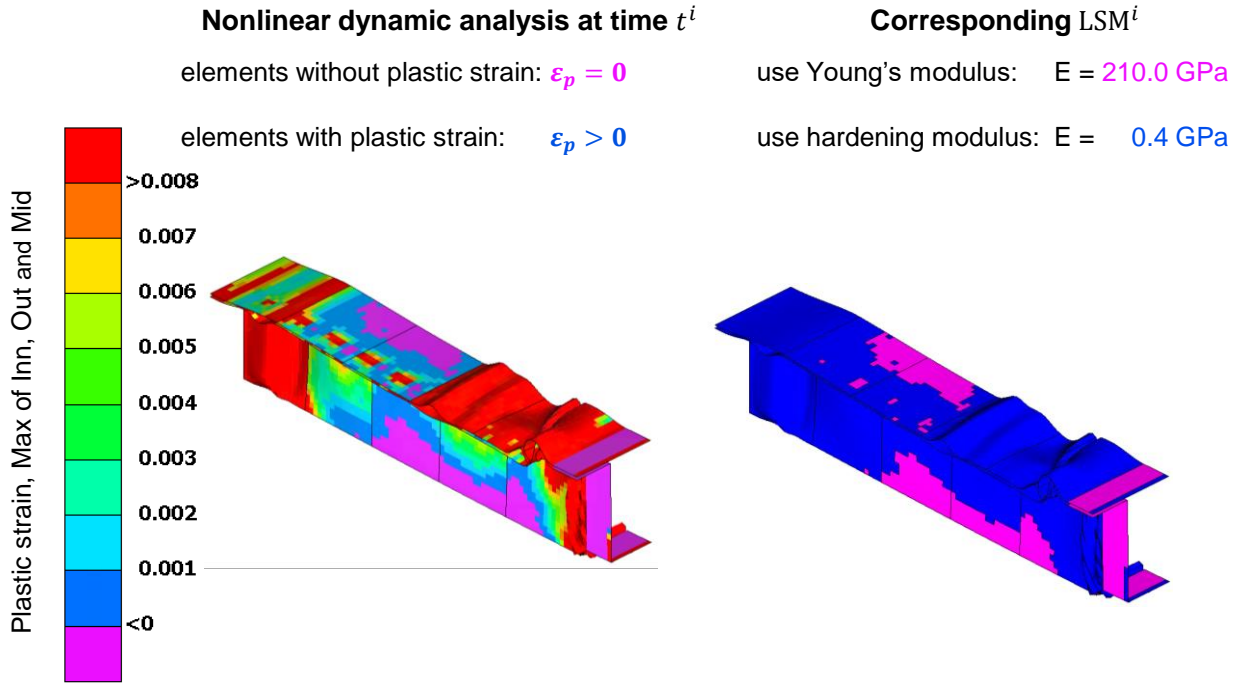
Figure 4.14: Crash box − plastic strain in nonlinear dynamic analysis for an initial design of the multistart study at an early time step $t^i = 8\,\mathrm{ms}$ (left) and modulus distribution in the corresponding LSM (right) (Triller et al. 2022a)

The crash box's design is specified by the thicknesses of twelve sheet metals, each corresponding to one design variable. The optimization's objective is again to minimize the mass while the maximum intrusion in y-direction $d(\mathbf{x})$ is constrained and the design variables must remain in the corridor between 0.5 mm and 2.5 mm. Mathematically the optimization is formulated as follows:

$$\min mass\,(\mathbf{x})\,; \qquad\qquad \mathbf{x} \in \mathbb{R}^{12} \qquad (4.4)$$

subject to

$$d\,(\mathbf{x}) \leq 160\mathrm{mm}; \qquad\qquad (4.5)$$

$$0.5 \leq x_j \leq 2.5; \qquad\qquad j = 1, ..., 12 \qquad (4.6)$$

Fig. 4.15 shows the contact force curve $f(t)$ of a very soft design ($d(\mathbf{x}) = 205.5$ mm) as well as the corresponding fits $l(t)$ using ET and AT. This highly unfeasible design is used to determine the largest ESL time to be considered for ET, this is the same approach as in the previous side impact example. The optimizer is expected to generate stiffer (feasible) designs, therefore $t_{n_\mathrm{T}} = 98$ ms is expected to capture the maximum intrusion $d(\mathbf{x})$ for the current soft as well as all following designs. As before in the side impact example, the last ESL time is set to the time of maximum intrusion t_d when applying AT. Additionally, the

time corresponding to the maximum crash force $t_{F_{\max}}$ is prescribed.
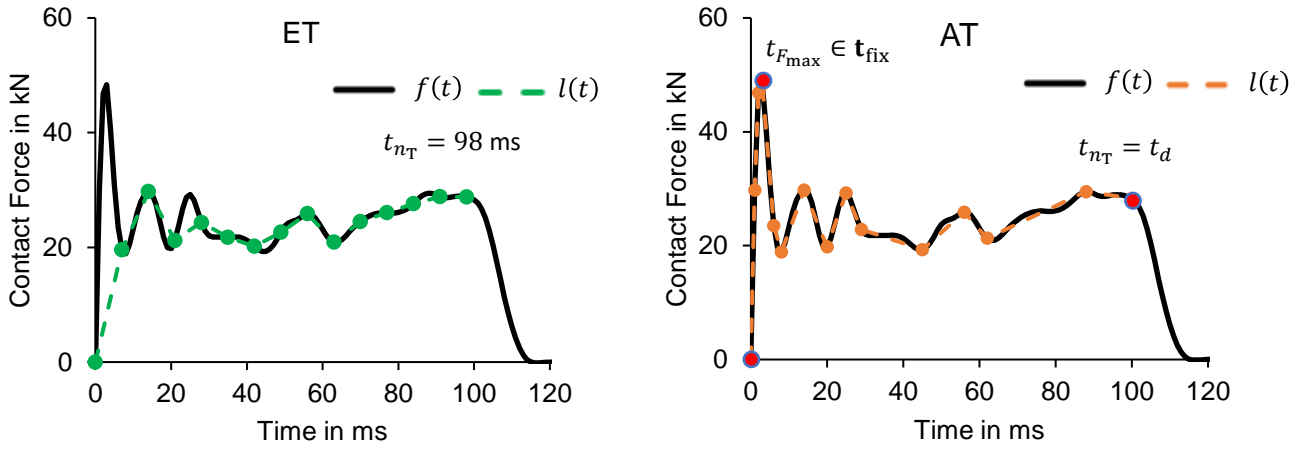
Figure 4.15: Crash box − contact force curve $f(t)$ for $x_j = 1.2\,\text{mm}$ and corresponding piecewise linear fit $l(t)$ using $n_\text{T} = 14$ ESL times distributed equidistantly (left) and $n_\text{T} = 14$ adaptively (right) (Triller et al. 2022a)

For evaluating the extensions AT and LA we follow the same procedure as before for the side impact example. First ET and AT are compared based on multistart studies employing different numbers of ESL times. The number of ESL times n_T is varied between 7, 14, and 31. The number of multistart optimization runs is increased to 40 uniformly distributed initial designs to account for the higher number of design variables in this example (Appendix 7.2). This study does not use local adaption of Young's moduli LA.

During most multistart runs, failed elements occurred in LSMs. This issue has been fixed using the presented automatic deleting approach. The failed elements typically occurred in LSMs representing the later ESL times with large deformations. The number of deleted elements per LSM was always smaller than ten, thus the influence on the subsequent optimization can be considered negligible.

The averaged results of the multistart study are given in table 4.5 for all combinations of ET, AT and all numbers of ESL times. Again, the resulting designs can be clustered. One group is identified by the optimized mass being smaller than or equal to 0.55 kg as illustrated in Fig. 4.16. This group is referred to as *best optimum* in the following. The reason for this division is shown in the right diagram where the averaged values of the resulting design variables $_*x_i$ as well as the corresponding standard deviations are plotted for the *best optimum* runs and all runs as parallel coordinates: all design variables of this group are in the same region. The *best optimum* runs are characterized by thinner upper parts (even design variables) and thicker lower parts (odd design variables) of the crash box. The standard deviation of all runs is significantly higher than for the *best optimum* runs, which means the multistart study converged to many different local optima. This is not surprising since no global optimizer has been employed and this is a highly nonlinear and multimodal example (Triller et al. 2022a). Table 4.5 and Fig. 4.16 left show that AT

statistically improves the convergence to the *best optimum*. As an example, for $n_\mathrm{T} = 14$ the *best optimum* is found 19 times using AT and only 4 times using ET. This supremacy of AT holds fo all numbers of ESL times investigated (table 4.5 and Fig. 4.17 right) and it is more pronounced for smaller numbers of ESL times.

Table 4.5: Crash box − averaged multistart results using NLA for equidistant distribution of ESL-times (ET) and adaptive time selection (AT) (Triller et al. 2022a)

n_T	ESL times	All runs			*Best optimum* runs $_*mass \leq 0.55$ kg		
		#	$\overline{_*cycle}$	$\overline{_*mass}$ kg	#	$\overline{_*cycle}$	$\overline{_*mass}$ kg
31	ET	40	20.9	0.563	21	23.6	0.531
31	AT	40	20.4	0.555	23	22.0	0.526
14	ET	40	19.6	0.605	4	27.5	0.533
14	AT	40	20.3	0.568	19	17.0	0.527
7	ET	40	25.4	0.634	1	34.0	0.538
7	AT	40	23.6	0.595	11	23.5	0.532
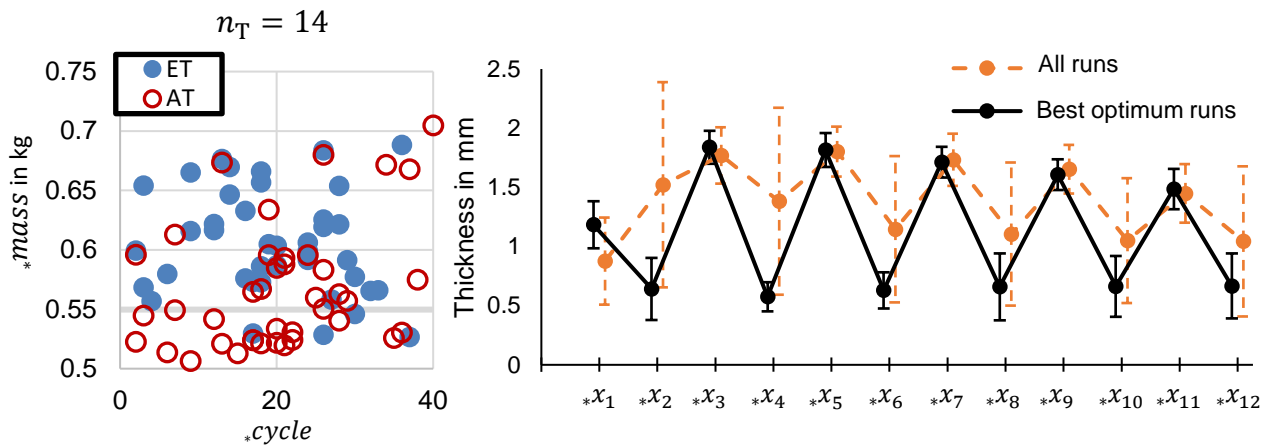
Figure 4.16: Crash box − resulting masses and corresponding cycles of multistart study using NLA (left) and averaged $_*$x with corresponding standard deviation for the two groups: a) all runs and b) runs converged to the *best optimum* (right) for $n_\mathrm{T} = 14$ (Triller et al. 2022a)

Table 4.5 and Fig. 4.17 also reveal that $\overline{_*mass}$ is smaller if AT is used, this holds for both groups *all* runs and *best optimum* runs and for all numbers of ESL times. Again, this supremacy becomes more pronounced if the number of ESL times n_T is reduced: The diagrams in Fig. 4.17 left and middle show that $\overline{_*mass}$ increases and on the right side that the number of runs converging to the *best optimum* reduces as n_T is decreased. This applies to both approaches AT and ET, but it is more pronounced for ET. The second evaluation criterion is the number of cycles required for convergence, for that purpose table 4.5 reports the

average value $\overline{_*cycle}$. The runs converging to the *best optimum* clearly need less cycles when using AT. In contrast to that, the averaged values for all runs do not show a clear trend.

Summarizing the findings of this comparison, the adaptive selection of ESL times leads to a number of benefits: lower objective values on average, a higher portion of runs converging to the *best optimum*, less cycles for converging to the *best optimum*, and even better objective values for runs converging to the best optimum. Therefore, it is concluded that adaptive time selection has the capability to improve the approximation quality of DiESL.
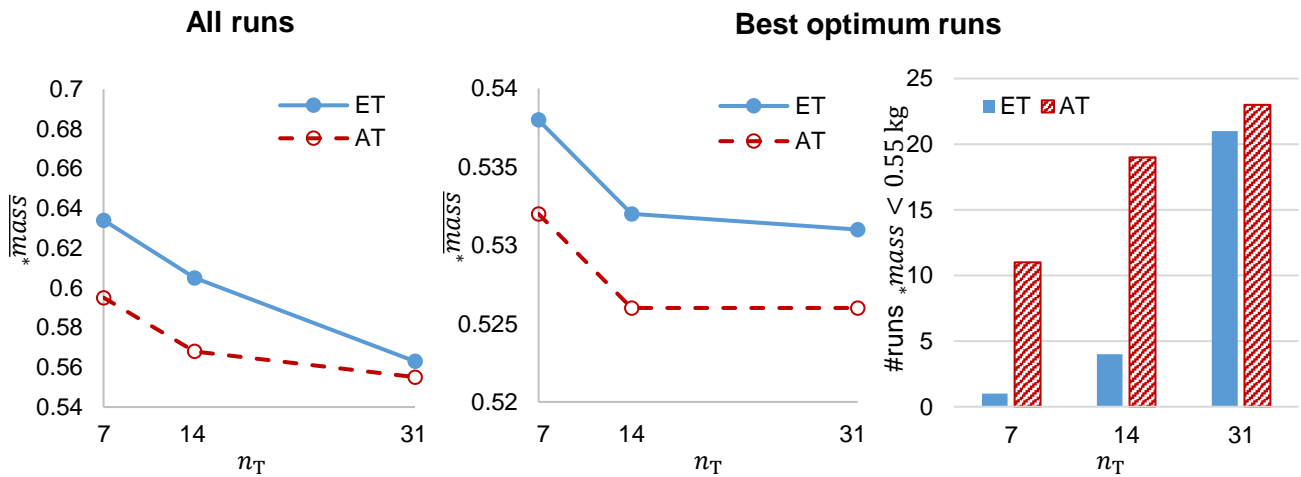
Figure 4.17: Crash box – average optimized mass against number of ESL times for all runs (left) and runs converged to the *best optimum* (middle); number of runs converged to the *best optimum* (right) (Triller et al. 2022a)

In a second comparison, the influence of LA in combination with ET and AT on the DiESL method's approximation quality is examined. The number of ESL times is set to $n_T = 31$ in this investigation. The general multistart approach is identical to the previous study, so is the definition of the *best optimum* group. A tabular comparison of the results is given in table 4.6. The evaluation of group *all runs* using ET shows that the average mass $\overline{_*mass}$ increases if LA is applied, at the same time the number of runs converging to the *best optimum* decreases. It seems that in this case, LA has a detrimental effect on the DiESL method's approximation quality. The following consideration may explain this: with LA, the tangent stiffness at the beginning of the increment is applied to the entire deformation occuring during the increment (being represented by an LSM). With ET, an increment may contain multiple buckling and contacting events that would individually require different local stiffness adaptions. This holds especially for the first increment in which the high initial velocity causes the largest deformation to the structure. The first increment is furthermore the one in which the contact force builds up and reaches its first maximum. This behavior can be observed in Fig. 4.15 (left) for the extremely soft design where the peak contact force reaches its maximum in the middle of the first ET interval while the first ET time coincides with the first force

minimum. The same happens in the fourth interval (21–28 ms) with the third force peak. If the ESL times are chosen without regard of the structure's nonlinear behavior, the local tangent stiffness may yield a worse approximation for the entirety of events occurring within the whole increment.

In combination with AT, mixed effects in both directions can be observed on both $\overline{_*mass}$ and $\overline{_*cycle}$. Thus, even in combination with AT, the local adaption of Young's moduli does not lead to a benefit here. Maybe the high number of elements entering the plastic range at early times (recall Fig. 4.14) provide an explanation. The simple implementation of local adaption of Young's moduli using a bilinear material ($E = 210$ GPa and $E_\mathrm{H} = 0.4$ GPa) falls short of distinguishing between elements with small and those with large plastic strains. For the chosen piecewise linear material in the analysis domain (depicted in Fig. 4.13 right) the value of plastic strain has an impact on the slope of the yield curve, this is neglected in the linear approximation in the design domain. In the extreme case, the plastic strain of all elements is higher than 0. Then, for all elements the same Young's modulus is employed, and all elements of the stiffness matrix are scaled by the same factor compared to NLA. The DiESLs $\mathbf{\Delta f}^i_{\mathrm{DiESL}}$ scale accordingly and the linear static response optimization will yield identical results then for both approaches NLA and LA. Obviously, LA in the implemented form can only improve the DiESL method's approximation quality if there is a mix of plastified and non-plastified elements (Triller et al. 2022a).

Table 4.6: Crash box – averaged multistart results for local adaption of Young's moduli in each LSM enabled (LA), and disabled (NLA) in combination with equidistant (ET) and adaptive (AT) selection of ESL times using $n_\mathrm{T} = 31$ (Triller et al. 2022a)

Young's modulus	ESL times	#	$\overline{_*cycle}$	$\overline{_*mass}$ kg	#	$\overline{_*cycle}$	$\overline{_*mass}$ kg
					Best optimum runs $_*mass \leq 0.55$ kg		
NLA	ET	40	20.88	0.563	21	23.57	0.531
LA	ET	40	20.98	0.579	17	21.65	0.531
NLA	AT	40	20.35	0.555	23	22.04	0.526
LA	AT	40	19.75	0.560	23	19.47	0.525

4.3 Crash Force Optimization

In the following, the previously introduced approximations for forces in DiESL are tested. For this purpose, a simple example (hinge model) is examined in which the contact force first increases linearly and subsequently decreases due to plastification. In addition, the approaches are compared based on a multistart study employing the crash box model. Subsequently, a side impact example from literature is optimized with DiESL and compared with the respective results (Ma et al. 2020).

4.3.1 Hinge Model

Fig. 4.18 illustrates the FE-model used to examine the suitability of the approaches *Inc* and *IncS* to approximate crash forces in DiESL. A rigid impactor collides with an initial velocity of 1 m/s into a sheet metal of thickness x oriented perpendicular to the impactor. The plate is made of steel (Young's modulus: $E = 210$ GPa, density: $\rho = 7850\,\text{kg/m}^3$, Poison's ratio: $\nu = 0.3$) and bilinear material behavior is employed (hardening modulus:$E_\text{H} = 0.6$ GPa, yield stress: 0.25 GPa). Symmetry conditions are applied at the rear end (opposite end with respect to the impactor) of the sheet metal as well as its middle (xz-plane). Two rows of nodes at the rear end of the sheet have been shifted by 0.01 mm in z-direction as a perturbation to initiate a deflection in this direction during the impact. At the front edge where the impactor hits the plate, the translational degrees of freedom in z-direction as well as the rotational in x- and z-direction are locked. The front node on the symmetry line is used to measure the displacement $d(t)$ in x-direction. A contact is defined between the impactor and the plate.
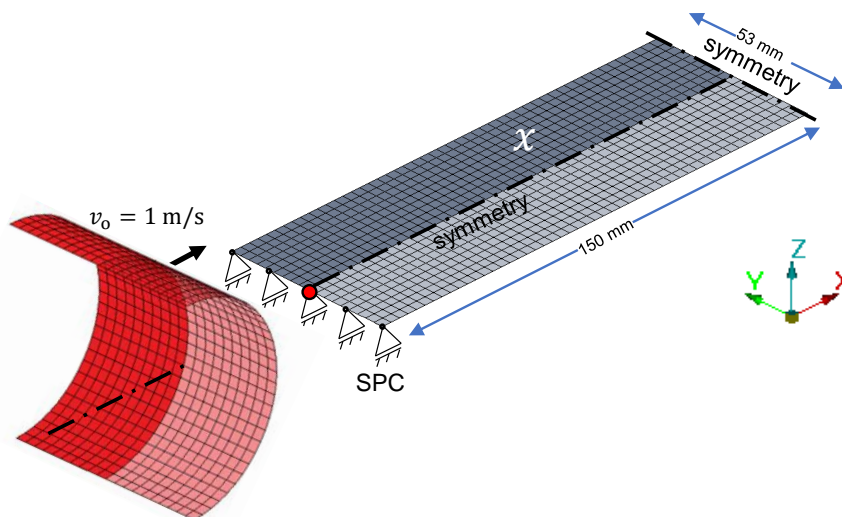
Figure 4.18: Hinge model – FE-model of sheet metal plate being crushed by rigid impactor for the examination of contact force approximation in DiESL

For a thickness of $x = 3$ mm, the contact force $F(t)$ between impactor and plate results as shown in Fig. 4.19. This force curve can be divided into 3 phases. The sheet metal's deformation and plastic strain

distribution of these phases are shown in Fig. 4.20 at representative times: first, there is elastic compression of the sheet metal in the longitudinal x-direction and the contact force increases linearly. In the second phase, the structure plastifies homogeneously, and the force level remains nearly constant until phase three sets in with the formation of two plastic hinges and a decrease of contact force.
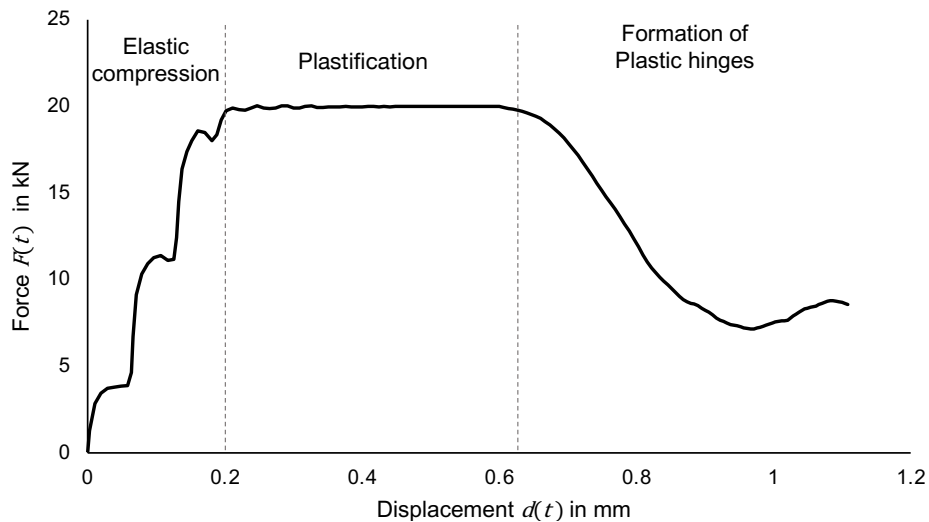
Figure 4.19: Hinge model − contact force over displacements for hinge model with sheet thickness $x = 3\,\mathrm{mm}$ and three deformation phases
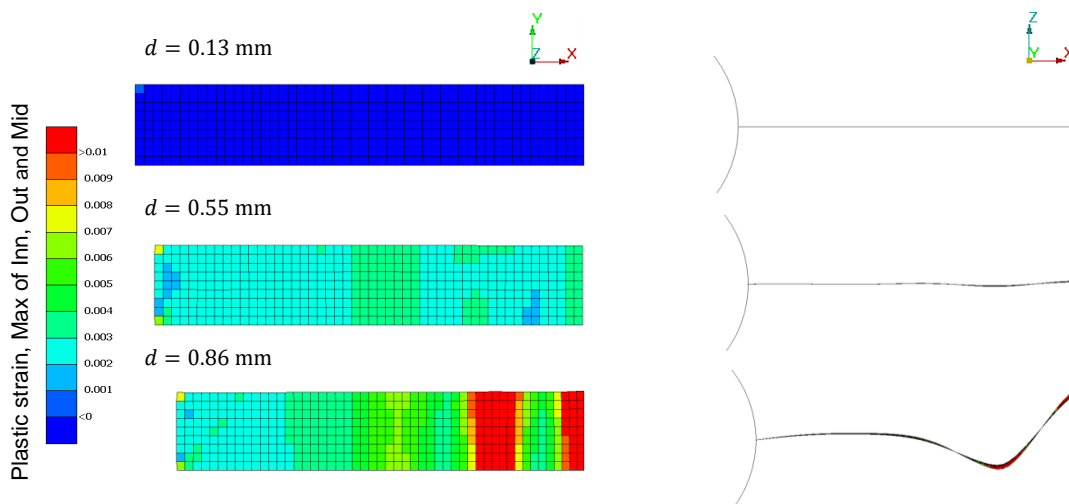
Figure 4.20: Hinge model − different states of deformation (right) for hinge model and corresponding plastic strains (left).
Top: Elastic compression
Middle: Plastification
Bottom: Formation of plastic hinges
Note: Deformations are scaled by factor 10 to enlarge visibility

Two studies were conducted to test the ability of the approaches *Inc* and *IncS* to approximate the change of forces due to a change in design. In the first study, the DiESL approximations are computed for a plate thickness of 3 mm using seven ESL times. Their approximation quality is evaluated for a thickness of 3.6 mm by comparing the predicted contact forces with those obtained from a nonlinear dynamic analysis. This is a relative change of 20 % and corresponds to the initial move limit $\delta_{\text{ini}} = 0.2$ used for all optimizations in this thesis. In the second study, the two thicknesses are swapped.

In Fig. 4.21 the results of the nonlinear dynamic analyses and the DiESL approximations *Inc* and *IncS* are shown. The results suggest, as detailed in the following, the introduction of a third DiESL approximation scheme for negative force increments. Here, the force increment ΔF^i remains constant in each iteration (i.e. retains the value $^0\Delta F^i$) if $\Delta F^i < 0$. This approach is referred to as *IncC* in the following, it predicted values lie in between those of *Inc* and *IncS*. It is implemented analogously to *IncS* using the transformation variable θ in the following expression:

$$\Delta F^i = (1 + \theta^i)\frac{^0\Delta F^i}{2\,\Delta u^i}{}^0\Delta u^i + (1 - \theta^i)\frac{^0\Delta F^i}{2}, \tag{4.7}$$

where

$$\theta^i = \begin{cases} 1 & if & \Delta F^i \geq 0 \\ -1 & if & \Delta F^i < 0. \end{cases} \tag{4.8}$$
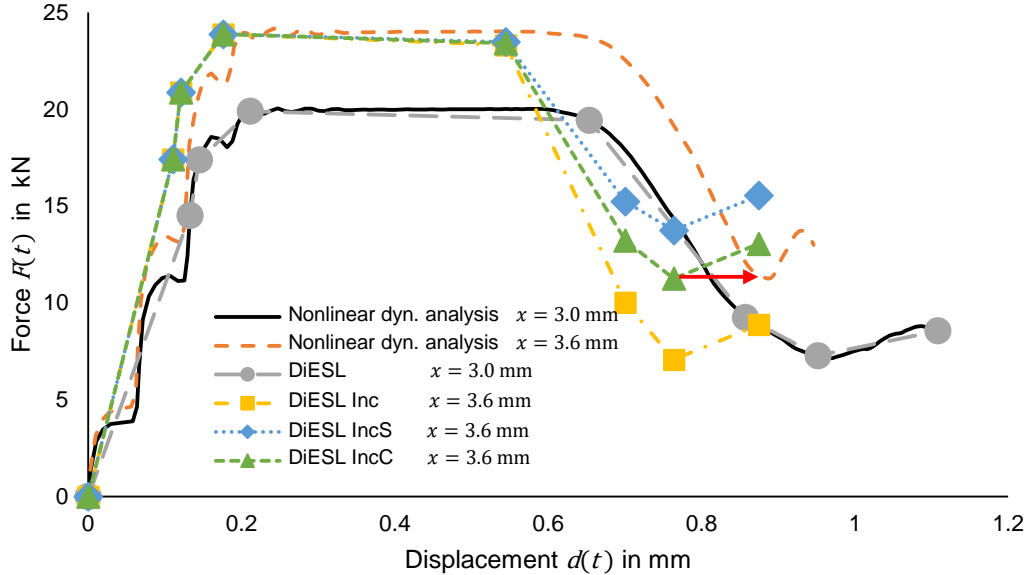
Figure 4.21: Hinge model − contact force F over displacement d for the sheet metal's thicknesses of $x = 3.0$ mm and $x = 3.6$ mm computed from nonlinear dynamic analyses and predictions of corresponding DiESL approximations developed in the design point $^0x = 3.0$ mm using the approaches *Inc*, *IncS*, and *IncC*

The DiESL approximations are each created with seven ESL times at the design point $x = 3$ mm. As can

be seen in Fig. 4.21, all approaches approximate the increase of the force due to elastic deformation very accurately. All three approaches produce the same approximated force values because they do not differ for rising force increments. Both the displacement and the force at the end of the associated phase are very precisely approximated. Note that for $x = 3.0$ mm all three DiESL approaches predict the same values which are identical to those of the nonlinear dynamic analysis, hence only one curve "DiESL" is plotted for all approaches. In the following phase, the DiESL approximations underestimate the displacement during plastification before the plastic hinges form. The computed linear static displacement decrease with increased structural stiffness. The latter formation of plastic hinges in the nonlinear dynamic analysis can most probably be attributed to nonlinear and/or dynamic effects. DiESL is not able to anticipate these effects here. Phase 3 reveals the differences of the three approaches. *IncC* using the constant negative force increments gives the best result (see red arrow). When using the *Inc* approach, the negative force increments are exaggerated as the thickness/stiffness increases. The opposite happens with the *IncS* approach where the negative force increment is reduced with the increasing stiffness. These results are consistent with the considerations in chapter 3.1.4. It is interesting to note that the force drop hardly changes in magnitude. This observation suggests to use the *IncC* approach during linear static response optimization.
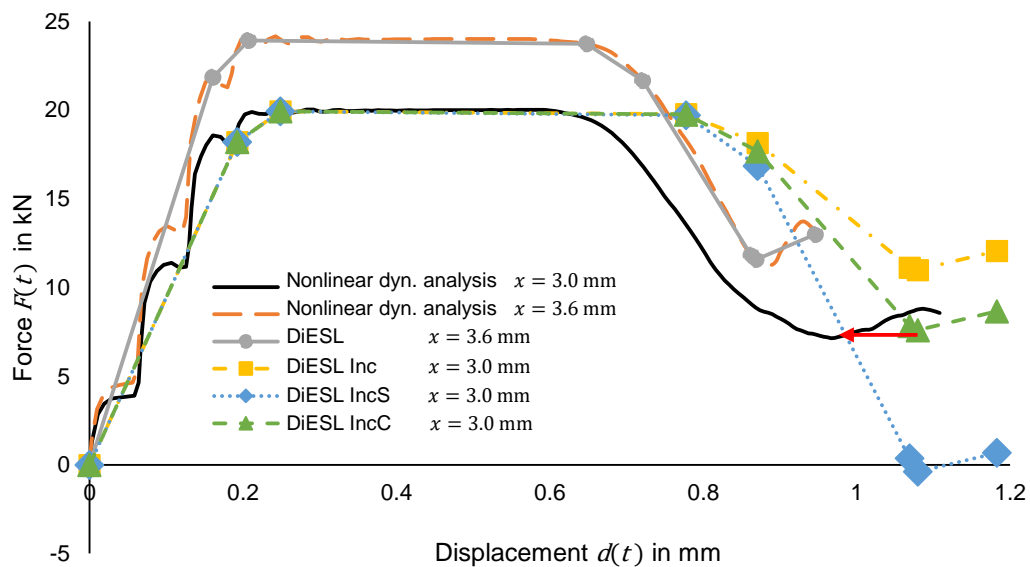
Figure 4.22: Hinge model − crash force over displacement derived in nonlinear dynamic analyses for the sheet metal's thicknesses of $x = 3.0$ mm and $x = 3.6$ mm and corresponding DiESL approximations using the approaches Inc, IncS, and IncC starting in the design point $^0 x = 3.6$

To investigate on how this approximations perform when the structural stiffness is reduced, the thickness of the sheet is now reduced from 3.6 mm to 3.0 mm. The results of the second study are illustrated in Fig. 4.22. The DiESL approximations are now created for 3.6 mm and they are tested at 3.0 mm. The same phenomena can be observed as before in inverted form. In phase 1, all approximations provide equally good results. In phase 2, the deformation prior to the formation of the plastic hinge is overestimated. The

faster formation of the plastic joints cannot be anticipated here either. In phase 3 the force drop predicted by *Inc* is too small now as a result of the stiffness reduction. Accordingly, *IncS* exaggerates the force drop to an extent that results in a negative total force and therefore provides a very unrealistic approximation. Again, the *IncC* approach provides the best prediction (red arrow).

4.3.2 Crash Box

In this section the approaches *Inc, IncS,* and *IncC* are tested again using a more realistic example. We employ the crash box model introduced in chapter 4.2.2, which is highly nonlinear and multimodal. As explained previously, crash boxes are a substantial part of automotive crush zones. To avoid damage of the safety cage we minimize the maximum contact force $F_{\max}$ between impactor and crash box, while the intrusion of the impactor is constrained. The target is a rectangular force displacement curve, which is the theoretical optimum with respect to a uniform energy absorption under the given constraints. The optimization is formulated as follows:

$$\min F_{\max}(\mathbf{x}); \qquad\qquad \mathbf{x} \in \mathbb{R}^{12} \qquad (4.9)$$

subject to

$$d(\mathbf{x}) \leq 160 \text{mm}; \qquad\qquad\qquad (4.10)$$
$$1.2 \leq x_j \leq 2.0; \qquad\qquad j = 1, ..., 12 \qquad (4.11)$$

This is a min max optimization problem, since the maximum force $F_{\max}$ must be determined as $F_{\max} = \max\left(F^i\right)$ in each analysis. We solve this using the β-method, where an artificial design variable β is used and minimized instead of $F_{\max}$. Moreover, constraints $F^i \leq \beta$ are added to minimize $F_{\max}$ implicitly, since the constraint $F_{\max} \leq \beta$ is always active.

This study uses 20 adaptively selected ESL times. As previously, the contact force between impactor and structure is fitted and the last ESL time is set as the time of maximum intrusion t_d. The Young's moduli in the LSMs are not adopted, since no major influence of the local adaption LA has been observed for this crash box model in the previous study.

As before the optimization problem is solved, for 40 uniformly distributed initial designs to achieve statistical independence from the initial designs. Each method uses the same 40 initial designs, they are given in appendix 7.2. In Fig. 4.23 the results of each method are illustrated, scattering the resulting maximum contact force $_*F_{\max}$ over the number of cycles necessary for convergence or termination $_*cycle$.
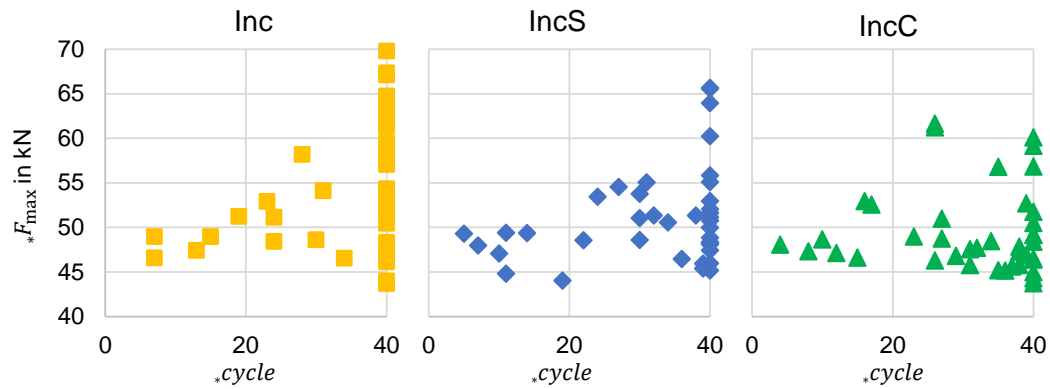
Figure 4.23: Crash box – resulting maximum crash force ${}_*F_\mathrm{max}$ and corresponding cycles of all multistart runs for the approximations: *Inc* (left), *IncS* (middle), and *IncC* (right)

The diagrams report a multitude of designs with ${}_*cycle = 40$. These runs failed to converge within 40 cycles and were terminated according to equation 3.37. Table 4.7 lists the number of converged runs as well as the averaged results of the converged runs for each method. The most runs converged using *IncC*, the least using *Inc*. This can be seen as a confirmation of the better approximation quality demonstrated in the previous hinge model example. Any conclusions based on the averaged results $\overline{{}_*cycle}$ and $\overline{{}_*F_\mathrm{max}}$ would be invalid for two reasons: firstly, the numbers of converged runs are different and secondly, the initial designs of the converged runs differ considerably between the methods. No clusters can be identified as in the previous studies to allow for a reasonable comparison. To remedy this issue the optimization results are investigated more deeply in order to identify suitable measures for a reasonable comparison.

Table 4.7: Crash box – number of converged multistart runs and averaged maximum contact force and cycles for all converged runs

Approach	Converged runs	$\overline{{}_*cycle}$	$\overline{{}_*F_\mathrm{max}}$ kN
Inc	12	21.25	50.26
IncS	20	24.45	49.40
IncC	27	27.0	49.29

Two attempts for extracting useful information out of the multistart runs were pursued. The first attempt was releasing the convergence criterion on the objective's relative change by dropping the requirement of two subsequent cycles. This was done by re-evaluating the previously recorded optimization histories. It yielded an abundancy of multistart runs that "converge" extremely early after a few cycles. However, reviewing the convergence histories of these runs revealed that most "convergences" were coincidences because a large number of design variables would still change significantly in the coming cycles. Obviously, this attempt introduced too much randomness and was not suited for extracting meaningful data for statistical evaluation.

The second attempt was executed in two steps. The first step is a manual review of all optimization histories (converged and un-converged) and a subjective evaluation. It is illustrated in Fig. 4.24 and Fig. 4.25 with an exemplary convergence history of an un-converged run using *IncC*. Fig. 4.24 right shows that most design variables are settled after 25 cycles and the design hardly changes anymore thereafter. This behavior can be observed in most un-converged runs. We therefore determine the cycle k_L after which the design does not change significantly anymore for each un-converged optimization run by visual inspection and subjective judgement. There is no objective criterion defined, only that at most two design variables should change by "not too much" after cycle k_L. The second step is then to determine the best feasible design with $k^* \geq k_L$, this design is referred to as *best design* $_{k^*}\mathbf{x}$ in the following. In the example the cycle $k_L = 25$ (Fig. 4.24 right and Fig. 4.25 left) and the corresponding iteration $i_L = 50$ (Fig. 4.24 left) are marked by dashed lines. The best feasible design $_{k^*}\mathbf{x}$ is marked with a green circle and is reached after 27 cycles. Fig. 4.25 (right) shows the contact force versus displacement curves of the initial ($k = 0$), *last* ($k = 40$), and *best* ($k = 27$) designs as well as of the theoretical optimum.

There is barely any difference between the force curves of the *best* and the *last* design. Based on this similarity, we conclude that the convergence issues can be attributed to the chosen convergence criteria, because the design variables as well as the contact force curve is hardly changing. Due to the non-smoothness of the min max optimization problem the objective function's relative change prevents the algorithm from converging. Fig. 4.26 and 4.27 plot the force curves for all multistart runs using *IncC*. With a few exceptions, the previously described findings are confirmed. Note that appendix 7.2 contains the resulting force versus displacement curves for the other two approaches *Inc* and *IncS* as well as parallel coordinate plots of the resulting *best designs* of all runs.

Concluding, the *best design* $_{k^*}\mathbf{x}$ obtained with the manual reviewing attempt can be used as a representative of each optimization run and is therefore qualified to be used for a statistical evaluation and a reasonable comparison. Furthermore, the quality of the results depicted in Fig. 4.26 and Fig. 4.27 should be emphasized. A significant improvement of the *best design* compared to the initial design can be observed in the majority of all multistart runs. The best contact force curves oscillates around the theoretical optimum (red), and the maximum intrusion of 160 mm is never exceeded.

Table 4.8 shows the averaged objective value and the corresponding standard deviation for the *best designs* $_{k^*}\mathbf{x}$ for each approximation method. In average, the best objective value is reached when *IncC* is used. Additionally, the standard deviation $stdv$ is the smallest for this approach. The differences, however, are relatively small. Furthermore, it should be repeated that the determination of k_L is a subjective procedure and the subsequent comparison therefore involves uncertainties. Hence, we cannot finally conclude, which approach is the best. Nevertheless, it is clear the *IncC* approach yields good results in terms of crashworthiness when comparing the individual *best design* force curves with the theoretical optimum and those of the initial designs (in Fig. 4.26 and Fig. 4.27). This is remarkable since the crash box is a highly nonlinear example and the initial design variables are distributed all over the design space. We therefore conclude that *IncC* is a suitable approach to approximate forces in DiESL. Based on this result and the previous findings from the hinge model, the *IncC* approach is applied for all following examples.
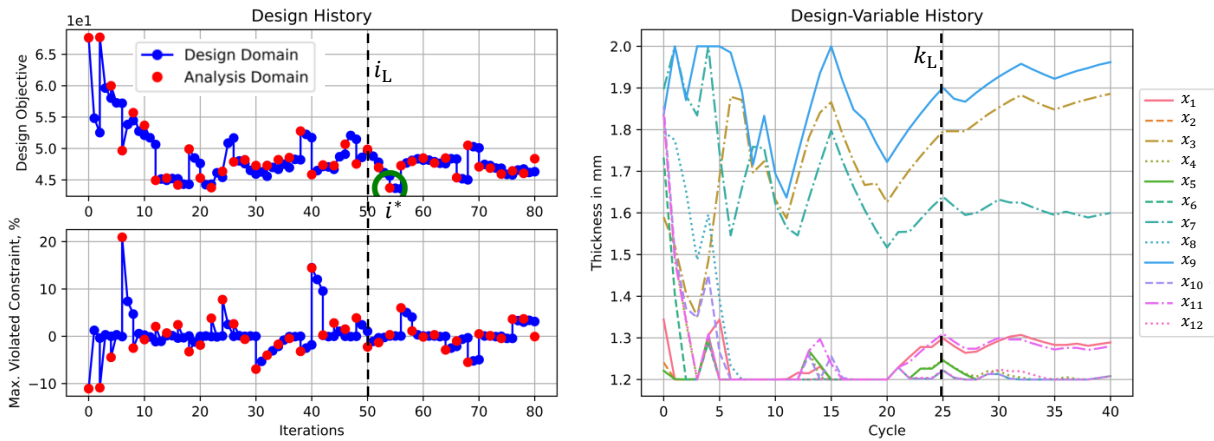
Figure 4.24: Crash box − objective function and maximum relative constraint violation over iterations (green circle: best feasible design; black dotted line: minimum iteration i_L) (left) and design variables over cycles (black dotted line: minimum cycle k_L) (right) demonstrating convergence issues when optimizing the crash force using *IncC*
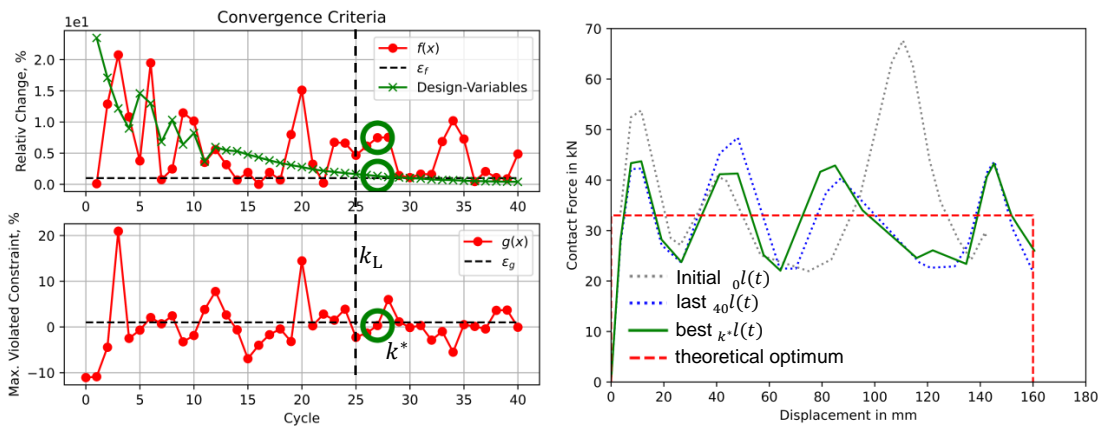
Figure 4.25: Crash box − convergence criteria and maximum relative change of design variables over cycles (green circle: best feasible design; black dotted line: minimum cycle k_L) (left) and resulting crash force for the initial ($k = 0$), the last cycle ($k = 40$) and the best cycle ($k^* = 27$) (right) demonstrating convergence issues when optimizing the crash force using *IncC*

Table 4.8: Crash box − averaged maximum contact force for the *best designs* $_{k^*}\mathbf{x}$ with $k^* \geq k_\mathrm{L}$ of all multistart runs and corresponding standard deviation $stdv$

Approach	#	$\overline{_*F_\mathrm{max}}$ kN	$stdv$ kN
Inc	40	49.70	3.73
IncS	40	47.20	3.25
IncC	40	46.89	2.81
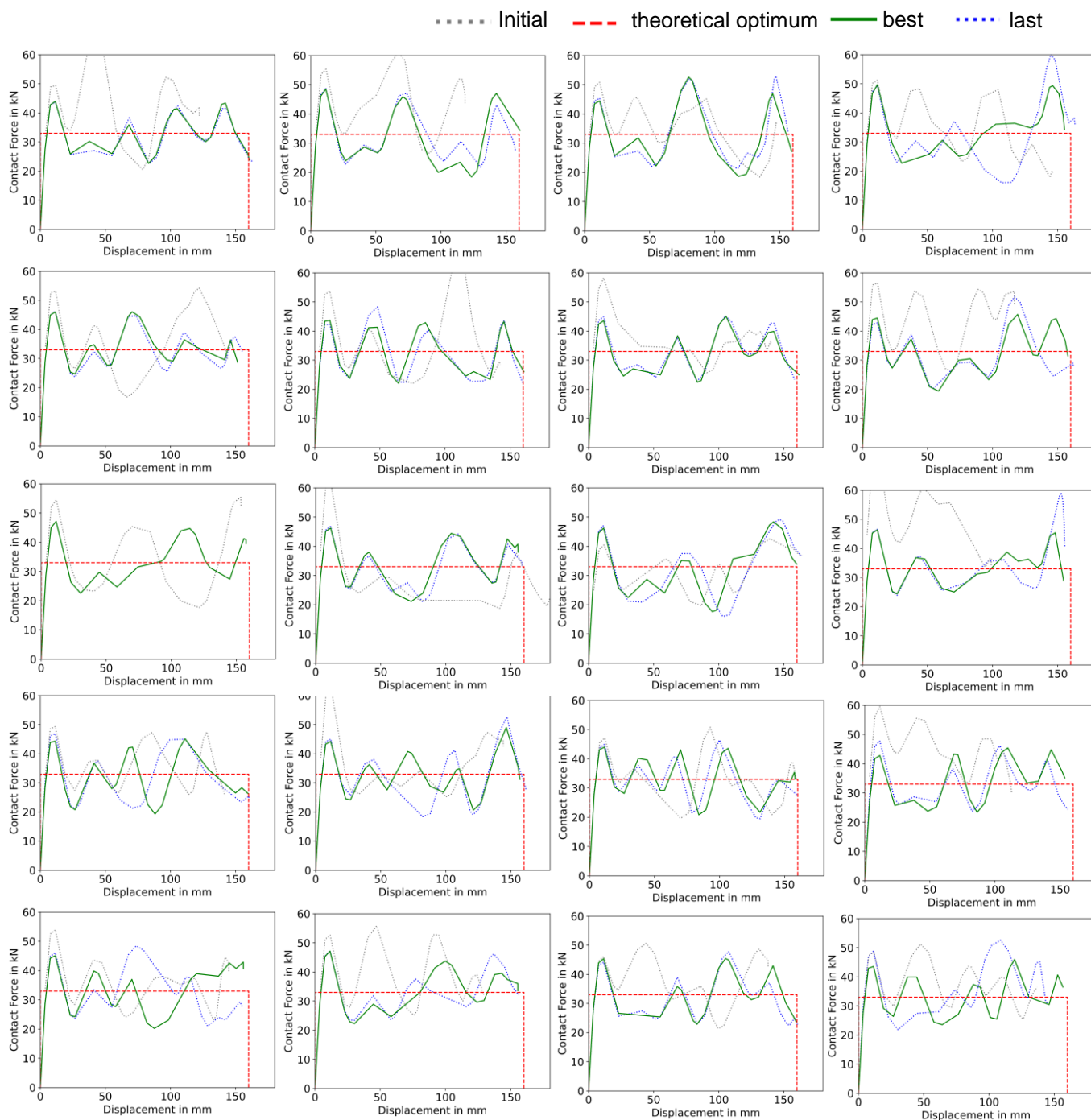
Figure 4.26: Crash box – contact force over displacement for *best designs* $_{k^*}\mathbf{x}$ with $k^* \geq k_\mathrm{L}$ (green) and the *last designs* $k = 40$ (blue) of multistart runs 1-20 employing *IncC*
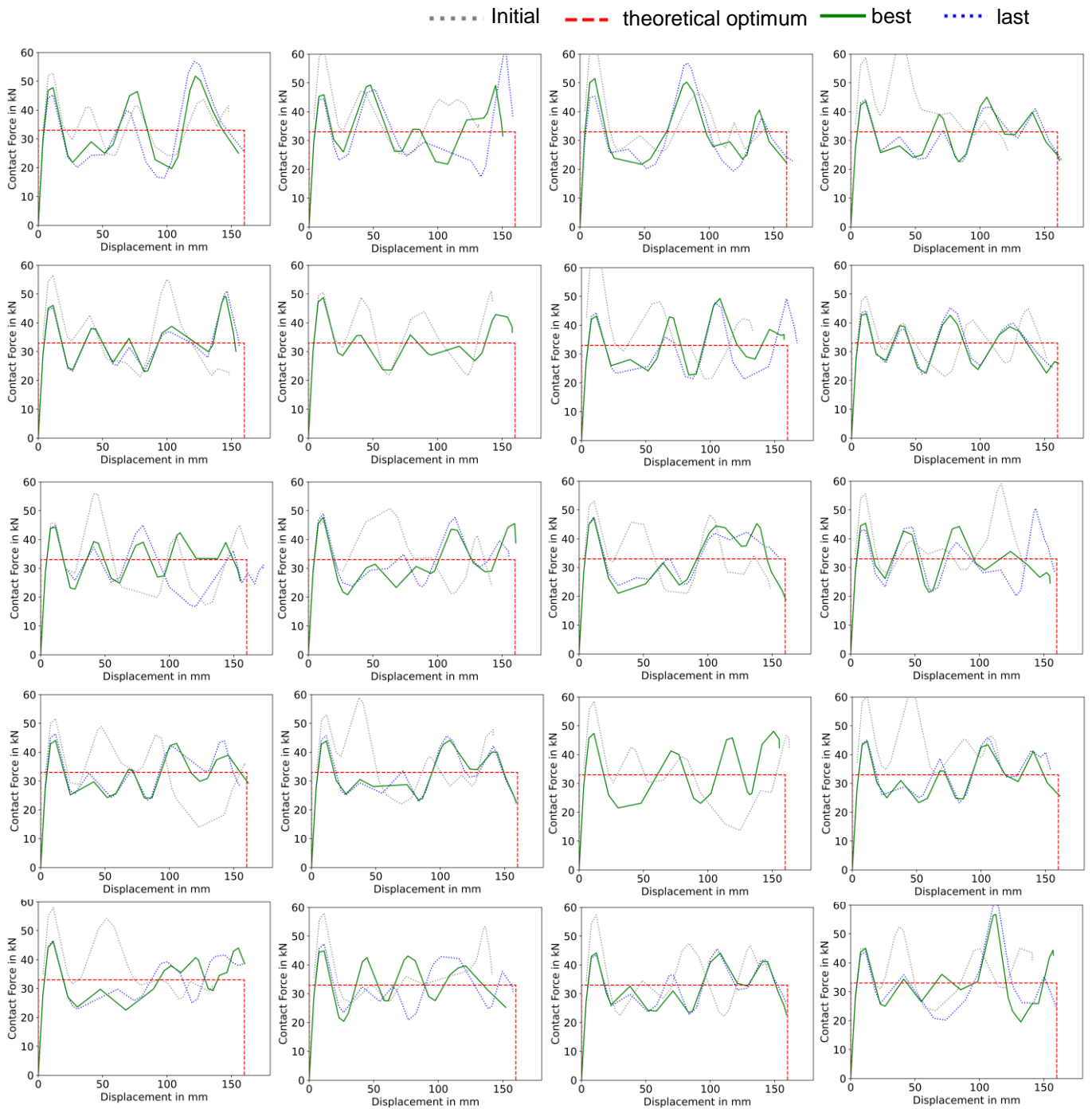
Figure 4.27: Crash box – contact force over displacement for the *best designs* $_{k^*}\mathbf{x}$ with $k^* \geq k_{\mathrm{L}}$ (green) and the *last designs* $k = 40$ (blue) of multistart runs 21-40 employing *IncC*

4.3.3 Side Impact B-Pillar

This section evaluates the performance of DiESL in combination with crash forces using a practical example from literature. This time, the DiESL method is not evaluated using a multistart study but by employing the same initial design as the literature reference. The example has been adapted from Ma et al. 2020, who used the ESD method for optimization. To ensure the comparability with Ma's findings no changes have been made to the model. As shown in Fig. 4.28 this is a side impact example. In this case a rigid pole ($mass = 965$ kg) with initial velocity $v_y = 8.3$ m/s impacts into the simplified side structure of a car containing B-pillar, upper rail, and rocker. The structure is made of aluminum (Young's modulus: $E = 64$ GPa, density: $\rho = 2730 \, \text{kg/m}^3$, Poison's ratio: $\nu = 0.3$), and a piecewise linear material is applied (yield stress: 0.197 GPa) (Fig. 4.30). The structure is clamped at the ends of both upper rail and rocker using SPCs locking all 6 degrees of freedom. Furthermore, the impactor's degrees of freedom are locked except of the translation in y-direction. For discretization 22519 fully integrated elements are employed connecting 22013 nodes. A contact between the impactor and the structure is defined in the nonlinear dynamic model only. In the design domain neither a contact nor an impactor is modeled. Four structural nodes are selected (red dots in Fig. 4.29) to approximate the intrusion of the impactor in the LSMs. In each LSM the respective node closest to the impactor is used to give the incremental intrusion $\mathbf{\Delta u}$. The impactor's total intrusion is then approximated as the sum of the displacements of the closest nodes. Adaptive time selection (AT) is used to fit 20 ESL times to the contact force curve between impactor and the B-pillar structure. The last ESL time is set as the time of maximum intrusion t_d. The material in the LSMs is not adapted locally (NLA).

There are 20 sizing design variables for the sheet metal gauges (Fig. 4.28, right). Some design variables represent multiple sheets. The design objective is to minimize the mass of the structure, while constraining the maximum crash force F_{max} to the corridor between 270 and 290 kN. Since the mass is minimized here, the optimizer is expected to reduce the structural stiffness and thus to meet the lower bound of 270 kN. The upper bound therefore seems to be unnecessary but is kept for consistency reasons with regard to the reference (Ma et al. 2020). Moreover, the design variables must remain between 1 and 10 mm. Mathematically the problem is formulated as follows:

$$\min mass\left(\mathbf{x}\right); \qquad\qquad \mathbf{x} \in \mathbb{R}^{20} \qquad (4.12)$$

subject to

$$270\,\text{kN} \leq F_{\text{max}}\left(\mathbf{x}\right) \leq 290\,\text{kN}; \qquad\qquad (4.13)$$

$$1.0\,\text{mm} \leq x_j \leq 10.0\,\text{mm}; \qquad\qquad j = 1, ..., 20. \qquad (4.14)$$
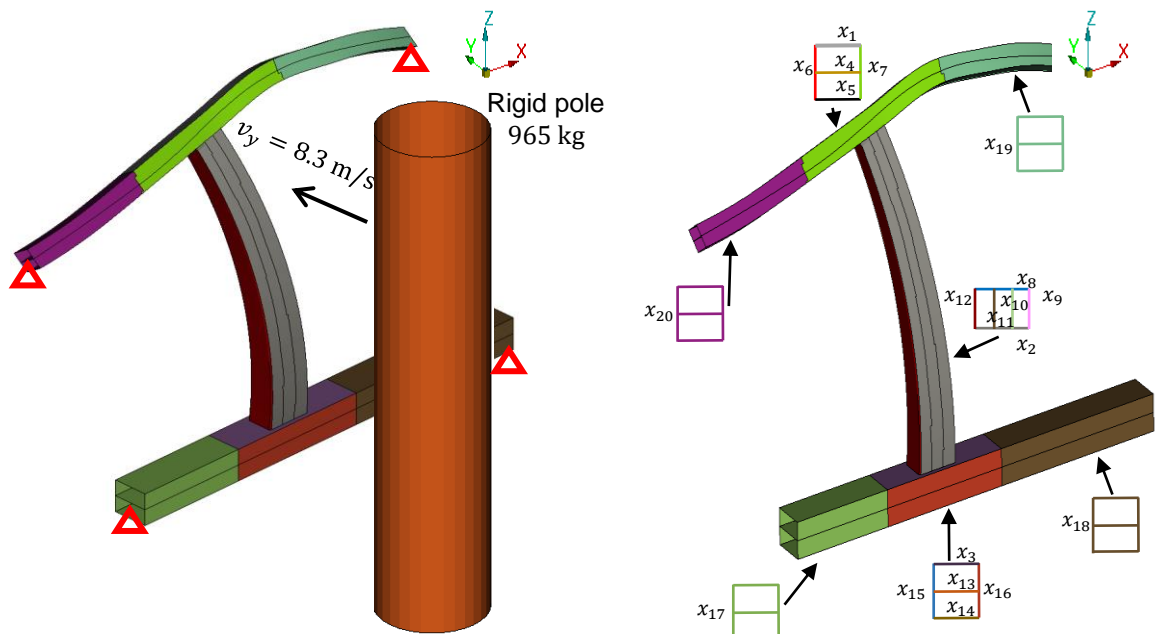
Figure 4.28: Side Impact B-Pillar – FE-model including pole, B-pillar, upper rail, and rocker (left) and labeling of design variables (right)
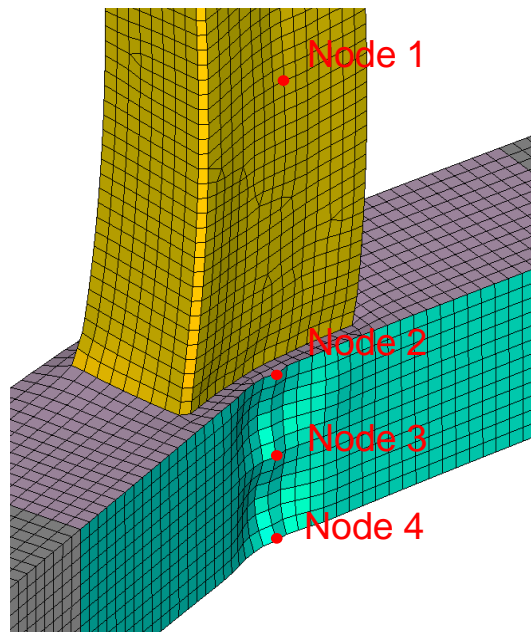
Figure 4.29: Side Impact B-Pillar – structural nodes to approximate the pole's intrusion in the LSMs
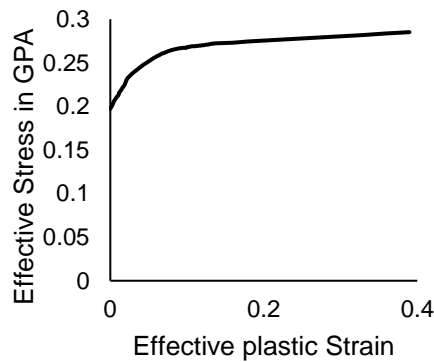
Figure 4.30: Side Impact B-Pillar – strain versus stress curve of piecewise linear material

Fig. 4.31 shows the optimization history of objective, constraint violation and design variables. The optimization terminates after 13 cycles, yielding the optimized design illustrated in Fig. 4.32. The left side shows the deformed structure at the time of maximum intrusion and the right side is a parallel coordinate plot of the initial design as well as the optimized designs obtained with the DiESL and ESD methods. The ESD and DiESL results are similar with respect to the relations of thicknesses: identical parts have been identified to be thick or thin. However, the DiESL approach leads to a significantly smaller mass than the ESD approach does. The results are compared in table 4.9. Both methods converge after 13 cycles. The resulting crash force is illustrated in Fig. 4.33. As expected, the lower force constraint is active for both optimized designs. The DiESL method yields significantly better results than the ESD method. Compared to the initial design the mass has been reduced by over 40%.
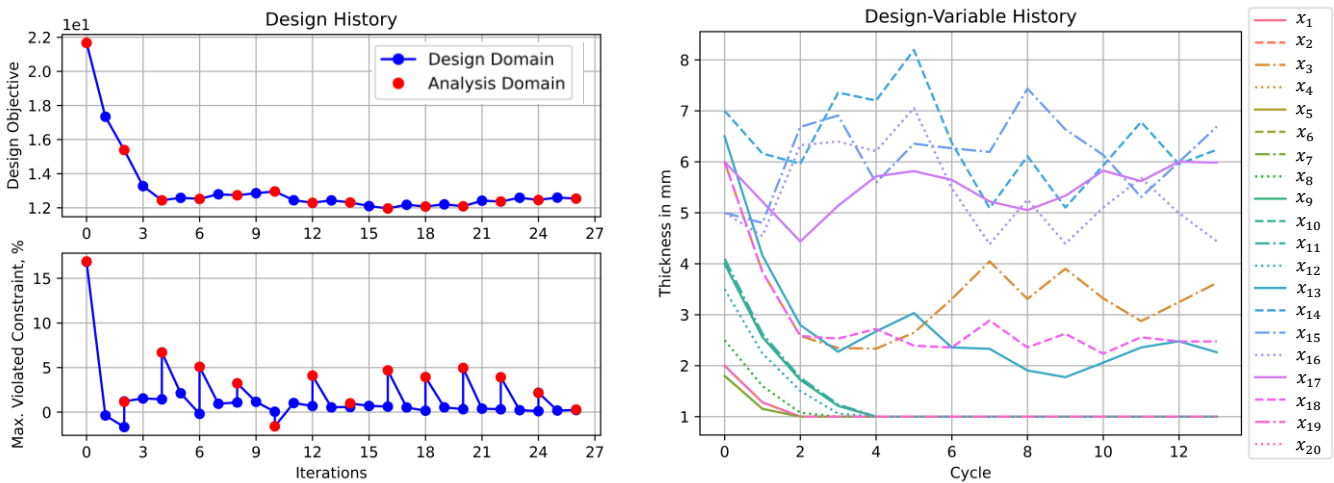
Figure 4.31: Side Impact B-Pillar – objective function and maximum relative constraint violation over iterations (left) and design variables over cycles (right)
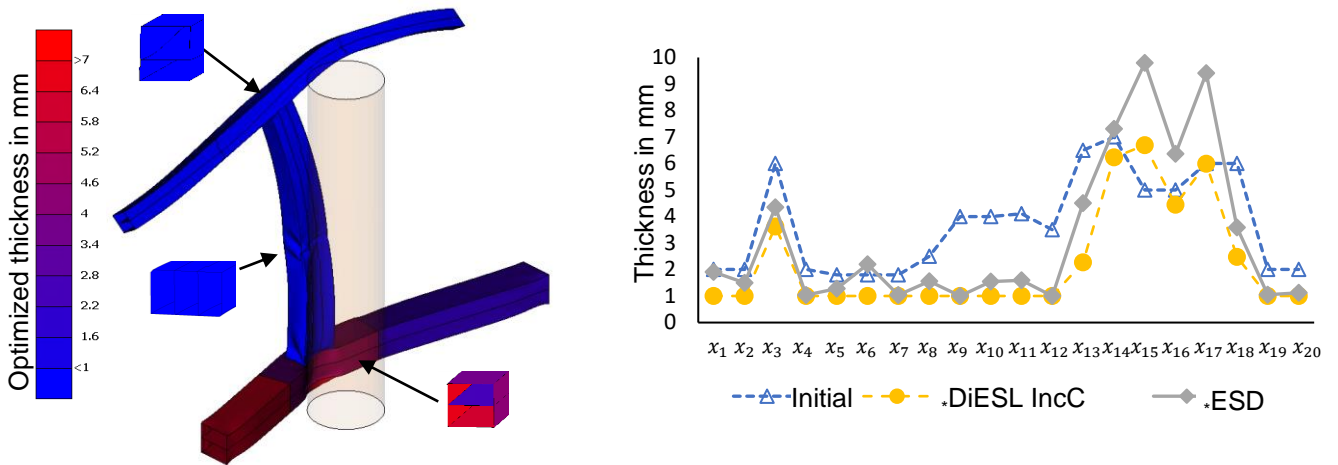
Figure 4.32: Side Impact B-Pillar – deformed structure of optimized design using DiESL (left), initial and optimized design variables obtainer from DiESL and ESD (right)
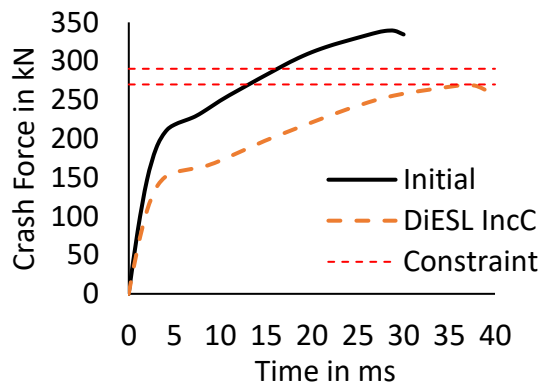
Figure 4.33: Side Impact B-Pillar – contact force between structure and B-pillar for initial design and optimized design using DiESL *IncC*

Table 4.9: Side Impact B-Pillar – $mass$ and $F_{\max}(\mathbf{x})$ for initial and optimized designs from DiESL and ESD approach (Ma et al. 2020)

Design	$_*cycle$	$mass(_*\mathbf{x})$ kg	$F_{\max}(_*\mathbf{x})$ kN
Initial	0	21.67	338.97
ESD	13	17.71	270.20
DiESL	13	**12.54**	269.18

5 Topology Optimization

So far, the DiESL method has only been tested for sizing optimization examples. It has been shown that the method yields satisfying results for both crash relevant objectives: the optimization of stiffness as well as energy absorption. In contrast to other state of the art optimization methods like metamodel-based approaches the computational effort does not scale directly with the number of design variables. Thus, the method shows great potential for the application of topology optimization. In this chapter the DiESL method will be extended to topology optimization employing the SIMP approach. For this purpose some adaptions of the general program flow given in chapter 3 are necessary and are elaborated in the following. Afterwards the method is tested using different numerical examples.

5.1 General Procedure

5.1.1 Density Interpretation

For sizing optimization the result of linear static response optimization in the design domain can be transferred directly to the nonlinear dynamic model and be analyzed. In case of topology optimization employing the SIMP approach this becomes more complicated. Here, the normalized densities of all design elements are used as design variables. In the standalone practical application of linear static response topology optimization, this is usually not a problem, since the result of the optimization – the design proposal – can be manually interpreted by expert engineers, and a detailed component can be realized. In the ESL and DiESL methodologies, however, this process must be automated, and in each cycle the density-based design proposal must be transformed from the design domain into a nonlinear dynamic model in the analysis domain. The simplest solution would be to transfer the resulting densities and corresponding material properties directly to the nonlinear dynamic model. Unfortunately, elements with low density and therefore low stiffness can lead to problems in the nonlinear dynamic analysis. This is a severe issue since the nonlinear dynamic analysis terminates with an error and thus leads to an unwanted abortion of the entire DiESL optimization.

This issue has already been addressed by previous researchers (H. A. Lee and Park 2015; Bai et al. 2019) in the context of topology optimization employing the ESL method. Their solution was to create a 0-1 design from the resulting density field in each cycle rather than transferring the continuous density distribution

to the nonlinear dynamic model. For this purpose, a threshold ϵ_{vf} is defined. All elements with densities smaller or equal ϵ_{vf} are interpreted as *voids* and all elements with a higher density than ϵ_{vf} are interpreted as *solids*. This approach is referred to as *0-1 interpretation*. Lee and Park propose to set ϵ_{vf} as the value of the volume-fraction constraint defined in the topology optimization problem. However, they also state that this "does not always work well" (H. A. Lee and Park 2015) and further research is required to find a technique to determine a suitable threshold.

To circumvent this issue, in the following, a new method of transferring the continuous density field to the nonlinear model is explained. This alternative approach is based on two thresholds ϵ_{v} and ϵ_{s}: Instead of creating a 0-1 design, only elements with a density below or equal a low threshold ϵ_{v} are interpreted as *voids* and thus deleted, elements with a density above a high threshold ϵ_{s} are interpreted as *solids* and assigned to the original solid material. The densities between both thresholds are transferred unchanged to the analysis domain. For this purpose a transformation variable χ_i for each element i is introduced:

$$\chi_i = \begin{cases} 0 & if & x_i \leq \epsilon_{\mathrm{v}} \\ x_i & if & \epsilon_{\mathrm{v}} < x_i \leq \epsilon_{\mathrm{s}} \\ 1 & if & x_i > \epsilon_{\mathrm{s}}. \end{cases} \tag{5.1}$$

For all elements with $\chi_i > 0$, the density χ_i is assigned. The remaining elements with $\chi_i = 0$ are deleted in the nonlinear dynamic model for the coming cycle. Note that this process is executed in each cycle starting from a full design space. This means that an element deleted in one cycle may not get deleted in a subsequent cycle. The resulting nonlinear dynamic model is called *container model*[1] in the following.

The transformation process is illustrated in Fig. 5.1[2]. As depicted in the middle diagram, it may happen that islands of unconnected elements remain after deleting the void elements. Since they do not contribute to the structure's stiffness and cause issues during the nonlinear dynamic analysis, they must be identified and deleted as well. The identification is done by using the "connectivity" tool of the preprocessor *ANSA*. Here, all interconnected elements are grouped. The unconnected elements can then be distinguished from the relevant main structure by their relatively small mass and can be deleted automatically.

---

[1] The name refers to the approach's implementation: For each material that is referenced in the design space, a set of n_{c} material containers is defined. Each container represents a density range of width $\Delta\chi = (\epsilon_{\mathrm{s}} - \epsilon_{\mathrm{v}})/n_{\mathrm{c}}$ such that the union of all containers spans the entire normalized density range from ϵ_{v} to ϵ_{s}. The actual density transformation is then realized by assigning each element in the design space to the material container associated to the respective normalized density. For testing this approach $n_{\mathrm{c}} = 200$ has been used. Since $\Delta\chi$ is very small then, the material distribution is considered to be continuous from ϵ_{v} to ϵ_{s} in the following (Triller et al. 2022b).

[2] The borders of all deleted elements (white) are still shown in this illustration. Beside the elements the corresponding nodes are also deleted.
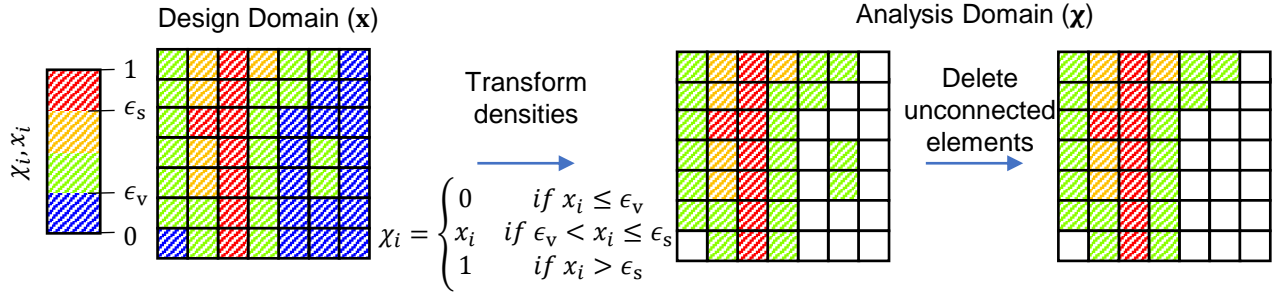
Figure 5.1: Interpretation of densities resulting from linear static response optimization (design domain) for usage in subsequent nonlinear dynamic analysis (Triller et al. 2022b)

In this thesis we set the thresholds $\epsilon_v = 0.1$ and $\epsilon_s = 0.9$. In doing so, most of the densities are transferred unchanged to the analysis domain, and the material distribution changes gradually from one cycle to the next. This way, the topology can evolve continuously in a smooth way. In comparison to the 0-1 approach, the continuity is considered as an advantage especially in the early stages of the DiESL procedure: At the very beginning of the optimization, typically all densities are initialized with a common intermediate value. From there, it takes a couple of cycles to evolve a discrete structure. During these early cycles in which no discrete structure has yet evolved, the threshold ϵ_{vf}, employed in the 0-1 approach, is of major influence on the resulting nonlinear dynamic model. This may be explained best by looking at both extreme cases: If the densities of all elements are smaller than ϵ_{vf}, then all elements are deleted. In the other extreme case all densities are greater than ϵ_{vf} and all elements are solid. This means either too many or too few elements are deleted depending on the choice of ϵ_{vf}. Thus, the structure's mass and the related stiffness and inertia effects do strongly depend on the choice of ϵ_{vf}. This is not the case for the *container model* approach presented here, since intermediate densities are kept and the number of deleted elements remains small even at the beginning of the optimization due to the relatively small value chosen for ϵ_v (Triller et al. 2022b).

The SIMP approach relates the element's densities to their mechanical properties. The analysis domain contains material nonlinearities, we therefore need to employ an extended SIMP approach here. As this work is limited to the use of elasto-plastic materials, the Young's modulus E, the yield stress σ_y and the hardening modulus E_H need to be related to the densities χ:

$$E(\chi) = \chi^{p_{NL}} \cdot E_1 \tag{5.2}$$

$$\sigma_y(\chi) = \chi^{p_{NL}} \cdot \sigma_{y,1} \tag{5.3}$$

$$E_{Hi}(\chi) = \chi^{p_{NL}} \cdot E_{H_i,1} \tag{5.4}$$

where E_1 is the Young's modulus, $\sigma_{y,1}$ is the yield stress, and $E_{H_i,1}$ is the hardening modulus of the corresponding solid material. Patel 2007 uses a similar material interpolation, but different exponents are employed for the hardening modulus and yield stress. Fig. 5.2 illustrates the nonlinear SIMP approach

presented here for a piecewise linear elasto-plastic material for different densities χ and exponent $p_{\text{NL}} = 1$. The exponent $p_{\text{NL}} = 1$ is used for illustration purposes here, but this value was also used during all applications in this thesis for building the nonlinear dynamic model. This is different to the SIMP approach in the linear static model using $p = 3$ for a specific reason. For an exponent $p_{\text{NL}} = 3$ the stiffness of elements with densities $\epsilon_{\text{v}} < \chi < 0.4$ becomes extremely small $E < 0.064 E_1$. This would cause mesh distortion problems in the nonlinear dynamic model as described before. Fig. 5.3 exemplifies such issues for $p_{\text{NL}} = 3$. Plasticized regions with excessive deformation or so-called *hedgehog* effects can occur (Karev et al. 2018). The latter can be observed especially in impact zones, where individual nodes are flying away in the nonlinear dynamic analysis. Elements with small densities suffer from a high mass/stiffness ratio, they are not able to retain the nodes in place if they are subjected to high contact forces like in impact zones. Even for elements with $\chi \approx 0.35$ this issue can be observed in Fig. 5.3. Thus, a lower threshold $\epsilon_{\text{v}} \approx 0.4$ would be necessary to resolve this issue. However, this would negate the benefits of the container model described above. Therefore, an inconsistency between the SIMP penalty exponents used in analysis and design domain is tolerated. For $p_{\text{NL}} = 1$ the mass/stiffness ratio remains constant for densities between ϵ_{v} and ϵ_{s}, and mesh distortion problems do not occur in the analysis domain.

At first thought this inconsistency may be considered a drawback of the presented approach. However, if compared to the 0-1 approach it may rather be seen as an improvement. The reason for this is illustrated in Fig. 5.4. The left side shows the normalized stiffness in the design domain $\xi_i = E(x_i)/E_1$ and analysis domain $\xi_{\text{NL},i} = E(\chi_i)/E_1$ plotted over the density x_i and χ_i, respectively. The right side plots the difference of each nonlinear approach (*container model* and *0-1 interpretation*) to the linear SIMP curve $\Delta\xi_i = \xi_{\text{NL},i} - \xi_i$. As can be seen, the difference and hence the inconsistency is considerably worse for the *0-1 interpretation*. It must be noted that this inconsistency is more pronounced for designs with intermediate densities, i.e. designs that are not discrete, in the design domain. Once the optimizer has converged to a discrete design, the inconsistency becomes negligible.
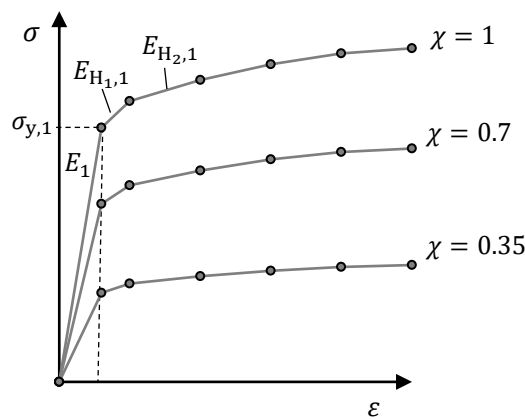
Figure 5.2: Elasto-plastic piecewise linear material model for different densities χ using SIMP with $p_{\text{NL}} = 1$ (Triller et al. 2022b)
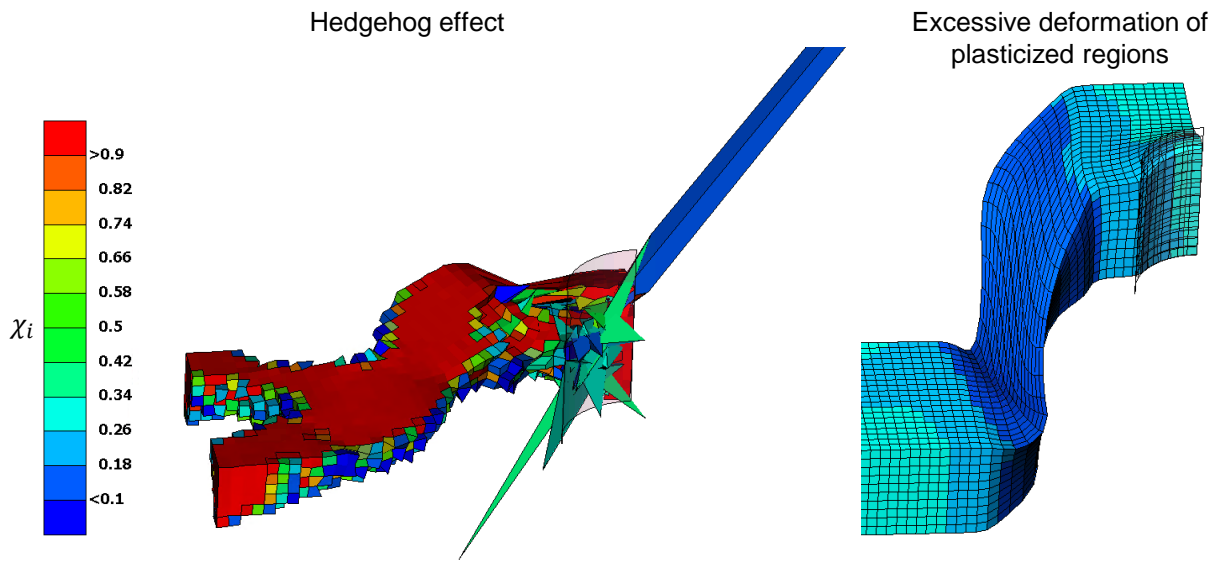
Figure 5.3: Mesh distortion problems during nonlinear dynamic analysis using SIMP approach with $p_{\mathrm{NL}} = 3$ and *container model* density distribution: hedgehog effect (left), excessive deformation (right) (Triller et al. 2022b)
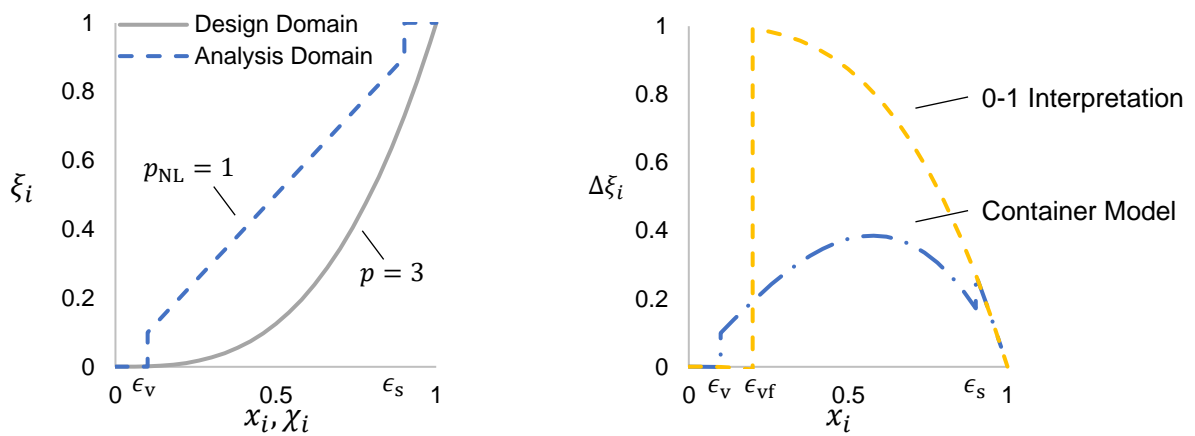
Figure 5.4: Relation between normalized density and normalized stiffness in design and analysis domain (left) and difference between normalized stiffness in analysis domain using *container model* with $p_{\mathrm{NL}} = 1$ and *0-1 interpretation* with $\epsilon_{\mathrm{vf}} = 0.2$ (right) (Triller et al. 2022b)

5.1.2 Reconstruction of the LSMs Mesh Coordinates

If elements are deleted in the nonlinear dynamic model, a similar problem as described in chapter 3.3.5 occurs. This is because the elements and associated nodes are deleted only in the analysis domain but not in the design domain. According to the container model approach, elements in the design space are deleted deliberately in the analysis domain if their density is too low, see equation 5.1. The FE-models used in analysis and design domain are thus non-congruent. As a consequence, the nonlinear dynamic analysis does not provide the displacements of the deleted element nodes. However, they are necessary to build the deformed LSMs meshes $\mathbf{r}(t^i)$ according to equation 3.2. This issue can be solved in the same way as previously suggested for sizing optimization in chapter 3.3.5, the procedure is illustrated in Fig. 5.5. A dedicated reconstruction FEA is executed in the design domain. For each ESL time a subcase is created in which the known displacements are imposed on the undeformed structure as SPCs (Fig. 5.5 bottom left, red arrows). All nodes missing in the analysis domain are pulled along. The missing nodal coordinate information can then be supplemented from the results of the linear static reconstruction analysis.
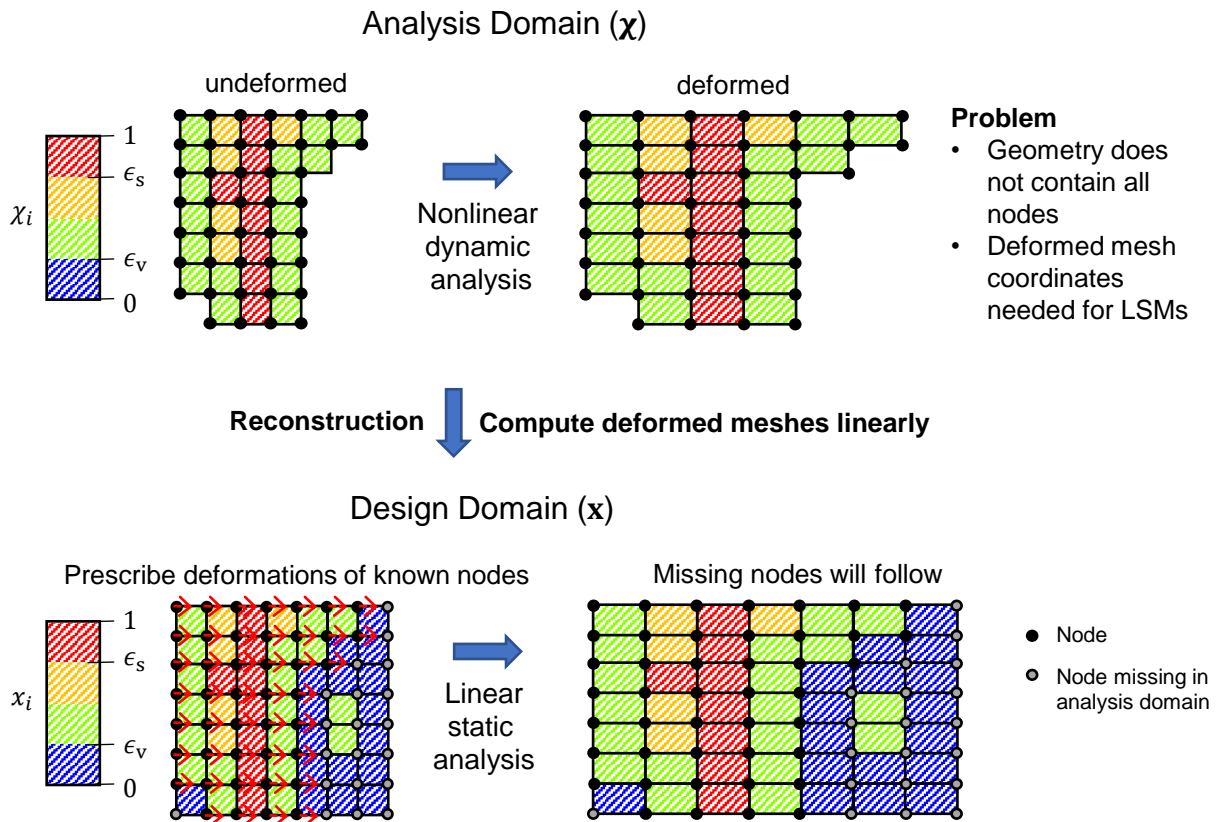
Figure 5.5: Workaround for calculating the deformed mesh coordinates of nodes deleted in the nonlinear dynamic model (analysis domain) (Triller et al. 2022b)

5.1.3 DiESL Procedure for Topology Optimization

The DiESL procedure for topology optimization must be extended by two major steps: the reconstruction of the deformed meshes and the interpretation of densities resulting of each linear static response optimization. The resulting optimization process is illustrated in Fig. 5.6.
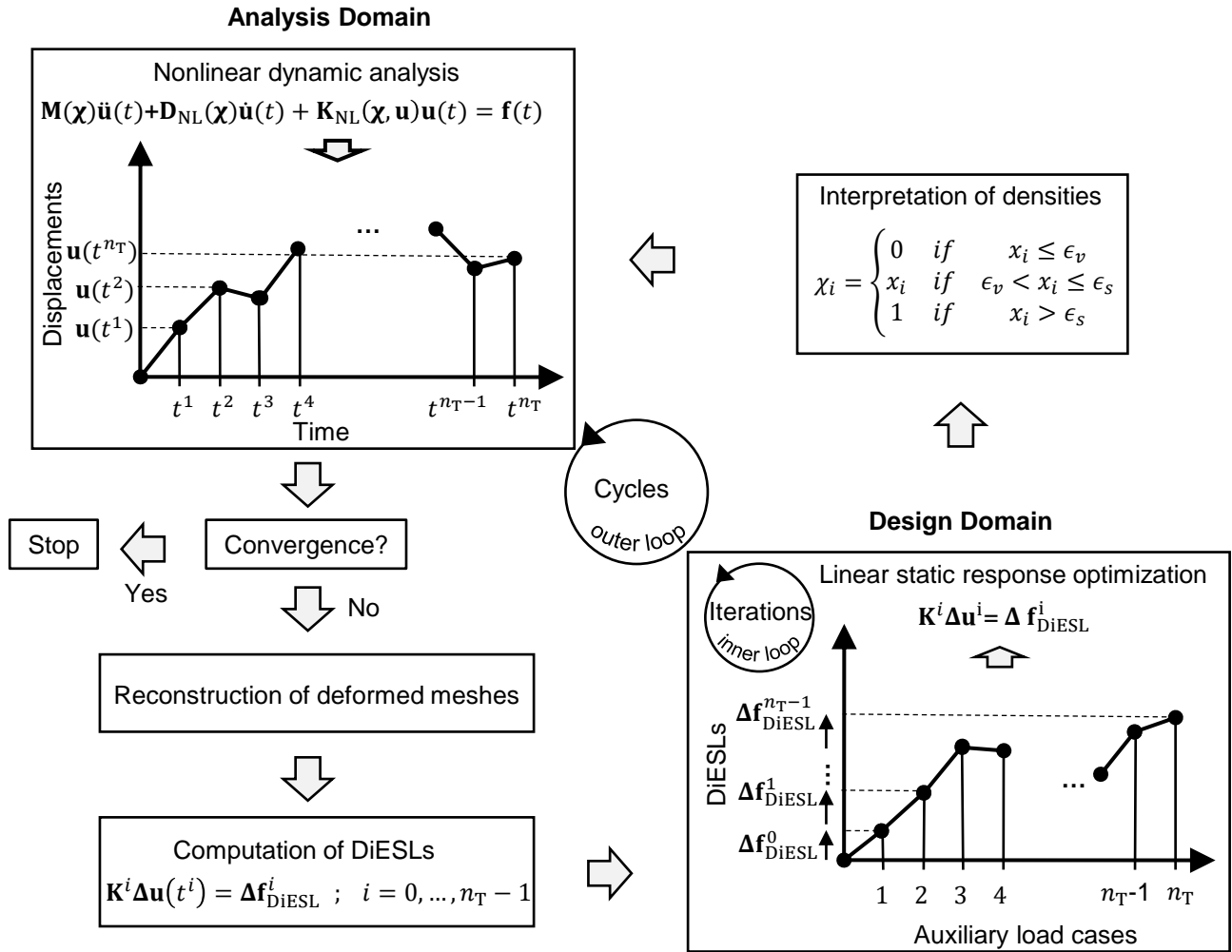
Figure 5.6: General optimization process of the DiESL method for nonlinear dynamic response topology optimization (Triller et al. 2022b)

5.1.4 Implementation

Beside the additional steps in the program procedure, some changes in the implementation of the methodology must also be made due to the used software. In the following, differences compared to sizing optimization are explained.

Unlike in sizing optimization, the initial values of the design variables cannot be defined individually as an input in topology optimization applications in OptiStruct. Only the single value of a homogeneously distributed density can be specified. This is a severe issue since the DiESL methodology requires to start a new linear static response optimization in each cycle, and we need to initialize the density distribution obtained in the previous cycle. This can be achieved with the restart functionality of OptiStruct. With this functionality, the linear static response optimization terminated in cycle k can be restarted in the subsequent cycle $k+1$. In between, the boundary conditions such as loads and SPCs for individual load cases as well as the LSM meshes can be changed. But the certain optimization parameters like move limits or iteration counter, or the value or number of design variables cannot be changed. Consequently, the deletion of failed elements in the design domain due to heavy mesh distortion as described in section 3.3.5 is no longer possible as this would change the number of design variables.

This requires another workaround. Instead of deleting failed elements, dummy nodes not connected to the structure are assigned to the respective elements such that they no longer participate in the structure's deformation and pass the element quality check. These dummy nodes are defined as a preprocessing step before starting the DiESL optimization for each used element type. Their degrees of freedom are all locked using SPCs. Consequently, failed elements assigned to the dummy nodes as well as their corresponding design variable remain in the model but do not have any influence on the remaining structure. Note that all failed elements of the same type (e.g. quad, hexa) share the same dummy nodes.

Another consequence is that the previously introduced move limit strategy cannot be employed for topology optimization. This is because the move limits are changed by OptiStruct internally in each iteration. Their value is saved to and retrieved from the restart file containing the design variables leaving no possibility for user control. The exact functionality of the employed move limit strategy has not been disclosed by Altair, except that the initially defined move limit δ_{ini} is never exceeded. As before we use $\delta_{\mathrm{ini}} = 0.2$ in the following. Since the exact strategy is unknown, we cannot assume that the move limits decrease during the optimization like it was the case with the previously applied strategy. This eliminates the motivation for employing the termination criterion 3.37 regarding the cycles. Hence, this criterion is not applied for topology optimization.

Instead, we employ a new convergence criterion based on the structure's discreteness, which is defined as follows (HyperWorks 2021):

$$D(\mathbf{x}) = \frac{\sum_i^{n_{\mathrm{E}}} x_i V_i \quad if \quad x_i \geq 0.9}{\sum_i^{n_{\mathrm{E}}} x_i V_i}, \tag{5.5}$$

where V_i is the volume of the i-th element. This means, the discreteness $D(\mathbf{x})$ gives the mass fraction of all elements with densities greater or equal 0.9 to the overall mass. $D(\mathbf{x}) = 1$ therefore corresponds to a design with no low or intermediate densities which is very close to a 0-1 design. The new criterion relates to the relative change of discreteness

$$_k\bar{D} = \frac{|D(_k\mathbf{x}) - D(_{k-1}\mathbf{x})|}{|D(_k\mathbf{x})|} \leq \epsilon_{\mathrm{D}}. \tag{5.6}$$

For all following examples we use $\epsilon_{\mathrm{d}} = 0.02$. Since this criterion is well suited for preventing early and coincidental convergence, the criterion on the relative change of the objective function (equation 3.35) is relaxed such that it only has to be fulfilled in one cycle, i.e. in the current but not in the previous cycle.

In addition, it has turned out to be useful to increase the maximum number of iterations per cycle to $max_{\mathrm{iter}} = 4$. Based on the author's experience, topology optimization runs usually require almost twice the number of iterations as sizing optimizations, which is supported by the increased number of iterations.

Furthermore, the minimum member size control is used in all examples. This is a topology optimization specific parameter that specifies a lower bound on the geometrical extension of structural members formed during topology optimization. A structural member cannot be smaller in lateral direction (height/width) than the parameter MINDIM. This can for example be accomplished by constraining the difference in density of two neighboring elements x_i and x_k

$$|x_i - x_k| \leq \frac{dist(i,k)}{\mathrm{MINDIM}} \tag{5.7}$$

where $dist(i,k)$ is the distance between the centers of two elements i and j (Harzheim 2014). Hence, if an element has density $\rho = 1$ then the densities of all elements within the distance MINDIM/2 must be larger than or equal to $\rho = 0.5$. The OptiStruct parameter MINDIM is activated by default when using MMO for topology optimization and cannot be disabled.

Additionally, the OptiStruct parameter TOPDISC is employed in the following examples. This is to enhance the resulting structures discreteness (HyperWorks 2021). Unfortunately, the OptiStruct manual does not provide any information about how this is accomplished. The minimum configurable value for MINDIM and thus the minimum width of the forming structures is two times the average element size in combination with TOPDISC.

5.2 Examples

In the following the proposed method is tested employing different numerical examples. The first example focuses especially on the functionality of the proposed method. An important evaluation criterion for this purpose is the result's interpretability. The discreteness index $D(_*\mathbf{x})$ is a good indicator in terms of interpretability. As the interpretation of a result with $D(_*\mathbf{x}) = 1$ is trivial, it can be stated: the higher $D(_*\mathbf{x})$, the easier the result's interpretation. According to OptiStruct the discreteness should be at least 0.5 to prevent interpretation difficulties (HyperWorks 2021). Additionally, two different strategies for interpretation will be employed. The performance of the resulting 0-1 interpretations and the respective container models will be compared to evaluate the interpretability. Furthermore, the first example is intended to study the capability of the DiESL method to account for inertia effects, as the ability of the ESL method to do so has been questioned in the past (Stolpe et al. 2018). Also, the ESL and DiESL method are compared using this example.

The second example is more practice related, it contains a large number of elements. This example has been adopted from literature. Originally it had been used to assess the GHT (Ortmann and Schumacher 2013; Ortmann 2015). Thus, the structural performance of the results stated in literature are used for comparison and for assessing the DiESL method's results.

Finally, the *IncC* approach for the incorporation of forces into the optimization problem is tested for topology optimization employing another practice relevant example.

5.2.1 Simple Beam subjected to Impact

The first example used for testing the DiESL method for topology optimization is a simple beam structure subjected to an impact by a rigid pole. This is illustrated in Fig. 5.7. The beam structure is clamped at both ends using SPCs. A pole with initial velocity v_0 hits the beam at its middle. The pole's rotational degrees of freedom and the translational degrees of freedom in x- and z-direction are locked. Again, for the sake of computational effort and numerical stability symmetry conditions are applied and only a quarter of the original model is analyzed.

A similar example has been used by Patel 2007 to test the HCA. Compared to Patel, some changes to the model have been made, which is why a direct comparison of results is not valid here. Nevertheless, an important finding of Patel was that depending on the pole's initial velocity, the HCA optimization schemes yields different results and the method is therefore capable of handling inertia effects. For examining the handling of inertia effects by the DiESL method, three different sets of initial velocity v_0 and mass $mass_i$ of the impactor, each defining one nonlinear dynamic load case, are studied here: $\{(10\,\text{m/s}, 65.7\,\text{kg})\,;(40\,\text{m/s}, 65.7\,\text{kg})\,;(150\,\text{m/s}, 4.69\,\text{kg})\}$. The impactor's mass is reduced in the last set to instate the same kinetic energy as in the set with $v_0 = 40$ m/s.
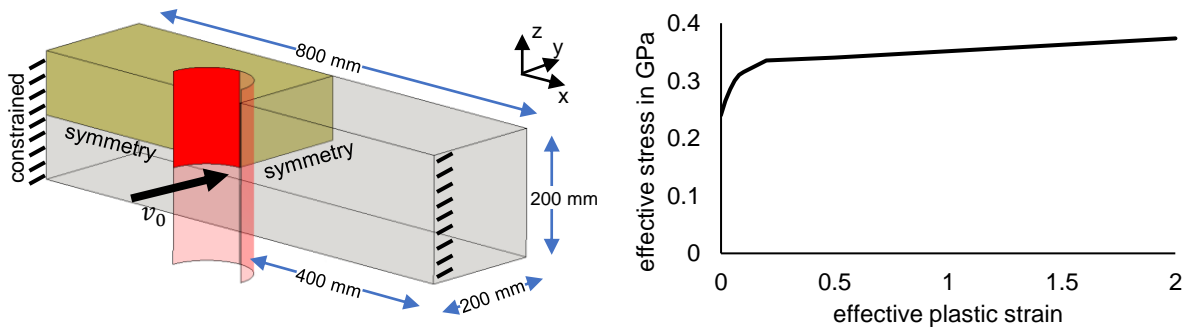
Figure 5.7: Simple beam – nonlinear FE-model of the beam exposed to an impact (left); piecewise linear material model (right) (Triller et al. 2022b)

The optimization's objective is to minimize the pole's intrusion $d(\mathbf{x})$ while the beam's mass $mass_{\mathrm{b}}$ is constrained. Mathematically this stiffness optimization is stated as:

$$\min d\left(\mathbf{x}\right); \tag{5.8}$$

subject to

$$mass_{\mathrm{b}}\left(\mathbf{x}\right) \leq 4.33\,\mathrm{kg}; \tag{5.9}$$

The mass constraint of 4.33 kg corresponds to a mass fraction of 20 % compared to a design with all solid elements. For all examined load cases the optimizer is initialized with a homogeneously distributed density of $\chi_i = x_i = 0.2$ such that the mass constraint is active. The nonlinear dynamic model defines contact between impactor and beam as well as self-contact within the beam structure. The linear static model defines neither contact nor an impactor. The pole's intrusion is approximated by averaging the y-displacement of one column of structural nodes in the impact zone (i.e. along the symmetry line in z-direction in the middle of the beam). The beam structure consists of aluminum (Young's modulus: $E = 70$ GPa, density: $\rho = 2700\,\mathrm{kg/m^3}$, Poison's ratio: $\nu = 0.33$), and piecewise linear material behavior is applied (Fig. 5.7, right). The beam consists of 8000 cubic elements with an edge length of 10 mm, its total number of nodes is $n_{\mathrm{N}} = 9471$. The minimum member size control parameter is set to the default OptiStruct value of three times the average element size (MINDIM $= 30$ mm). 20 adaptively selected ESL times are employed. Again the contact force curve between impactor and beam structure is used for adapting the ESL times. The optimization problem is solved for each of the three given load cases individually. Afterwards the results are compared visually.

In Fig. 5.8 the optimization history of the $v_0 = 40$ m/s load case is shown as an example. In addition to the objective function's history, the relative change of objective function, the relative constraint violation, and the discreteness D as well as its relative change is plotted. The optimization converges after 26 cycles reaching a discreteness of almost $80\,\%$. It may seem unusual that the constraint violation increases up to

12 % in cycle 3 and gradually declines thereafter until convergence is reached. This behavior is a side effect of the optimization parameter TOPDISC in OptiStruct, used to increase the structure's discreteness. It is also remarkable that the objective value (i.e. the beam's intrusion) at the beginning of the optimization has a similar value as the final result. Apparently, the initial structure with a homogeneously distributed density of $\chi_i = 0.2$ has a similar stiffness as the resulting container model. This effect can mainly be attributed to the choice of $p_{\mathrm{NL}} = 1$ for the transferring the densities from the design domain to the analysis domain according to equations 5.2 to 5.4. At this point it is important to remember that the intermediate initial densities are an artificial construct to define continuous design variables. They do not represent a real material, and in that sense the initial design is an invalid design.
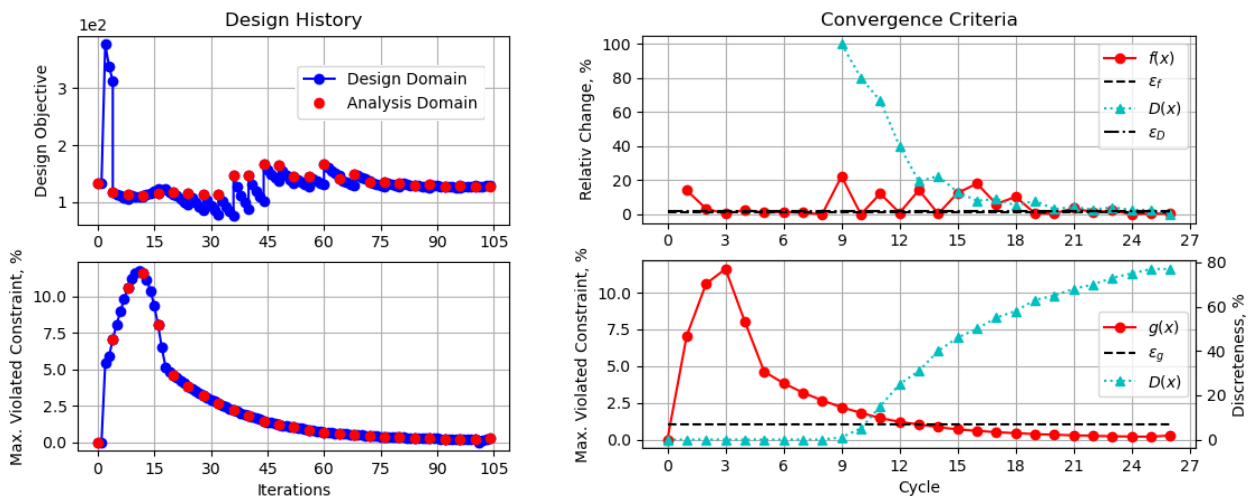
Figure 5.8: Simple beam – objective function and maximum relative constraint violation over iterations (left) and convergence criteria over cycles (right) using DiESL and $v_0 = 40$ m/s (Triller et al. 2022b)

For the same reason, the resulting container model needs to be interpreted and transferred to a 0-1 design. The resulting container model is shown on the left side of Fig. 5.9. As can be seen, this still contains intermediate densities, in particular a connection in the area between the impact zone and the structure's rear part (Fig. 5.9 dashed ellipse). During interpretation the question arises whether this connection should be maintained or discarded. In this example, it would be possible to quickly find out whether or not the connection has a decisive influence on the structural behavior by testing both options. Since in practice there is usually more than one feature at disposal, this can become more laborious. The following interpretation scheme is performed and tested to address this issue: The design is interpreted two times according to two different well-defined strategies. Both strategies focus on achieving the container model's performance with a 0-1 design in a nonlinear dynamic analysis. For this purpose, the two threshold values ε_{v} and ε_{s} are set equal to prevent any intermediate densities. Then the value $\varepsilon_{\mathrm{v}} = \varepsilon_{\mathrm{s}}$ is determined using bisection such that either one of the following conditions are fulfilled (Triller et al. 2022b):

1 The objective function's value of the 0-1 model and the container model are equal.

2 The mass constraint is active.

In the following it will be referred to the first and the second strategy as "*same objective*" and "*same constraint*", respectively. Usually, it is not possible to find a threshold that fulfills both conditions simultaneously. If this common threshold exists, it is a hint that the solution is robust (Triller et al. 2022b). In Fig. 5.9 right both 0-1 interpretations are illustrated. They are very similar in their appearance. The intermediate density connection between front and back does not show up in either design, it seems to have a negligible influence. Table 5.1 reports the used thresholds as well as the model's performance indicators are listed: the intrusion $d(_*\boldsymbol{\chi})$, discreteness index $D(_*\mathbf{x})$, and beam's mass $mass_{\mathrm{b}}(_*\boldsymbol{\chi})$. For all three load cases there is never a big difference between the chosen thresholds ε_{v} and ε_{s}. The same applies to the corresponding performances $d(_*\boldsymbol{\chi})$, $D(_*\mathbf{x})$, and $mass_{\mathrm{b}}(_*\boldsymbol{\chi})$ such that no significant trade-off between both designs has to be made. It is worth mentioning that the $mass_{\mathrm{b}}(_*\boldsymbol{\chi})$ of all container models is considerably smaller than the defined constraint 4.33 kg. This is caused by the deletion of elements in the container model with densities smaller than $\varepsilon_{\mathrm{v}} = 0.1$. In the design domain all elements with low density are preserved such that the mass constraint is active during inner loop iterations.

Based on the high similarity of both interpretations with the corresponding container model, we conclude that the introduced procedure for topology optimization with DiESL yields easy-to-interpret designs. This is also indicated by the relatively high discreteness value of all results. For sake of simplicity, we will use the container models in all following illustrations and comparisons of this simple beam example. This is also justified by the high similarity of the container models and both 0-1 interpretations.
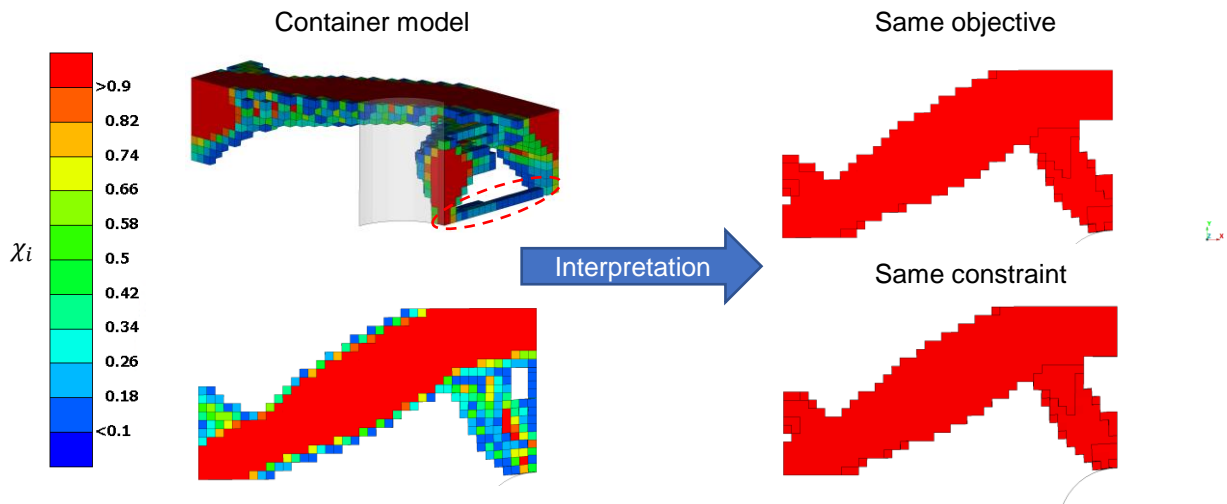
Figure 5.9: Simple beam − container model in final cycle=26 for $v_0 = 40$ m/s (left) as isometric (top) and top view (bottom); corresponding 0-1 interpretations as top view (right) using "same objective" (top) and "same constraint" (bottom) strategies (Triller et al. 2022b)

Table 5.1: Simple beam – optimization results using DiESL and corresponding interpretations (Triller et al. 2022b)

v_0 m/s	$E_{\mathrm{kin},0}$ kJ	Model type	$_*cycle$	ϵ_{v}	ϵ_{s}	$d(_*\boldsymbol{\chi})$ mm	$D(_*\mathbf{x})$	$mass_{\mathrm{b}}(_*\boldsymbol{\chi})$ kg
		Container model	33	0.1	0.9	13.2	0.82	4.17
10	3.3	*Same objective*			0.355	13.3	1.0	4.36
		same constraint			0.37	13.4	1.0	4.33
		Container model	26	0.1	0.9	128.1	0.77	4.16
40	52.6	*Same objective*			0.37	128.0	1.0	4.28
		Same constraint			0.355	127.3	1.0	4.32
		Container model	23	0.1	0.9	113.9	0.79	4.16
150	52.6	*Same objective*			0.4	113.9	1.0	4.36
		Same constraint			0.35	112.3	1.0	4.32

In order to check the plausibility of the results obtained for each load case, a cross validation is performed, where each optimal structure is exposed to the other load cases for which it had not been optimized. Table 5.2 shows the results of this cross validation. It must be read as follows: Each column "Optimum $v_0 = ...$" corresponds to a design obtained by the optimization of the load case with the respective initial velocity v_0. Each row corresponds to the actual conditions applied to each design. Comparing the intrusions in any row, it can be observed that exactly one structure performs best, namely the one that had been optimized for the respective load case. The difference between the best and worst performing structure in each row is sufficiently big to assume that the best solutions are distinct. This confirms the plausibility of each optimization result.

Table 5.2: Simple beam – cross validation: resulting intrusions $d(_*\boldsymbol{\chi})$ for the optimal structures (Fig. 5.11) resulting of the nonlinear dynamic load cases subjected to each of the three load cases (Triller et al. 2022b)

actual v_0 m/s	Optimum $v_0 = 10\,m/s$ $d(_*\boldsymbol{\chi})$ mm	Optimum $v_0 = 40\,m/s$ $d(_*\boldsymbol{\chi})$ mm	Optimum $v_0 = 150\,m/s$ $d(_*\boldsymbol{\chi})$ mm
10	**13.2**	14.0	14.9
40	178.3	**128.1**	142.8
150	136.2	120.9	**113.0**

As a next step, the resulting structures are discussed and compared on a visual basis. As a reference, a linear static load case is introduced, it is illustrated in Fig. 5.10. Instead of the impactor, a static force is imposed in the impact zone. The nodes in the impact zone are connected by rigid elements (RBE2, blue line) to distribute the loading across the entire zone. The optimization problem defined previously in

equation 5.8 and 5.9 is solved for this linear static load case. Note that this is a conventional linear static response optimization purely within OptiStruct and the DiESL method is not applied.
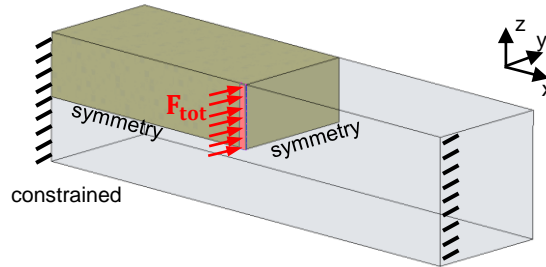
Figure 5.10: Simple beam – linear static load case for comparison with DiESL and ESL results for nonlinear dynamic response optimization (Triller et al. 2022b)

Fig. 5.11 presents the optimized designs of both linear static and all dynamic load cases as iso-surface of the respective container models. Each iso-surface is created for a density $\chi_i \geq 0.4$. For each load case, an isometric (left) as well as a front, top, and rear view (right, top to bottom) are given. For the linear static load case, the most prominent structural part is a diagonal connection between the impact zone and the rear part of the clamping (dashed ellipse). This connection is mainly loaded by compression. The dynamic load case with $v_0 = 10$ m/s contains similar diagonal compression loaded structural members but they are less dominant. The two designs optimized for the higher velocities do not have these members at all. Instead, the tensile loaded connection between the rear part of the impact zone and the front part of clamping (bottom right, dotted ellipse) becomes dominant.

Furthermore, it can be observed that with increasing velocity more mass accumulates in the structure's centre. This indicates the increasing influence of inertia effects. The more mass is accumulated in the impact zone, the higher is the structure's tendency to resist accelerations (Triller et al. 2022b). As mentioned before, this trend has also been observed by Ivarsson et al. 2018, who optimized similar 2D structures using the adjoint method. However, recall that the computational effort using the adjoint method is extremely high and exceeds that of the DiESL method by far. Based on the above findings, we conclude that the DiESL method is able to take inertia effects into account.

As a next step, it is examined how the ESL method performs for the load cases $v_0 = 10$ m/s and $v_0 = 40$ m/s. The container model approach, as detailed before, is used here in the exact way as for the DiESL method. Since the ESL method employs the undeformed mesh geometry for each auxiliary load case, no MMO is performed and there is no need to reconstruct deformed meshes. The resulting container models are illustrated in 5.12. The same iso-surface visualization as before is used. Both results are dominated by the compression loaded connection between the impact zone and the clamping's rear. In table 5.3 the performance indicators of the resulting container models are given. The ESL method needs less cycles to

converge. However, the result's discreteness is smaller for both load cases than for the respective results obtained with the DiESL method. In terms of intrusion, it can be seen that for $v_0 = 10$ m/s the ESL method performs slightly better than the DiESL method. However, the resulting structures are quite similar, both are dominated by the compression loaded member. Since the intrusion for this load case is relatively small compared to the structure's overall dimensions, the DiESL method obviously draws no substantial benefits from employing the deformed mesh geometries and from following the displacement path incrementally (Triller et al. 2022b). For the initial velocity $v_0 = 40$ m/s the intrusion rises significantly, and here the DiESL method outperforms ESL by far. The deformed container models are illustrated in Fig. 5.13 at the time of maximum intrusion. The compression loaded members created by the ESL method buckle and cause an excessive intrusion, this does not happen in the tensile loaded DiESL design. Obviously, the ESL method is not able to incorporate the geometric nonlinearities and inertia effects as DiESL does.
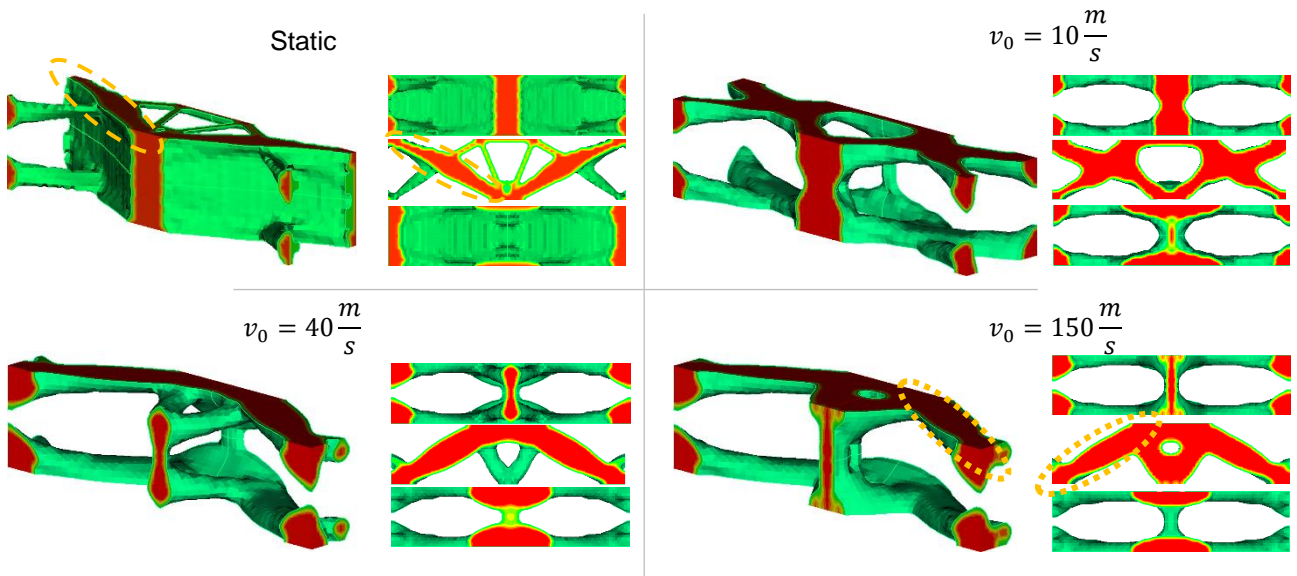
Figure 5.11: Simple beam − resulting container model in iso-surface visualization ($\chi_{\text{iso}} = 0.4$) for linear static load case (top left) and using DiESL: $v_0 = 10$ m/s (top right), $v_0 = 40$ m/s (bottom left), and $v_0 = 150$ m/s (bottom right) (Triller et al. 2022b)

Table 5.3: Simple beam − optimization results using ESL (Triller et al. 2022b)

v_0 m/s	$_*cycle$	ϵ_{v}	ϵ_{s}	$d(_*\boldsymbol{\chi})$ mm	$D(_*\mathbf{x})$	$mass_{\text{b}}(_*\boldsymbol{\chi})$ kg
10	10	0.1	0.9	12.9	0.65	4.16
40	21	0.1	0.9	233.1	0.69	4.17
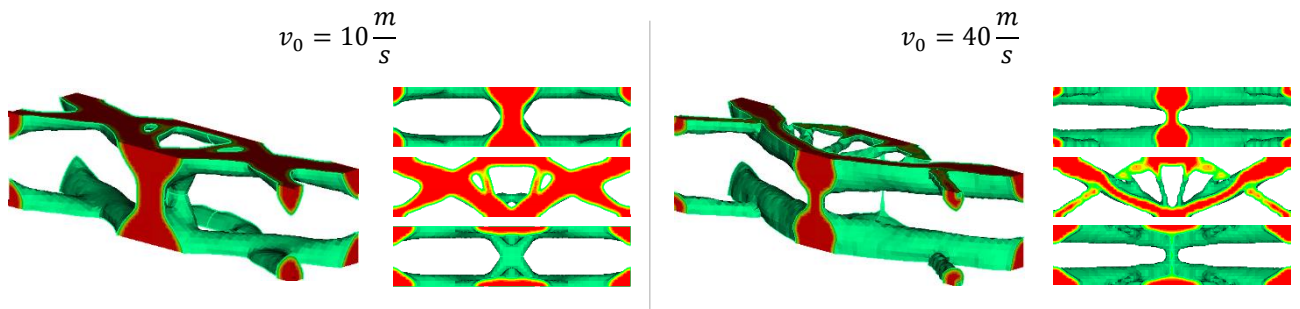
Figure 5.12: Simple beam – resulting container model in iso-surface visualization ($\chi_{\text{iso}} = 0.4$) using ESL for $v_0 = 10$ m/s (left) and $v_0 = 40$ m/s (right) (Triller et al. 2022b)
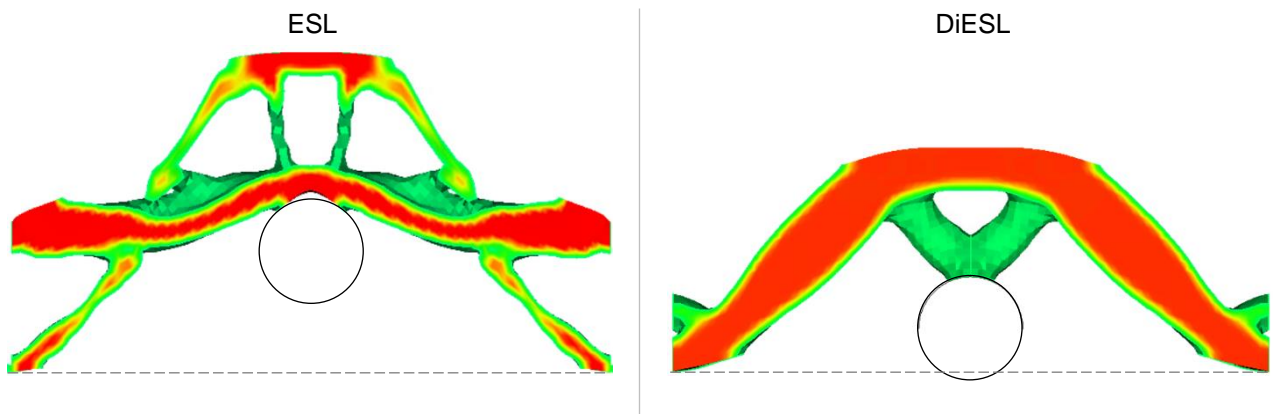
Figure 5.13: Simple beam – deformed container model in iso-surface visualization ($\chi_{\text{iso}} = 0.4$) using ESL (left) and DiESL (right) for $v_0 = 40$ m/s (Triller et al. 2022b)

5.2.2 Rocker Profile

The next example is a more practical simplified side impact example, which original has been used for testing the GHT approach (Ortmann and Schumacher 2013; Ortmann 2015). As illustrated on the left side of Fig. 5.14, this is an extruded rocker profile and parts of a crossbeam with an initial velocity $v_0 = -8.05556\,m/s$ in y-direction colliding with a rigid pole. The GHT has been used to optimize the extruded rocker profile. The intrusion of the pole into the rocker is minimized, while the rocker's mass $mass_\mathrm{R}$ is constrained. Additionally, the rocker's bending stiffness k_B and torsional stiffness k_T are constrained. For this purpose, two additional linear static load cases are incorporated into the optimization. These are illustrated on the right side of Fig. 5.14. Here, the rocker is clamped at one end and subjected to a force of 1 kN and torque of 0.5 kNm for the bending and torsional load case, respectively. Both loads are applied to a central node that is rigidly connected to all nodes around the circumference of the rocker's end. The initial rocker design has no support structures inside, the outer profile thickness is 3.5 mm for each panel. It yields an initial deflection $d_\mathrm{B,ini} = -0.1932$ mm and an initial rotation $r_\mathrm{T,ini} = 1.773$ mrad for the bending and torsional load case, respectively. The optimized design must have at least half the stiffness of the initial unfilled profile for both linear static load cases. Furthermore, the thicknesses ζ_i of the resulting profile structure are constrained to be between 1.6 and 3.5 mm. The optimization problem is therefore defined as:

$$\min d\left(\mathbf{x}\right); \tag{5.10}$$

subject to

$$mass_\mathrm{R}\left(\mathbf{x}\right) \leq 2.801\,\mathrm{kg}; \tag{5.11}$$

$$k_\mathrm{B}\left(\mathbf{x}\right) = \frac{d_\mathrm{B}(\mathbf{x})}{d_{\mathrm{B},ini}} \geq 0.5 \quad \text{(linear static)}; \tag{5.12}$$

$$k_\mathrm{T}\left(\mathbf{x}\right) = \frac{r_\mathrm{T}(\mathbf{x})}{r_{\mathrm{T},ini}} \geq 0.5 \quad \text{(linear static)}; \tag{5.13}$$

$$1.6\,\mathrm{mm} \leq \zeta_i \leq 3.5\,\mathrm{mm} \tag{5.14}$$

The application of the GHT in this case is advantageous with respect to pre-processing and interpretability since the topology of the extruded rocker profile can be described using 2D graphs. The shell structures described by these graphs can then directly be modeled and simulated. If a density-based approach, as in DiESL, is applied some obstacles arise. Then, the rocker profile needs to be filled with solid elements. These elements need to be sufficiently small to model the targeted profile structure with thicknesses in the range of 1.6 to 3.5 mm. The minimum member size option MINDIM in OptiStruct is used to support this topic. However, OptiStruct has a limitation on the smallest value for MINDIM, it must be at least two times the average element size MINDIM$\geq 2 \cdot \bar{T}$. Hence an average element size $\bar{T} = 0.8$ mm would be necessary to realize structures with a minimal thickness of 1.6 mm. Fig. 5.15 shows the rocker filled with solid elements from a side view perspective using two different averaged element sizes. On the left side, the averaged element size in the yz-plane is $\bar{T}_\mathrm{yz} = 5$ mm. This average element size has been used for the

outer profile shell structure in the original publication (Ortmann and Schumacher 2013). On the right side of Fig. 5.15 the averaged element size $\bar{T}_{yz} = 1.6$ mm is employed, which can be considered as a very fine discretization already. Employing regular elements with an average edge length of approximately $\bar{T} = 1.6$ mm in each dimension x, y, and z would result in more than $2.400.000$ elements. Cutting the average element length $\bar{T}$ in half would lead to an eightfold increase in the number of elements. Reducing $\bar{T}$ further than 1.6 mm is therefore inconceivable, since the handling of $2.400.000$ elements already requires the computation on an HPC. This is complicated by the fact that no HPC was available at the time this work has been done.
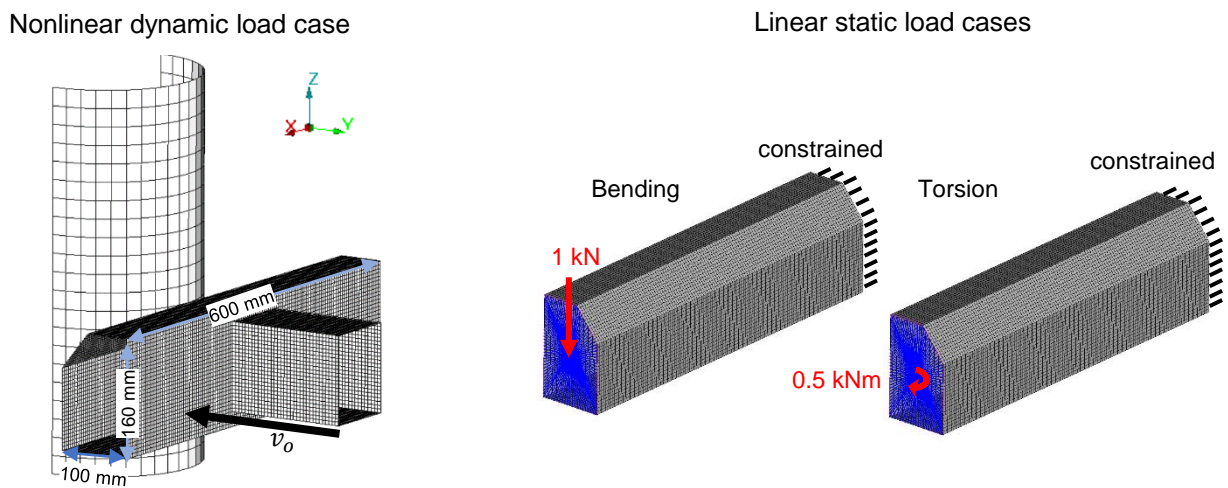
Figure 5.14: Extruded Rocker Profile – Nonlinear dynamic and linear static load cases
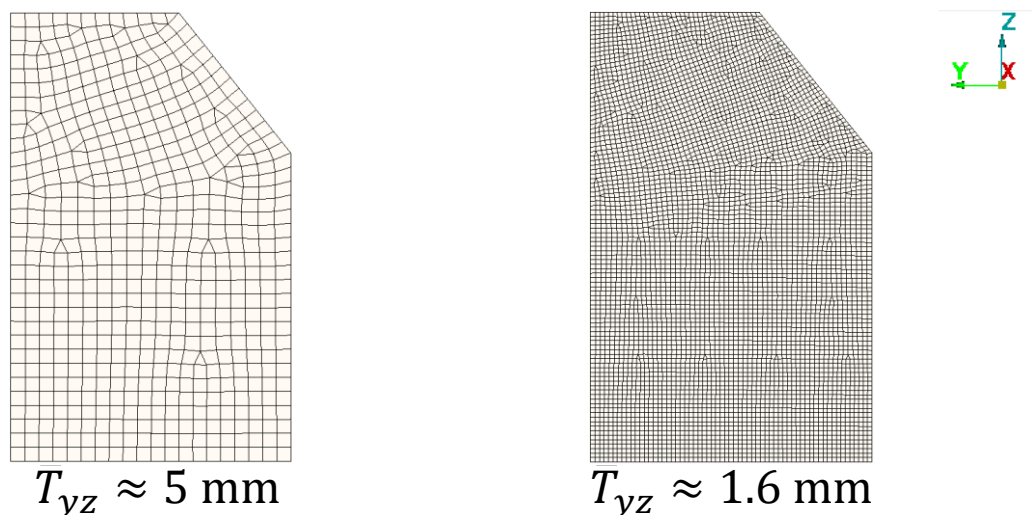
Figure 5.15: Extruded Rocker Profile – Finite element discretization of yz-plane using the average element size $\bar{T}_{yz} = 5$ mm and $\bar{T}_{yz} = 1.6$ mm

For the above reasons, the following two related issues need to be solved before optimizing this example:

1. The number of elements must be reduced according to the available computing capacity: a desktop computer with 48 CPU: Intel(R) Xeon(R) Silver 4116; CPU speed 2.1 GHz; 64 GB RAM.

2. The structural behavior of profile members with a thickness of 1.6 mm must be modeled using larger solid elements.

Reducing the number of elements

The following changes are made to the shell model compared to Ortmann and Schumacher 2013 before creating the solid topology design space, they are illustrated in Fig. 5.16. First, symmetry conditions are employed and only half of the rocker is simulated. It is shown on the left side of Fig. 5.16. Note that the right side of that figure shows the right half of the original full model for comparison. Secondly, the shell element aspect ratio is varied for the outer profile structure following this consideration: Most of the deformation occurs in the yz-plane, deformations in x-direction are negligible. Therefore, the mesh must be fine in the yz-plane and may be coarse in x-direction. Furthermore, deformations are largest in the middle of the rocker where the pole is hit, while they are minuscule at the far end of the rocker. Therefore, the mesh may be even coarser in x-direction near the far end. This is implemented with a varying element length in x-direction. The resulting aspect ratios of elements $T_x : T_{yz}$ are approximately 3 in the middle (black dashed frame) and approximately 20 at the far end (red dashed frame). These two changes allow for a relatively small average element size of $\bar{T}_{yz} = 1.6$ mm in the yz-plane. Then, the number of elements for the rocker (outer shell and solid design space) is 121864. This can be simulated on a desktop computer. To assure comparability between the original model and the modified, the maximum intrusion of both are compared visually and quantitatively. Fig. 5.16 shows both deformed models at the time of maximum intrusion (recall that only the right half of the original full model is shown). Also, in table 5.4 the value of the maximum intrusion d is given. There are only small differences, and the modified model is considered to give valid results.

Table 5.4 also reports the overall averaged element size $\bar{T}$, the averaged element size $\bar{T}_{yz}$ in yz-plane, and the lower bound of the parameter MINDIM imposed by OptiStruct. Since an extruded profile is optimized here, the densities must be constant in x-direction. The OptiStruct extrusion constraint is defined to obtain such constant cross-sections in z-direction. Then, all elements lying in a row in z-direction are combined to a group and assigned to the same design variable, such that the optimization problem effectively is reduced to a 2D problem. Consequently, it would be logical to use the average element size in the yz-plane $\bar{T}_{yz}$ to calculate the MINDIM parameter's lower bound. Unfortunately, this is not the case and OptiStruct uses the overall average element size $\bar{T}$, which can be considered an unnecessary limitation on MINDIM. Hence, the minimum width of the forming structures is 6.4 mm using the half model with mixed aspect ratio.
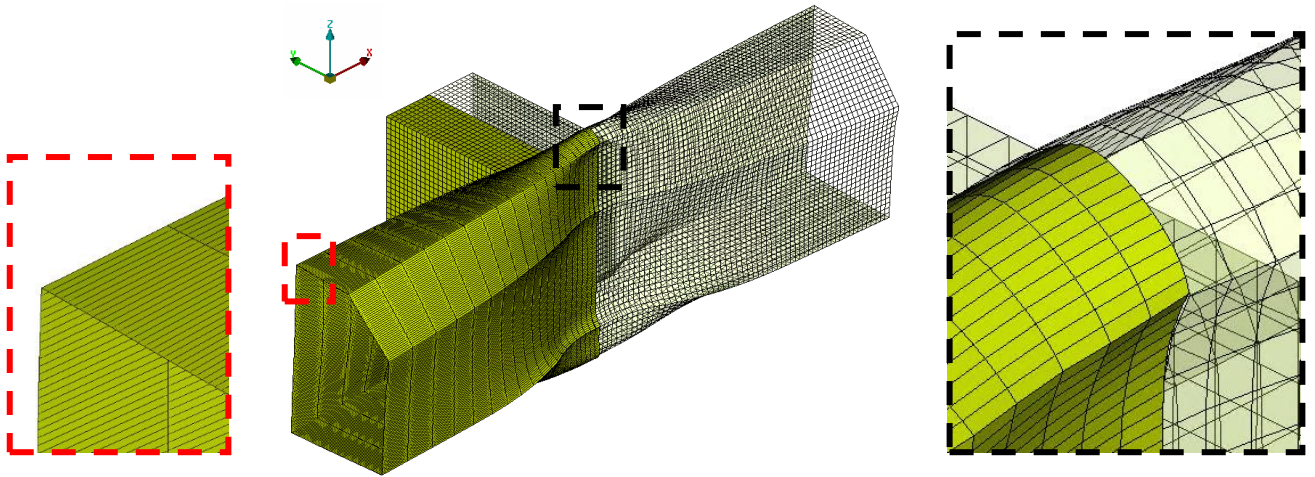
Figure 5.16: Extruded Rocker Profile – FE-mesh and deformation of full model ($\bar{T} = 5$mm) and half model with mixed aspect ratio ($\bar{T}_{\text{yz}} = 1.6$mm) for an outer profile thickness $\zeta_{\text{outer}} = 3.5$mm

Table 5.4: Extruded Rocker Profile – Intrusion of pole into rocker employing different meshs and symmetry

Mesh	# Elements Solids included	Maximum Intrusion d	averaged Element Size		Lower Bound MINDIM
			$\bar{T}$	$\bar{T}_{\text{yz}}$	
		mm	mm	mm	mm
full	86244	68.80	5	5	10
half	43122	68.78	5	5	10
mixed aspect ratio	121864	69.26	3.2	1.6	6.4

Modeling sub-scale structures using solid elements

The second challenge is to model the stiffness of thin structures with a thickness ζ by structures with a greater thickness Z. This is required because the minimum permissible thickness of the structures in the design space MINDIM $= 6.4$ mm is greater than the minimum profile thickness ζ^{L} defined in the optimization problem in equation 5.10 to 5.14. This is illustrated in Fig. 5.17.
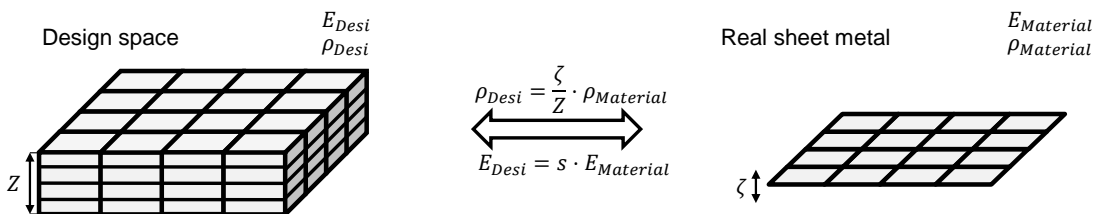
Figure 5.17: Extruded Rocker Profile – Scaling of solid element material properties to model sub-scale sheet metal with thickness ζ

The subscript *Desi* denotes all measures in the design space and the subscript *Material* the measures of the real sheet metal to be modeled. To achieve mass equality in both models, the density in the design space must be adjusted as follows:

$$\rho_{Desi} = \frac{\zeta}{Z} \cdot \rho_{Material}. \tag{5.15}$$

Please note that the properties with the subscript *Desi* cover both the design and the analysis domain and should not be confused with the adaptions regarding the SIMP approach. The same applies for the mechanical properties, the Young's modulus E_{Desi}, the yield stress $\sigma_{\mathrm{y,Desi}}$ and the hardening modulus $E_{\mathrm{H,Desi}}$. These also need to be scaled in the design space to account for the thickness difference between ζ and Z. For this purpose, we define the scaling factor s:

$$E_{\mathrm{Desi}} = s \cdot E_{\mathrm{Material}}, \tag{5.16}$$

$$\sigma_{\mathrm{y,Desi}} = s \cdot \sigma_{\mathrm{y,Material}}, \tag{5.17}$$

$$E_{\mathrm{H,Desi}} = s \cdot E_{\mathrm{H,Material}}. \tag{5.18}$$

In the following, the scaling factor s is determined empirically employing a representative design with a horizontal connection member of variable thickness ζ (Fig. 5.18). The deformation behavior of both rocker and crossbeam is examined for both representations of the member: real sheet metal representation using shell elements with thickness ζ and design space representation using solids with an overall thickness of Z. The objective is to determine a scaling factor s for which the deformation behavior is similar for both representations. This is done both visually by comparing the deformation behavior and numerically by comparing the values of maximum intrusion.
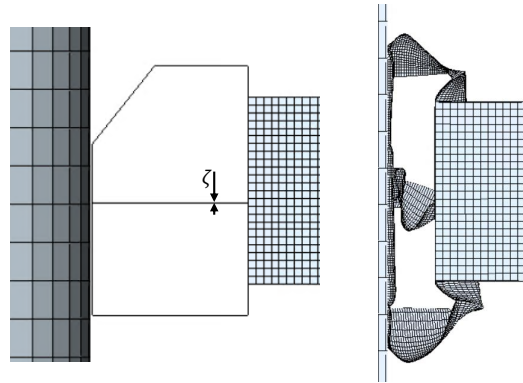
Figure 5.18: Extruded Rocker Profile – example used to determine scaling factor s: undeformed (left), deformation at time of maximum intrusion for $\zeta = 1.6$ mm (right)

In a first attempt, the design space representation is correlated to the real sheet metal representation according to the following consideration: The mesh of the design space has an average element size $\bar{T}_{\mathrm{yz}} = 1.6$ mm in the modified model. According to the limitation in OptiStruct, the minimum member size is MINDIM $= 6.4$ mm (table 5.4). This value is designated to represent the lower bound of the structural

members $\zeta^{\mathrm{L}} = 1.6$ mm according to equation 5.14. Consequently, MINDIM/$\zeta^{\mathrm{L}} = 4$ rows of solids are employed to model the smallest sheet thickness $\zeta^{\mathrm{L}} = 1.6$ mm. These solids are distributed symmetrically around the center line of the horizontal connection member. Note that for that reason, only even numbers of solid rows (4, 6, 8, 10) were chosen.

Fig. 5.20 shows the rocker's deformation for both representations shell (top row) and solid (bottom row) and for different thicknesses $\zeta = Z/4$ of the horizontal connection member (columns). Note that each solid member model in the bottom row represents the shell model with the given thickness ζ in the same column. Note also that the four thickness values cover the entire valid range according to equation 5.14. Their values are determined by the requirement of even numbers of corresponding solid rows. This comparison shows visually that both the maximum intrusions and the deformation behavior of the rocker's outer profile structure are represented good by each solid connection member model. However, the deformation of the connection member itself cannot be approximated very well. Furthermore, for the thicknesses $\zeta = 3.2$ mm and $\zeta = 4.0$ mm, the deformation of the crossbeam does not match well. A possible reason for the mismatches is the thickness ratio $Z/\zeta = 4$ being too large.

Fig. 5.19 plots the maximum intrusion d over the thickness ζ and $Z/4$ for a number of simulation runs using different scaling factors s employed to model the solid connection member. As can be seen, the maximum intrusion of the shell elements (blue in Fig. 5.19) is fitted best using the scaling factor $s = 0.05$. The deformed rocker structures for this scaling factor are shown in Fig. 5.20.
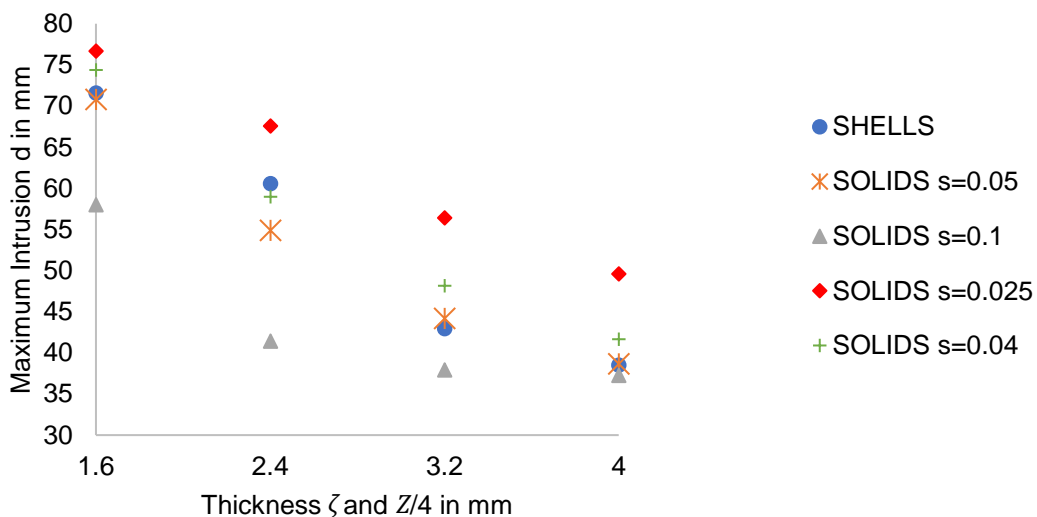
Figure 5.19: Extruded Rocker Profile – maximum intrusion depending on the thickness ζ and $Z/4$ using shell and solid representation of the connection member for different scaling factors s. Four rows of solids with a total thickness $Z = 6.4$mm correspond to the shell thickness $\zeta = 1.6$mm (Thickness ratio $Z/\zeta = 4$)
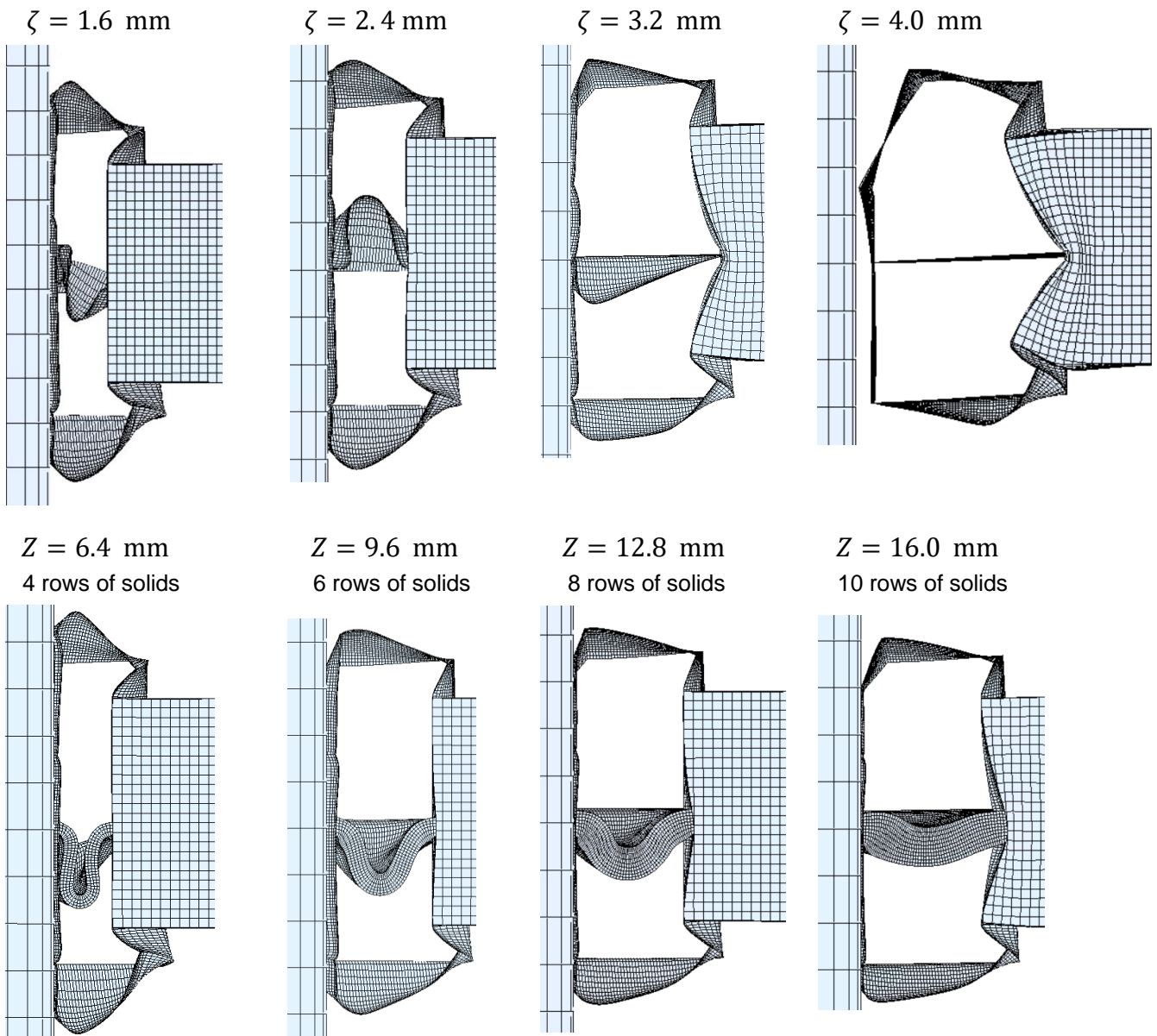
Figure 5.20: Extruded Rocker Profile – Deformed structures at time of maximum intrusion using connection member representation with shells of thickness ζ (top) and solids with a total thickness of Z and scaled stiffness using $s = 0.05$ (bottom). Four rows of solids with a total thickness $Z = 6.4$mm correspond to the shell thickness $\zeta = 1.6$mm (Thickness ratio $Z/\zeta = 4$)

A second attempt aimed at a better match in the resulting deformation behavior between shell and solid representation of the connection member. The previous consideration has been adapted to obtain thinner members, i.e. with less rows of solids. This can be achieved by ignoring the MINDIM restriction and defining 2 rows of solids instead of 4 to represent the smallest sheet thickness $\zeta^{\mathrm{L}} = 1.6$ mm. The new thickness ratio according to this approach is then $Z/\zeta = 2$. As a consequence, it is not possible to represent the minimum sheet thickness $\zeta^{\mathrm{L}} = 1.6$ mm by corresponding solid structures using a 0-1 design. The minimum sheet thickness of 1.6 mm can only be modeled using intermediate densities. Note that in this attempt, only 2, 4, and 6 numbers of rows are needed to cover the permitted range for the thickness ζ.

Fig. 5.21 plots the maximum intrusion d over the thicknesses $\zeta = Z/2$ according to the second attempt for different scaling factors s. The best approximation is obtained using the scaling factor $s = 0.2$. As before, the deformed rocker structures are shown in Fig. 5.22 for this best scaling factor. The deformation plots suggest that with this attempt both the crossbeam and the outer profile are approximated better for all thicknesses when compared to Fig. 5.20. However, the deformation of the connections member still cannot be approximated perfectly.

In the following, optimization results will be computed for both scaling factors. The results will ultimately be used to evaluate which scaling factor is more suitable for modeling sub-scale structures.
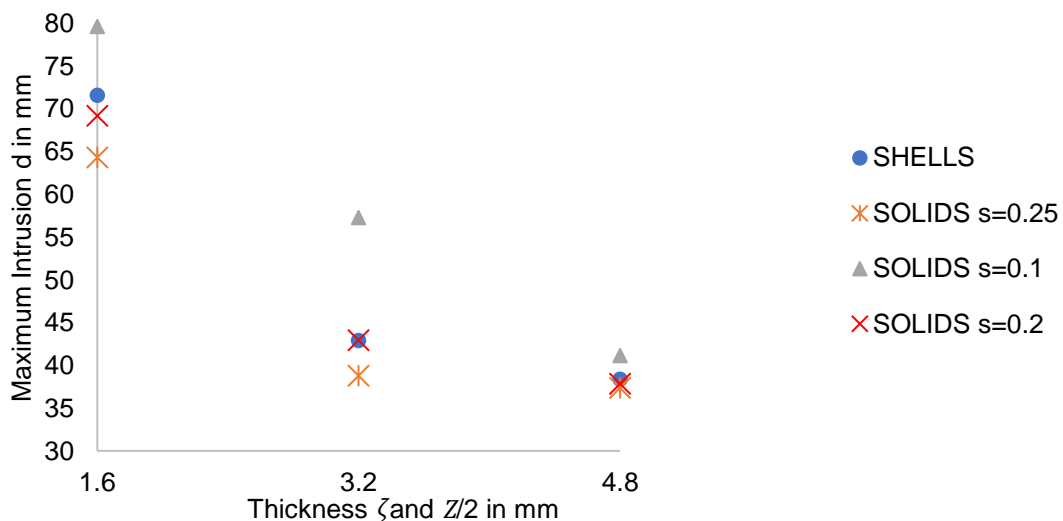
Figure 5.21: Extruded Rocker Profile − maximum intrusion depending on the thickness ζ and $Z/2$ using shell and solid representation of the connection member for different scaling factors s. Two rows of solids with a total thickness $Z = 3.2$mm correspond to the shell thickness $\zeta = 1.6$mm (Thickness ratio $Z/\zeta = 2$)

$\zeta = 1.6$ mm $\qquad$ $\zeta = 3.2$ mm $\qquad$ $\zeta = 4.8$ mm

$Z = 3.2$ mm $\qquad$ $Z = 6.4$ mm $\qquad$ $Z = 9.6$ mm
2 rows of solids $\qquad$ 4 rows of solids $\qquad$ 6 rows of solids
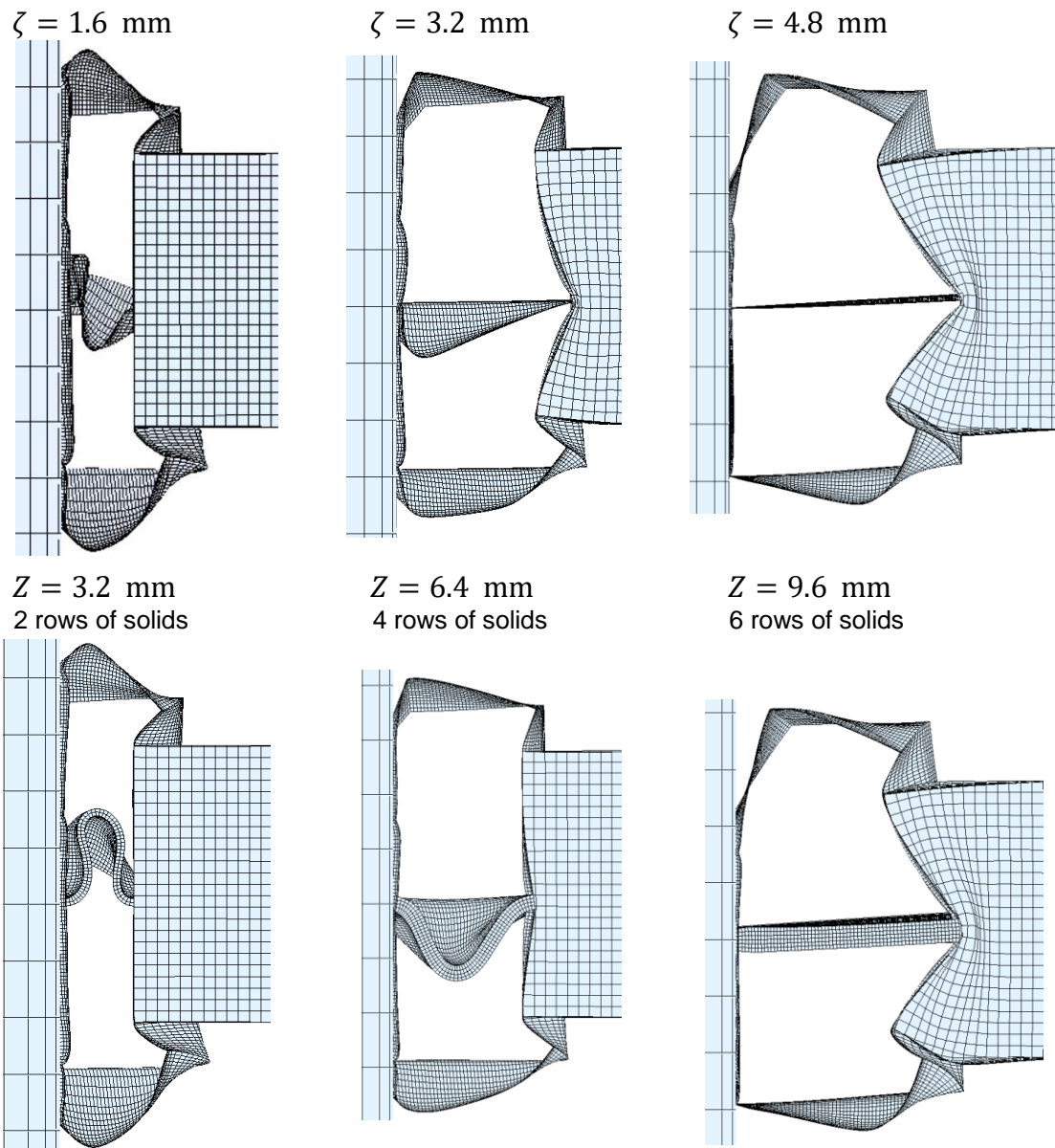
Figure 5.22: Extruded Rocker Profile – Deformed structures at time of maximum intrusion using connection member representation with shells of thickness ζ (top) and solids with a total thickness of Z and scaled stiffness using $s = 0.2$ (bottom). Two rows of solids with a total thickness $Z = 3.2$mm correspond to the shell thickness $\zeta = 1.6$mm (Thickness ratio $Z/\zeta = 2$)

Detailed description of Rocker FE-model

In addition to the previously described specifications of the considered load cases, according to Ortmann 2015 there are some further characteristics which are detailed in the following. Furthermore, the applied boundary conditions for enforcing symmetry and all necessary adoptions in the model used in the design domain are explained. On the left side of Fig. 5.23 the rocker's outer profile structure, the crossbeam, the rigid pole as well as all applied boundary conditions are illustrated. As described before, only half of the rocker is modeled. This is accomplished by applying SPCs at the rocker's and crossbeam's center. At the rocker's other end the translational degrees of freedom in z-direction are locked to prevent the rocker from buckling in the z-direction. Since this model is only a substructure of a car's overall body, additional mass and kinetic energy is added by a rigid wall with a mass of 42.5 kg, which has the same initial velocity $v_0 = -8.05556$ m/s in y-direction[3]. This rigid wall faces the crossbeam at the rear end. Contact between the rigid wall and the crossbeam as well as all remaining surfaces is defined in the nonlinear dynamic model. Additionally, a large portion of the crossbeam is guided by locking all degrees of freedom except the translation in y-direction. This is intended to achieve a similar deformation behavior as in the full car. The rocker and the crossbeam are made of aluminum (Young's modulus: $E = 70$ GPa, density: $\rho = 2700 \, \text{kg/m}^3$, Poison's ratio: $\nu = 0.33$), which is modeled with a piecewise linear material (Fig. 5.23, right) in the nonlinear dynamic model.
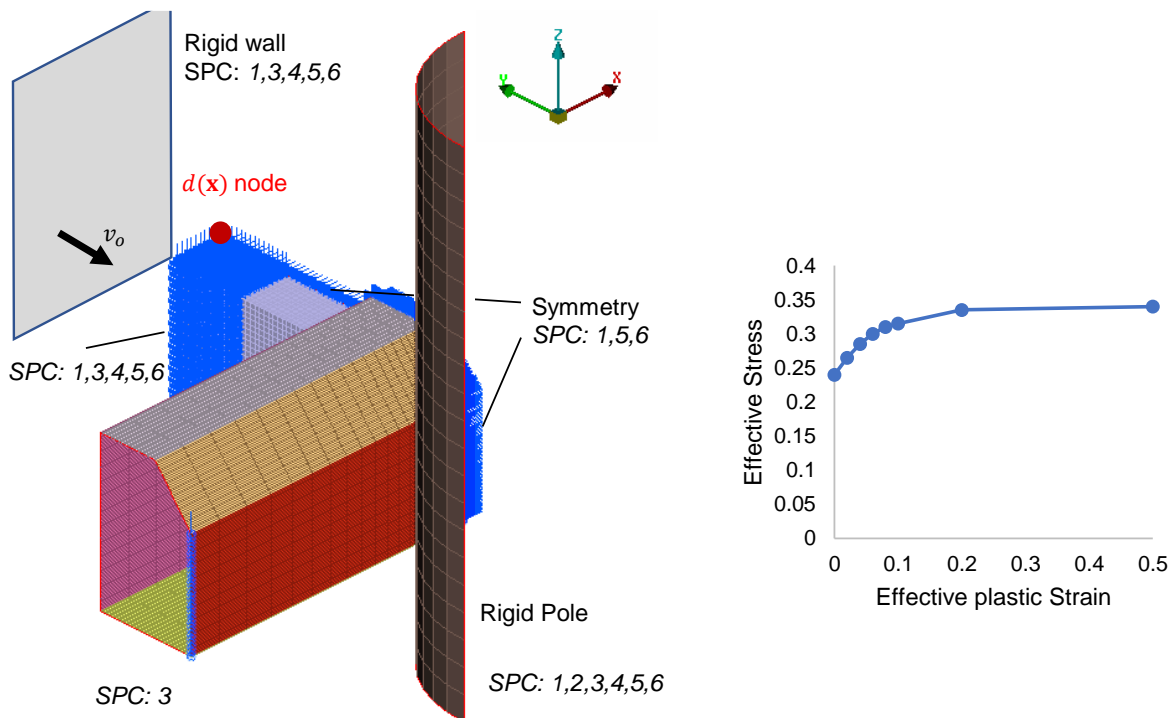
Figure 5.23: Extruded Rocker Profile – FE-model and applied boundary conditions (left); piecewise linear material model (right)

---

[3]Due to the symmetry conditions the rigid wall's mass is half compared to Ortmann 2015

Except for the rigid wall, the same model is employed in the design domain. The Young's moduli are not adopted locally, which means $E = 70$ GPa is applied for all elements. In contrast to all side impact examples examined before, the rigid pole is fixed here and the initial velocity is applied to the structure. Therefore, it is necessary to model the pole and its contact with the rocker in the design domain as well. Otherwise, the rocker would be unbound and the DiESLs would cause infinite displacements in y-direction. For the same reason, the contact cannot be modeled as in the previous examples. There, the stiffness of contact elements had been set to minimal values to eliminate their impact on the remaining structure. Here, very stiff contact elements between the pole and the rocker are required, to ensure the rocker is bound to the pole. This is accomplished by setting the parameter GPAD $= 1.5$ mm in the contact definition between rocker and pole in OptiStruct. In doing so, closed and hence very stiff contact elements are created between the rocker's nodes and the pole's surface whenever their distance is smaller than 1.5 mm. This is not a realistic contact definition, but is necessary to keep the DiESL method running. In this case, it is possible that the unrealistic contact elements have an influence on the optimization result. A node at the middle of the crossbeam facing the rigid wall is used to measure the intrusion $d(\mathbf{x})$ (Fig. 5.23, red dot).

Optimization Strategies

The technique described above for modeling sub-scale structures imposes a new challenge on the interpretation of the optimization results. The resulting density field needs to be interpreted and translated into a shell structure design. This means the interpretation strategies introduced in section 5.2.1 cannot be employed here. The challenge here is to identify locations where shell structures should be placed and to determine their thickness. To address this challenge, two different optimization strategies are pursued in the following. Both can be split into two phases, conception and fine-tuning. In the conception phase, the topology of the rocker profile is optimized and interpreted afterwards to obtain a shell structure design, this is referred to as conceptional design. The fine-tuning phase aims at optimizing the individual thicknesses of the shell members created in the conceptual design. The interpretation of the density field obtained from topology optimization is thus simplified, since the thicknesses of the representative shell structure members do not have to be determined manually.

The first strategy is illustrated in Fig. 5.24. It starts with a topology optimization of the rocker's inner profile. The shell thickness of the outer profile is kept constant $\zeta_{\text{outer}} = 1.6$ mm during topology optimization. It turned out that the linear static load cases have no influence on the optimization's outcome. Consequently, they are omitted during the conception. This means a relaxed optimization problem is solved here, where the intrusion $d(\mathbf{x})$ is minimized and the mass is constrained $mass_{\text{R}} \leq 1.400$ kg [4]. After the conceptual design has been derived, the structure is fine-tuned. Then, the linear static load cases are included for verification and the optimization problem as defined in equation 5.10 and following is solved. The initial

---

[4] Compared to Ortmann and Schumacher 2013 only half the mass $mass_{\text{R}}$ is used here to attribute the employed symmetry condition.

sheet thicknesses are set to $_0\zeta_i = 2.0$, this also includes the thicknesses of the outer rocker profile which are optimized as well during the fine tuning.
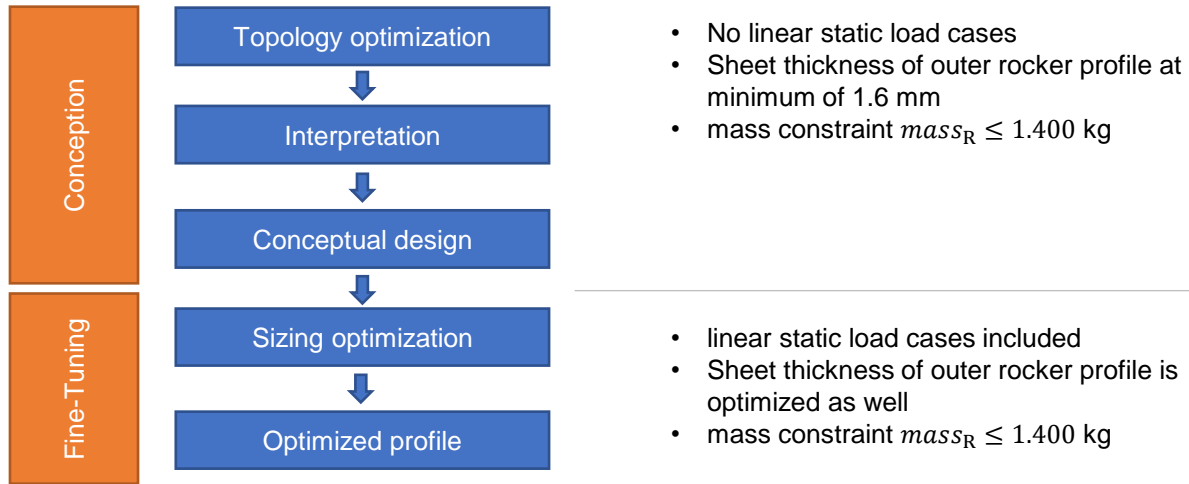
Figure 5.24: Extruded Rocker Profile – Optimization Strategy 1: pure topology optimization with subsequent sizing optimization of interpreted topology

The second strategy differs only in the conception phase from strategy 1 as illustrated in 5.25. Here, the topology is derived in two steps. First, a pure topology optimization is performed with an adapted mass constraint which is reduced by the factor 0.6 to save some mass for the second step. With less mass granted the optimizer is expected to create less connection members inside the profile. The following interpretation is optimized again in a second step. This is a combined sizing and topology optimization. For this purpose the previously derived profile design is filled with solids. The topology of the solids is then optimized, while simultaneously optimizing the thicknesses of the derived inner profile structure. The initial thicknesses is set to $_0\zeta_{i,\text{inner}} = 2.0$ mm. In this combined optimization the original mass constraint is used and the outer profile's thickness is kept constant $\zeta_{\text{outer}} = 1.6$ mm. This strategy aims at reducing uncertainties involved during the interpretation. The optimizer now can react on previously made decisions and can mitigate possible misinterpretations in the second combined optimization.

In all following topology optimizations, the initial densities are set such that the respective mass constraint is active at the beginning. Due to the high number of elements only ten ESL times are used for all optimizations. The ESL times are selected adaptively in each cycle by fitting the nonlinear contact force curve between rocker and pole.
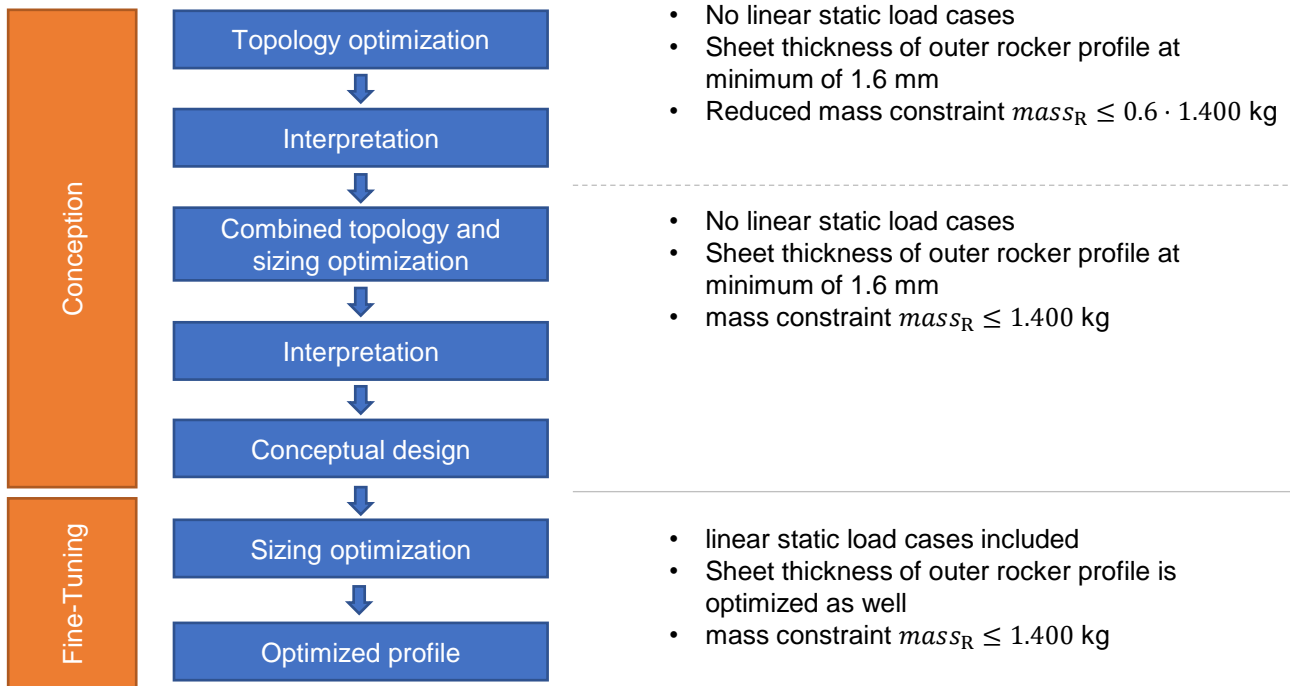
Figure 5.25: Extruded Rocker Profile – Optimization Strategy 2: first pure topology optimization then combined topology/sizing optimization in conception phase

Results

Four optimizations were conducted, they are the combination of the two strategies with the two thickness ratios $Z/\zeta = 4$ and $Z/\zeta = 2$ (using scaling factors $s = 0.05$ and $s = 0.2$, respectively). First, strategy 1 using thickness ratio $Z/\zeta = 4$ and scaling factor $s = 0.05$ is employed. In Fig. 5.26 the results of each step are illustrated. The left side shows the resulting density field from the topology optimization. As can be seen, a discrete structure has evolved. This is also indicated by the high discreteness index $D(_*\mathbf{x}) = 0.84$. The resulting density field suggests to use two major connections between the front and rear of the rocker. They are located close to the top and bottom end of the crossbeam, respectively. The shell member interpretations are positioned such that they are approximately in the middle of the areas of high-density elements. This interpretation has been performed manually, no additional iterations have been performed and no competing interpretations have been evaluated. The interpretation is depicted on the left side by dotted white lines and shown separately in the middle of Fig. 5.26. The result of the sizing optimization is depicted on the figure's right side. The thickness of both main connection members are at the upper bound of 3.5 mm. The smaller parts seem to be less important since their thickness is at the lower bound of 1.6 mm. The outer profile has a thickness of $\zeta_{\text{outer}} \approx 2.0$ mm.
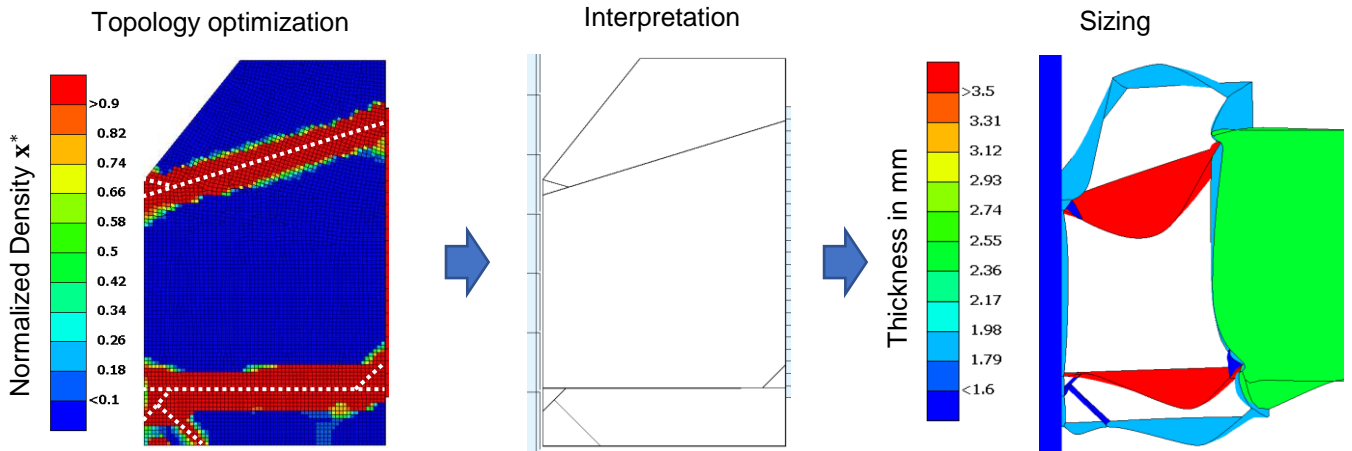
Figure 5.26: Extruded Rocker Profile – Optimization results and corresponding interpretations employing strategy 1 and thickness ratio $Z/\zeta = 4$ (respective scaling factor $s = 0.05$)

In the same manner as described before, Fig. 5.27 shows the results of strategy 1 in combination with the thickness ratio $Z/\zeta = 2$ and scaling factor $s = 0.2$. As to be expected, the resulting structure is much more filigree than the one for $Z/\zeta = 4$ and therefore easier to interpret. However, the resulting structure is also less discrete, which is reflected by $D(_*\mathbf{x}) = 0.68$. The optimizer seems to use the intermediate densities to model structural parts with thicknesses less than $\zeta = 3.2$ mm. This is confirmed by the outcome of the sizing optimization, where a similar thickness distribution is derived as before for $Z/\zeta = 4$.
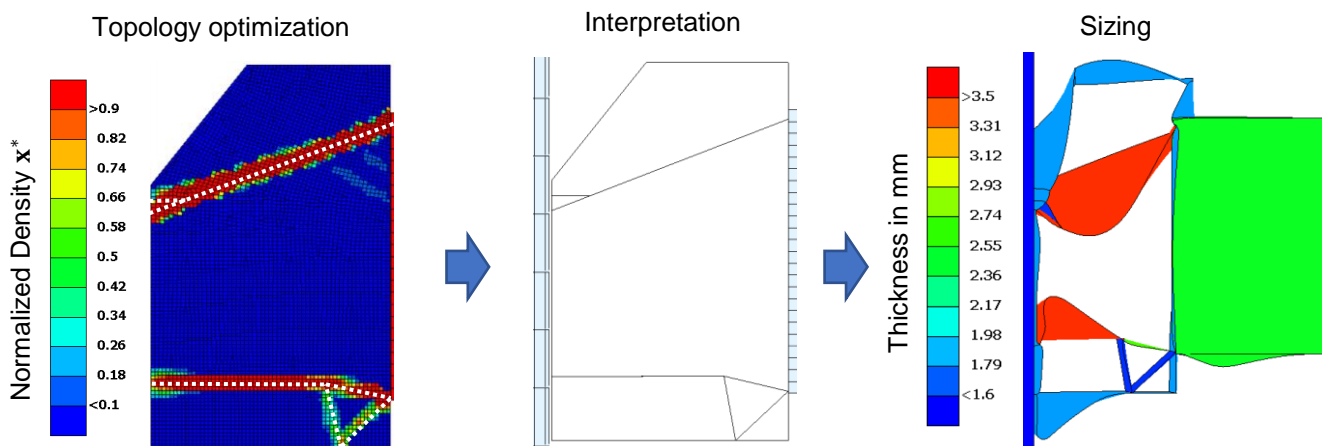
Figure 5.27: Extruded Rocker Profile – Optimization results and corresponding interpretations employing strategy 1 and thickness ratio $Z/\zeta = 2$ (scaling factor $s = 0.2$)

Fig. 5.28 shows the results of the second strategy employing $Z/\zeta = 4$ and $s = 0.05$. The strategy includes an additional topology optimization. The results of the optimizations are shown in the top row and the interpretations in the bottom row. Like before, the interpretations are also indicated in the density fields by white dotted lines. As can be seen, during the first topology optimization, a large connection member forms from the lower end of the crossbeam to the front of the rocker. Accordingly, it appears to have a greater influence on the intrusion than the upper connection member in the previous examples. The upper connection is formed during the subsequent combined sizing and topology optimization. However, the thickness of the lower connection does not reach the upper limit of 3.5 mm, as indicated by the previous results. This contrasts with the resulting thickness distribution in the subsequent sizing optimization. Here, the results are again very similar to those of the previous sizing optimizations. During both topology optimizations, again a relatively high discreteness is reached. The first optimization yields $D({}_*\mathbf{x}) = 0.82$ and the second $D({}_*\mathbf{x}) = 0.85$.
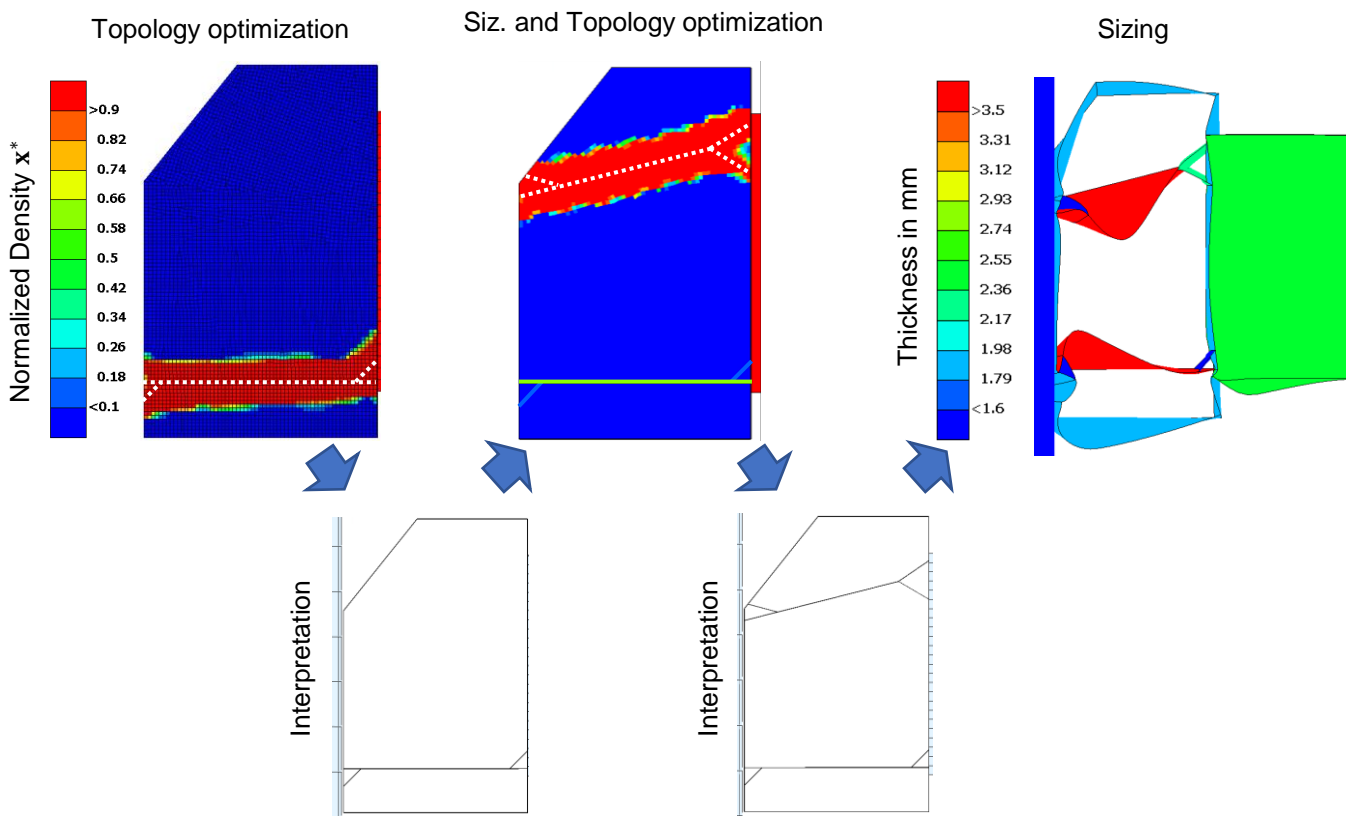
Figure 5.28: Extruded Rocker Profile – Optimization results and corresponding interpretations employing strategy 2 and thickness ratio $Z/\zeta = 4$ (scaling factor $s = 0.05$)

Fig. 5.29 shows the results of the second strategy in combination with $Z/\zeta = 2$ and $s = 0.2$. Again, all optimization results are shown in the top row and the corresponding interpretations below. The previous findings are reconfirmed here: Using $Z/\zeta = 2$, much more filigree structures form. The resulting

discreteness values also indicate that intermediate densities are utilized by the optimizer to circumvent the MINDIM constraint. The first optimization yields $D(_*\mathbf{x}) = 0.55$ and the second $D(_*\mathbf{x}) = 0.7$. Again, during the first topology optimization only the lower connection member forms, and the upper connection forms in the second step. The resulting thickness distribution derived from sizing again is very similar to the previous one. The fact that all four optimizations yield these same distinct load paths can be seen as a confirmation of the optimality and robustness of this design.
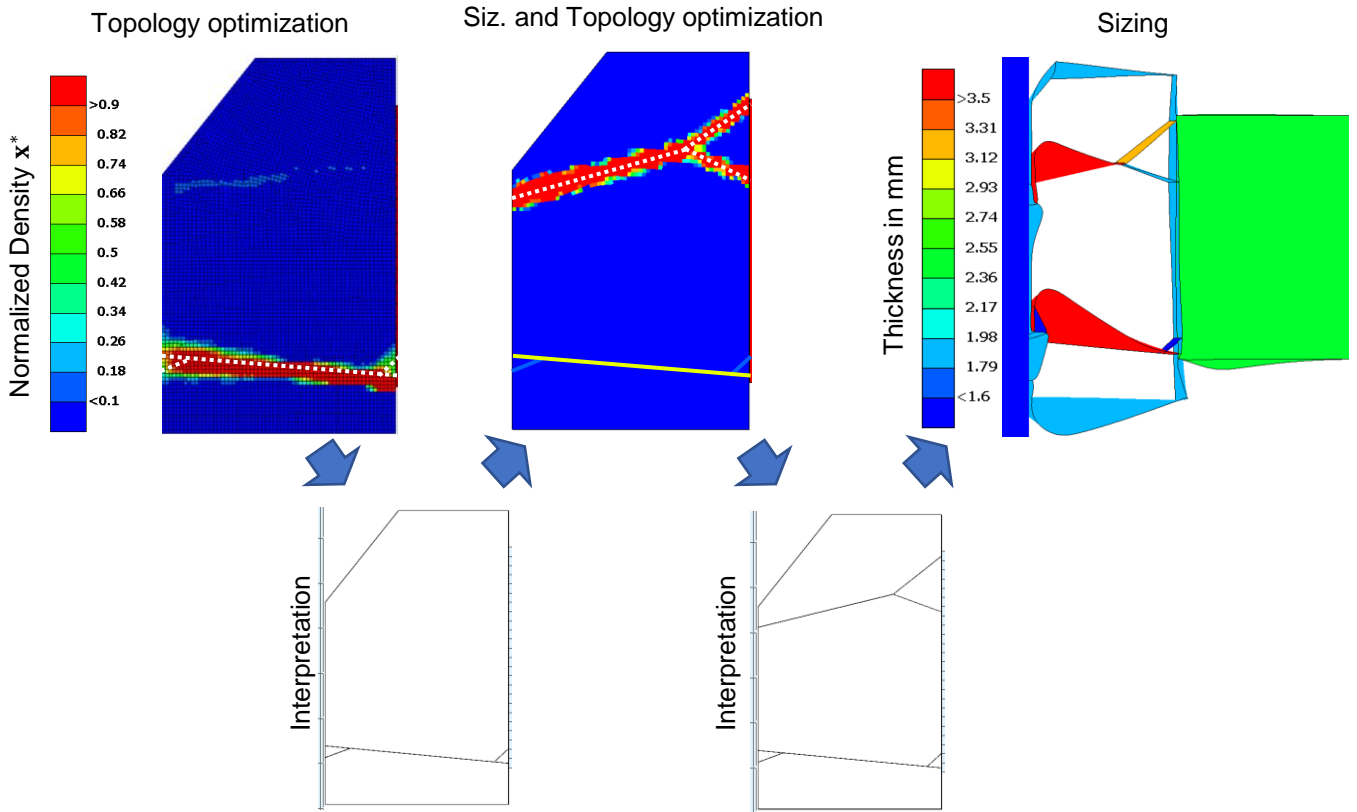
Figure 5.29: Extruded Rocker Profile – Optimization results and corresponding interpretations employing strategy 2 and thickness ratio $Z/\zeta = 2$ (scaling factor $s = 0.2$)

The resulting mass $mass(_*\mathbf{x})$, intrusion $d(_*\mathbf{x})$, the relative bending and torsional stiffnesses k_B and k_T, as well as the number of nonlinear dynamic analyses is given in table 5.5 for all employed strategies and thickness ratios as well as for the GHT (Ortmann and Schumacher 2013; Ortmann 2015). Ortmann provides two different results for this example, the abbreviation *GHT 2013* is used for the first and *GHT 2015* for the second. The major difference seems to be that in Ortmann and Schumacher 2013 a uniform thickness of the whole profile structure is enforced, whereas in Ortmann 2015 structural members are distinguished between inner profile and outer profile and their thickness ratio is optimized. Ortmann 2015 does not disclose explicit information regarding the differences to the previous publication. We can therefore not rule out that there are further differences than the ones described. All results in table

5.5 satisfy the constraints on torsional and bending stiffness by far. The best performance in terms of objective value is achieved by *GHT 2015*. The DiESL method yields close performance using strategy 2 and the thickness ratio $Z/\zeta = 4$. The worse performance of the DiESL method may be attributed to the necessity of scaling the element stiffness in the design space or due to poor interpretations of the topology results. The easiest way to address this issue would be to remove the unnecessary limitation in OptiStruct, by eliminating the MINDIM parameter's lower bound. This could potentially decrease the minimum size of members to be formed during topology optimization by half. Then, the scaling factor may not be necessary in terms of stiffness, as we observed that the optimizer also utilized intermediate densities to model members smaller the limit defined by MINDIM. This way the DiESL method's results may be improved while simultaneously keeping the computational effort low. Reviewing the number of nonlinear analyses necessary for convergence, the benefits of the DiESL methodology compared to GHT become evident. For DiESL, the overall number of nonlinear analyses is given as both sum and contributions of each individual optimization step. The individual contributions are listed besides as a summing of sizing and topology optimization contributions in chronological order. As can be seen, DiESL clearly outperforms GHT by far.

Table 5.5: Extruded Rocker Profile – Performance of optimized designs obtained using different DiESL optimization strategies and thickness ratios compared to the GHT (Ortmann and Schumacher 2013; Ortmann 2015)
Note: For the sake of comparability the masses resulting of the GHT are reduced by half

Approach	thickness ratio Z/ζ	s	$mass({}_*\mathbf{x})$ kg	$d({}_*\mathbf{x})$ mm	${}_*k_B$ %	${}_*k_T$ %	# nonlinear analyses
Strategy 1	4	0.05	1.400	29.85	68.7	64.6	**30**=24+6
Strategy 1	2	0.2	1.399	31.08	68.7	62.1	**40**=30+10
Strategy 2	4	0.05	1.400	**26.58**	68.1	65.3	**38**=24+9 +5
Strategy 2	2	0.2	1.399	28.88	65.5	62.0	**51**=23+19+9
GHT 2013	-	-	1.400	29.78	77.3	66.7	≈3500
GHT 2015	-	-	1.400	**25.87**	68.4	56.1	3128

5.2.3 Reinforced Rail

So far, only displacement and mass responses have been involved in the topology optimization problems. In the following, the *IncC* approach for the consideration of forces in DiESL is tested for a topology optimization application. The structural component investigated is a rail structure reinforced by an additive manufactured rib. The component is part of the occupant compartment and should therefore be as stiff as possible. In Fig. 5.30 the part as well as the considered load case are illustrated. The component is clamped in all degrees of freedom at the right end employing an SPC and an RBE2 spider. At the upper end another RBE2 spider is attached. An extremely stiff spring element connects the RBE2's independent node and node 108 to measure the reaction force F. The rail is deflected, by applying a constant velocity $v = 1$ m/s at node 108 for 50 ms. The direction of v is in the xz-plane at an angle of $25°$ to the x-axis. In addition, there is a rigid shell structure behind the rail (guide) to prevent it from buckling in this direction. The guide represents other components in the vehicle at the same location. This load case models a test bench on which the deformation behavior of the rail during a front crash is simulated. A more detailed specification of the component's place in the car as well as the test bench cannot be made due to the confidential agreement with Opel Automobile GmbH.
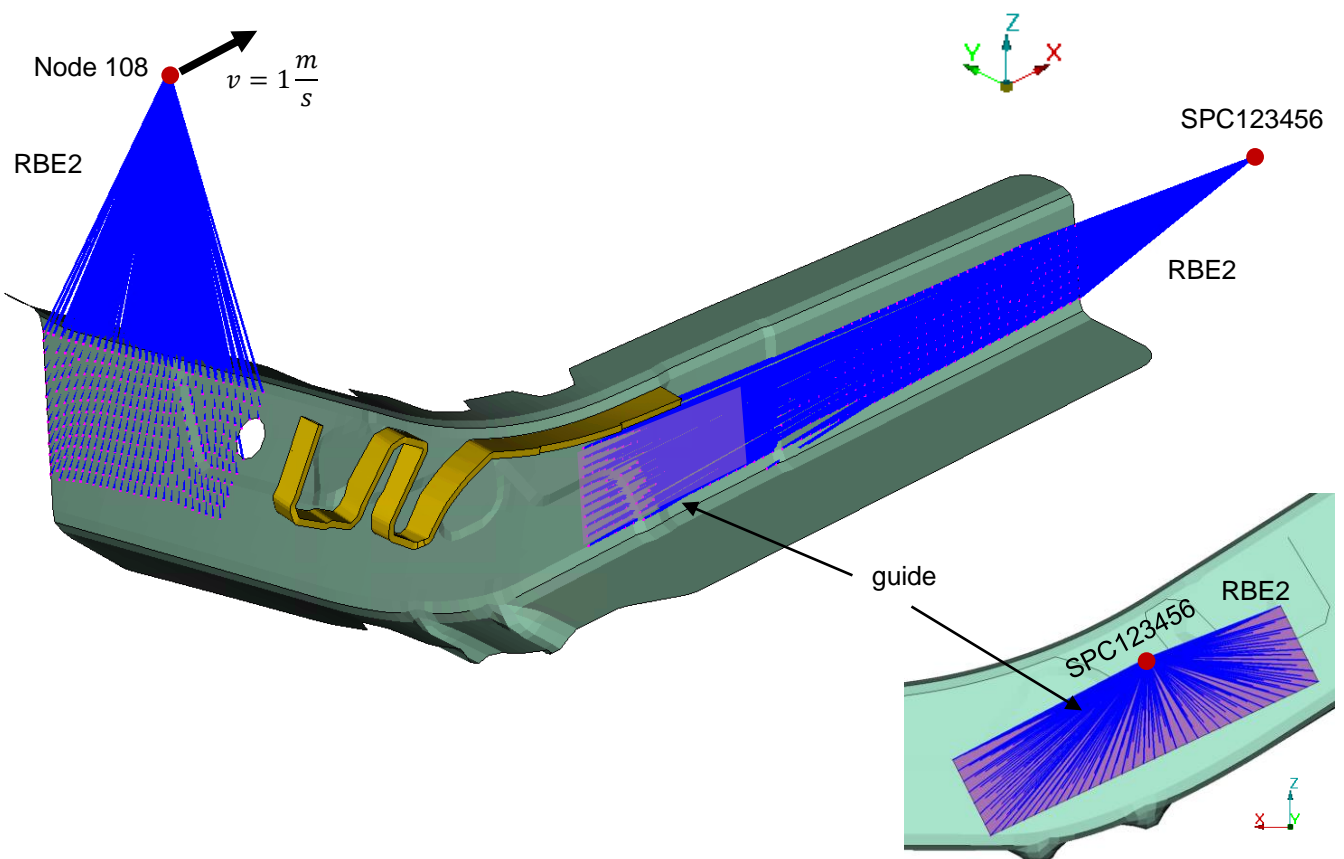
Figure 5.30: Reinforced Rail – description of FE-model and load case

The rail structure as well as the rib are made of steel (Young's modulus $E = 210$ GPa, Poison's ratio $\nu = 0.33$). For both, strain-rate dependent visco-plastic material behavior is assumed. A more precise specification of the material can also not be made here for reasons of confidentiality.

The rib is manufactured using wire arc additive manufacturing. In this process, metal is deposited layer by layer onto a carrier structure. Fig. 5.31 illustrates the discretization of the rib by fully integrated hexa volume elements. The height of the elements in y-direction is 1 mm, this exactly represents the height of a deposit layer. The length of the elements in the thickness direction of the rib is 3 mm such that only one element is used in thickness direction. The rib is connected to the beam structure by a "contact tie" option. This creates extremely stiff elements between the bottom nodes of the rib and the underlying rail structure. The rib consists of 3942 hexa elements and the support structure consists of 3757 shell elements. The overall number of nodes is 16789.
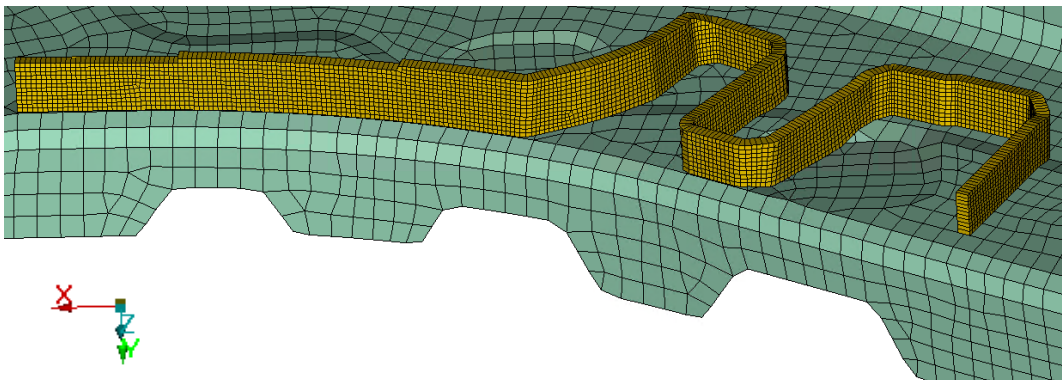
Figure 5.31: Reinforced Rail – discretization of rib using volume elements

The shape of the rib shown was largely derived from design space restrictions. The rib can hardly be enlarged because other manufacturing processes require the remaining space. The optimization goal is therefore not to completely redefine the shape of the rib but to reduce the mass of the existing rib $mass_\mathrm{r}$ and thus indirectly decrease the necessary production cycle time. In doing so, the stiffness of the structure must be maintained such that buckling of the structure and thus possible injuries to the occupant are prevented. As shown in 5.32, the stiffening effect of the rib significantly contributes to preventing buckling. This is also reflected in the maximal reaction force F_max measured at the previously described spring, which is 15.7 kN without rib and 20.1 kN with rib.

No Reinforcement   With Reinforcement

Figure 5.32: Reinforced Rail − maximum deformed rail with (right) and without reinforcement (left)

To generate several design proposals with different masses, we maximize F_{max} measured at the spring element at node 108, while constraining the mass of the rib:

$$\max F_{\mathrm{max}}\left(\mathbf{x}\right); \tag{5.19}$$

subject to

$$mass_{\mathrm{r}}\left(\mathbf{x}\right) \leq \lambda \cdot 95.2\,\mathrm{g}; \tag{5.20}$$

where the mass of the original rip is 95.2 g. The constraint is varied between $\lambda = 0.4$ and 0.9.

Compared to the previously explained nonlinear model, some adjustments have been made to the model employed in the design domain. First, the rigid guide on the rear side of the rail is omitted to avoid a contact definition. In addition, a local coordinate system is defined at the deflected node. The coordinate system is rotated such that the x-axis coincides with the displacement direction of node 108. This way, an SPC can be applied restricting the direction of motion of node 108 to the x-direction in the local coordinate system. The reaction force F can then be approximated using the *IncC* approach from the incremental displacement in the x-direction in each LSM.

The nonlinear problem is approximated using $n_{\mathrm{T}} = 20$ adaptively selected ESL times by fitting the reaction force. The MINDIM parameter is set to 3 mm but it plays a subordinate role here. Much more important is a draw direction constraint defined in the negative y-direction. This guarantees the manufacturability of the resulting design proposal, because then material can only be removed starting from the top of the rib. This is handled by OptiStruct internally, but can for example be accomplished by constraining the densities in the defined direction: $0 \leq \rho_i \leq \rho_{i+1} \leq ... \leq \rho_m$, where ρ_m is the density of an element closest to the rail structure and ρ_i the density of an element above, in the defined direction. In other words this ensures that no holes are evolving and each layer can be added on top of a previous layer. Since a constant velocity is imposed in the presented problem (cf. roof crush load case) inertia effects do not play a role here. Hence, elements with a high mass/stiffness ratio are not expected to cause issues in the nonlinear analysis, as it

has been exemplified in section 5.1.1. To increase the consistency between analysis and design domain, the SIMP exponent in the analysis domain $p_{NL} = 3$ is used here.

Table 5.6 summarizes the optimization results for all mass fractions λ, it also includes the original rib ($\lambda = 1$) and no rib ($\lambda = 0$). The table lists the cycles necessary for convergence ${}_*cycle$, the container model's maximum reaction force $F_{\max}({}_*\boldsymbol{\chi})$ relative to that of the original full rib, and the discreteness $D({}_*\mathbf{x})$. All optimizations converge after few cycles already. The discreteness of all runs with $\lambda \geq 0.6$ is extremely high, such that the container models can be expected to yield similar results as corresponding 0-1 interpretations. However, the discreteness of the remaining runs still is sufficiently high. All container models achieve a relatively high maximum reaction force $F_{\max}$ when compared to the original rib. This means the mass of the rib can be reduced considerably without significant influence on the maximum reaction force $F_{\max}$.

Table 5.6: Reinforced Rail – optimization results varying the mass fraction by λ

λ	${}_*cycle$	$F_{\max}({}_*\boldsymbol{\chi})/F_{\max}(\text{full rib})$ %	$D({}_*\mathbf{x})$
1.0		100	1.0
0.9	4	99.9	0.89
0.8	7	99.3	0.91
0.7	6	98.4	0.90
0.6	13	98.3	0.94
0.5	7	98.2	0.75
0.4	7	97.5	0.72
0.		78.1	0.

In Fig. 5.33 the resulting optimal container models are illustrated at time $t = 50$, where the rail's deformation is maximal. The left straight portion of the rib obviously has the greatest influence on $F_{\max}$, as it never gets eliminated even for small λ. Portions at the right end and in the middle, on the other hand, seem to be rather unimportant and begin to vanish as λ is reduced.

Fig. 5.33 also allows for an analysis of the rail's deformation behavior. It is obvious that with decreasing λ, buckling increases in the area encircled by the yellow dashed line. This is also reflected In Fig. 5.34 where the force fraction $F({}_*\boldsymbol{\chi})/F_{\max}(\text{full rib})$ relative to the full rib design is plotted over the displacement of node 108. After reaching the peak force, each curve drops with a different slope. This slope of the force drop becomes steeper as λ is reduced. Although it has not been targeted directly in the optimization problem's formulation, it is desirable to maintain the reaction force as high as possible after the maximum has been reached. For $\lambda = 0.7$ the force drop is still relatively small compared to the full rib design. Hence, this result can be considered as a good trade-off between performance and mass. For this reason, an interpretation is derived according to the strategy defined in chapter 5.2.1 for the $\lambda = 0.7$. The threshold $\epsilon_v = \epsilon_s = 0.26$ yields an interpretation where both the mass constraint is active and the objective is approximately the same as in container model design (table 5.7).
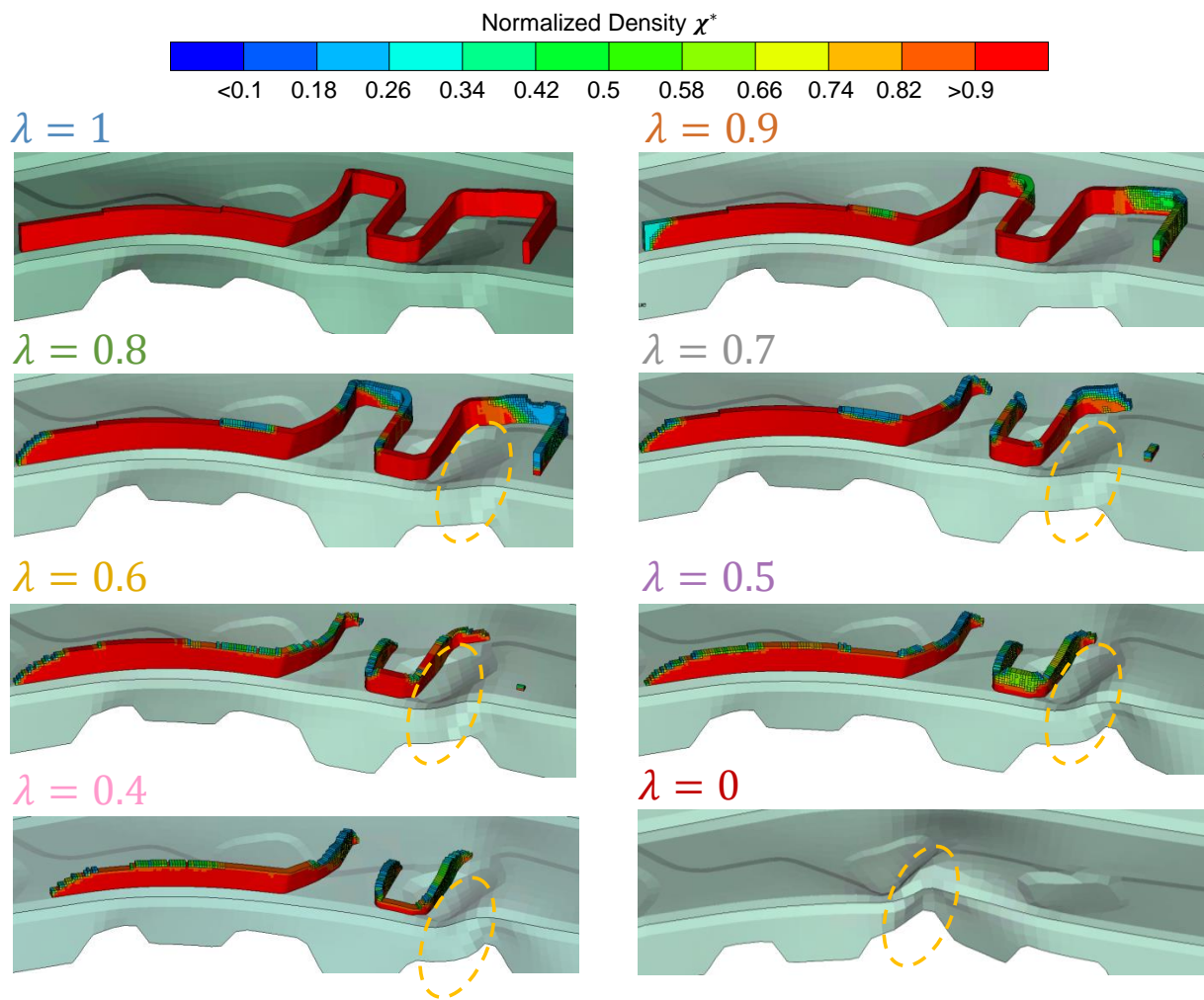
Figure 5.33: Reinforced Rail – maximally deformed rail with optimized rip for various mass fractions λ
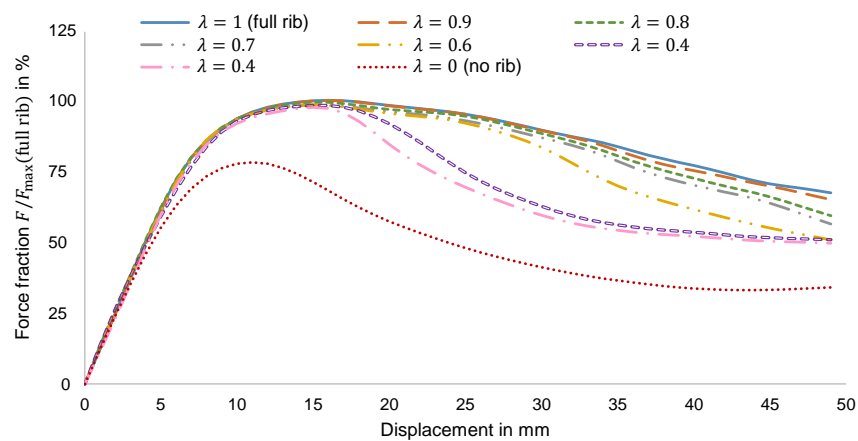
Figure 5.34: Reinforced Rail – Force fraction with regard to the full rib design over displacement for all optimization results varying the mass fraction λ

Table 5.7: Reinforced Rail – optimization results $\lambda = 0.7$ and corresponding interpretation

Model type	$_*cycle$	ϵ_v	ϵ_s	$F_{\max}(_*\boldsymbol{\chi})/F_{\max}(\mathrm{full\,rib})$ %	$D(_*\mathbf{x})$	$mass_\mathrm{r}(_*\boldsymbol{\chi})$ g
Container model	6	0.1	0.9	98.4	0.9	65.5
0-1 Interp. same obj. & constr.		0.26		98.7	1.0	66.6

The resulting 0-1 interpretation is shown in Fig. 5.35 at the time of maximum deflection $t = 50$ ms. Obviously, this interpretation still contains irrelevant parts (e.g. small island at the right end) and can potentially be optimized further. The structural performance, however, is slightly improved compared to the container model, as the rail buckles less. This can also be seen in Fig. 5.36, where the force fraction $F(_*\boldsymbol{\chi})/F_{\max}(\mathrm{full\,rib})$ relative to the full rib design is plotted over the displacement of node 108 for the container model ($\lambda = 0.7$), the corresponding 0-1 interpretation, the full rib design, and the rail without rib. The 0-1 interpretation shows almost the same performance as the full rib design, although the mass has been reduced by $30\,\%$. It can be expected that the production cycle time can also be significantly reduced using this interpretation. We can therefore conclude that the consideration of forces in DiESL for the purposes of topology optimization works well and can be a valuable tool when optimizing real world problems.

Container model $\lambda = 0.7$
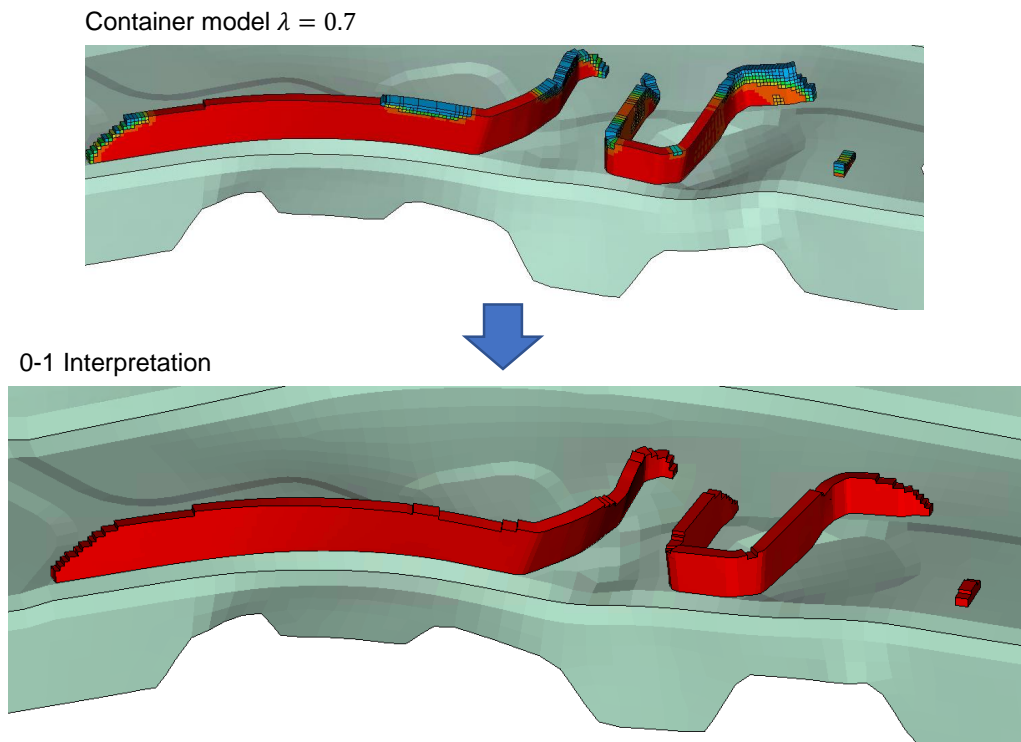
0-1 Interpretation

Figure 5.35: Reinforced Rail – interpretation of optimized rip for $\lambda = 0.7$
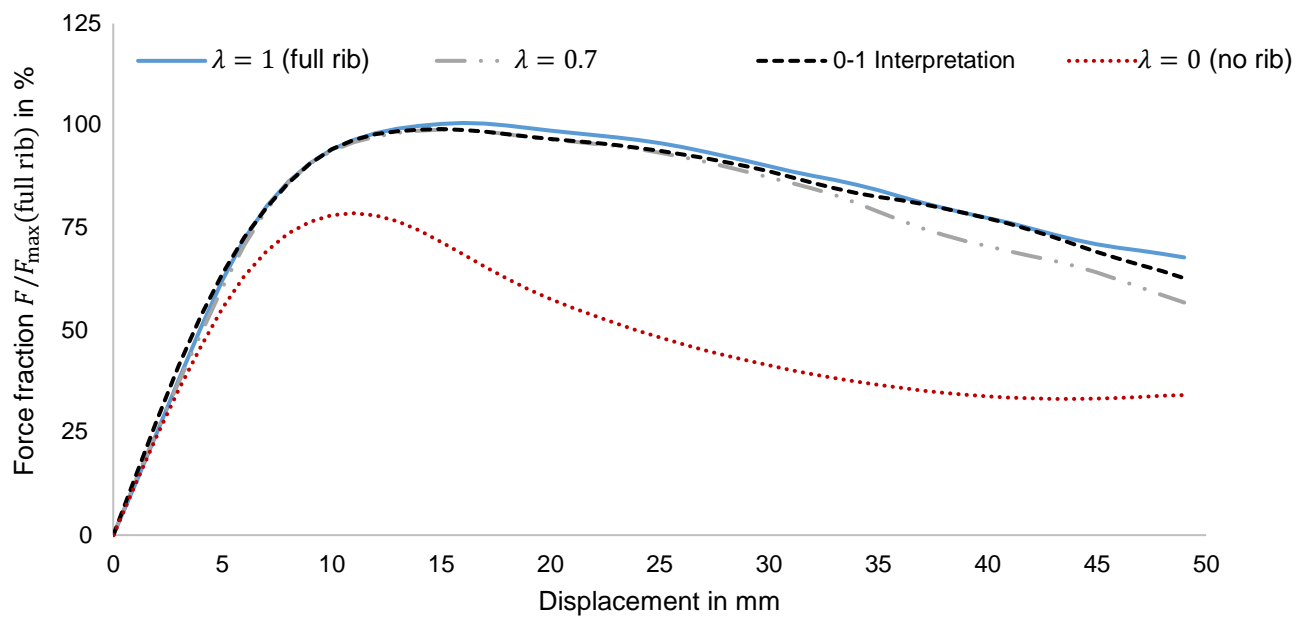
Figure 5.36: Reinforced Rail – Force fraction with regard to the full rib design over displacement of resulting container model for $\lambda = 0.7$ and corresponding 0-1 interpretation compared to full rib- and no rib-design

6 Summary, Discussion, and Outlook

This thesis deals with structural optimization in the context of crashworthiness design. These kinds of problems involve nonlinearities in geometry, material, and from contact. Sensitivities are either very expensive to compute or not even available, and efficient gradient-based optimization methods cannot be employed directly. The DiESL method provides a workaround by creating linear static auxiliary load cases which in turn enable gradient-based optimization.

The DiESL approach is extended in this thesis by several features. For this purpose, the necessary theoretical basics of structural optimization have been elaborated in chapter 2, and an overview of competing methods for nonlinear dynamic response optimization has been given. Afterwards, the DiESL method has been presented in chapter 3 with a brief discussion of various response types. Furthermore, two potential improvements have been elaborated in chapter 3. The first is the adaptive selection of ESL times. A time dependent quantity that represents the nonlinear structural behavior (e.g. a contact force curve) is fitted by a piecewise linear curve. The resulting breakpoints are used as ESL times. The second extension is the local adaptation of the Young's moduli (LA) on element level in all linear sub models (LSMs) to give a better approximation of the elements' stiffness change due to plasticization occurring in the nonlinear dynamic analysis. To achieve this, the elements in the LSMs are assigned to one of two materials using the nonlinear Young's or tangent modulus, respectively. To enable a robust application of the methodology in the industrial context, two additional features were presented. One is a simple automatism for handling failed elements in deformed LSMs, the other is a methodology for handling non-congruent models in analysis and design domain. Furthermore, several approaches for the incorporation of contact forces into the auxiliary DiESL optimization problem have been developed. They establish relationships between the contact force and a representative nodal displacement in direction of the force. This aims to enable the optimization of the energy absorption behavior of crash structures in addition to stiffness optimization applications using DiESL. The treatment of contact forces is not trivial in the design domain because all ESLs are held constant during linear static response optimization, so the use of nodal forces is prohibitive. Three approaches were presented within this thesis to quantify contact forces for linear static response optimization. The first approach *Inc* relates the force increment to a reciprocal displacement increment. A modification *IncS* uses *Inc* for rising force increments but inverts the behavior for falling force increments. The third approach *IncC* is like *IncS* but a negative force increment is kept constant independently of the displacement increment.

In chapter 4, the DiESL method and all presented extensions have been tested for various sizing optimization examples and the results were compared with competing methods. Most of the comparisons were made based on multistart studies, in which the initial designs were uniformly distributed over the design space, such that a statistical independence between the results and the initial designs can be expected.

The first example is a simple side impact, it demonstrated the advantages of DiESL over both the ESL method and a metamodel-based approach. The mass of the structure has been minimized with a constraint on the impactor's intrusion. It turned out that the DiESL method, in contrast to the ESL method, converges to a true optimum of the nonlinear dynamic problem. It can be assumed that the found optimum is a true optimum, because the metamodel-based approach converged to a similar design. The fundamental advantage of the DiESL methodology over the metamodel-based approaches is that the computational effort involved does not scale directly with the number of design variables. This advantage already became evident for the examined side impact example, although only seven design variables had been defined. The number of nonlinear analyses necessary for convergence was ten times smaller for DiESL compared to the metamodel-based approach. For applications with many design variables such as topology optimization, metamodel-based approaches are therefore not an alternative.

The next study examined the adaptive selection of ESL times (AT) and the local adaptation of the Young's moduli (LA) as well as the combination of both. For this purpose, the same side impact example with bilinear material behavior and a highly nonlinear crash box example with piecewise linear material behavior have been used. In both examples the structure's mass was minimized while the intrusion of an impactor was constrained. Three criteria were defined to evaluate the extensions' influence on the DiESL method's approximation quality: the average number of cycles required for convergence, the number of multistart runs converging to the best optimum found, and the resulting average objective value. The number of ESL times n_T has been varied systematically as a parameter. The benefits obtained with the adaptive selection of ESL times depend on the example. For the side impact, the following observations have been made: For sufficiently large numbers of ESL times, the AT has no significant influence on the chosen criteria. For only few ESL times, the number of cycles necessary for convergence can be reduced using AT. For the crash box example, AT leads to significant improvement of all criteria: With AT the DiESL method convergences faster and more often to the presumed global optimum. Also, the average objective value is better for all multistart runs. If the number of ESL times is reduced, these advantages become more pronounced. Adaptive selection of ESL times therefore can be used to reduce the computational effort without drastically reducing the approximation quality as it is the case with equidistant spacing. This is especially advantageous for large models or if computational resources are limited. It is plausible that the differences between both approaches grows smaller with increasing number of ESL times n_T because in that case the spacing of ESL times grows smaller and hence the exact placement of ESL times becomes less significant. The influence of AT is larger in the crash box example compared to the side impact example. This is likely to be caused by the degree of structural nonlinearities forming in the course of the deformation, it is much higher for the crash box. Here, the deformation behavior strongly depends on the repeated and successive formation of contacts and plastic hinges, this is not the case for the side impact. This difference

is reflected in the shape of the contact force curve, it is relatively smooth for the side impact and oscillates wildly for the crash box. It can therefore be concluded that AT leads to a considerable improvement of the DiESL method's approximation quality in the presence of sufficient structural nonlinearities. However, in some cases the usage of ET may also be beneficial, for example if structural responses like velocities or accelerations need to be approximated employing finite differences of ESL times.

The optimal number of ESL times n_T is a user defined parameter. At the beginning of an optimization there is little information to guide the user in the choice of a reasonable value. A trade-off between computational effort and approximation quality is required. To address this, the algorithm could be extended. Furthermore, the number of ESL times n_T could be optimized in addition to their distribution. This may be accomplished by simply computing the sum of squared residuals (SSR) for a predefined range of n_T values and selecting the smallest n_T still satisfying the predefined accuracy requirement. The SSR gives a number to classify the accuracy of the fits and could therefore be used as measure of the expected approximation quality.

The local adaption of the Young's moduli (LA) also yielded different results for the examples examined. For the side impact example, where a bilinear material behavior is employed in the analysis domain, a new and better optimum was found by employing LA. This optimum has been found using LA only and the accompanying increased accuracy of the DiESL approximation. The reason for this has been illustrated by comparing the contour lines of constraint and objective for the original nonlinear dynamic problem and the DiESL method's approximation with and without LA. This advantage could not be observed for the crash box example, where a piecewise linear material model has been applied in the analysis domain. Here, the combination of ET with LA yielded worse results than ET without LA. Combining AT with LA did not show comparable disadvantages, but no improvements could be observed either. This may be attributed to the ratio of plasticized and non-plasticized elements. The crash box plasticizes already at very early stages of the deformation process such that most elements are in the plastic domain. The bilinear material model employed in the design domain is not able to distinguish between elements with small and with high plastic strains, it only accounts for one hardening modulus. This is different for the side impact problem. First, the material model for the nonlinear dynamic analysis is bilinear only and second, a smaller portion of the structure plasticizes here, whereas a significant portion remains in the elastic range for the entire deformation process. It therefore can be concluded that LA in the current bilinear implementation only improves the approximation quality if neither the elements in the elastic nor in the plastic domain are dominating the structure's behavior (Triller et al. 2022a). Extending the bilinear material model used in the design domain to a piecewise linear material model could potentially mitigate this drawback. Elements with small strains would be assigned to a higher hardening modulus than elements with high plastic strains. The linear static response optimization would thus be able to distinguish between elements with high and small structural stiffness, even if all elements are plasticized.

The next study examined the approaches to integrate contact forces as responses into the optimization problem, e.g. as objective function or constraint. A simple hinge model has purposely been designed such that the contact force first increases linearly and then drops due to the formation of plastic hinges. It turned

out that in the falling phase of the contact force, the negative force increment stays constant independently from the structure's stiffness. This behavior is best represented by the *IncC* approach.

Afterwards all approaches have been tested on the crash box model by means of a multistart study. The maximum contact force between impactor and structure was minimized while the impactor's intrusion was constrained. This was to target an optimal energy absorption behavior. Convergence issues have been observed for all approaches with *Inc* and *IncC* having the most and least issues, respectively. A detailed analysis of the un-converged optimization histories revealed that most of the convergence issues could be attributed to the objective function's high sensitivity with respect to the design variables. To allow for a reasonable comparison of all multistart results, a best representative design has been determined manually for each optimization run. A design has been considered representative if the design was feasible and the design variables only differ "slightly" compared to the previous cycles. Comparing these best points, the *IncC* approach statistically provided the best results with the greatest reliability. However, the advantage over the *IncS* approach is relatively small and the manual procedure to determine the representative runs involves uncertainties, such that a final conclusion on which approach is best could not be made. Nevertheless, the visual comparison of the resulting design's contact force curves for *IncC* with the theoretical optimum confirmed the result's high quality. The approach has therefore been considered useful to handle contact forces with DiESL and has been applied for all following examples involving crash forces.

Afterwards, the *IncC* has been tested again employing an example from literature. This is a side impact example including a B-Pillar and has originally been used to test the ESD method. The structure is defined by 20 design variables. The structure's mass has been minimized while the contact force must remain within a predefined corridor. The structure's mass has been reduced by 42% with the DiESL method compared to the initial design. In contrast, the ESD method reduced the mass by only 18%. The number of nonlinear dynamic analyses was identical for both methods. However, the difference in mass reduction is significant in favor of the DiESL method.

In chapter 5 the DiESL method has been extended to topology optimization. The SIMP approach has been utilized to relate the density design variables to the mechanical properties of an elasto-plastic material, namely Young's modulus, yield stress, and strain hardening modulus. To prevent mesh distortion problems, a penalty exponent $p_{\mathrm{NL}} = 1$ has been used in the analysis domain for all nonlinear dynamic examples, this is a deviation from the exponent $p = 3$ in the design domain. To further address this issue, elements with very small densities have been deleted from the nonlinear dynamic FE-model. The previously developed mechanism for handling non-congruent models has been applied to reconstruct the nodal coordinates of the elements deleted in the analysis domain. Intermediate densities have been transferred unchanged from the design domain to the analysis domain to enable a continuous and smooth change of design from cycle to cycle.

The proposed method has been tested using three examples. The first was a simple beam structure impacted by a rigid pole. Again, the pole's intrusion has been minimized while the structure's mass was constrained.

Three dynamic load cases were defined in which the pole's initial velocity and mass have been varied to examine the influence of inertia effects on the resulting optimized structures. The DiESL method yields discrete and hence easy-to-interpret designs for all load cases. The plausibility of each result has been confirmed by a cross validation where each optimal structure has been exposed to the remaining other load cases. For each dynamic load case exactly one design performed best, namely the design that had been optimized for the respective load case. Furthermore, the resulting designs of all dynamic load cases and an additional linear static load case have been compared and discussed on a visual basis. It has been found that the two designs obtained with the linear static and the slowest dynamic load case bear strong similarity in that they developed a compression loaded member as main load path. For higher initial velocities the optimal structures change significantly, most prominent are the development of tensile loaded members and accumulation of mass in the impact zone. It can therefore be concluded that the DiESL method is able to handle inertia effects. The good quality of the DiESL method's results could further be confirmed by comparing it to the standard ESL method. For both small and high velocities the structures obtained with the ESL method are dominated by the characteristics of the linear static load case design, most prominently by the compression loaded members. This reconfirms the superiority of the DiESL method over the ESL method. For the high velocity load case, the DiESL method outperforms the ESL method by far, this is mainly due to buckling of ESL's compression loaded members. Moreover, the DiESL method yields more discrete and thus easier-to-interpret structures than the ESL method does.

The second topology example was a more practice relevant one, an extruded rocker profile colliding with a rigid pole. Here, the topology of the rocker profile has been optimized. The intrusion of the structure has been minimized while the rocker's mass was constrained. This problem has originally been used to test the Graph and Heuristic Topology optimization (GHT) which is especially well suited for optimizing extruded profile structures. In contrast, when employing the DiESL method some obstacles occur. Sufficiently small elements must be used in the design space to model a good representation of the small thicknesses of the resulting profile members. This results in a huge number of elements increasing the computational costs. The simulations had to be conducted using a desktop computer with limited resources, and OptiStruct imposed (potentially unnecessary) limitations on the minimum size of profile members, therefore a larger element size than required had to be used in the design space. Consequently, a workaround for modeling sub-scale structures has been developed. Both element densities and stiffnesses have been scaled in the design space such that they are mimicking the behavior of smaller shell structures. For this purpose, two different scaling factors have been determined empirically.

Two different strategies have been employed for gradually optimizing the rocker's profile. Both strategies involve the major steps topology optimization, interpretation, and sizing optimization. The combination of both strategies and scaling factors yielded four similar results, the best of which has been slightly worse than the result reported for the GHT. The DiESL method's inferiority may be attributed to bad interpretations or inaccuracies due to the scaling. Both of these sources of inaccuracy may be eliminated if the minimum member size during topology optimization could be reduced. This may be achieved either by decreasing the element size and executing the linear static response optimization problem on a high performance

cluster (HPC) or by enabling smaller member sizes in OptiStruct. Nevertheless, some advantages of the DiESL method over the GHT method became apparent. The total number of nonlinear dynamic analyses was about 50 with DiESL and 3500 with GHT, this is a ratio of 70. Also, it should be emphasized that the GHT today is no alternative when optimizing three dimensional structures, in contrast to the DiESL method.

The third example used for the evaluation of topology optimization was also a practice relevant one with forces involved in the optimization problem. A rail has been reinforced by a rib that is applied to the rail using additive manufacturing, more specifically seam welding. The rail is originally part of the occupant's safety compartment of a car and should therefore be as stiff as possible to protect the occupant during a front crash. The model examined here represents a component test bench to simulate the rail's deformation behavior and resistance when deformed with a constant velocity. The optimizations target was to reduce the rib's mass and therefore the related production cycle time without significant loss of stiffness. For this purpose, the maximum reaction force of the rail has been maximized using the *IncC* approach while the mass has been constrained. In order to derive several design proposals, the mass constraint has been varied between various fractions of the original rib's mass. Since a constant velocity is applied to the structure here and thus no inertia effects are involved, the same SIMP penalty exponent $p_{NL} = p = 3$ has been used in the analysis and design domain without running into mesh distortion problems. Most of the design proposals could be obtained with a small one-digit number of cycles and featured a very high discreteness value. The best trade-off between mass reduction and performance loss has been identified for mass fraction of 70% of the original rib. The corresponding 0-1 interpretation yields an almost identical force versus displacement curve as the original rib design and therefore maintains the rail's stiffness. The mass reduction of 30% can be expected to yield a similar reduction in production cycle time and thus cost. Based on this example, it can be concluded that the *IncC* approach yields valuable results for topology optimization problems where a force is maximized. Future work should further examine the DiESL method's capability to optimize the energy absorption behavior by means of topology optimization and therefore target an almost rectangular force versus displacement curve. Furthermore, dynamic effects should be considered in the example.

A frequently observed problem in the studied examples was the oscillation of design variables during several subsequent cycles. This behavior is generally undesirable, as it usually does not lead to an improvement in design. This is particularly frustrating since during the optimization process, information about these repetitive design points have already been obtained by nonlinear dynamic analyses. However, information from previous cycles do not have any influence on the search direction and step size in the following cycles. The utilization of this unused information in the algorithm therefore offers additional potential for improvement. Maybe it can be utilized to define individual move limits for each design variable and thus avoid unnecessary oscillations. For sizing optimization, the relationship between the design space spanned by the individual move limits and the optimization history, i.e., all previously collected information, could potentially be established by a neural network. For this purpose, however, it would be necessary to investigate on how strongly the neural network's predictability depends on the example under consideration.

In this thesis the DiESL method has been compared to various alternative methods for nonlinear dynamic response optimization. Overall, the DiESL method highlights itself by the comparatively small computational effort required. It enables the handling of a huge number of design variables in contrast to metamodel-based approaches, including topology optimization for nonlinear dynamic problems as exemplified. Additionally, the DiESL method yields significantly better results than the ESL and ESD method. This also applies for sizing and topology optimization problems involving contact forces. The DiESL method can therefore be considered suitable for the optimization of crash structures including responses with regard to stiffness and energy absorption behavior. Hence, nothing should prevent the optimization of full-size automotive problems on an HPC. Besides, the DiESL method may also be a valuable tool in other areas where nonlinearities in material or geometry are dominating the structural behavior.

7 Appendix

7.1 Side Impact

Table 7.1: Uniformly distributed initial designs for side impact multistart study generated using STOA

run #	$_0x_1$ mm	$_0x_2$ mm	$_0x_3$ mm	$_0x_4$ mm	$_0x_5$ mm	$_0x_6$ mm	$_0x_7$ mm
1	0.5	2.5833	2.167	3	2.5833	0.5	0.9167
2	3	0.5	0.5	0.5	0.5	1.75	0.9167
3	2.167	1.33	3	0.5	3	2.5833	2.167
4	1.33	0.5	3	2.167	1.75	0.5	3
5	0.5	3	0.9167	2.167	0.9167	1.33	2.167
6	2.167	2.5833	1.75	1.33	1.75	2.167	1.33
7	3	0.9167	1.75	3	0.9167	2.5833	3
8	0.5	1.75	1.33	0.5	1.75	0.9167	0.5
9	1.75	3	0.5	1.33	2.5833	2.5833	0.5
10	3	1.75	3	2.5833	2.5833	1.33	1.33
11	0.5	0.9167	3	1.33	0.5	3	2.5833
12	1.33	2.5833	0.5	2.5833	1.33	3	2.167
13	2.5833	0.5	2.167	1.33	3	1.33	1.75
14	1.75	1.33	0.9167	1.75	0.5	0.5	1.33
15	0.5	2.167	0.5	1.75	3	2.167	3
16	2.167	0.5	0.9167	3	2.167	3	0.5
17	1.33	2.167	1.75	0.9167	0.5	1.33	0.5
18	2.5833	3	1.75	0.5	1.33	0.5	2.5833
19	3	1.33	2.167	2.167	1.33	2.167	0.5
20	1.75	2.5833	2.5833	0.5	2.167	1.33	3
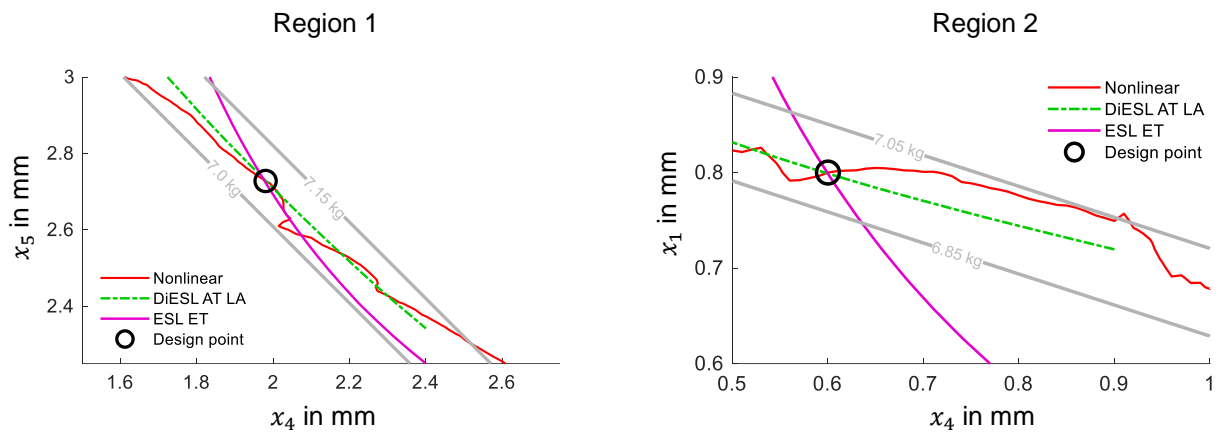
Figure 7.1: Side impact – contour lines of objective mass (grey) and maximum intrusion d for the nonlinear dynamic problem, the DiESL and ESL approximation for
region 1: design point $x_1 = 0.5\,\text{mm}$; $x_4 = 1.98\,\text{mm}$; $x_5 = 2.73\,\text{mm}$; $d(\mathbf{x}) = 199.1\,\text{mm}$ (left) and
region 2: design point $x_1 = 0.8\,\text{mm}$; $x_4 = 0.6\,\text{mm}$; $x_5 = 3\,\text{mm}$; $d(\mathbf{x}) = 200.6\,\text{mm}$ (right).
Notes:
(1) All design variables x_2, x_3, x_6, x_7 are set to the lower bound ($0.5\,\text{mm}$)
(2) The assumptions made to identify the two 2D ranges for plotting the contour lines do not necessarily apply for the ESL method

7.2 Crash Box

Table 7.2: Crash box – uniformly distributed initial designs for multistart study generated using STOA. Designs for smaller design space are scaled accordingly

run #	$_0x_1$ mm	$_0x_2$ mm	$_0x_3$ mm	$_0x_4$ mm	$_0x_5$ mm	$_0x_6$ mm	$_0x_7$ mm	$_0x_8$ mm	$_0x_9$ mm	$_0x_{10}$ mm	$_0x_{11}$ mm	$_0x_{12}$ mm
1	0.7	2.1	2.5	0.9	1.9	0.7	1.9	2.3	1.1	2.1	0.5	2.3
2	1.9	1.1	0.7	1.9	0.9	2.1	1.1	1.3	2.5	0.7	2.1	2.3
3	1.1	1.7	1.7	0.5	0.5	1.7	2.5	0.7	1.3	2.1	2.1	1.1
4	2.3	1.7	0.7	2.5	1.5	2.5	1.9	1.7	0.7	0.9	0.7	0.7
5	0.7	0.5	1.3	1.3	0.5	2.1	2.1	1.7	1.5	2.5	1.5	1.5
6	1.9	1.7	2.3	1.7	1.9	1.3	0.5	1.1	2.1	2.5	1.3	0.5
7	2.5	0.9	0.5	2.5	0.9	1.3	0.7	0.5	0.5	2.1	2.5	1.5
8	0.5	0.5	1.1	0.9	2.1	2.5	0.7	2.5	2.1	1.3	2.1	1.9
9	1.5	2.3	2.1	1.7	0.5	0.7	1.1	2.5	0.9	1.7	2.5	0.7
10	1.7	1.3	1.7	0.9	0.9	0.5	1.5	1.7	1.7	1.7	1.3	2.5
11	2.3	2.5	2.5	1.3	1.7	1.7	0.7	1.1	2.5	1.7	0.9	1.7
12	2.5	0.5	0.7	1.7	2.5	1.7	1.5	2.1	1.9	1.1	0.5	1.3
13	0.7	2.5	1.5	0.5	1.1	2.5	1.1	0.5	1.9	0.5	1.3	0.9
14	1.1	0.7	2.3	2.1	2.5	2.5	2.1	1.9	0.5	1.7	1.7	2.3
15	0.7	1.9	1.7	2.5	2.5	1.1	2.3	1.3	0.9	1.3	0.9	0.5
16	2.1	1.1	1.9	1.3	2.5	0.9	1.9	0.7	2.1	0.5	2.5	2.5
17	2.5	2.5	1.9	0.9	1.3	2.1	0.5	0.9	0.9	0.9	1.7	1.1
18	1.3	2.1	2.3	2.5	0.5	1.5	1.5	0.9	2.5	0.5	1.9	1.9
19	0.5	0.9	1.3	2.1	1.9	1.5	1.1	2.1	1.3	0.9	0.9	2.5
20	0.5	0.7	0.7	1.3	1.3	0.7	2.5	0.5	1.7	2.3	1.9	0.5
21	0.9	1.3	0.5	0.5	0.7	0.9	2.1	2.5	2.5	0.9	0.5	0.5
22	0.7	1.7	1.1	2.1	1.3	0.5	1.7	1.5	2.5	1.9	2.5	1.3
23	1.7	1.7	0.9	1.3	2.3	2.3	1.1	0.9	0.5	1.3	0.5	2.1
24	1.5	0.5	2.5	0.5	1.5	1.1	0.5	1.5	0.5	0.7	1.9	2.5
25	1.9	2.3	0.5	0.9	1.5	2.3	2.5	1.9	1.5	0.5	0.9	1.3
26	1.1	1.1	2.5	1.7	2.3	0.5	2.3	0.5	1.5	0.9	2.3	1.9
27	2.3	2.1	1.3	1.7	0.9	0.9	2.5	1.5	2.3	1.3	1.7	0.9
28	1.3	0.7	1.1	0.5	0.9	2.3	1.9	2.1	0.9	2.5	2.3	1.7
29	2.1	2.1	0.7	2.3	1.1	0.5	0.9	2.5	0.5	2.5	0.9	1.1
30	2.3	1.1	1.5	0.9	0.5	1.9	1.3	2.1	0.5	1.9	1.1	0.5
31	1.5	1.3	2.3	2.3	1.7	2.1	1.9	0.5	1.3	1.3	1.1	1.3
32	1.5	2.5	0.9	2.5	0.7	0.5	2.5	2.1	2.1	1.5	1.5	2.3
33	2.3	0.7	2.1	1.1	2.1	0.5	0.5	1.3	1.3	0.5	0.5	1.5
34	0.9	2.1	1.7	1.9	1.7	2.5	0.5	2.1	1.5	2.3	2.5	2.1
35	1.9	1.5	1.3	0.5	2.5	0.5	0.7	0.9	1.1	2.3	1.1	0.7
36	0.5	2.1	1.9	0.5	2.3	1.3	1.3	1.3	0.7	1.7	1.5	1.3
37	1.9	2.5	1.7	2.1	2.3	1.9	1.9	2.5	2.3	1.1	1.9	1.5
38	2.5	1.7	1.3	0.7	1.7	1.1	1.3	2.5	1.7	0.5	2.3	2.3
39	2.5	1.3	2.5	2.1	0.5	2.3	0.9	1.3	2.1	2.3	0.7	0.9
40	1.1	1.3	0.7	1.5	1.9	1.9	0.7	1.5	0.9	0.5	1.5	2.1
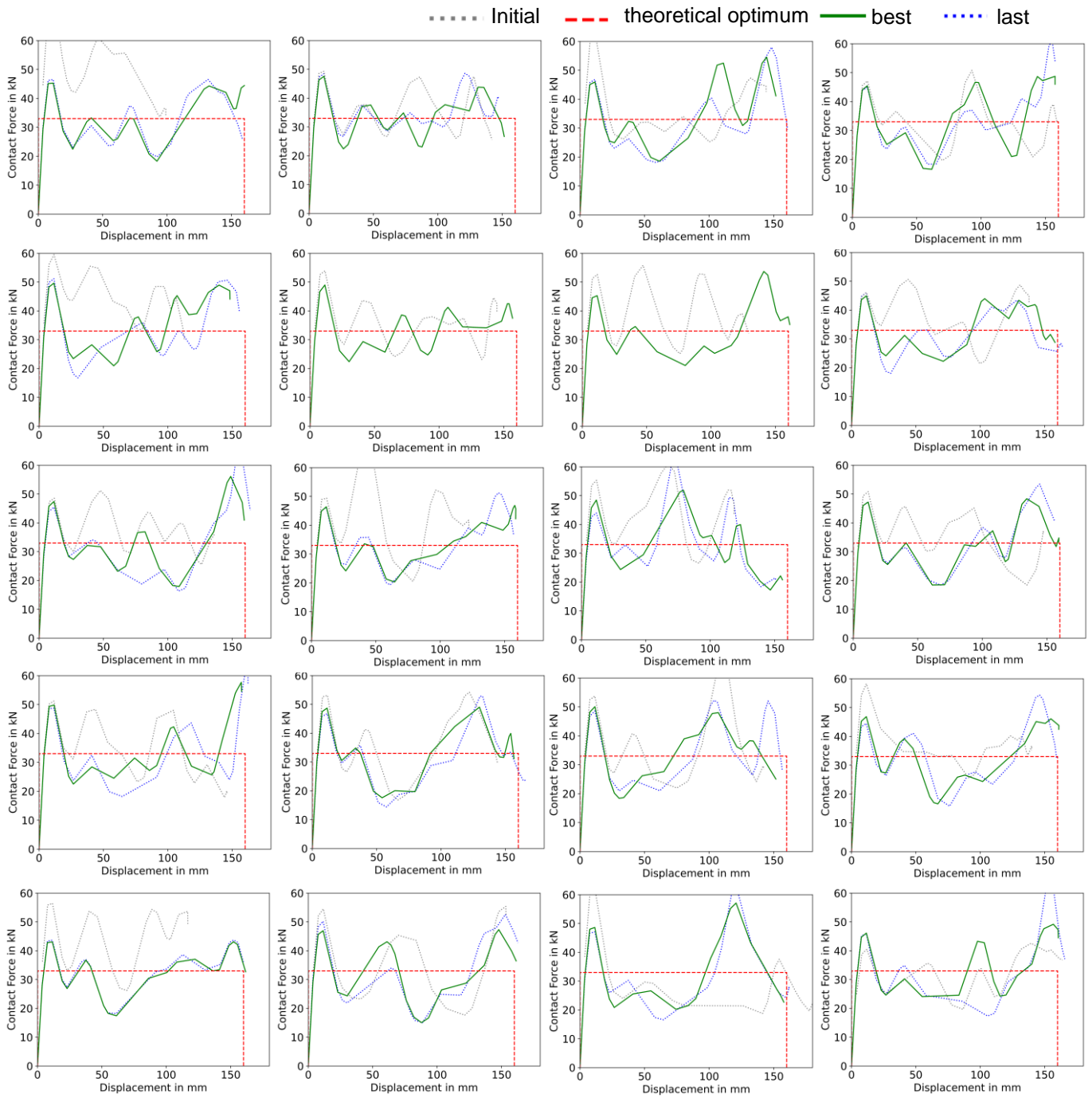
Figure 7.2: Crash box – contact force over displacement for the best designs $_{k^*}\mathbf{x}$ with $k^* \geq k_{\mathrm{L}}$ (green) and the last designs $k = 40$ (blue) of multistart runs 1-20 employing Inc

Figure 7.3: Crash box – contact force over displacement for the best designs $_{k^*}\mathbf{x}$ with $k^* \geq k_{\mathrm{L}}$ (green) and the last designs $k = 40$ (blue) of multistart runs 21-40 employing lnc

Figure 7.4: Crash box – contact force over displacement for the best designs $_{k^*}\mathbf{x}$ with $k^* \geq k_{\mathrm{L}}$ (green) and the last designs $k = 40$ (blue) of multistart runs 1-20 employing IncS

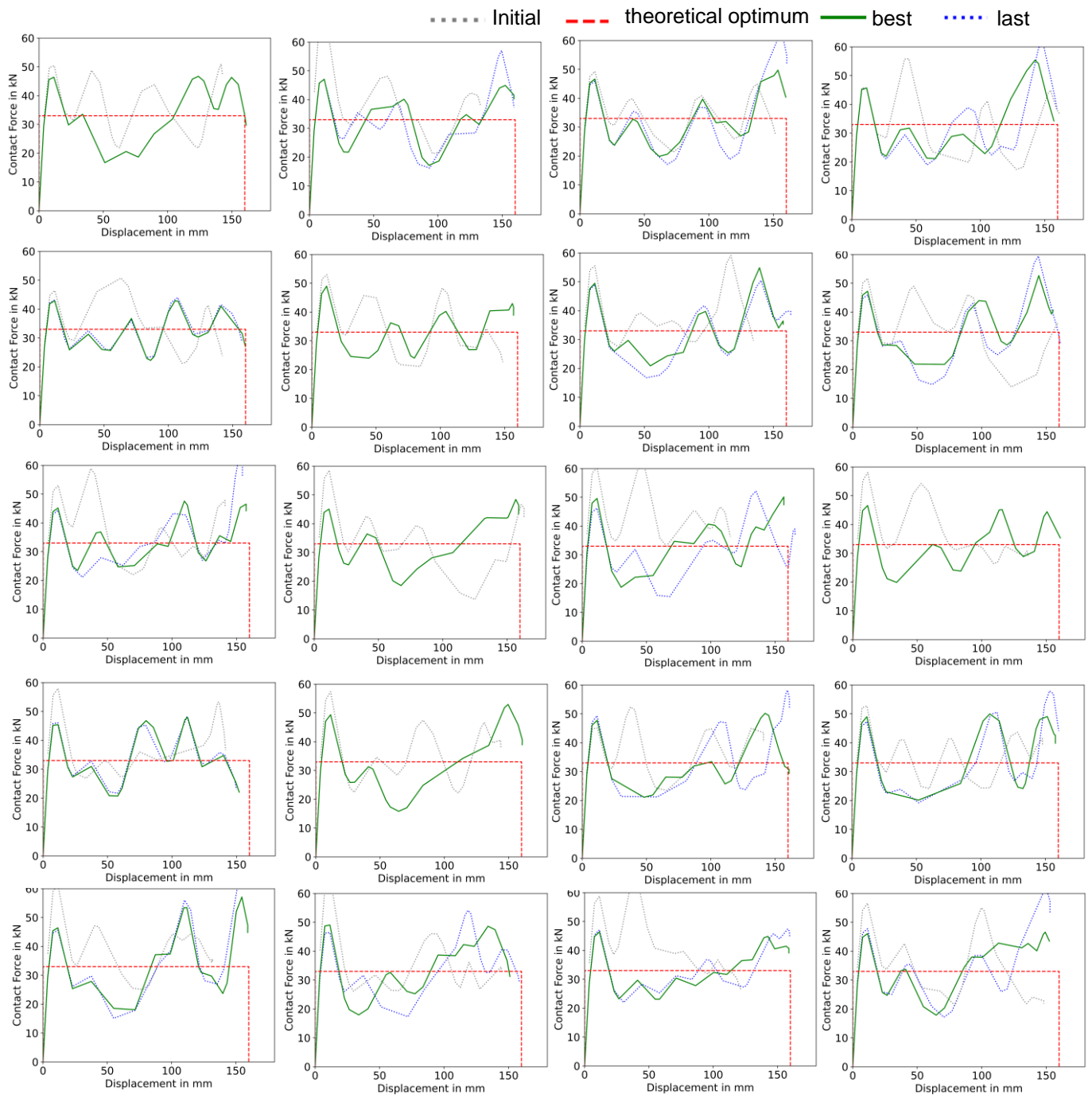Figure 7.5: Crash box – contact force over displacement for the best designs $_{k^*}\mathbf{x}$ with $k^* \geq k_{\mathrm{L}}$ (green) and the last designs $k = 40$ (blue) of multistart runs 21-40 employing lncS
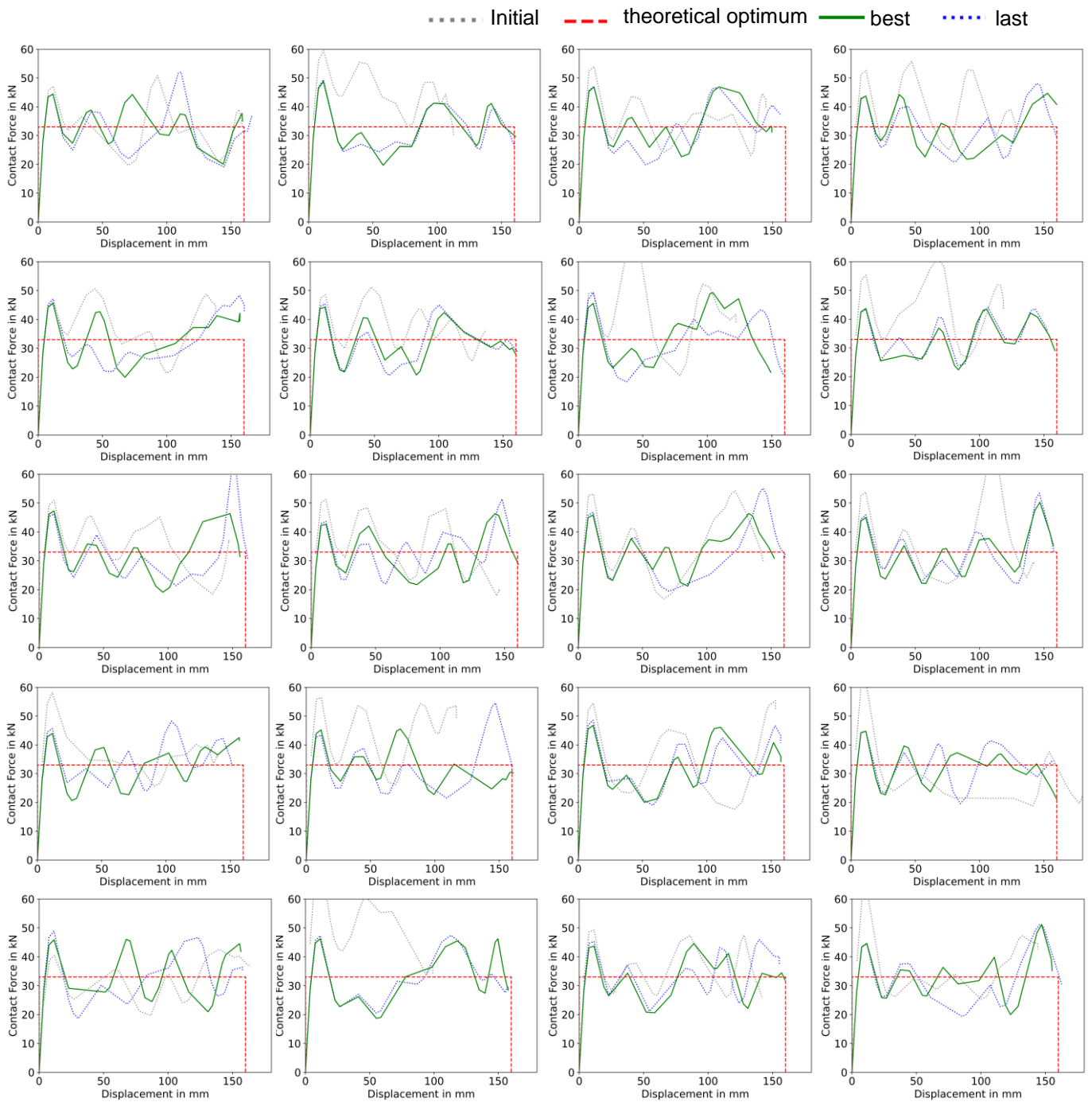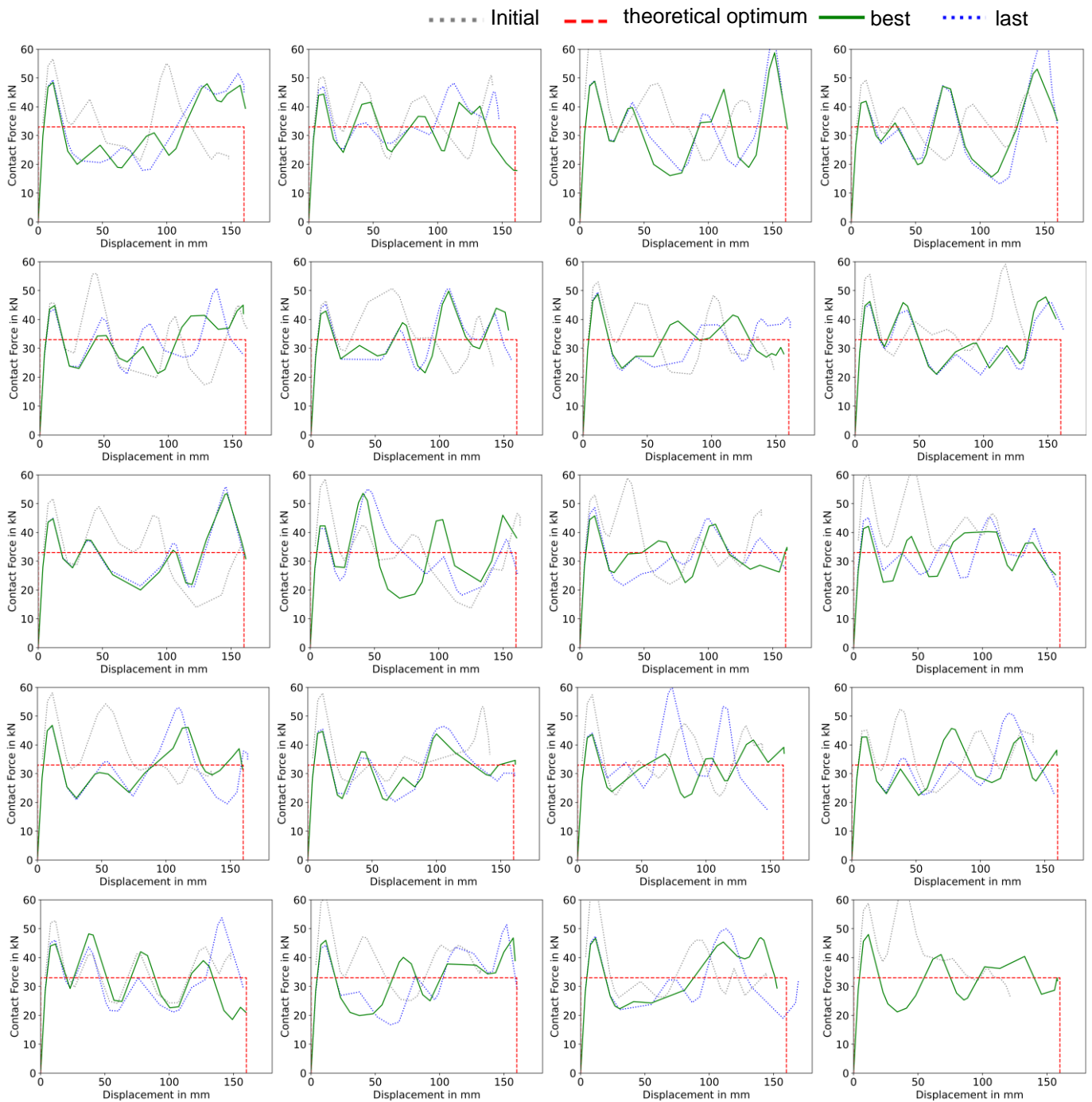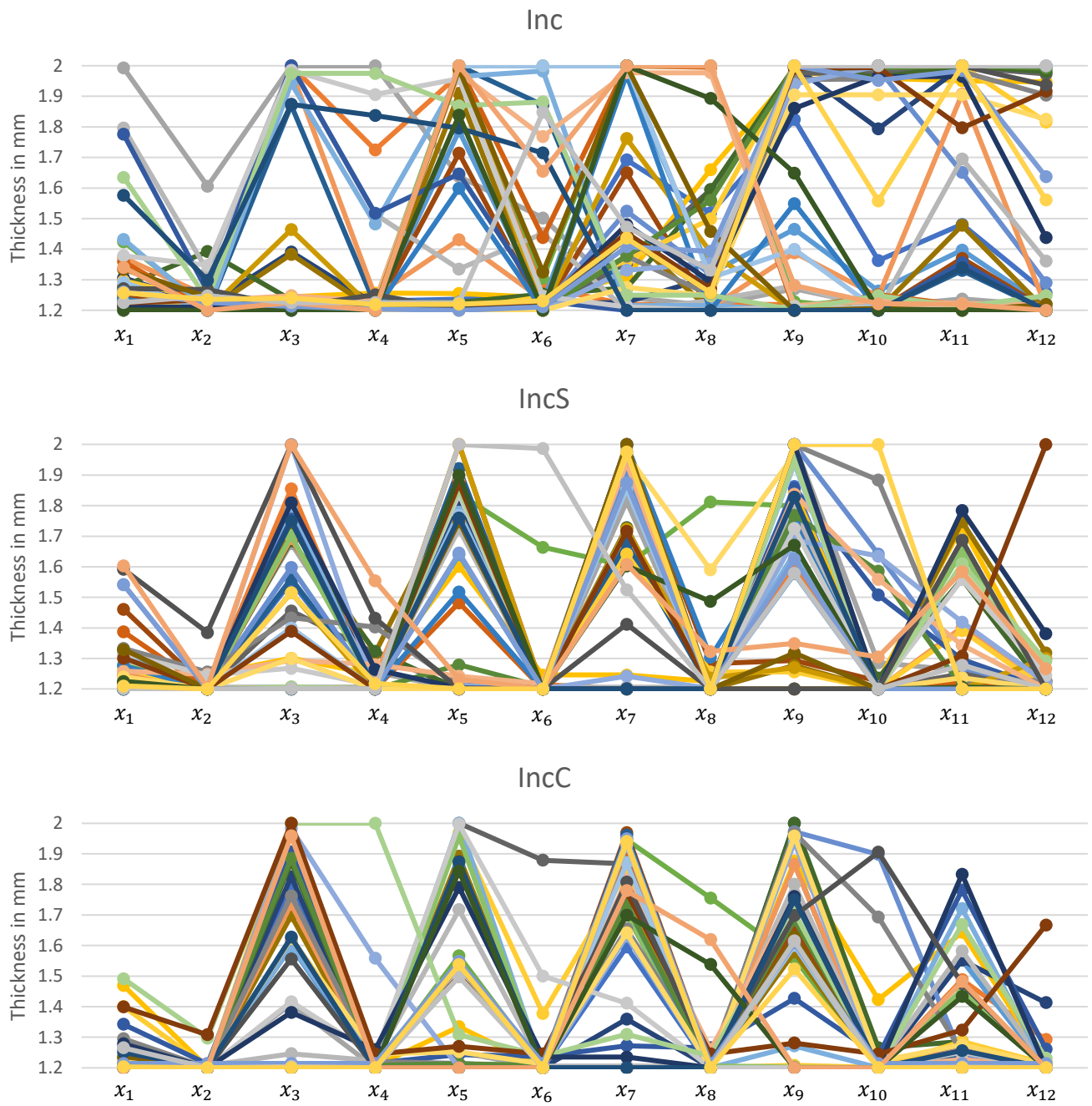
Figure 7.6: Crash box – best designs $_{k^*}\mathbf{x}$ with $k^* \geq k_L$ of all multistart runs employing Inc (top), IncS (middle), and IncC (bottom)

7.3 Side Impact B-Pillar

Table 7.7 reports the averaged elapsed compute times per cycle for $n_T = 6$ and $n_T = 20$ for the Side Impact B-Pillar model consisting of 22013 nodes.

Table 7.3: Averaged elapsed compute time per cycle for $n_T = 6$ and $n_T = 20$ on desktop computer with 48 CPU: Intel(R) Xeon(R) Silver 4116 CPU @ 2.10GHz, CPU speed 2100 MHz, 49368 MB RAM, 130468 MB swap

n_T	averaged time elapsed s	# cores
6	503	13
20	663	41

This is also illustrated in Fig. 7.7. Here, the total time is given as a stacked bar. Each part of the bar represents the averaged time per cycle of an computational operation as it was implemented in python. To get a connection to the previously described program flow, the program flow as implemented in Python is given in Fig. 7.8 and the major operations are briefly explained in the following. Each of these operations efforts pre- and post-processing steps, which are denoted by ".pre" and ".post", respectively:

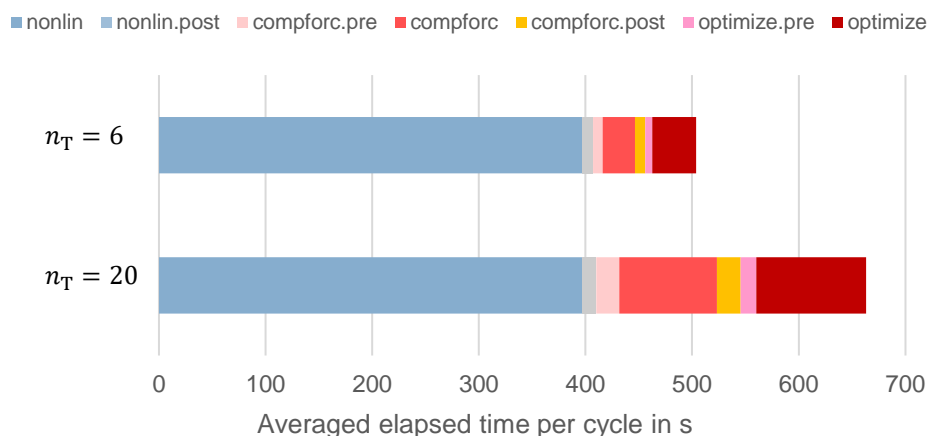|	
nonlin	Nonlinear dynamic analysis
comprgrid	Reconstruction of deformed meshes (not required in this example)
compforc	Calculation of ESLs
optimize	Linear static response optimization

Figure 7.7: Side Impact B-Pillar – elapsed compute time per cycle illustrated for different computational operations for different n_T
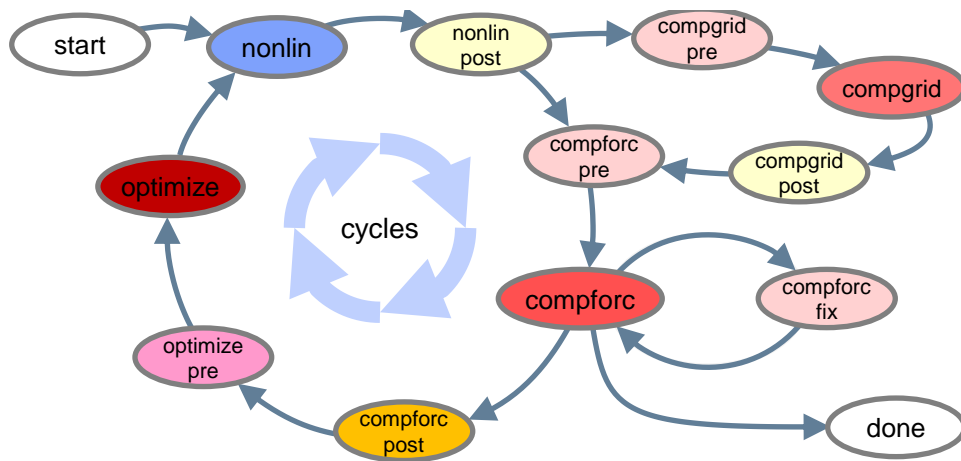
Figure 7.8: Program flow as implemented in Python

Bibliography

Allaire, Grégoire, François Jouve, and Anca Maria Toader (Feb. 2004). "Structural optimization using sensitivity analysis and a level-set method". In: *Journal of Computational Physics* 194.1, pp. 363–393. ISSN: 0021-9991. DOI: 10.1016/J.JCP.2003.09.032.

Arora, Jasbir Singh and Edward J Haug (1979). "Methods of design sensitivity analysis in structural optimization". In: *AIAA journal* 17.9, pp. 970–974.

Aulig, Nikola and Markus Olhofer (2016). "Evolutionary computation for topology optimization of mechanical structures: An overview of representations". In: *2016 IEEE Congress on Evolutionary Computation, CEC 2016*, pp. 1948–1955. DOI: 10.1109/CEC.2016.7744026.

Bai, Y. C., H. S. Zhou, F. Lei, and H. S. Lei (Jan. 2019). "An improved numerically-stable equivalent static loads (ESLs) algorithm based on energy-scaling ratio for stiffness topology optimization under crash loads". In: *Structural and Multidisciplinary Optimization* 59.1, pp. 117–130. ISSN: 16151488. DOI: 10.1007/s00158-018-2054-8.

Bathe, Klaus Jürgen (1996). *Finite Element Procedures*. ISBN: 0133014584.

Baumgartner, A., L. Harzheim, and C. Mattheck (Nov. 1992). "SKO (soft kill option): the biological way to find an optimum structure topology". In: *International Journal of Fatigue* 14.6, pp. 387–393. ISSN: 0142-1123. DOI: 10.1016/0142-1123(92)90226-3.

Belytschko, T, W K Liu, B Moran, and K Elkhodary (2014). *Nonlinear Finite Elements for Continua and Structures*. John wiley & sons. ISBN: 9781118632703.

Bendsøe, Martin P. (1989). "Optimal shape design as a material distribution problem". In: *Structural Optimization* 1.4, pp. 193–202. ISSN: 09344373. DOI: 10.1007/BF01650949.

Bendsøe, Martin P. and Noboru Kikuchi (1988). "Generating optimal topologies in structural design using a homogenization method". In: *Computer Methods in Applied Mechanics and Engineering* 71.2, pp. 197–224. ISSN: 00457825. DOI: 10.1016/0045-7825(88)90086-2.

Bendsøe, Martin P. and Ole Sigmund (1999). "Material interpolation schemes in topology optimization". In: *Archive of Applied Mechanics* 69.9-10, pp. 635–654. ISSN: 09391533. DOI: `10.1007/s004190050248`.

Bendsøe, Martin P. and Ole Sigmund (2003). *Topology optimization: theory, methods, and applications*. Springer Berlin, Heidelberg. ISBN: 978-3-540-42992-0. DOI: `10.1007/978-3-662-05086-6`.

Bendsøe, Martin P. and Carlos A. M. Soares (1993). *Topology design of structures*. Vol. 227. Springer, Dordrecht. DOI: `10.1007/978-94-011-1804-0`.

Beyer, F., D. Schneider, and A. Schumacher (2020). "Finding three-dimensional layouts for crashworthiness load cases using the graph and heuristic based topology optimization". In: *Structural and Multidisciplinary Optimization*. ISSN: 16151488. DOI: `10.1007/s00158-020-02768-0`.

Bourdin, Blaise and Antonin Chambolle (2003). "Design-dependent loads in topology optimization". In: *ESAIM - Control, Optimisation and Calculus of Variations* 9.January, pp. 247–273. ISSN: 12623377. DOI: `10.1051/cocv:2002070`.

Bujny, Mariusz (2020). "Level Set Topology Optimization for Crashworthiness using Evolutionary Algorithms and Machine Learning". Doctoral Thesis. Technische Universität München, pp. 1–275.

Choi, Woo Seok and Gyung Jin Park (2002). "Structural optimization using equivalent static loads at all time intervals". In: *Computer Methods in Applied Mechanics and Engineering* 191.19-20, pp. 2105–2122. ISSN: 00457825. DOI: `10.1016/s0045-7825(01)00373-5`.

Choi, Wook Han, Youngmyung Lee, Jong Min Yoon, Yong Ha Han, and Gyung Jin Park (2018). "Structural Optimization for Roof Crush Test Using an Enforced Displacement Method". In: *International Journal of Automotive Technology* 19.2, pp. 291–299. ISSN: 12299138. DOI: `10.1007/s12239-018-0028-x`.

Cressie, Noel (1988). "Spatial prediction and ordinary kriging". In: *Mathematical geology* 20.4, pp. 405–421.

Cressie, Noel (1990). "The origins of kriging". In: *Mathematical geology* 22.3, pp. 239–252.

Darwin, Charles (1859). *On the origin of species*. London: J. Murray.

De Borst, René, Mike A Crisfield, Joris J C Remmers, and Clemens V Verhoosel (2012). *Nonlinear finite element analysis of solids and structures*. John Wiley & Sons.

Euro NCAP (2022). *Euro NCAP | Full Width Rigid Barrier*. URL: `https://www.euroncap.com/en/vehicle-safety/the-ratings-explained/adult-occupant-protection/frontal-impact/full-width-rigid-barrier/`.

Faß, Markus (2017). "Roof crash performance optimization using the Equivalent Static Load Method". Unpublished Master's Thesis. Technical University Darmstadt.

Firl, Matthias and Kai-Uwe (Prof. Dr.) Bletzinger (2010). "Optimal Shape Design of Shell Structures". Doctoral Thesis. Technische Universität München.

Fletcher, R and C M Reeves (1964). "Function minimization by conjugate gradients". In: *The Computer Journal* 7.2, pp. 149–154. ISSN: 0010-4620. DOI: 10.1093/comjnl/7.2.149. URL: https://doi.org/10.1093/comjnl/7.2.149.

Gandikota, Imtiaz, Guilian Yi, and Willem Roux (2019). "LS-TaSC Application Crashworthiness and Lightweight Optimization of an Automotive". In: *FEA Information Engineering Solutions*. October. Livermore Software Technology Corporation, pp. 35–44.

Gerzen, N., P. M. Clausen, and Claus B. W. Pedersen (2016). "Sizing optimization for industrial applications and best practice design process". In: *High Performance and Optimum Design of Structures and Materials II* 1, pp. 41–49. DOI: 10.2495/hpsm160041.

Haftka, Raphael T and Howard M Adelman (1989). "Recent developments in structural sensitivity analysis". In: *Structural optimization* 1.3, pp. 137–151. DOI: 10.1007/BF01637334.

Haftka, Raphael T, Zafer Gürdal, and Manohar P Kamat (2012). *Elements of structural optimization*. 2nd ed. Vol. 11. Springer Dordrecht. ISBN: 978-94-015-7864-6. DOI: 10.1007/978-94-015-7862-2.

Harzheim, Lothar (2014). *Strukturoptimierung Grunlagen und Anwendungen*. 2nd ed. Haan-Gruiten: Europa-Lehrmittel (Verlag). ISBN: 978-3-8085-5882-9.

Höfler, A, U Leysser, and J Wiedeman (1973). "Optimization of the layout of trusses combining strategies based on Michell's theorem and on the biological principles of evolution". In: *Proceedings of the 2nd Symposium on Structural Optimization*. Milan, Italy.

Holland, John H (1992). *Adaptation in natural and artificial systems: an introductory analysis with applications to biology, control, and artificial intelligence*. MIT press. ISBN: 9780262581110.

Hong, E. P., B. J. You, C. H. Kim, and Gyung Jin Park (2010). "Optimization of flexible components of multibody systems via equivalent static loads". In: *Structural and Multidisciplinary Optimization* 40.1-6, pp. 549–562. ISSN: 1615147X. DOI: 10.1007/s00158-009-0384-2.

Hornik, Kurt, Maxwell Stinchcombe, and Halbert White (1990). "Universal approximation of an unknown mapping and its derivatives using multilayer feedforward networks". In: *Neural networks* 3.5, pp. 551–560.

Hornik, Kurt, Maxwell Stinchcombe, and Halbert White (1992). *Universal approximation of an unknown mapping and its derivatives.* Inc. Cambridge, Ma, USA: Blackwell. ISBN: 1557863296.

Hsieh, Ching Chieh and Jasbir Singh Arora (1984). "Design sensitivity analysis and optimization of dynamic response". In: *Computer methods in applied mechanics and engineering* 43.2, pp. 195–219.

Huang, X., Z.H. Zuo, and Y.M. Xie (2010). "Evolutionary topological optimization of vibrating continuum structures for natural frequencies". In: *Computers & Structures* 88.5-6, pp. 357–364. DOI: `10.1016/j.compstruc.2009.11.011`.

HyperWorks, Altair (2021). *OptiStruct-2021.1 user's guide*.

Ivarsson, Niklas, Mathias Wallin, and Daniel A. Tortorelli (2018). "Topology optimization of finite strain viscoplastic systems under transient loads". In: *International Journal for Numerical Methods in Engineering* 114.13, pp. 1351–1367. ISSN: 10970207. DOI: `10.1002/nme.5789`.

Jang, H. H., Hyun Ah Lee, J. Y. Lee, and Gyung Jin Park (Jan. 2012). "Dynamic response topology optimization in the time domain using equivalent static loads". In: *AIAA Journal* 50.1, pp. 226–234. ISSN: 00011452. DOI: `10.2514/1.J051256`.

Jeong, S. B., S. I. Yi, C. D. Kan, V. Nagabhushana, and Gyung Jin Park (2008). "Structural optimization of an automobile roof structure using equivalent static loads". In: *Proceedings of the Institution of Mechanical Engineers, Part D: Journal of Automobile Engineering*. ISSN: 09544070. DOI: `10.1243/09544070JAUTO855`.

Jeong, S. B., S. Yoon, S Xu, and G. J. Park (2010). "Non-linear dynamic response structural optimization of an automobile frontal structure using equivalent static loads". In: *Proceedings of the Institution of Mechanical Engineers, Part D: Journal of Automobile Engineering* 224.4, pp. 489–501.

Jonsson, Anders, Marcus Carlberg, and Tobias Eriksson (2019). "Roof-crush Analysis of the Volvo XC40 Using the Implicit Solver in LS-DYNA ®". In: *12th European LS-DYNA Conference 2019*. Koblenz.

Karev, Artem, Lothar Harzheim, Rainer Immel, and Matthias Erzgräber (2018). "Comparison of Different Formulations of a Front Hood Free Sizing Optimization Problem Using the ESL-Method". In: *Advances in Structural and Multidisciplinary Optimization*. Ed. by Axel Schumacher, Thomas Vietor, Sierk Fiebig, Kai-Uwe Bletzinger, and Kurt Maute. June. Cham: Springer International Publishing, pp. 933–951. ISBN: 978-3-319-67988-4. DOI: `10.1007/978-3-319-67988-4_71`.

Karev, Artem, Lothar Harzheim, Rainer Immel, and Matthias Erzgräber (2019). "Free sizing optimization of a front hood using the ESL method: overcoming challenges and traps". In: *Structural and Multidisciplinary Optimization*. ISSN: 16151488. DOI: `10.1007/s00158-019-02285-9`.

Kazanc, Zafer and Klaus Jürgen Bathe (2012). "Crushing and crashing of tubes with implicit time integration". In: *International Journal of Impact Engineering* 42, pp. 80–88. ISSN: 0734743X. DOI: 10.1016/j.ijimpeng.2011.10.003.

Kicinger, Rafal, Tomasz Arciszewski, and Kenneth De Jong (2005). "Evolutionary computation and structural design: A survey of the state-of-the-art". In: *Computers and Structures* 83.23-24, pp. 1943–1978. ISSN: 00457949. DOI: 10.1016/j.compstruc.2005.03.002.

Kim, Yong Il and Gyung Jin Park (2010). "Nonlinear dynamic response structural optimization using equivalent static loads". In: *Computer Methods in Applied Mechanics and Engineering* 199.9-12, pp. 660–676. ISSN: 00457825. DOI: 10.1016/j.cma.2009.10.014.

Kleiber, Michael, Tran Duong Hien, H Antúnez, and Piotr Kowalczyk (1997). *Parameter sensitivity in nonlinear mechanics: Theory and finite element computations*. John Wiley Son Limited. ISBN: 9780471968542.

Komkov, Vadim, Kyung K Choi, and Edward J Haug (1986). *Design sensitivity analysis of structural systems*. Vol. 177. Academic press.

Krige, Daniel G (1951). *A statistical approach to some basic mine valuation problems on the Witwatersrand*.

Lancaster, P and K Salkauskas (1981). "Surfaces Generated by Moving Least Squares Methods". In: *Mathematics of Computation* 37.155, pp. 141–158. DOI: 10.2307/2007507.

Lee, Hyun Ah, Yong Il Kim, Gyung Jin Park, R M Kolonay, M Blair, and R A Canfield (2007). "Structural optimization of a joined wing using equivalent static loads". In: *Journal of aircraft* 44.4, pp. 1302–1308.

Lee, Hyun Ah and Gyung Jin Park (2015). "Nonlinear dynamic response topology optimization using the equivalent static loads method". In: *Computer Methods in Applied Mechanics and Engineering* 283, pp. 956–970. ISSN: 00457825. DOI: 10.1016/j.cma.2014.10.015. URL: http://dx.doi.org/10.1016/j.cma.2014.10.015.

Lee, Jae Jun, Ui Jin Jung, and Gyung Jin Park (2013). "Shape optimization of the workpiece in the forging process using equivalent static loads". In: *Finite Elements in Analysis and Design* 69, pp. 1–18. ISSN: 0168874X. DOI: 10.1016/j.finel.2013.01.005. URL: http://dx.doi.org/10.1016/j.finel.2013.01.005.

LSTC (2006). *(Lifermore Software Technology Cooperation), LS-DYNA Theory Manual*.

LSTC (2015). *(Lifermore Software Technology Cooperation), LS-OPT User's Manual*.

Ma, Yanhua, Xueqian Chen, and Wenjie Zuo (2020). "Equivalent static displacements method for contact force optimization". In: *Structural and Multidisciplinary Optimization* 62. ISSN: 16151488. DOI: 10.1007/s00158-020-02500-y.

Martins, Joaquim R. R. A. and Andrew Ning (2021). *Engineering Design Optimization*. Cambridge University Press. DOI: 10.1017/9781108980647.

Matheron, Georges (1963). "Principles of geostatistics". In: *Economic geology* 58.8, pp. 1246–1266.

Michaleris, Panagiotis, Daniel A. Tortorelli, and Creto A. Vidal (1994). "Tangent operators and design sensitivity formulations for transient non-linear coupled problems with applications to elastoplasticity". In: *International Journal for Numerical Methods in Engineering* 37.14, pp. 2471–2499. ISSN: 10970207. DOI: 10.1002/nme.1620371408.

National Highway Traffic Safety Administration (2009). *Laboratory Test Procedure for FMVSS No . 216a , Roof Crush Resistance*. Tech. rep. Washington, DC: U.S. Department of Transportation.

Newmark, Nathan M (1959). "A method of computation for structural dynamics". In: *Journal of the engineering mechanics division* 85.3, pp. 67–94.

Ortmann, Christopher (2015). "Entwicklung eines graphen-und heuristikbasierten Verfahrens zur Topologieoptimierung von Profilquerschnitten für Crashlastfälle". Doctoral Thesis. Bergische Universität Wuppertal.

Ortmann, Christopher and Axel Schumacher (2013). "Graph and heuristic based topology optimization of crash loaded structures". In: *Structural and Multidisciplinary Optimization* 47.6, pp. 839–854. ISSN: 1615147X. DOI: 10.1007/s00158-012-0872-7.

Ortmann, Christopher, Johannes Sperber, Dominik Schneider, Simon Link, and Axel Schumacher (2021). "Crashworthiness design of cross-sections with the Graph and Heuristic based Topology Optimization incorporating competing designs". In: *Structural and Multidisciplinary Optimization* 64.3, pp. 1063–1077. ISSN: 1615-1488. DOI: 10.1007/s00158-021-02927-x. URL: https://doi.org/10.1007/s00158-021-02927-x.

Park, Gyung Jin (2011). "Technical overview of the equivalent static loads method for non-linear static response structural optimization". In: *Structural and Multidisciplinary Optimization* 43.3, pp. 319–337. ISSN: 1615147X. DOI: 10.1007/s00158-010-0530-x.

Park, Gyung Jin and B. S. Kang (2003). "Validation of a structural optimization algorithm transforming dynamic loads into equivalent static loads". In: *Journal of Optimization Theory and Applications* 118.1, pp. 191–200. ISSN: 00223239. DOI: 10.1023/A:1024799727258.

Park, Gyung Jin and Youngmyung Lee (2019). "Discussion on the optimality condition of the equivalent static loads method for linear dynamic response structural optimization". In: *Structural and Multidisciplinary Optimization* 59.1, pp. 311–316. ISSN: 16151488. DOI: 10.1007/s00158-018-2059-3.

Patel, Neal M (2007). "Crashworthiness design using Topology Optimization". Doctoral Thesis. University of Notre Dame.

Patel, Neal M, Byung-Soo Kang, John E Renaud, and Andrés Tovar (May 2009). "Crashworthiness Design Using Topology Optimization". In: *Journal of Mechanical Design* 131.6. ISSN: 1050-0472. DOI: 10.1115/1.3116256. URL: https://doi.org/10.1115/1.3116256.

Powell, Michael J D (1992). "The theory of radial basis function approximation in 1990, Advances in Numerical Analysis II: Wavelets, Subdivision, and Radial Functions (WA Light, ed.)" In: *Oxford University Press, Oxford* 105, pp. 105–210.

Rechenberg, Ingo (1970). "Optimierung technischer Systeme nach Prinzipien der biologischen Evolution". Doctoral Thesis. Technische Universität, Fakultät für Maschinenwissenschaft.

Rechenberg, Ingo (1994). *Evolutionsstrategie'94*. Ed. by G. Holzboog. Stuttgart: Friedrich Frommann Verlag. ISBN: 3772816428.

Roux, Willem (2016). "The LS- TaSC ™ Multipoint Method for Constrained Topology Optimization". In: *14 th International LS-DYNA Users Conference*. April, pp. 1–15.

Schumacher, Axel (2020). *Optimierung mechanischer Strukturen*. 3rd ed. Springer-Verlag. DOI: 10.1007/978-3-662-60328-4.

Schwarz, S (2001). "Sensitivitätsanalyse und Optimierung bei nichtlinearem Strukturverhalten". Doctoral Thesis. Universität Stuttgart. ISBN: 3000074198. URL: http://elib.uni-stuttgart.de/opus/volltexte/2001/825/.

Shin, Moon Kyun, Ki Jong Park, and Gyung Jin Park (2007). "Optimization of structures with nonlinear behavior using equivalent loads". In: *Computer Methods in Applied Mechanics and Engineering* 196.4-6, pp. 1154–1167. ISSN: 00457825. DOI: 10.1016/j.cma.2006.09.001.

Sigmund, Ole and Kurt Maute (Dec. 2013). *Topology optimization approaches: A comparative review*. DOI: 10.1007/s00158-013-0978-6.

Simo, Juan C and Thomas JR Hughes (2006). *Computational inelasticity*. Vol. 7. Springer Science & Business Media. ISBN: 978-0-387-22763-4. DOI: 10.1007/b98904.

Stander, Nielen (2001). "The successive response surface method applied to sheet-metal forming." In: *First MIT conference on computational fluid and solid mechanics*, pp. 481–485.

Stander, Nielen and K J Craig (2002). "On the robustness of a simple domain reduction scheme for simulation-based optimization". In: *Engineering Computations* 19.4, pp. 431–450.

Stolpe, Mathias (2014). "On the equivalent static loads approach for dynamic response structural optimization". In: *Structural and Multidisciplinary Optimization* 50.6, pp. 921–926. ISSN: 16151488. DOI: 10.1007/s00158-014-1101-3.

Stolpe, Mathias and Krister Svanberg (2001). "An alternative interpolation scheme for minimum compliance topology optimization". In: *Structural and Multidisciplinary Optimization* 22.2, pp. 116–124. ISSN: 1615-1488. DOI: 10.1007/s001580100129.

Stolpe, Mathias, Alexander Verbart, and Susana Rojas-Labanda (2018). "The equivalent static loads method for structural optimization does not in general generate optimal designs". In: *Structural and Multidisciplinary Optimization* 58.1, pp. 139–154. ISSN: 16151488. DOI: 10.1007/s00158-017-1884-0.

Svanberg, Krister (1987). "The method of moving asymptotes—a new method for structural optimization". In: *International Journal for Numerical Methods in Engineering* 24.2, pp. 359–373. ISSN: 10970207. DOI: 10.1002/nme.1620240207.

Tortorelli, Daniel A. and Panagiotis Michaleris (1994). "Design sensitivity analysis: Overview and review". In: *Inverse Problems in Engineering* 1.1, pp. 71–105. ISSN: 10290281. DOI: 10.1080/174159794088027573.

Tovar, Andrés, Neal M Patel, Glen L Niebur, Mihir Sen, and John E Renaud (2006). "Topology optimization using a hybrid cellular automation method with local control rules". In: *Journal of Mechanical Design, Transactions of the ASME* 128.6, pp. 1205–1216. ISSN: 10500472. DOI: 10.1115/1.2336251.

Triller, Jens (2019). "Improvement of the Equivalent Static Load Method Based on a Difference Approach". Unpublished Master's Thesis. Technical University Darmstadt.

Triller, Jens, Rainer Immel, and Lothar Harzheim (2020). "Nichtlineare dynamische Strukturoptimierung unter Berücksichtigung der Deformationsgeschichte mit differenzenbasierten äquivalenten statischen Lasten". In: *NAFEMS Online-Magazin* 55.3, pp. 74–80. ISSN: 2311-522X.

Triller, Jens, Rainer Immel, and Lothar Harzheim (2022a). "Difference-based Equivalent Static Load Method with adaptive time selection and local stiffness adaption". In: *Structural and Multidisciplinary Optimization* 65 (89). DOI: 10.1007/s00158-021-03160-2.

Triller, Jens, Rainer Immel, and Lothar Harzheim (2022b). "Topology optimization using difference-based equivalent static loads". In: *Structural and Multidisciplinary Optimization* 65 (226). ISSN: 1615-1488. DOI: 10.1007/s00158-022-03309-7.

Triller, Jens, Rainer Immel, Alexander Timmer, and Lothar Harzheim (2019). "Difference-based Equivalent Static Load (DiESL) Method , an extension of the ESL method to improve the nonlinear approximation quality". In: *Proceedings of the 13th World Congress of Structural and Multidisciplinary Optimization*. Beijing.

Triller, Jens, Rainer Immel, Alexander Timmer, and Lothar Harzheim (2021). "The difference-based equivalent static load method: an improvement of the ESL method's nonlinear approximation quality". In: *Structural and Multidisciplinary Optimization* 63.6, pp. 2705–2720. ISSN: 16151488. DOI: 10.1007/s00158-020-02830-x.

Van Keulen, F, R T Haftka, and N H Kim (2005). "Review of options for structural design sensitivity analysis. Part 1: Linear systems". In: *Computer methods in applied mechanics and engineering* 194.30-33, pp. 3213–3243.

Von Neumann, John (1951). "The General and Logical Theory of Automata, Cerebral Mechanisms in Behavior. The Hixon Symposium". In: *New York: John Wiley&Sons*.

Wang, Michael Yu, Xiaoming Wang, and Dongming Guo (Jan. 2003). "A level set method for structural topology optimization". In: *Computer Methods in Applied Mechanics and Engineering* 192.1-2, pp. 227–246. ISSN: 0045-7825. DOI: 10.1016/S0045-7825(02)00559-5.

Waszczyszyn, Zenon (1999). "Fundamentals of artificial neural networks". In: *Neural Networks in the Analysis and Design of Structures*. Ed. by Zenon Waszczyszyn. Springer Vienna, pp. 1–51. ISBN: 978-3-7091-2484-0. DOI: https://doi.org/10.1007/978-3-7091-2484-0_1.

Weider, Katrin, André Marschner, and Axel Schumacher (2017). "A Systematic Study on Topology Optimization of Crash Loaded Structures using LS-TaSC TM". In: *11th European LS-DYNA Conference 2017*. Salzburg.

Weider, Katrin and Axel Schumacher (2018). "A Topology Optimization Scheme for Crash Loaded Structures Using Topological Derivatives". In: *Advances in Structural and Multidisciplinary Optimization*, pp. 1601–1614. DOI: 10.1007/978-3-319-67988-4_120.

Weider, Katrin and Axel Schumacher (2019). "Adjoint Method for Topological Derivatives for Optimization Tasks with Material and Geometrical Nonlinearities". In: *EngOpt 2018 Proceedings of the 6th International Conference on Engineering Optimization*, pp. 867–878. DOI: 10.1007/978-3-319-97773-7_75.

Wriggers, P (1998). *Nonlinear finite element analysis of solids and structures*. Vol. 17. 6, p. 1044. ɪsʙɴ: 9780470666449. ᴅᴏɪ: `10.1016/s0997-7538(98)90517-4`.

Wriggers, P (2006). *Computational Contact Mechanics*. Vol. 2. Springer Berlin, Heidelberg. ɪsʙɴ: 978-3-540-32609-0. ᴅᴏɪ: `https://doi.org/10.1007/978-3-540-32609-0`.

Wu, Jun, Ole Sigmund, and Jeroen P. Groen (2021). "Topology optimization of multi-scale structures: a review". In: *Structural and Multidisciplinary Optimization* 63.3, pp. 1455–1480. ɪssɴ: 16151488. ᴅᴏɪ: `10.1007/s00158-021-02881-8`.

Xie, Y. M. and G. P. Steven (Dec. 1993). "A simple evolutionary procedure for structural optimization". In: *Computers and Structures* 49.5, pp. 885–896. ɪssɴ: 00457949. ᴅᴏɪ: `10.1016/0045-7949(93)90035-C`.

Zhou, Ming and G. I.N. Rozvany (1991). "The COC algorithm, Part II: Topological, geometrical and generalized shape optimization". In: *Computer Methods in Applied Mechanics and Engineering* 89.1-3, pp. 309–336. ɪssɴ: 00457825. ᴅᴏɪ: `10.1016/0045-7825(91)90046-9`.